



## City Research Online

### City, University of London Institutional Repository

---

**Citation:** Malgarinos, I. (2017). Development of a two-phase flow model for the investigation of collisions between heavy gasoil droplets and catalytic particles in Fluid Catalytic Cracking Reactors. (Unpublished Doctoral thesis, City, University of London)

This is the accepted version of the paper.

This version of the publication may differ from the final published version.

---

**Permanent repository link:** <http://openaccess.city.ac.uk/19271/>

**Link to published version:**

**Copyright and reuse:** City Research Online aims to make research outputs of City, University of London available to a wider audience. Copyright and Moral Rights remain with the author(s) and/or copyright holders. URLs from City Research Online may be freely distributed and linked to.

---

City Research Online:

<http://openaccess.city.ac.uk/>

[publications@city.ac.uk](mailto:publications@city.ac.uk)

---

**Development of a two-phase flow model for  
the investigation of collisions between heavy  
gasoil droplets and catalytic particles in Fluid  
Catalytic Cracking Reactors**

**Ilias Malgarinos**

Thesis submitted for the fulfilment of the requirements for  
the Degree of Doctor of Philosophy

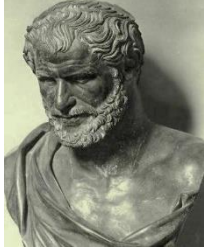


School of Mathematics, Computer Science &  
Engineering

Department of Mechanical Engineering & Aeronautics

December 2017





*“Τα πάντα ρει...” Translation: “Everything flows...”*

Heraclitus of Ephesus, 535 - 475 BC.

Bust of Heraclitus by National Archaeological Museum of Naples. Licensed under CC BY-SA 3.0.



*...to my family...*



# Contents

<b>Contents</b> .....	<b>vii</b>
<b>List of Figures</b> .....	<b>xi</b>
<b>List of Tables</b> .....	<b>xix</b>
<b>Acknowledgements</b> .....	<b>xxi</b>
<b>Declaration</b> .....	<b>xxiii</b>
<b>Abstract</b> .....	<b>xxv</b>
<b>Nomenclature</b> .....	<b>xxvii</b>
<b>Chapter 1 Introduction</b> .....	<b>1</b>
1.1 Background and Motivation.....	1
1.2 Literature review of relevant studies .....	3
1.2.1 Large scale FCC reactor simulations .....	3
1.2.2 Droplet-particle collisions in FCC reactor simulations.....	5
1.2.3 Droplet impingement on flat and spherical surfaces .....	6
1.2.3.1 Flat surfaces .....	6
1.2.3.2 Spherical surfaces .....	8
1.3 Flow field in the injection zone .....	10
1.3.1 Operating conditions .....	10
1.3.2 Non-dimensional Numbers.....	11
1.3.3 Chemical reactions and lumping .....	11
1.4 State of the art in two-phase flow models .....	12
1.4.1 Interface modelling.....	12
1.4.2 Advection modelling .....	13
1.4.3 Surface tension modelling .....	14
1.4.4 Wettability Modelling .....	16
1.4.5 Evaporation Modelling .....	17
1.5 Summary.....	19



1.6 Scope of PhD thesis .....	19
1.7 Thesis Outline .....	20
<b>Chapter 2 Numerical Methodology.....</b>	<b>21</b>
2.1 Fluid flow and Volume of Fluid .....	21
2.2 Phase change evaporation model.....	23
2.3 Surface Reactions .....	27
2.4 Dynamic local grid refinement.....	27
2.4.1 Distance Function.....	29
2.4.1.1 Accurate Distance.....	29
2.4.1.2 Fast marching algorithm for the computation of iso-surfaces .....	29
2.4.2 Refinement/Coarsening .....	31
2.5 Wettability.....	33
2.5.1 Contact angle as Boundary Condition.....	33
2.5.1.1 Quasi-dynamic contact angle mode.....	34
2.5.1.2 Kistler’s law .....	35
2.5.1.3 Shikhmurzaev’s model .....	35
2.5.2 Wetting Force Model .....	36
2.6 Sharpening Equation .....	39
2.7 Mass Conservation Algorithm .....	42
2.8 Droplet Initialization.....	43
2.9 Model development using UDFs.....	44
<b>Chapter 3 Model Validation under realistic droplet flow conditions</b> .....	<b>47</b>
3.1 Benchmark cases .....	47
3.1.1 Introduction .....	47
3.1.2 Zalesak’s disk.....	49
3.1.3 Single Vortex in a deformation field .....	51
3.1.4 Conclusions .....	53
3.2 Gravitational acceleration of a free-falling droplet .....	54
3.2.1 Introduction .....	54
3.2.2 Analytical solution.....	54
3.2.3 Numerical domain.....	56
3.2.4 Cases studied.....	56

3.2.5 CFD results .....	58
3.2.6 Conclusions .....	63
<b>3.3 Isothermal droplet impingement onto a flat surface .....</b>	<b>64</b>
3.3.1 Introduction .....	64
3.3.2 Cases studied .....	64
3.3.3 Numerical domain .....	65
3.3.4 CFD results .....	66
3.3.4.1 Grid size verification .....	66
3.3.4.2 Global performance of WFM .....	68
3.3.4.3 Dynamic contact angle evolution .....	69
3.3.4.4 Wetting force magnitude vs surface tension.....	70
3.3.4.5 Spreading on hydrophobic surfaces .....	71
3.3.4.6 Spreading on hydrophilic surfaces.....	76
3.3.4.7 Impact at very low Weber numbers .....	81
3.3.5 Conclusions .....	82
<b>3.4 Isothermal droplet impingement onto a spherical surface .....</b>	<b>82</b>
3.4.1 Introduction .....	82
3.4.2 Cases studied .....	83
3.4.3 Numerical domain .....	84
3.4.4 CFD results .....	86
3.4.4.1 Reference case-droplet rebound .....	86
3.4.4.2 Droplet-particle collisions for varying DTP and We .....	88
3.4.4.3 Liquid film thickness .....	94
3.4.4.4 Particle wetted area.....	95
3.4.5 Conclusions .....	96
<b>Chapter 4 Single droplet-particle collisions in FCC injection zone ...</b>	<b>97</b>
4.1 Introduction .....	97
4.1.1 Cracking Reactions.....	97
4.1.2 Liquid/Gas Properties .....	99
4.2 Cases studied .....	100
4.3 Numerical domain .....	101
4.4 CFD results .....	103
4.4.1 Equally sized droplet-particle collisions, DTP=1 .....	103
4.4.1.1 Droplet deformation .....	103
4.4.1.2 Effect of impact velocity and temperature on gas layer thickness .....	105

4.4.1.3 Induced Vortex rings .....	107
4.4.1.4 Cracking Yields.....	108
4.4.2 Double sized droplet-particle collisions, DTP=2.....	109
4.4.2.1 Droplet deformation and gas layer thickness .....	109
4.4.2.2 Cracking Yields.....	110
4.4.3 Global Performance of the model.....	111
4.5 Conclusions.....	113
<b>Chapter 5 3D droplet-particle cluster collisions in FCC injection zone</b> .....	<b>115</b>
5.1 Introduction.....	115
5.2 Cases studied.....	115
5.3 Numerical domain .....	116
5.4 CFD results.....	118
5.4.1 Equally sized droplet-particle collisions, DTP=1.....	118
5.4.1.1 Droplet deformation and gas layer thickness (2D vs 3D).....	118
5.4.1.2 Cracking Yields and global parameters (2D vs 3D).....	121
5.4.2 Double sized droplet-particle collisions, DTP=2.....	121
5.4.2.1 Droplet deformation and gas layer thickness (2D vs 3D).....	121
5.4.2.2 Cracking Yields (2D vs 3D) .....	123
5.4.3 Droplet-particle cluster collisions .....	124
5.4.3.1 Droplet deformation and gas layer thickness .....	124
5.4.3.2 Velocity field and vortex rings.....	127
5.4.3.3 Cracking Yields and global parameters .....	128
5.5 Conclusions.....	130
<b>Chapter 6 Conclusions and future work .....</b>	<b>133</b>
6.1 Conclusions.....	133
6.2 Future Work .....	135
<b>Appendix A WFM implementation details .....</b>	<b>139</b>
<b>Appendix B Properties of fluids used in the Thesis .....</b>	<b>141</b>
<b>Appendix C Validation of the evaporation model .....</b>	<b>143</b>
<b>Contributions .....</b>	<b>147</b>
<b>Bibliography .....</b>	<b>149</b>

# List of Figures

<b>Figure 1.1:</b> FCC unit petroleum refineries. Riser reactor and regenerator. Reproduced from [2] with permission from the Royal Society of Chemistry.....	2
<b>Figure 1.2:</b> Flow reactor hydrodynamics. Reprinted from [4] with permission from Elsevier.....	4
<b>Figure 1.3:</b> Outcomes of droplet impingement on a solid flat surface. Image taken from [27]. Courtesy of Begell House, Inc. ....	6
<b>Figure 1.4:</b> a) Mean path of injected droplets and b) Operating conditions of droplet-particle collisions.....	10
<b>Figure 1.5:</b> Differences between Eulerian, Lagrangian and Eulerian-Lagrangian approaches.....	12
<b>Figure 2.1:</b> a) Interface cells that evaporate, b) Cell on direction that represents conditions outside of interface.....	25
<b>Figure 2.2:</b> Dynamic local grid refinement applied at the case of a droplet impinging onto a solid flat surface. ....	27
<b>Figure 2.3:</b> Number of computational cells when using the local refinement technique for 1 level of refinement in comparison with uniform refinement. ....	28
<b>Figure 2.4:</b> Local refinement algorithm. Specific width is given for each level of refinement. ....	28
<b>Figure 2.5:</b> a) Schematic representation of the fast marching algorithm steps to calculate distance function starting from a single cell; step 1: red, step 2: blue and step 3: light blue. b) Calculation of the distance function at a random cell located far from the interface...	30
<b>Figure 2.6:</b> Splitting algorithm. Hanging node adaption .....	32
<b>Figure 2.7:</b> Unit vectors on the wall face, as well as unit free surface normal vector. ....	33
<b>Figure 2.8:</b> Adhesion force. a) Droplet sliding down an incline. At the moment it starts moving, $f_{adh} = mg \sin \alpha$ . b) Projection of the contact area of the droplet on the incline. Reprinted with permission from [171] Copyright 2009 American Chemical Society.....	36
<b>Figure 2.9:</b> Direction of the proposed adhesion term at the contact line for dynamic conditions: $f_{WFM}$ points to the left/right until $\theta_{eq}$ is reached. ....	37
<b>Figure 2.10:</b> Outline of the Sharpening scheme used.....	41

<b>Figure 2.11:</b> Cell categories used in the mass conservation algorithm. ....	42
<b>Figure 2.12:</b> Volume fraction initialization at the interface cells, a) points to approximate volume fraction value b) point is inside the cell.....	44
<b>Figure 3.1:</b> Comparison between a) CICSAM and b) Modified-HRIC discretization schemes for predicting the absolute velocity of a free-falling droplet after 30ms of simulation time (initial zero velocity). The volume fraction field is also plotted (gray-scale), values between 0.001 and 0.999.....	48
<b>Figure 3.2:</b> Initial domain and dimensions for Zalesak’s disk benchmark case. ....	49
<b>Figure 3.3:</b> Zalesak’s disk after one revolution. Isoline of $\alpha=0.5$ is plotted, together with the reference shape.....	50
<b>Figure 3.4:</b> Initial domain and dimensions for Single Vortex benchmark case and exact solution at $t=2.5$ . ....	51
<b>Figure 3.5:</b> Single Vortex case at $t=2.5$ . Isolines of $\alpha=0.1, 0.5, 0.9$ are plotted. ....	52
<b>Figure 3.6:</b> Temporal evolution of a) velocity and b) displacement of a single droplet accelerated by gravity. Results of the 1-D analytical solution. ....	55
<b>Figure 3.7:</b> a) Initial Domain + Boundary conditions for the free-falling droplet case. b) grid locally refined around interface. ....	56
<b>Figure 3.8:</b> Temporal evolution of droplet velocity as calculated from CFD compared with the 1-D analytical solution. Cases1-4. ....	58
<b>Figure 3.9:</b> Comparison between different methods (Cases1a-4a) with locRef4 for predicting the volume fraction field at $t=200$ ms. Volume fraction values between 0.001 and 0.999 are shown. ....	59
<b>Figure 3.10:</b> Comparison between Cases1c and 3c, for the prediction of a-b) relative velocity field, as well as the volume fraction field values between 0.001 and 0.999 and c-d) velocity vectors at a zoomed region (reference vector inside black circle has magnitude 1.394m/s). ....	60
<b>Figure 3.11:</b> a) Temporal evolution of droplet velocity as calculated from CFD compared to the 1-D analytical solution. Relative velocity streamlines are depicted for a) Case5 b) Case6 at $t=500$ ms. ....	61
<b>Figure 3.12:</b> Boundary layer in droplet interface. Cases4a,b,c at $t=200$ ms. Velocity vectors have the same units. ....	62
<b>Figure 3.13:</b> Comparison of internal (liquid) and external (gas) recirculation. Simulation results for Case7 obtained after 5ms of run. Image on the right taken from [182] Courtesy of ASME (Figure2b, $Re=100, \rho_l/\rho_g=7$ ). ....	63

<b>Figure 3.14:</b> a) Initial Domain + Boundary conditions for all cases, b) Depiction of the local refinement technique. ....	66
<b>Figure 3.15:</b> Effect of grid size for Cases a) 1. LW-HCA-HH and b) 7. LW-MCA-LH of Table 3.7. Comparison against a) experimental/numerical data from [54], b) experimental data [113]. ....	67
<b>Figure 3.16:</b> Summary of simulation results with the use of WFM model. a) Droplet maximum spreading plotted against the experimental values, b) Maximum spreading plotted against experimental values and results of Eq 3-10. ....	68
<b>Figure 3.17:</b> Contact line velocity temporal evolution for Case1. LW-HCA-HH. ....	70
<b>Figure 3.18:</b> Surface tension and wetting force vectors predicted by a) Kistler’s model and b) WFM for Case2 (MW-HCA-HH) at t=2.7ms. Ref. vector $\rightarrow (1.6e+07N/m^3)$ . Yellow, pink and blue lines represent 0.1, 0.5, 0.9 $\alpha$ isolines respectively. ....	71
<b>Figure 3.19:</b> Surface tension and wetting force vectors predicted by a) Kistler’s model and b) WFM for Case9 (HW-MCA-HH) at t=3.1ms. Ref. vector $\rightarrow (3e+07N/m^3)$ . Yellow, pink and blue lines represent 0.1, 0.5, 0.9 $\alpha$ isolines respectively. ....	71
<b>Figure 3.20:</b> Comparison of WFM results and predictions from dynamic contact angle models against experimental/simulation data for the hydrophobic surfaces of Cases1-4 listed in Table 3.7 (where references can be found). ....	72
<b>Figure 3.21:</b> Comparison of WFM results against experimental data for Case3.MW-HCA-LH. Experimental images taken from [43], Courtesy of Springer. $C_p$ contour and velocity vectors colored by velocity magnitude are plotted. $C_p$ values below 0.01 are cutoff. The first $C_p$ contour legend applies to the first two images, while the second one applies to all the following. ....	74
<b>Figure 3.22:</b> Comparison of WFM results against experimental data for Case4. HW-HCA-LH. Experimental images reproduced from [58] with permission from AIP Publishing LLC. $C_p$ contour and velocity vectors colored by velocity magnitude are plotted. $C_p$ values below 0.01 are cutoff. The first contour legends apply to the first image, while the second one applies to all the other. ....	75
<b>Figure 3.23:</b> Non-dimensional spreading diameter from WFM simulation plotted against non-dimensional time for hydrophobic surfaces. $\theta_{adv} = 105^\circ - 120^\circ$ . $We = 8-91$ , x-axis, logarithmic scale. ....	76
<b>Figure 3.24:</b> Comparison of WFM results and predictions from dynamic contact angle models against experimental/simulation data for the hydrophilic surfaces of cases 5,7-9 listed in Table 3.7 (where references can be found). ....	77

<b>Figure 3.25:</b> Prediction of “hysteresis” time for WFM in comparison to Adv-Rec model. Velocity vectors colored by velocity magnitude are plotted. Quicker recoiling phase is predicted by the WFM. ....	78
<b>Figure 3.26:</b> Comparison of WFM results against experimental data for Case5. VLW-MCA-LH. Experimental images reprinted from [113] with permission from Elsevier. $C_p$ contour and velocity vectors colored by velocity magnitude are plotted. $C_p$ values below 0.01 are cutoff. ....	79
<b>Figure 3.27:</b> Comparison of WFM results against experimental data for Case7. LW-MCA-LH. Experimental images reprinted from [113] with permission from Elsevier. $C_p$ contour and velocity vectors colored by velocity magnitude are plotted. $C_p$ values below 0.01 are cutoff. ....	80
<b>Figure 3.28:</b> Non-dimensional spread factor from WFM simulation plotted against non-dimensional time for hydrophilic surfaces. $\theta_{adv}= 10^\circ-70^\circ$ . $We=0.2-117$ , x-axis, logarithmic scale. ....	81
<b>Figure 3.29:</b> Comparison of simulated results for very low Weber numbers. ....	81
<b>Figure 3.30:</b> Computational domain along with the applied boundary conditions. ....	84
<b>Figure 3.31:</b> Computational grid used for a) the validation cases 1,1a and b) cases 2-9. ....	85
<b>Figure 3.32:</b> Same cell width achieved by using the appropriate locRef levels. a) cases 1-3, locRef4, b) cases 4-6, locRef3, c) cases 7-9, locRef2. $\tau=0$ . ....	85
<b>Figure 3.33:</b> a) Spreading diameter $D_w$ definition for spherical particle impacts; b) Temporal evolution of dimensionless droplet spreading diameter compared to experimental data and simulation results taken from Mitra et al. [21]. ....	86
<b>Figure 3.34:</b> Comparison between experimental photos (left) and simulation results (center) as reprinted from [21] with permission from Elsevier against the present simulation results (right). ....	87
<b>Figure 3.35:</b> a) Droplet-particle collision outcomes for cases 1-9. b) $We$ -DTP collision outcome map. Circle, ‘x’ markers denote coating/rebound regime respectively. ....	88
<b>Figure 3.36:</b> Effect of $We$ number on the dimensionless wetting diameter for cases 1-3. ....	89
<b>Figure 3.37:</b> Effect of $We$ number on the liquid phase mean velocity along the drop-particle axis (z direction) for cases 1-3. ....	90
<b>Figure 3.38:</b> Temporal evolution of drop-particle collision for Case5 (DTP=0.62_We=40). Drop iso-surface ( $\alpha=0.5$ ) and symmetry plane $y=0$ coloured by the dimensionless velocity magnitude. Values below 0.15 are cut-off. ....	91

<b>Figure 3.39:</b> Droplet-particle collision mechanism (coating, mass accumulation and satellite drop formation) shown for Case5 (DTP=0.62_We=40). .....	91
<b>Figure 3.40:</b> a, b) Evolution of thin film break-up and c) close up view of the break-up region. ...	92
<b>Figure 3.41:</b> Temporal evolution of $C_p$ for Case5 (DTP=0.62_We=40) at slices $x=0$ and symmetry plane $y=0$ .....	93
<b>Figure 3.42:</b> Effect of We number on the liquid phase mean velocity along the drop-particle axis (z direction) for a) cases4-6 and b) cases7-9.....	93
<b>Figure 3.43:</b> a) Definition of film thickness calculation at impact point, b, c, d) predicted non-dimensional film-thickness for cases 1-3, 4-6 and 7-9, respectively. ....	94
<b>Figure 3.44:</b> Temporal evolution of drop-particle wetted area coverage for cases 1-9 (We=8-80 and DTP=0.31-1.24). ....	95
<b>Figure 4.1:</b> Steps of catalytic cracking reaction. ....	98
<b>Figure 4.2:</b> Cracking path used in this work. From gasoil liquid to gasoline gas.....	99
<b>Figure 4.3:</b> Computational domain used for the simulated cases. ....	101
<b>Figure 4.4:</b> Gasoil gas mass fraction initialization. ....	103
<b>Figure 4.5:</b> Effect of impact velocity on collision outcome for wall temperature 800K, Case1 (top), Case3 (bottom). Contour of the produced gasoline mass fraction (kg-gasoline/kg-gas). ....	104
<b>Figure 4.6:</b> Effect of impact velocity on collision outcome for wall temperature 1000K, Case2 (top), Case4 (bottom). Contour of the produced gasoline mass fraction (kg-gasoline/kg-gas). Close up to the resolved gas layer cell thickness.....	104
<b>Figure 4.7:</b> Breakup of the liquid sheet for cases 1-4. Case1 (up-left) - Case2 (up- right) – Case3 (bottom-left) – Case4(bottom-right). Contour of the produced gasoline mass fraction (kg-gasoline/kg-gas). ....	105
<b>Figure 4.8:</b> a) Definition of the vapour layer thickness at the impact point, b) Temporal evolution of the vapour layer thickness at the impact point for cases 1-4.....	106
<b>Figure 4.9:</b> Vortex rings formed during impingement for a) Case1 (low impact velocity) and b) Case3 (high impact velocity) for wall temperature 800K at $\tau=1.7$ . Figures coloured with gasoil vapour mass fraction (kg-gasoil vapour/kg-gas, blue colour denotes zero gasoil vapor, i.e. pure liquid phase). ....	107
<b>Figure 4.10:</b> a) Percentage of gasoil converted to gasoline yield (kg-gasoline/kg-liq %) and b) cracking reaction rate, both plotted against non-dimensional time for cases 1-4. ....	108



<b>Figure 4.11:</b> Effect of impact velocity on collision outcome for wall temperature 800K, Case5 (top), Case7 (bottom). Contour of the produced gasoline mass fraction (kg-gasoline/kg-gas). .....	109
<b>Figure 4.12:</b> Effect of impact velocity on collision outcome for wall temperature 1000K, Case6 (top), Case8 (bottom). Contour of the produced gasoline mass fraction (kg-gasoline /kg-gas).....	109
<b>Figure 4.13:</b> Temporal evolution of vapour layer thickness at impact point for cases 5-8. ....	110
<b>Figure 4.14:</b> a) Percentage of gasoil converted to gasoline yield (kg-gasoline/kg-liq %) and b) cracking reaction rate, both plotted against non-dimensional time for cases 5-8. ....	111
<b>Figure 4.15:</b> Droplet a) mass and b) temperature evolution for all cases, (solid lines-DTP1, dashed lines-DTP2). .....	112
<b>Figure 4.16:</b> a) Definition of drop maximum radial deformation, b) Temporal evolution of the maximum radial deformation for all cases 1-8 (solid lines-DTP1, dashed lines-DTP2). .....	112
<b>Figure 4.17:</b> Droplet mass weighted velocity non-dimensionalized with impact velocity for all cases 1-8, (solid lines-DTP1, dashed lines-DTP2).....	113
<b>Figure 4.18:</b> a) Definition of liquid film thickness, b) Temporal evolution of the non-dimensional liquid film thickness for all cases 1-8 (solid lines-DTP1, dashed lines-DTP2). ....	113
<b>Figure 5.1:</b> Computational domain used for cases a) 2* and b) 4*. Bottom plane coloured by gasoil vapour initial mass fraction. ....	116
<b>Figure 5.2:</b> a) Computational domain used for the simulation of Case9. b) Particle cluster arrangement and notation used. ....	117
<b>Figure 5.3:</b> Effect of CFD simulation dimensions on collision outcome for a DTP=1, $U_0=15\text{m/s}$ , $T_p=1,000\text{K}$ impact, Case2 (top), Case2* (bottom). Contour of the produced gasoline mass fraction (kg-gasoline/kg-gas). The iso-surface of $\alpha=0.5$ is depicted for the 3D case (bottom). .....	118
<b>Figure 5.4:</b> Formation of finger structures ( $\tau=2.1$ ) and sudden break-up ( $\tau=2.9$ ) are predicted in Case2* (3D). Gasoil vapour mass fraction (kg-gasoil/kg-gas) is depicted on the symmetry boundary. Corresponding images from the revolution of 2D-axi results for 3D representation are added on top of the figure. ....	119
<b>Figure 5.5:</b> Effect of CFD simulation dimensions on collision outcome for a DTP=1, $U_0=30\text{m/s}$ , $T_p=1,000\text{K}$ impact, Case4 (top), Case4* (bottom). Contour of the produced gasoline mass fraction (kg-gasoline/kg-gas). The iso-surface of $\alpha=0.5$ is depicted for the 3D case (bottom). .....	120

<b>Figure 5.6:</b> a) Definition of the vapour layer thickness at the impact point, b) Temporal evolution of the vapour layer thickness at the impact point for cases 2,2*,4,4* .	120
<b>Figure 5.7:</b> a) Percentage of gasoil converted to gasoline yield (kg-gasoline/kg-liq %) and b) cracking reaction rate, both plotted against non-dimensional time for cases 2,2*,4,4* .	121
<b>Figure 5.8:</b> Effect of CFD simulation dimensions on collision outcome for a DTP=2, $U_0=30\text{m/s}$ , $T_p=800\text{K}$ impact, Case7 (top), Case7* (bottom). Contour of the produced gasoline mass fraction (kg-gasoline/kg-gas). The iso-surface of $\alpha=0.5$ is depicted for the 3D case (bottom).	122
<b>Figure 5.9:</b> Igloo shaped form ( $\tau=0.66$ ) and “copy” droplet ( $\tau=1.9$ ) are predicted in the 3D Case7*. Temperature contour (K) is depicted on the symmetry boundary.	122
<b>Figure 5.10:</b> a) Vapour layer thickness temporal evolution for Cases7,7*, b) Solid particle partial wetting at $\tau=0.66$ is predicted in the 3D case.	123
<b>Figure 5.11:</b> a) Percentage of gasoil converted to gasoline yield (kg-gasoline/kg-liq %) and b) cracking reaction rate, both plotted against non-dimensional time for cases 7,7* .	123
<b>Figure 5.12:</b> Drop impact onto a particle cluster. Top row shows iso-surface of $\alpha=0.5$ , bottom row shows gasoline mass fraction volume rendering.	124
<b>Figure 5.13:</b> Vapour layer levitating droplet on top of particles ( $\tau=0.05$ ). Two slices of volume fraction field at the proximity of spherical particles are shown, where $\alpha=0.001-0.999$ .	125
<b>Figure 5.14:</b> Drop break-up after impact on a particle cluster at $\tau=1.05$ .	126
<b>Figure 5.15:</b> Local refinement algorithm application in the case of drop-particle cluster simulation case. a) Global view, b) Close-up view.	127
<b>Figure 5.16:</b> Temporal evolution of drop-particle cluster collision. Droplet is represented by the $\alpha=0.5$ iso-surface coloured by velocity magnitude.	127
<b>Figure 5.17:</b> Recirculation zones induced by fluid flow at a) $\tau=1.05$ for droplet impact onto a particle cluster, b) $\tau=0.66$ for droplet impact onto a single particle.	128
<b>Figure 5.18:</b> a) Percentage of gasoil converted to gasoline yield (kg-gasoline/kg-liq %) and b) cracking reaction rate, both plotted against non-dimensional time for cases 8 and 9.	129
<b>Figure 5.19:</b> a) Droplet mean temperature and b) Non-dimensional mass, both plotted against non-dimensional time.	129
<b>Figure 5.20:</b> Temporal evolution of the percentage of particles’ area which is wetted.	130

<b>Figure 6.1:</b> Effect of surface temperature boundary condition in vapour layer thickness prediction. Cases 1, 2 from Chapter 4, $\tau=0.7$ . .....	136
<b>Figure A.1:</b> Unphysical diffusion of volume fraction field, followed by the breakup of small secondary droplet observed when the WFM is applied in a wide region around the contact line. Velocity vectors are plotted in the same manner for all images. ....	139
<b>Figure C.1:</b> Computational domain used for the validation of the CFD evaporation model in single droplet evaporation. ....	144
<b>Figure C.2:</b> Validation of the CFD phase change model against the experiments of [197] for n-heptane droplets evaporating at 101,325 Pa. ....	144
<b>Figure C.3:</b> a) Computational domain (grid=30x60 cells) used for the validation of the CFD model in hot wall impingement cases, b) 5 levels of local refinement used in order to resolve the thin vapour layer. ....	145
<b>Figure C.4:</b> Temporal evolution of a) maximum non-dimensional radius and b) maximum non-dimensional height of spreading droplet for the 3 cases examined against experimental data of [198]. ....	145
<b>Figure C.5:</b> Temporal evolution of drop deformation for validation cases of impingement on a heated wall. Images split in two sides, left side-non-dimensional temperature, right side-heptane vapour mass fraction (kg-vap/kg-gas). ....	146

# List of Tables

<b>Table 2.1:</b> General settings used in ANSYS Fluent VOF model.....	23
<b>Table 2.2:</b> Evaporation source terms incorporated in respective equations in ANSYS Fluent VOF model .....	24
<b>Table 2.3:</b> Weighting of species in gas mixture.....	26
<b>Table 2.4:</b> Refinement stages for refinement/coarsening procedure .....	31
<b>Table 2.5:</b> Fluent UDFs developed in this Thesis and their application .....	45
<b>Table 3.1:</b> Algorithms tested for volume fraction advection and interface thickness achieved.....	48
<b>Table 3.2:</b> Numerical settings for the Zalesak’s disk benchmark case .....	49
<b>Table 3.3:</b> Initial Conditions and Results of the 1-D analytical solution of a water droplet on freefall.....	55
<b>Table 3.4:</b> Test cases Investigated for a 0.5mm droplet on freefall.....	57
<b>Table 3.5:</b> Grid size for local refinement vs uniform refinement (same resolution at interface). ..	57
<b>Table 3.6:</b> Mean pressure predicted inside the liquid phase. Reference pressure is $p_{\sigma K} = \sigma K = 2\sigma/R$ . .....	60
<b>Table 3.7:</b> Initial conditions for the droplet impingement on a flat wall. The following abbreviations are used: Weber number (W), advancing contact angle (CA) and contact angle hysteresis (H). Symbols VL, L, M, H represent the words very low, low, moderate and high. (* equilibrium angles, when only the equilibrium angle is given, the advancing/receding angles take this value, as in Cases5-7.).....	65
<b>Table 3.8:</b> Numerical settings for the droplet flat impingement case .....	66
<b>Table 3.9:</b> Summary of maximum droplet spreading WFM results, experimental data (refs in Table) and estimations from Pasandideh correlation (Eq. 3-10). .....	69
<b>Table 3.10:</b> Simulated cases for droplet-particle collisions. $D_0=3.1\text{mm}$ , $\theta=90^\circ$ .....	83
<b>Table 3.11:</b> Number of cells and simulation times for all runs performed. ....	84
<b>Table 3.12:</b> Numerical settings for the droplet spherical impingement case .....	85

<b>Table 4.1:</b> Cracking reaction kinetics (pre-exponential factor, activation energy and SSA) taken from [188] for gasoil to gasoline reaction. ....	99
<b>Table 4.2:</b> Default operating conditions for all cases. ....	100
<b>Table 4.3:</b> Cases investigated for single droplet-particle collisions in FCC reactor injection zone. ....	100
<b>Table 4.4:</b> Numerical settings for the single droplet-particle collisions in FCC case. ....	102
<b>Table 5.1:</b> Cases investigated for droplet-particle/particle cluster collisions in FCC reactor injection zone. ....	116
<b>Table 5.2:</b> Number of cells and simulation time for runs performed .....	118
<b>Table B.1:</b> Fluids and property libraries used in the Thesis. ....	141
<b>Table C.1:</b> Test cases investigated for the validation of the CFD phase change model in drop impact on a heated wall, n-heptane, contact angle 100° [198]. ....	145

# Acknowledgements

First of all, I would like to thank Professor Gavaises for giving me the opportunity to enroll in this PhD programme, and make come true one of my desires in life, that started off as a joke with my friends, that is to become a “Doctor”. His guidance, and continuing urge to work harder and promote our work by attending conferences, workshops and seminars, has given me a view of the research world and a peak into a very exciting lifestyle, where people from all around the world come together to exchange their opinions about ongoing research activities.

Secondly, I would like to express my deepest feelings of gratitude towards Dr. Nikolaos Nikolopoulos, who was the one that recruited me into this group, supervised my research in a day to day basis and has stood by my side throughout the whole research activity. His help and time invested on me will never be forgotten. Nikos’ never lasting thirst for research has inspired me and showed me the way to proceed.

Furthermore, I would like to thank Dr. George Strotos, a fellow colleague, with whom I collaborated during the second year of my research. Our evening meetings that included drinking, eating and most of all programming and fruitful discussions were a highlight. George helped me understand that attention should be paid to detail and not fear of looking into the unknown.

Not to forget, the significant collaboration with Prof. Marco Marengo and Dr. Carlo Antonini during the first year of my research. The two scholars initiated the idea and derivation of the Wetting Force Model, while also helped with their remarks and fruitful discussions in the implementation of the model in CFD which culminated in a joint publication.

Special thanks should go to Dr. Aris Nikolopoulos, a colleague at CERTH. He was the one that actually introduced me to the colourful world of CFD and believed in me. Not to forget, my colleagues at CERTH and City University, Panagiotis Drosatos, Myrtw Zeneli, Kwstis Papadopoulos, Foivos Koukouvinis, Yiannis Karathanassis, Nikos Kyriazis, Hesam

Jadidbonab and Nikos Chatziarsenis, for the excellent collaboration and helpful discussions.

I would never forget the ongoing help of my best friend Alexis Mileounis, who acted as my talk-to person and urged me to go on.

Finally, I would like to thank my girl, Eleni Karatza, for her continuous support, time she invested on me and the endless conversations we had about matters of work. Her unconditional efforts and patience helped me move forward.

This thesis is the final outcome of continuous hard work and dedication, a period in which I evolved both as a person, as well as a research engineer, so I would be fool not to dedicate it to my parents Nikolaos and Maria Malgarinos, as well as my brother Giannis Malgarinos for all their help throughout this time as well as the previous years.

*London, December 2017*

*Dipl MEng, Ilias Malgarinos*

# Declaration

I hereby declare that the contents of this dissertation are original and have not been submitted in whole or in part for consideration for any other degree or qualification in this, or any other university. This dissertation is my own work, except where specific reference is made to a joint effort in the text and Acknowledgements accordingly.

I grant powers of discretion to the University Librarian to allow the thesis to be copied in whole or in part without further reference to me. This permission covers only single copies made for study purposes, subject to normal conditions of acknowledgement.

*London, December 2017*

*Dipl MEng, Ilias Malgarinos*





# Abstract

The goal of this work is to study computationally the flow induced by the collision between a single gasoil droplet and a spherical catalytic particle under realistic Fluid Catalytic Cracking (FCC) conditions. FCC reactors are found in the fossil fuel refineries and are used to upgrade heavy fuel (gas oil) to lighter products (gasoline or LPG), which are industrially more important. Gasoil is injected in the reactor and atomizes; the produced droplets vaporize intensely and come in contact with the hot fluidized solid catalysts. The “cracking” reactions accommodated at the particle porous surface (ex. zeolite) result in the decomposition of gasoil to lighter products.

The two-phase flow model developed solves the incompressible Navier-Stokes equations for mass and momentum, along with the energy conservation equation. The VOF methodology is used to track the liquid-gas interface, while a dynamic local grid refinement technique is adopted, so that high accuracy is achieved with a relative low computational cost. A local evaporation model coupled with the additional solution of the species transport equation is utilized to consider phase change. Cracking surface reactions are taken into account via a simplified 2-lump scheme.

The model is successfully validated in fundamental droplet dynamics flow conditions, such as droplet acceleration, droplet impingement onto flat and solid surfaces under isothermal conditions and droplet evaporation. Insights into these phenomena provide important information that are missing from experimental measurements. The numerical novelties of the current work include the implementation of a new Wetting Force Model to simulate drop-solid interaction, as well as the proposition of a sharpening scheme for the volume fraction field, to suppress diffusion.

Concerning FCC collisions, the numerical model is able to reproduce both the hydrodynamics (drop deformation, spreading, breakup), as well as the chemical products (gasoil converted to gasoline). It is found that droplets of similar size to the catalytic particles tend to be levitated more easily by hot catalysts, thus resulting in higher cracking reaction rates/cracking product yield, and limited possibility for liquid pore blocking. For larger sized droplets, solid-liquid contact increases.

The main ambition of the current Thesis, which is to combine the droplet hydrodynamics with the chemical reactions acts as a novel step towards the understanding of such micro-scale physical phenomena that are difficult to capture/measure in experimental apparatus. This fundamental numerical tool can provide insight to the spray system strategy of an FCC reactor for a wide range of operating conditions.



# Nomenclature

## Latin characters

Symbol	Description	Unit
$[X]$	Concentration	kmol-Xspecie/m <sup>3</sup> -gas
A	Pre-exponential factor	m <sup>6</sup> / (kmol · kg <sub>cat</sub> · s)
$\bar{a}$	Acceleration	m/s <sup>2</sup>
A <sub>int</sub>	Interfacial surface area	m <sup>2</sup>
A <sub>face</sub>	Face surface area	m <sup>2</sup>
C <sub>d</sub>	Drag Coefficient	-
C <sub>p</sub>	Pressure Coeff.	-
C <sub>p</sub>	Specific heat capacity	J/kgK
Ca = $\mu u / \sigma$	Capillary Number	-
cpR	Equiv. cells R is resolved	-
D	Droplet Diameter	m
D <sub>diff</sub>	Diffusivity	m <sup>2</sup> /s
d <sub>f</sub>	Distance function	m
dl	Contact line length	m
D <sub>max</sub>	Maximum spreading diameter	m
DTP	Droplet-to-particle size ratio	-
D <sub>y</sub>	Droplet radial deformation	m
D <sub>w</sub>	Wetting Diameter	m
E = $h - p / \rho + u^2 / 2$	Energy	J/kg
E <sub>a</sub>	Activation Energy	consistent units with R <sub>u</sub>
Eo = $g \Delta \rho d_{liq}^2 / \sigma$	Eotvos number	-
F	Force	N
$\vec{f}_{WFM}^v$	WFM volumetric stress term	N/m <sup>3</sup>
f <sub>H</sub>	Hoffman's function	-

$\bar{f}_\sigma^v$	Surface Tension	N/m <sup>3</sup>
$\bar{g}$	Gravitational acceleration	m/s <sup>2</sup>
H	Liquid Film Thickness	m
h	Enthalpy	J/kg
J	Diffusion flux	kg/m <sup>2</sup> s
K	Constant for adhesion	-
k	Kinetic constant	m <sup>6</sup> / (kmol·kg <sub>cat</sub> ·s)
k <sub>cond</sub>	Effective conductivity	W/mK
L	Latent Heat	J/kg
L <sub>w</sub>	Wake length	m
m	Mass	kg
$\dot{m}, \dot{m}'$	Vaporization rate	kg/m <sup>2</sup> s, kg/m <sup>3</sup> s
$Mo = g\mu_{air}^4\Delta\rho/\rho_{air}\sigma^3$	Morton number	-
MW	Molecular weight	kg/kmol
$\hat{n}$	Free-surface unit normal	-
p	Pressure	Pa
r	Rim axisymmetric distance	m
R	Droplet Radius	m
$Re = \rho uD/\mu$	Reynolds number	-
$RR', RR$	Reaction rate	kmol/m <sup>2</sup> s, kmol/g <sub>cat</sub> s
$R_u (=8314.47)$	Universal Gas Constant	J/kmolK
$S_{e,v,l}$	Source term (energy, vapour, liquid)	dependent on equation
SSA	Specific Surface Area	m <sup>2</sup> /g
t	Time	s
T	Temperature	K
$\bar{u} (u,v,w)$	Velocity (its components)	m/s
V	Volume	m <sup>3</sup>
$We = \rho uD/\sigma$	Weber number	-
$\bar{x} (x,y,z)$	Position vector (distance of x,y,z-axis)	m
X	Mole fraction	mole-specie/mole-gas
Y	Mass fraction	kg-specie/kg-gas

### Greek characters

Symbol	Description	Unit
$\alpha$	Volume fraction	-
$\beta$	Sharpening intension constant	-
$\beta_m$	Thermal accommodation coefficient	
$\Delta\rho$	$\rho_l - \rho_g$	kg/m <sup>3</sup>
$\Delta x$	Cell width	m
$\varepsilon$	Interface thickness constant	-
$\eta$	Direction normal to wall	-
$\theta$	Contact angle	°
$\kappa$	Curvature	1/m
$\mu$	Dynamic viscosity	kg/ms
$\rho$	Density	kg/m <sup>3</sup>
$\sigma$	Surface tension coefficient	N/m
$\tau = tu/D$	Non-dimensional time	-
$\phi$	Phi variable (for sharpening)	-
$\Psi$	Stream Function	1/s
$\Omega$	Rotational Velocity	1/s

### Superscripts and subscripts

Symbol	Description
$\infty$	Freestream (or outside the Knudsen layer in evaporation)
adv	Advancing
cl	Contact line
cur	Current
dyn	Dynamic
eq	Equilibrium
g	Gas
int	interface
l	Liquid
n	Random time instant
o	Initial
p	Particle
rec	Receding
sat	Saturated
v	Vapour

## Abbreviations

Symbol	Description
CFD	Computational Fluid Dynamics
CICSAM	Compressive Interface Capturing Scheme for Arbitrary Meshes
CSF	Continuum Surface Force
CSS	Continuum Surface Stress
FCC	Fluid Catalytic Cracking
IBM	Immersed Boundary Method
LBM	Lattice-Boltzmann method
locRef	Local refinement levels
LPG	Liquefied petroleum gas
LS	Level-set
M-HRIC	Modified High Resolution Interface Capturing
THINC	Tangent of Hyperbola for INterface Capturing
UDF	User defined Function
VOF	Volume of Fluid





# Chapter 1

## Introduction

### 1.1 Background and Motivation

The collision of a liquid droplet with a solid surface of any shape is a physical phenomenon that appears in many technological applications, such as for example, spray cooling, spray coating and fuel injection in internal combustion engines. Another very interesting application of droplet dynamics, which concerns the subject of this Thesis, is found in the Fluid Catalytic Cracking (FCC) units in the petroleum industry and concern droplet-particle collisions.

FCC units, which are integral parts of modern fossil fuel refineries worldwide (about 45% of gasoline originates from FCC and ancillary units such as the alkylation unit [1]), are used to convert heavy fuel, named as “gas oil” coming from the distillation unit, to lighter products like gasoline or LPG, which are industrially more important. The conversion is achieved via the “cracking” reactions, i.e. the decomposition of long carbon chain/high molecular weight hydrocarbons to smaller chain/lower molecular weight products. These reactions are accommodated within the FCC reactor, a fluidized bed riser reactor, where hot fluidized solid catalysts come in contact with the atomized heavy oil droplets, and take place at the surface of the catalysts, which are porous solids, such as zeolites.

A general view of the FCC unit operation, i.e. the riser reactor, the regenerator and the cyclone is given in Figure 1.1. As soon as the liquid droplets enter the hot environment of the bed reactor from its bottom section and come in contact with the hot catalysts, they vaporize rapidly and “crack” at the surface of the porous catalysts to produce lighter products. Then, the mixture of catalysts, dispersion steam and gas products flow upwards to reach the outlet of the riser reactor.

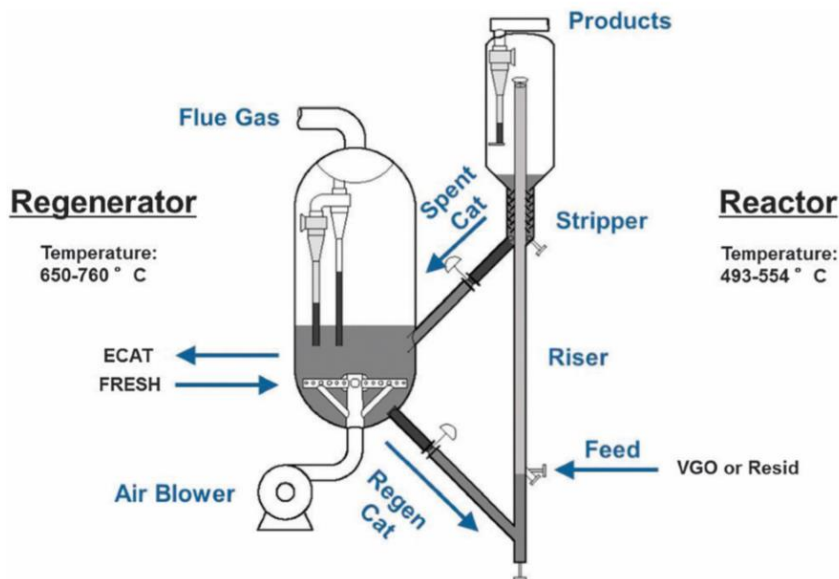


**Figure 1.1:** FCC unit petroleum refineries. Riser reactor and regenerator. Reproduced from [2] with permission from the Royal Society of Chemistry.

Then, the cyclones are used to separate the gas products from the catalysts, while a stripping section helps in the removal of any excess hydrocarbon vapours from the catalysts. The catalysts are recycled again into the reactor, after passing through the regenerator where they are combusted with air. The practical presence and importance of the regenerator is two-fold. Firstly, due to the fact that the cracking reactions are endothermic in nature, the catalysts should be hotter than the mean bed temperature, so that they absorb the energy of the reactions, without affecting the mean bed temperature. Secondly, when the catalysts are combusted in the regenerator, the coke deposits, which are by-products of the cracking reactions are burned off the catalysts, thus the spent (deactivated) catalysts are “regenerated”. The deactivation of catalysts, i.e. the blocking of their pores, that prohibits cracking reactions is due to the coke deposits as well as non-evaporated liquid that enters the pores and stays [2, 3].

The proper operation of such a unit relies on the balance between the heat offered to the catalysts in the regenerator and the heat absorbed by them in the riser reactor. A fair mixing of the catalysts, dispersion steam and injected liquid droplets, as well as the droplets quick vaporization might reduce the possibility of liquid pore blocking by enhancing catalyst ‘activity’ for cracking reactions, which could ultimately improve the unit efficiency. From the engineering point of view, a closer look into the injection process of the liquid gasoil droplets, as well as how they mix with the catalyst and dispersion steam would help in the understanding of the phenomena involved.

Numerical models and their intrinsic ability to analyze physical phenomena can shed light into the reactor dynamics and aid in the investigation of different spray injection scenarios. However, most works so far, as is shown in the following section rely on crude assumptions for the behavior of the spray, as the resolution used is not enough to capture the complex hydrodynamics of the injection region. Most researchers try to simulate the whole process in one numerical tool. However, there is a scale problem inherent, that spray injection, droplet dispersion and vaporization might take ms, while the residence time of the catalysts inside the riser reactor on the other hand is a matter of 5-20 seconds.

Therefore, as a first step, there is a need to alleviate the problems of spray modelling and focus on a specific engineering region, the injection zone of the FCC reactor, in such a way that conclusions can be made and engineering observations can be provided. Focusing on the micro-scale and investigating how single droplet-particle collisions may affect product yields might shed light into these processes. Moreover, in this way, droplet-particle direct contact can be quantified for different operating conditions.

A proper literature review will aid the formulation of the Thesis objectives, as well as the gaps in knowledge and advancements that need to be made.

## 1.2 Literature review of relevant studies

### 1.2.1 Large scale FCC reactor simulations

In most CFD works published on the FCC reactors, the whole reactor hydrodynamics and the respective catalytic cracking yields are simulated without considering the detailed mechanisms taking place at the time and length scales of droplet impact. Figure 1.2 presents a typical picture of how the flow field looks like in a FCC riser reactor simulation, as taken from the work of [4]. Spray injection regions at the lower section of the reactor are quite apparent, however it is evident that the cell sizes used are not enough to resolve droplet-particle collisions.

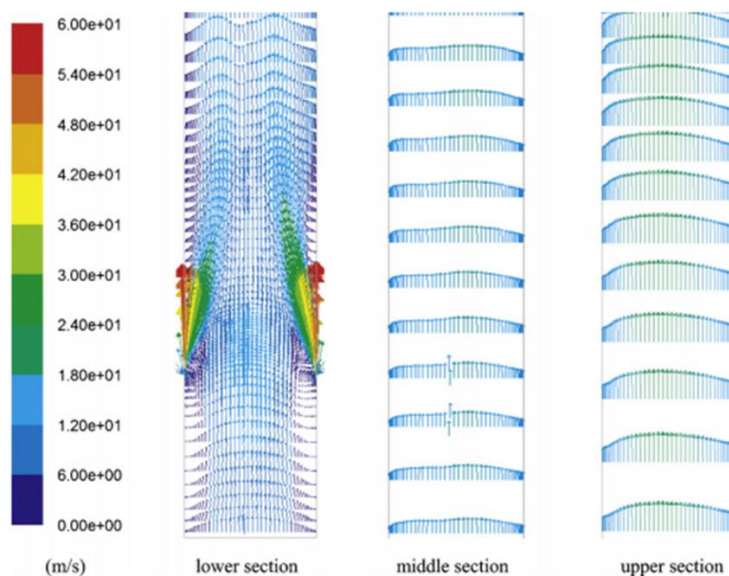


**Figure 1.2:** Flow reactor hydrodynamics. Reprinted from [4] with permission from Elsevier.

A common assumption which is made in these works [5-9] is that the feed is quickly vaporized after its spraying into the reactor, due to the high temperature of the solid catalyst (higher than the liquid boiling point). In these studies, a simplistic 2-phase flow approach is used in order to simulate the mixing/reactions between solid catalysts and gas flowing inside FCC reactors. These works are divided in Eulerian [5-8] and Eulerian-Lagrangian [9], depending on how the authors treat the solid phase catalysts.

However, in [10-12] the importance of studying the FCC injection zone, and more specifically the liquid feed vaporization is highlighted, as it is noted to be an important aspect for the correct calculation of the cracking yields and products selectivity.

For this reason, in more detailed CFD works [4, 10, 11, 13-15] the additional investigation of the injected droplets motion, coupled with a vaporization model, has been performed. This has allowed the full 3-phase (solid catalysts/liquid droplets/gas) problem exhibited in real FCC reactors to be resolved. Again these studies can be categorized based on the treatment of the solid phase (catalysts) and the liquid phase (gasoil droplets) to either Euler-Eulerian [4, 11, 13, 14], or Euler-Lagrangian [10, 15].

Finally, following a very different approach, Patel et al. [16] solve numerically the 1-D transport equations of the interacting solid/liquid/gas phases along the spray centerline using a Lagrangian description of the spray behaviour.

In the majority of the aforementioned works [4, 5, 7-11, 13, 14], the hydrodynamics equations are coupled with reaction kinetics in order to present a more comprehensive view of the reactor/catalytic cracking yields.

However, the fact still remains that in all these works, the detail achieved in the injection zone is not enough to capture the real interactions occurring between cold injected droplets and hot catalytic particles. Moreover, by studying the micro-scale collision between a droplet and a catalyst inside the FCC reactor, it is possible to estimate, at an extent, the possibility of direct solid-liquid contact which is hindered by the drop levitation on the particle surface due to the Leidenfrost effect [10, 17].

It has been observed that the direct contact between liquid drops and porous catalysts that occurs in the FCC injection zone, may lead to the deactivation of the catalysts, from the insertion/blocking of their pores with non-evaporated liquid [3]. This phenomenon, signifies the importance to focus more in this zone and particularly in droplet-particle interactions and specifically investigate the direct solid-liquid contact. Moreover, the life duration of a single droplet is very important, considering that the catalyst to oil mass weight ratio within FCC reactors is in the range of 4:1 up to 10:1 [18]. Interface tracking methods can provide the advanced level of detail needed in order to study these micro-scale phenomena.

### 1.2.2 Droplet-particle collisions in FCC reactor simulations

Turning now to the previous works that concern the investigation of droplet dynamics in FCC reactors, only three works were tracked in the open literature [19-21]. Gac and Gradon [19] investigated the outcome of droplet-particle isothermal collisions using the Lattice-Boltzmann method (LBM); in their work, all operating conditions are provided in dimensionless format. Mitra et al. [21] have presented numerical simulations and experiments related to droplet impingement onto a spherical particle under both isothermal and non-isothermal conditions. However, the liquids they used were water, isopropyl alcohol and acetone, the choice of which seems to be far from resembling real gasoil behaviour. Finally, Ge and Fan [20] have presented numerical simulations of non-isothermal droplet collision with a solid particle using the Level-Set (LS) method and the Immersed Boundary Method (IBM) for the representation of the solid phase. In their work, they have coupled their numerical model with a 2D model for the vapour boundary layer, in order to incorporate the effect of the thermal boundary layer formed between the liquid interface and the solid surface, in collisions under film boiling conditions.

Overall, the temperature and impact velocity range of values examined in the last two works are significantly lower than the ones exhibited under realistic FCC conditions.

### 1.2.3 Droplet impingement on flat and spherical surfaces

Since the available material on droplet-particle collisions under conditions realized inside FCC reactor injection zone is scarce, relevant studies concerning droplet impingement onto both flat/spherical surfaces are used to interpret the impingement dynamics and validate the numerical model.

#### 1.2.3.1 Flat surfaces

Droplet dynamics and their interaction with solid surfaces have fascinated researchers from the time of 1805 [22] and 1867 [23]. Since then, a vast number of studies have been published that deal with the underlying physics theoretically, experimentally and by using numerical models implemented in Computational Fluid Dynamics (CFD) codes.

A comprehensive review on the phenomenon of drop impact onto a solid flat surface, from the flow dynamics point of view, can be found in the works of Rein [24], Yarin [25] and Marengo et al. [26]. In the study of Rioboo et al. [27], the expected outcomes of this process are identified. More specifically, droplet impingement onto a flat solid surface can lead to “deposition”, “rebound” or “splashing”. In Figure 1.2, these outcomes are presented in an image taken from their work.

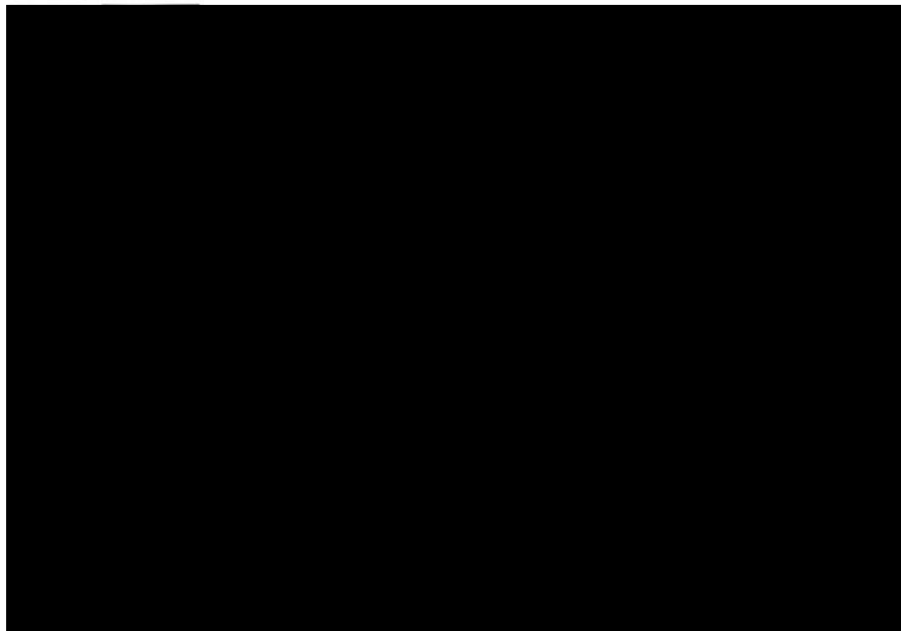


**Figure 1.3:** Outcomes of droplet impingement on a solid flat surface. Image taken from [27].  
Courtesy of Begell House, Inc.

In the scope of theoretical works, some researchers focus on the complex dynamics governing the three phase (liquid-gas-solid) contact line [28, 29], while an issue arises due

to the hydrodynamic singularity at this region [30]. In other theoretical approaches, the droplet maximum spreading is estimated based on an energy conservation approach, in terms of initial kinetic and surface energy before impact and surface energy along with viscous dissipation at its maximum spreading. In 1991, Chandra and Avedisian [31] using such an approach reached to a derivation of maximum spread for impact of a droplet on a hot flat surface, while afterwards, in 1996, Pasandideh et al. [32] provided an estimation of the spreading factor for a cold surface, taking into consideration the existence of a viscous boundary layer in which most of the kinetic energy is dissipating. This equation takes into account the Reynolds and Weber numbers, the contact angle at the end of the advancing phase, to estimate the maximum spreading factor. Similar equations can be found in following works [33-35]. Other analytical works assume that the deformed shape of the droplet, when it spreads, is the same with that of a truncated sphere [36] or a cylindrical disk [37].

Concerning experimental works, the results of a vast number of relevant campaigns [27, 33, 35, 36, 38-50] can be found in literature, where the effect of basic parameters such as droplet physical properties (viscosity, density, surface tension), droplet size, impact velocity, solid surface roughness and wettability on droplet spreading are investigated explicitly. More recently, the interest has been turned towards super-hydrophobic and complex surfaces [26, 51], as there is a great challenge in studying the behavior of droplets coming in contact with such substrates. One common realisation resulting from the aforementioned investigations is the appearance of the wetting contact angles, namely the advancing and the receding ones, as influential parameters during droplet spreading onto solid substrates [52]. These have been measured in some cases as a function of substrate manufacture properties, i.e. smooth/rough glass in Rioboo et al. [43], or even substrate roughness amplitude [40, 51]. Moreover, as it has been proved from very early times (Jiang et al. [53] in 1979), the dynamic contact angle of the rim varies considerably, especially during the advancing phase of droplet spreading.

More recently, due to the advancements in high-speed photography, the dynamic contact angle was investigated more explicitly. In fact, Hung et al. [50], using a “droplet impingement imaging system” managed to digitize the shape of the droplet at each time instant during the spreading process extrapolating considerable information about its variation as function of the rim velocity. Selective experimental works depicting this change of contact angle values during the spreading period can be found [32, 35, 47, 49, 54].



Concerning CFD works for droplet impingement onto flat surfaces, there is a vast number available in literature, as is presented in the state of the art in wettability modelling section, where a comprehensive review on the available models is presented. Researchers have studied droplet impingement onto flat surfaces for a wide range of operating conditions, namely Weber numbers and surface temperatures, while using different models [32, 54-58], but it is found that there is a lack of simulated works for water droplet impingement onto hydrophilic surfaces and for low and moderate Weber numbers. Fukai et al. [55] simulated impingement onto hydrophilic surfaces for a range of We numbers between 112 and 733. Ganesan et al. [59] simulated case the impingement of a water droplet onto a slightly hydrophobic wax surface ( $\theta_{adv} = 105^\circ$ ) and afterwards presented their simulations for a droplet impact characterized by a very low contact angle ( $\theta_{adv} = 10^\circ$ ), without a comparison against experimental data. Gunjal et al. [60] simulated the impingement of a water droplet on a glass surface using stepwise time variation of contact angles according to the experimental values, so that they can simulate the temporal evolution observed during the experiment, in a validated way.

### *1.2.3.2 Spherical surfaces*

In 1971, Levin and Hobbs [61] published the first experimental work on droplet impingement onto a spherical surface, under the effect of gravity, where the regime of the impingement included droplet splashing. In 1999, Hardalupas et al. [62] also studied droplet splashing onto spherical targets. After a number of different experiments, the authors reached to a very interesting graph depicting the transition from splashing to deposition for a droplet impinging onto the solid surface in relation to spherical surface curvature.

In 2001, Pasandideh et al. [63], using a 3D VOF based numerical method simulated the phenomenon of a droplet impacting a cylindrical surface, taking into account the wettability of the solid surface in respect to the specific liquid. The initial position of the droplet was off-center in respect to the center of the cylinder diameter, just as in their experiment, while they also studied variable ratios of droplet-to cylindrical pipe-diameter. In 2003, Gunjal et al. [64] used the VOF methodology in order to simulate the liquid shape formations after the off-center impingement of a liquid droplet on a spherical surface, taken from their experiments. However, the simplification of the phenomenon in two dimensions (planar) was not enough for the accurate representation of the physics that lie behind the asymmetric impingement.

Most recently, interest is regained in spherical surface impingement, given the increased capabilities of recent computers, in order to study complex micro phenomena related to large scale reactors, where particles and droplets are present.

In 2007, Bakshi et al. [65] performed experiments of the coating of a spherical solid particle by a droplet of similar size. This was one of the first studies where the droplet to particle size ratio was close to unity (as in FCC) and therefore, coating could be observed. The authors also presented an analytical model for the prediction of droplet spreading (calculating the formation of a thin inner film with a thicker rim at the external spreading side). During the same year, Ge and Fan [20] presented Level-Set simulations and experiments on droplet impact on a spherical particle of similar size, under the Leidenfrost regime. The motivation of their work was the collisions of droplets with particles in an FCC reactor. For the levitation of the droplet due to the Leidenfrost phenomenon, a vapour layer model was implemented. In 2009, Bangonde et al. [66], in a similar work to the aforementioned one of Pasandideh et al. [63] presented VOF simulations and experiments at low Weber number droplet impingement on a cylindrical pipe, followed also by the case of impact on a spherical surface.

Reaching now to 2012, in their work, Gac and Gradon [67] described the dynamics of the droplet-particle collision using the Lattice-Boltzmann method and categorized the collision outcomes in three regimes, i.e, coalescence, ripping and coating (1-5 satellite droplets) and skirt-scattering, based on the initial droplet Weber number. Moreover, they observed that the outcome scenarios don't change significantly with other solid target shapes (cubical, ellipsoidal). Their work was purely numerical, while no validation with experiments was presented. They also refer to the FCC process, as a motivation of their study. Again referring to FCC process, in 2013, Mitra et al. [21] presented simulations and experiments on droplet impingement on spherical particle, under isothermal and Leidenfrost conditions. In their work, they simulate the levitation of the droplet due to the Leidenfrost phenomenon with the simplistic use of a  $180^\circ$  contact angle, meaning no liquid-solid contact. Finally, most recently, very interesting experiments concerning drop-particle collisions in mid-air are published [68], while a review on the dynamics of drop-particle collisions is presented in [69].

The main conclusion that can be drawn, is that the numerical works concerning droplet impingement onto a spherical particle, which is the main goal of the research work, are limited.

## 1.3 Flow field in the injection zone

The most important step of this thesis is the identification of the operating conditions that are realized in the injection zone of a typical FCC reactor. By knowing the exact conditions that droplets endure when injected inside the reactor, it is easier to determine the correct models that apply in these specific situations.

### 1.3.1 Operating conditions

In Figure 1.4a, a typical image of the path that a droplet follows in the injection zone of an FCC reactor is depicted, while in Figure 1.4b the mean operating conditions for droplet-particle collisions inside the FCC injection zone, as produced by a literature review on selective representative studies [4, 5, 7-11, 13, 14, 16, 18, 70, 71] are summarized.

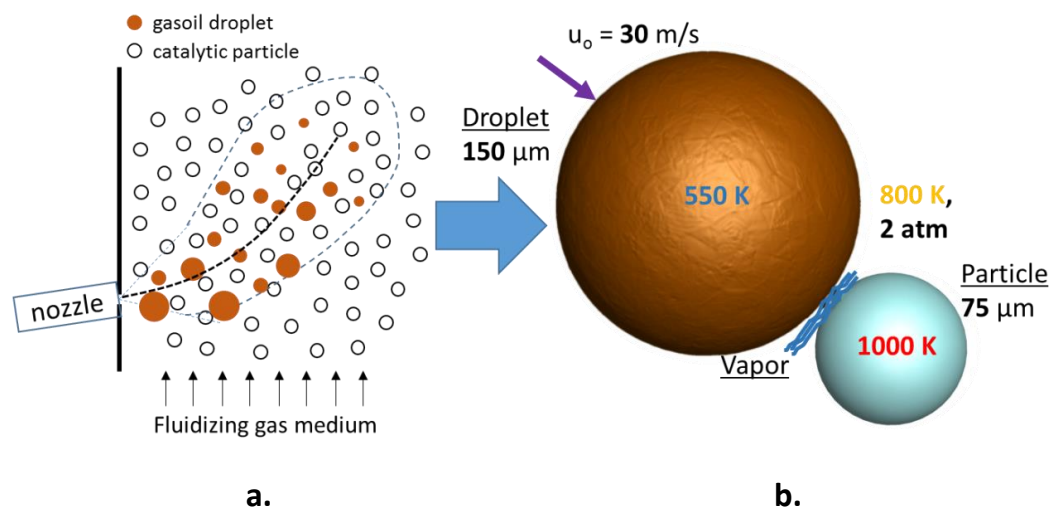


**Figure 1.4:** a) Mean path of injected droplets and b) Operating conditions of droplet-particle collisions

These conditions, which should be taken into account when simulating this phenomenon are:

- a. injection (droplet) conditions
  - feed preheat (478-673 K [18, 70])
  - injected drop velocity (45 to 100m/s [18])
  - drop sizes (50-500μm [10, 13, 16])
- b. reactor conditions
  - bed pressure (1.5-3 bar (Table 10.2 of [71]))
  - bed temperature (769-838K [18])

- c. catalyst conditions
- size (60-75  $\mu\text{m}$  [10, 11, 16])
  - temperature (950-1005K [18]).

### 1.3.2 Non-dimensional Numbers

The most crucial dimensionless parameters, which govern the impingement phenomenon, are the initial Reynolds and Weber numbers, as well as the Capillary number.

$$\text{Re} = \frac{\rho_l u_0 D_0}{\mu_l}, \text{We} = \frac{\rho_l u_0^2 D_0}{\sigma}, \text{Ca} = \frac{\mu_l u}{\sigma}, \tau = \frac{t u_0}{D_0} \quad (1-1)$$

Knowing these numbers, the initial ratios of inertia to viscous (Re) and surface tension forces (We), as well as inertia to surface tension force throughout the phenomenon (Ca) are known. These numbers show how significant the effect of every one of these parameters is to the whole phenomenon (spreading-recoiling, rebound, deposition, splashing).

### 1.3.3 Chemical reactions and lumping

Another very important aspect concerning the simulation of this complex process is the treatment of the chemical species that appear in the liquid feed as well as the gaseous mixture of the cracking products. In real situations, the number of different species that constitute the gasoil petroleum fraction feed which is initially injected, as well as the exact products of the cracking process, is enormous.

The authors in most CFD works related to the FCC reactors [4, 5, 7-11, 13, 14], use lump reaction kinetics in order to represent a holistic view of the catalytic cracking yields. The “lump” species, as they are called, are groups of different species that exhibit similar behavior. The lump reaction network is assumed to be a good representation of the most influential reactions taking place in such complex systems (in substitution of a large variety of species in the real case).

The first lumping scheme was proposed by Weekman and Nace in 1970 [72], namely the 3-lump kinetic scheme, which grouped the kinetics of an FCC reactor in gasoil, gasoline, light gases and coke species. Later on, in 1988, Yen et al. [73] split the third lump to separate light gases and coke lumps respectively, and formulated the most commonly

used [5, 7, 10, 16, 74] 4-lump scheme. More detailed 9-lump [8] and 12-lump schemes [4] can also be found.

All these models have not been coupled so far with the detailed hydrodynamic and heat transfer taking place during the collisions between liquid droplets and solid particles.

## 1.4 State of the art in two-phase flow models

### 1.4.1 Interface modelling

Based on the level of detail needed to achieve in order to simulate droplet-particle collisions, interface capturing/tracking methodologies seem a perfect choice. The different methodologies found in literature are categorized in three basic groups based on the way the interface is tracked. These are presented in Figure 1.5.

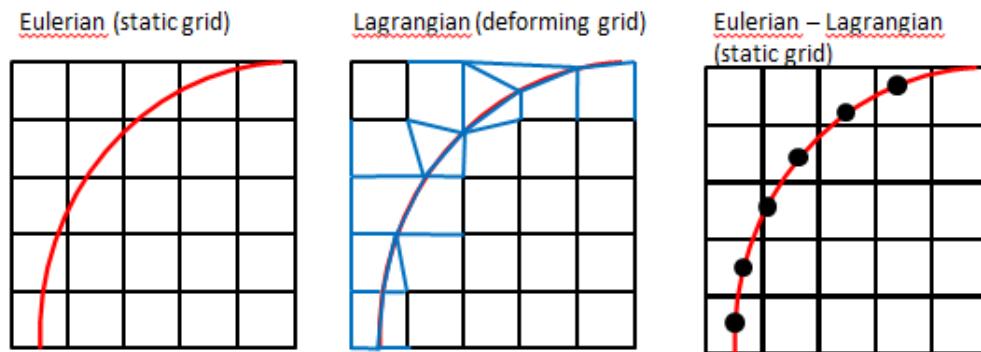


**Figure 1.5:** Differences between Eulerian, Lagrangian and Eulerian-Lagrangian approaches.

In pure Eulerian methods, the interface is represented by a scalar field, which is advected in a fixed or a moving grid. This scalar field may be either the volume fraction, as in the cases of Volume of Fluid Method [75] and later descendants, or the distance function in Level Set approaches [76]. In Lagrangian methods [77], the grid deforms and follows the shape of the free-surface. In Hybrid Eulerian-Lagrangian methods [78, 79], the flow is solved in a fixed grid, while the interface is tracked using Lagrangian particles.

The advantages and disadvantages associated with using one of these approaches are presented in detail in [80]. The Eulerian approaches are easily applicable in three-dimensions and can handle topology changes, but exhibit poor performance in under-resolved interface areas, can be diffusive and mostly rely on the accuracy of the advection algorithm. In Lagrangian methods the interface location is explicitly known, while the computation of the surface tension force is straightforward. However, they become

complex and time-consuming for three-dimensional applications. In hybrid Eulerian-Lagrangian methods, the advantages of both models are combined (interface location known, flow solved on Eulerian grid), nevertheless the extension to three-dimensions and the ability to handle coalescence/breakup still remain.

In the current Thesis, the VOF Eulerian model is used, given the exhibited mass conservation capabilities [80], the ability to handle topology changes easily and the direct upgrading to three dimensions. However, as in all numerical algorithms, numerical issues may become important in specific flows, under certain operating conditions. The most important parameters to influence the VOF model are addressed in the following sections, namely liquid advection, surface tension modelling, evaporation model, liquid-solid wettability.

## 1.4.2 Advection modelling

In VOF method, as in all Eulerian approaches, the exact location of the interface is not known. Volume fraction equation is solved to update the interface location. The accuracy, therefore, of the computation strongly relies on the flux term calculation. However, there are three main physical criteria that should be met and are the source of most VOF errors, namely:

- a) keep a sharp interface, avoid diffusion
- b) conserve mass
- c) bound volume fraction values by the physical limits of zero and unity

If the advection scheme is not accurate, numerical diffusion of the liquid-gas interface will arise, and subsequently the results of the simulation will not be physical. Numerous studies can be found in literature that deal with the volume fraction advection algorithm, trying to remedy the artificial diffusion issue of VOF. The authors follow two basic paths, the direct or indirect approaches.

In the direct approach, comprehensive high order schemes are developed and applied in the volume fraction equation explicitly. In the geometric family of models, the liquid-gas interface is reconstructed and further advected in a Lagrangian manner. Selective works are [81-84], while recently, the efforts of researchers are targeted towards unsplit methods in unstructured grids [85, 86]. Another family of models concerns the development and application of high resolution schemes directly in the discretization of the volume fraction flux term. Such schemes include, for example the CICSAM [87], the HRIC [88], or THINC [89].

In the indirect approach, sharpening algorithms are utilized to artificially restrict interface diffusion. This method of suppressing numerical diffusion has become popular during the last decade. Olsson and Kreiss [90, 91] proposed and applied a sharpening equation, solved right after the advection of the liquid phase in order to avoid diffusion and achieve mass conservation in Level Set simulations. Sato and Niceno [92] used the same equation, however enhanced it with a parameter of variable sharpening intensity across the interface, based on the direction of interface velocity. Most recently, Shukla et al. [93] using a modification of the Olsson's equation, applied the sharpening algorithm in the density equation as well to predict compressible shock-capturing droplet dynamics.

Similar numerical schemes are also implemented by other authors to simulate two-phase flow phenomena. Weller [94], introduced an additional convective term (he refers to it as the 'compression term') in volume fraction equation, and coupled it with a 'compression velocity' that accounts for the direction of possible diffusion. This has been implemented in the core of OpenFoam software, and is adopted by many researchers for various applications afterwards. So et al. [95, 96] solved an anti-diffusion equation after liquid phase advection, discretizing the diffusion term using the minmod limiter. Finally, in a very interesting work, Lentine et al. [97] used a numerical sharpening procedure right after a semi-Lagrangian advection using very large time-steps.

In this Thesis, the sharpening equation of Olsson and Kreiss is implemented. Overall, the implementation of a sharpening algorithm seems a promising route since it does not interfere with the advection flux term. Furthermore, such types of techniques apply to unstructured grids unconditionally (no geometric restrictions).

### 1.4.3 Surface tension modelling

The inclusion of surface tension forces in the simulation of flows with free surfaces is a well-known issue of the Eulerian methodologies, and especially VOF. The discontinuity of the pressure jump at the interface should be accurately predicted in the finite-volume framework, which approximates the interface as continuous.

In most numerical implementations of two phase flows, the widely used Continuum Surface Force (CSF) model [98] and its variant the Continuum Surface Stress (CSS) [99] are used. In both models the theoretically discontinuous surface tension force is applied as a volumetric force and is consistent with the volume fraction framework.

However, a typical issue emerges for the case of a stationary drop in a quiescent fluid, as the surface tension force calculated by these models cannot be balanced by the

pressure gradient and a parasitic velocity field is predicted instead of the theoretical zero. This problem arises due to the discontinuity of the volume fraction at the interface, and any small errors coming from the inaccurate calculation of the free surface gradient and curvature (gradient and divergence operators) or the volume fraction field advection deteriorate accuracy.

Many authors propose solutions for the more accurate calculation of curvature. Cummins et al. [100] presented a detailed literature review on the methods that can be applied for dealing with this issue. Renardy and Renardy [82] reconstructed the interface shape to parabolic segments. Level-Set methods, given that the distance function is continuous at the interface, offer better calculation of surface curvature [76]. For this reason, Coupled Level-Set with VOF is employed by many researchers to improve the curvature calculation [101-104], as well as the use of the Ghost Fluid Method [105]. The height function technique, introduced by [106, 107] provides second-order accuracy in curvature calculation, and seems a very promising method [108], but is difficult to upgrade to unstructured grids. Several tries have been made to expand the height function model to unstructured grids [109, 110], but the authors present high errors for wedge and tetrahedral meshes when increasing the resolution, owed to interpolation of volume fraction data from the unstructured mesh to the height-function stencils.

An innovative turn concerning surface tension in VOF simulations was initiated by Renardy and Renardy [82] and Francois et al. [111], namely the balanced force algorithm. Based on this approach, the same handling should be applied in the discretization of the volume fraction/pressure gradients in the momentum equation. Popinet [108] applied this model in Gerris flow solver, coupled it with the height function technique and showed tremendous parasitic current reduction. Denner and van Wachem [112] presented their implementation of the balanced force algorithm, while they also show that the convolution of the volume fraction is an important aspect to be considered in realistic runs.

The errors in two phase flow simulations become larger for the cases where surface tension forces become dominant (capillary-driven flows) and for large density/viscosity ratios. In this Thesis, the widely used CSF model was applied, as the surface tension effects are not dominant.



#### 1.4.4 Wettability Modelling

Simulations' main goal for the past two decades has been to improve the understanding on the physics of moving contact lines, a physicochemical phenomenon that includes the interaction between the liquid-gas-solid phases at the three-phase contact line. When a drop impinges on a solid surface, significant variation of the contact angle during the spreading period has been observed and measured experimentally [28, 32, 35, 49, 54, 113, 114]. This forced the researchers to derive dynamic contact angle models, mostly relating the contact angle to contact line velocity [115-118].

Roisman et al. [54] stressed out that the use of a dynamic contact angle model is very important in a CFD simulation, so that the temporal evolution of the phenomenon can be captured more accurately. Yokoi et al. [89] showed that in order to achieve a very good agreement between experimental data and simulation results, especially for the recoiling phase, the right use of a contact angle model is a necessity. For a more thorough and interesting review of the available dynamic contact angle models, the readers can read the work of Saha and Mitra [119].

Another interesting issue that concerns numerical studies is how to implement the contact angle at the wall boundary. A recent review on how different computational methods deal with the moving contact line phenomena is presented in [120]. The main modeling approach followed in literature is to impose the contact angle as a boundary condition at the wall boundary cells. Indeed, the only variation among all the methods followed so far lies upon the method of imposition, rather than the dynamic prediction of the angle from the local flow/stress field.

Fukai et al. [55] were the first to apply the contact angle as a boundary condition in cases of water droplet impingement onto a cold flat surface following a 2-D axisymmetric Lagrangian approach. In their approach, the mean curvature of the free surface next to the wall was adjusted so that the desired pre-defined contact angle was reached. Most studies that followed [32, 54, 56-60] couple the widely used CSF model [98] for surface tension with the contact angle boundary condition by adjusting the interface normal and curvature at the wall cells according to the predefined contact angle value.

In other methods, the free surface is extrapolated outside of the wall, so that the free surface normal at the wall can be adjusted and used afterwards in the reconstruction process [89, 121]. Mukherjee and Abraham [122] using the Lattice-Boltzmann method (LBM), introduced an external force field at the wall boundary cells. Finally, in the Level

Set function, utilized in the work of Caveziel et al. [123], a different re-initialization method near the wall was adopted, while Griebel et al. [124] used a fixed value Neumann boundary condition at the wall for the free surface normal of the Level Set function.

For the cases of droplet impingement onto non-flat and spherical surfaces, similar methodologies are used [20, 21, 63, 66], where the contact angle is prescribed in respect to the local wall surface normal.

Another interesting issue that concerns the numerical models is the singularity that arises at the wall surface. The no-slip condition imposed for the velocity values at the wall boundary surface does not comply with the moving contact line. In all aforementioned works, this singularity is resolved implicitly by the adjustment of free-surface curvature which changes the surface tension force near the wall, assuming a temporarily static contact line. In other tries, a slip boundary condition is applied at the wall surface [125, 126].

Efforts towards the development of models that can predict the dynamic change of contact angle during the droplet impact and not impose it have also been reported. Shikhmurzaev [118] presents a comprehensive interface formation model that claims to resolve all open singularities in interface dynamics. In [58] the authors impose a wetting force that relates to the contact angle value needed to achieve. In their simulations, however, this was only an alternative way to apply the Hoffmann's law: the force applied at the contact line was calculated as function of the dynamic contact angle, which was derived from using the Hoffman's law, or alternatively by the theoretical solutions based on creeping flow in the neighborhood of the contact line.

In Chapter 2, a new dynamic contact angle model is proposed, the Wetting Force Model (WFM), one that does not prescribe the contact angle (or its temporal evolution), but lets the net of forces acting on the free surface of the droplet (capillary, surface tension) and the 3-phase contact line to determine the liquid/gas interface interaction with the surface.

### 1.4.5 Evaporation Modelling

Droplet evaporation is an important phenomenon realized in engineering applications and it has been addressed in several review articles and textbooks [127-131]. The simulation of an evaporating free surface in the Volume of Fluid methodology is not a trivial matter. Based on the theoretical works of Hertz and Knudsen [132, 133], the

evaporation rate of an interface is related to the molecular fluxes coming to or leaving the surface and kinetic theory is valid.

The earliest CFD works on droplet evaporation used a body-fitted grid at the liquid-gas interface, thus limiting the applicability of the methodology in 2D axisymmetric flows and spherical droplets. Single [134-141] and multicomponent [142-145] spherical droplets were studied, as well as high pressure conditions [146]. Given the body-fitted grid methodology, the jump conditions at the interface are captured nicely, which results in an accurate representation of the flow field and thus accurate calculation of local momentum-heat-mass transfer rates.

On a different perspective, the Volume of Fluid and Level Set methodologies among others are not limited to spherical droplet shapes, as they can capture the droplet deformation. In order to incorporate phase change phenomena, a local mass transfer rate should be applied at the interface to accommodate the generation/sink of mass in vapour/liquid phases. Mass transfer rate may be based on the kinetic theory [132, 133] or other approaches [147, 148].

Droplet impingement onto a heated flat surface for conditions below and above the Leidenfrost temperature was studied in [149] where the authors coupled a local evaporation rate at the interface based on the kinetic theory with the VOF methodology. The vapour mass fraction equation was solved as well. Similar works coming from the same research group followed, where the authors used a local evaporation rate based on Fick's law of diffusion for estimating the cooling effectiveness of a droplet impinging onto a hot surface [150, 151]. Cooling effectiveness was studied in [152] as well, but without the addition of mass transfer effects.

Schlottke & Weigand [153] focused on the calculation of liquid and gas velocities at the interface region for VOF simulations and showed that adding a virtual mass averaged velocity source term in the continuity equation at this region improved model performance. Bi-component droplet evaporation was studied in [154, 155] based on Fick's law of diffusion, while in [156] the authors included the effect of thermocapillary stresses at the interface to study the vaporization of fiber-suspended droplets.

Harvie and Fletcher [157] coupled VOF with a one-dimensional vapour layer model to simulate the impact of a droplet onto a heated flat surface for the film boiling regime. In the work of [20], a 2D vapour layer was developed to study the droplet-particle collisions under the film boiling regime using the Level-Set method. The particle was represented using the Immersed Boundary Method. The VOF method was used in [21, 158] to study

the impact of a droplet on a heated spherical particle where a local vaporization model based on the kinetic theory was applied [159].

In this work, a local evaporation model based on the kinetic theory of gases is implemented in the numerical solver.

## 1.5 Summary

Following the extended description of the relevant FCC studies, operating conditions of FCC injector zone and two-phase flow models, there is a definite gap in the understanding of complex flows related to droplet-particle collisions under the FCC reactor conditions. Similar works related to droplet-particle collisions are limited, while the range of conditions studied falls far from the real ones exhibited in the reactors. Moreover, the influence of catalytic reactions on the droplet-particle collision dynamics and quantification of cracking products has not been presented before. A gap is identified relating to droplet impingement on hydrophilic flat surfaces for low and moderate Weber numbers. Finally, some developments needed to improve VOF's features, such as numerical diffusion and wettability model are identified.

## 1.6 Scope of PhD thesis

The research goal of this PhD thesis is to develop a CFD model that can accurately predict the flow phenomena induced when a single droplet impinges onto a spherical particle under realistic FCC conditions, meaning under non-isothermal reacting flows. The two-phase flow model which is developed includes a local evaporation model as well as a numerical approach for simulating surface reactions. Predictions of droplet dynamics, under such elevated conditions, is a novel step towards the understanding of such micro-scale physical phenomena that are difficult to capture/measure in experimental apparatus.

More importantly, the developed numerical tool can be used to produce engineering conclusions concerning either the spray system strategy of an FCC reactor, or the general behavior of different catalytic particle materials under a wide range of operating conditions.

Moreover, droplet collision with solid particles, of particularly similar size, is a hot engineering subject. This study, aims at simulating this phenomenon both at isothermal and at elevated temperature conditions.

## 1.7 Thesis Outline

In Chapter 2, the numerical methodology used in the current study is presented, along with the description and development of new algorithms.

In Chapter 3, model validation in a wide range of realistic cases is presented. Firstly, droplet motion under gravitational effect is tested, followed by drop impingement onto a flat surface. The model is then tested against the case of droplet impact onto a spherical particle. Finally, the evaporation model is validated in Appendix C.

In Chapter 4, the simulation of single droplet-particle collisions in 2D axisymmetric domains is presented, where the main flow features are presented.

In Chapter 5 the numerical model is expanded to three dimensions, for both single droplet-particle collisions as well as droplet impact onto a particle cluster.

Finally, in Chapter 6, conclusions of the current work, and propositions for future work are presented.

# Chapter 2

## Numerical Methodology

### 2.1 Fluid flow and Volume of Fluid

For solving the two-phase flow of a liquid droplet moving inside a gaseous medium the Volume of Fluid Method (VOF) is used. The Volume of Fluid Method (VOF), which is appropriate for the simulation of fluid flow between two immiscible fluids, was first proposed by Hirt and Nichols [75] and is based on the solution of a scalar transport equation, which is named as colour function or volume fraction ( $\alpha$ ).

$$\frac{\partial \alpha_i \rho_i}{\partial t} + \nabla(\bar{u} \alpha_i \rho_i) = 0 \quad (2-1)$$

The volume fraction is a simple scalar quantity that takes the value of 1 when inside the one phase (liquid in this thesis) and the value of 0 when inside the second phase (gas in this thesis):

$$\alpha_i = \frac{\text{cell volume occupied by liquid}}{\text{total volume of the computational cell}} \quad (2-2)$$

$$\alpha_i = \begin{cases} 0 & \text{gas} \\ 1 & \text{liquid} \\ 0 < \alpha_i < 1 & \text{gas-liquid interface} \end{cases} \quad (2-3)$$

For in-between values, the cell lies in a region called the “interface” between the two fluids. The interface region does not apply to a real-life existing quantity, but exists as a finite region in numerical terms, due to the precondition of a continuous solution of the governing numerical equations. As the computational cells are occupied by only gas and liquid, the following equation is valid:

$$\sum_q \alpha_q = 1 \Rightarrow \alpha_l + \alpha_g = 1 \quad (2-4)$$

And thus no equation for the gas volume fraction is solved, as the values of  $\alpha_g$  are calculated from the  $\alpha_l$  ones. Volume fraction equation is coupled with the solution of the continuity and momentum conservation equations:

$$\frac{\partial \rho}{\partial t} + \nabla(\rho \bar{u}) = 0 \quad (2-5)$$

$$\frac{\partial \rho \bar{u}}{\partial t} + \nabla(\rho \bar{u} \otimes \bar{u}) = -\nabla p + \nabla \cdot [\mu(\nabla \bar{u} + \nabla \bar{u}^T)] + \rho \bar{g} + \bar{f}_\sigma^v \quad (2-6)$$

The characteristic feature of VOF model in comparison to other techniques is that a single momentum equation is solved for the two phases (gas, liquid), where the fluid properties, density and viscosity, are updated according to the volume fraction value of the cell:

$$\mu = \alpha_l \mu_l + (1 - \alpha_l) \mu_g \quad (2-7)$$

$$\rho = \alpha_l \rho_l + (1 - \alpha_l) \rho_g \quad (2-8)$$

Surface tension term is included in the momentum equation as a volumetric force and is taken from the work of Brackbill et al. [98]:

$$\bar{f}_\sigma^v = \sigma \frac{\rho \kappa \nabla \alpha}{\frac{1}{2}(\rho_l + \rho_g)} \quad (2-9)$$

where “ $\kappa$ ” is the curvature of the interface and is approximated as the divergence of unit surface normal, i.e.

$$\kappa = -\nabla \cdot \hat{n} \quad (2-10)$$

$$\hat{n} = \frac{\nabla \alpha}{|\nabla \alpha|} \quad (2-11)$$

The solution of the aforementioned equations, is performed in the commercial package of ANSYS FLUENT [160]. The general settings used throughout the whole thesis, if not stated otherwise are presented in Table 2.1.

Parameter	Setting
p-V coupling	PISO
Momentum flux term discretization	Second-order upwind
Flux term discretization, volume fraction	CICSAM
Time discretization, volume fraction	Explicit
Time discretization, momentum	Euler First-order implicit
Curvature calculation	Node-based
Courant	0.25

**Table 2.1:** General settings used in ANSYS Fluent VOF model.

As mentioned in Chapter 1, the discretization of the flux term in the volume fraction equation (Eq. 1-1) needs special care, so that diffusion can be avoided and physical results can be obtained. In this study, the CICSAM [87] discretization scheme is used, which is highly compressive. CICSAM has been proved to provide a reliable way of predicting droplet dynamics phenomena as presented in [149-151, 161-165] concerning droplet impingement on a wall film, droplet-droplet collisions and impingement onto heated surfaces from works of researchers from the author's group.

## 2.2 Phase change evaporation model

The extension of the VOF model to non-isothermal flows in order to account for the evaporation of the liquid phase is achieved with the additional solution of the energy equation, the transport equation of the produced vapour mass fraction, as well as the updated volume fraction equation, accounting for the mass transfer between the two phases:

$$\frac{\partial \rho E}{\partial t} + \nabla \cdot [\bar{u}(\rho E + p)] = \nabla \cdot \left[ k_{cond} \nabla T - \sum_q \alpha_q \left( \sum_j h_{q,j} J_{q,j} \right) \right] + S_e \quad (2-12)$$

$$\frac{\partial (1-\alpha) \rho_g Y_j}{\partial t} + \nabla \cdot [(1-\alpha) \rho_g \bar{u} Y_j] = \nabla \cdot [-(1-\alpha) J_j] + S_v \quad (2-13)$$

$$\frac{1}{\rho_l} \left[ \frac{\partial \alpha \rho_l}{\partial t} + \nabla \cdot (\bar{u} \alpha \rho_l) \right] = S_l \quad (2-14)$$

Energy E and temperature T are treated as mass-weighted variables:



$$E = \frac{\sum_q \alpha_q \rho_q E}{\sum_q \alpha_q \rho_q} \quad (2-15)$$

The specific internal energy equals to:

$$E = h - \frac{p}{\rho} + \frac{u^2}{2} \quad (2-16)$$

Where enthalpy, for incompressible flows equals to:

$$h = \sum_j Y_j h_j + \frac{p}{\rho} \quad (2-17)$$

and  $h_j$  is calculated as:

$$h_j = \int_{T_{ref}}^T c_{p,j} dT \quad (2-18)$$

Heat transport due to inter-species diffusion is accounted for by the second term on the right hand side of the energy equation, where  $J_j$  is the diffusion flux of species  $j$  of the gas mixture:

$$J_j = -\rho_g D_{diff,j} \nabla Y_j \quad (2-19)$$

In this term, the summation over species transport from all phases is included in order to account for multi-component liquid evaporation.

The gas phase is considered as a two-specie mixture (vapour, air), while heat and mass transfer due to phase change is taken into account by including source terms in energy conservation, vapour specie conservation and volume fraction equations (Eq. 2-12 - 2-14). The source terms used are presented in Table 2.2 and represent the mass transfer of liquid to vapour phase, as well as the latent heat of evaporation during the phase change process.

Equation	Source Term
Energy	$S_e = -\dot{m}'L = -\dot{m}'(h_v^f - h_l^f)$
Vapour	$S_v = \dot{m}'$
Volume fraction	$S_j = -\dot{m}'$

**Table 2.2:** Evaporation source terms incorporated in respective equations in ANSYS Fluent VOF model

The latent heat is replaced by the difference of formation enthalpies of liquid and vapour [166]. The mass transfer rate applied is based on the kinetic theory of gases [148] and is given by the following equation:

$$\dot{m} = \frac{2\beta_m}{\beta_m} \sqrt{\frac{MW_j}{2\pi R_u}} \left( \frac{p_{sat}}{T_{sat}} - \frac{p_\infty}{T_\infty} \right) \quad [\text{kg/m}^2\text{s}] \quad (2-20)$$

This equation is valid to be used for the operating conditions of this study (weak evaporation for  $Kn \ll 1$  and  $(T_{oo}-T_b)/T_b \ll 1$ ) as stated in [167]. The thermal accommodation coefficient  $\beta_m$  represents the proportion of molecules that hit the liquid surface and are absorbed by it [167]. Its value ranges from 0 to 1, and in this thesis it takes the value of 0.5 [149], as scarce information can be found on its exact values especially concerning heavy hydrocarbons [167] which are the focus of this research work.

The application of the mass transfer rate only in the liquid-gas interface area is a difficult task when dealing with the continuum approximation of the interface thickness. This is mentioned in Chapter 1, where it is presented how other authors deal with this issue. In this thesis, the mass transfer rate is calculated at the cells where two conditions are realised:

- a) non-zero volume fraction gradient value, cell belongs in interface
- b) non-zero volume fraction value, cell has liquid to “vaporize”

This is schematically presented in Figure 2.1

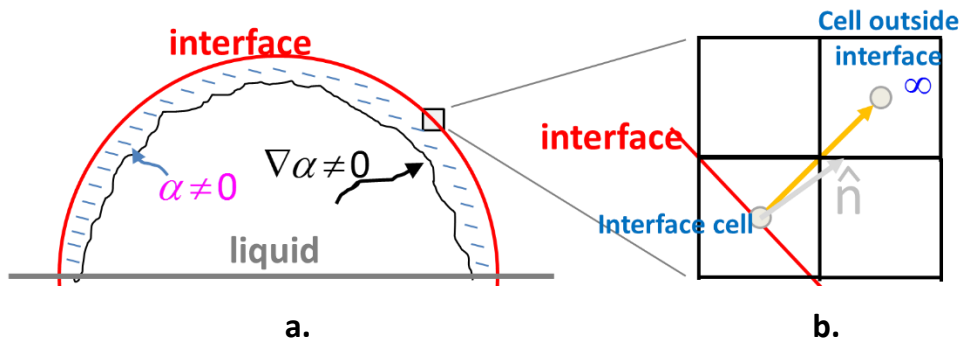


**Figure 2.1:** a) Interface cells that evaporate, b) Cell on direction that represents conditions outside of interface.

For the implementation of Eq. 2-20, in the interface cells, saturation pressure  $p_{sat}$  is derived from local cell value  $T_{sat}=T_{cell}$ , as the interface is supposed to be saturated. Typically, a table or graph from literature is used to relate vapour pressure of the specific specie in the gas medium with temperature [168]. The conditions far from the interface,

outside the Knudsen layer [167] (denoted with the symbol  $\infty$ ) are calculated from the neighbour cell whose centre is closer to the direction of the interface unit normal vector (negative so that it points outwards of the interface) as shown in Figure 2.1b. A subroutine which finds the nearest neighbor of a specific cell in respect to a reference vector is used for this reason.

The partial pressure of the vapour specie in the gas phase is calculated by Dalton's Law, given the vapour mass fraction in the specific cell:

$$p_{\infty} = X_j p_g, \quad X_j = \frac{Y_j / MW_j}{\sum_j Y_j / MW_j} \quad (2-21)$$

where  $X_i$  is the mole fraction and  $Y_i$  is the mass fraction of each specie in a multicomponent droplet approximation.  $P_{\text{gas}}$  is the operating pressure (2 atm in this work).

Finally, the mass transfer rate, in order to be compliant with the units of the volume fraction and transport of vapor species equations is transformed into:

$$\dot{m}' = \dot{m} \frac{A_{\text{int}}}{V_{\text{cell}}} = \dot{m} \frac{|\nabla \alpha| V_{\text{cell}}}{V_{\text{cell}}} = \dot{m} |\nabla \alpha| \quad [\text{kg}/\text{m}^3\text{s}] \quad (2-22)$$

where  $A_{\text{int}}$  is the interfacial surface area of the droplet, and it is equal to the magnitude of the volume fraction gradient multiplied by the computational cell volume [151, 159].

Using this evaporation model, the cells of the interface are not explicitly set as saturated, but this condition is derived from the solution of vapour transport equation. The weighting of specie properties in the gas mixture is given in the following Table, while the phase averaging is volume-weighted, using the volume fraction values (as in 2-7).

Gas-mixture properties	Method or Weighting
$\rho$	Ideal-gas law
$C_p$	Mass-weighted average
$k$	Mass-weighted average
$\mu$	Mass-weighted average
$D_{\text{diff}}$	Dilute approximation

**Table 2.3:** Weighting of species in gas mixture.

## 2.3 Surface Reactions

For the inclusion of surface reactions, a simple equation is solved on the wall surface:

$$\rho_g D_j \frac{\partial Y_j}{\partial \eta} = MW_j \cdot RR' \quad [\text{kg/m}^2\text{s}] \quad (2-23)$$

where  $\eta$  is the distance from the wall face to the cell center of the boundary cell. When this equation is solved, the unknown value of  $Y_j$  is found at each wall boundary face, and afterwards it is used as a fixed value boundary condition in the specie transport equation (same as Eq. 2-13).

## 2.4 Dynamic local grid refinement

In order to save computational time, whilst keeping a high resolution at the area of interest, i.e. the liquid-gas interface, a dynamic local grid refinement technique is used. The grid is refined dynamically close to the interface, and coarsened far away from it, thus “following” the droplet deformation as can be seen in Figure 2.2.

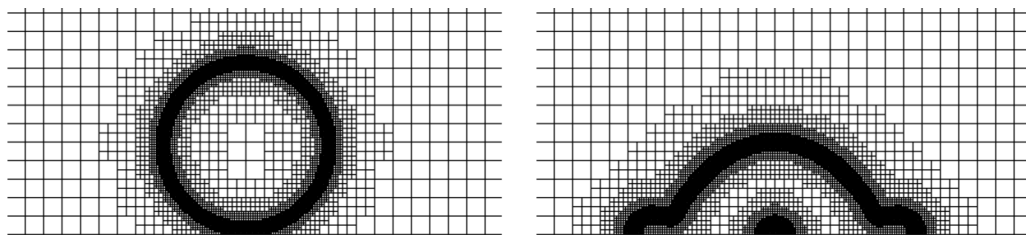


**Figure 2.2:** Dynamic local grid refinement applied at the case of a droplet impinging onto a solid flat surface.

Dynamic local refinement has been applied successfully in simulations of the research group in [150, 162, 165] for a wide range of different cases. These works were originally based in the study of Theodorakakos and Bergeles [169] as concerns the local refinement algorithm.

The profound advantage of using such technique is that the numerical accuracy of the results can be as high as possible with the minimum computational cost. An example of the amount of cells which are saved is depicted in Figure 2.3 for an initial 64x64 cell domain.

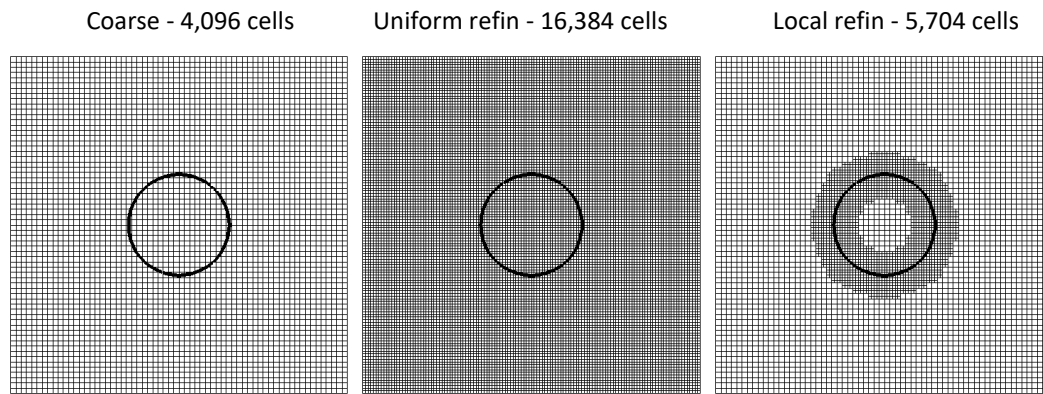


**Figure 2.3:** Number of computational cells when using the local refinement technique for 1 level of refinement in comparison with uniform refinement.

Of course, as the levels of local refinement are increased, the computational gain is higher.

The basic idea of the refinement algorithm is that the grid should be refined at a specific distance to the interface. Moreover, a gradual change in cell width is desired in the refinement level change. This method is presented in Figure 2.4 where different distances between each refinement level are included.

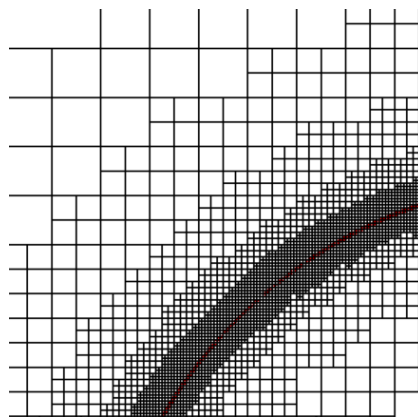


**Figure 2.4:** Local refinement algorithm. Specific width is given for each level of refinement.

The basic steps executed in order to apply this technique are:

- a) Calculate the interface distance function, i.e. the minimum distance of each computational cell from the interface.
- b) Based on this distance function and the desired width of each refinement level region (Figure 2.4), the cells to be refined/coarsened are selected.

## 2.4.1 Distance Function

The demand for an accurate and quick approximation of a distance function in relation to the interface location, is dictated by the local refinement algorithm. In this thesis, two ways to approximate the distance function are used, and their description follows. In both methods, the interface location is firstly found as the iso-surface of  $\alpha=0.5$ .

### 2.4.1.1 Accurate Distance

The minimum distance of each cell to the interface is calculated in a straightforward fashion as:

$$df = \min |\vec{x} - \vec{x}_{int}|, \quad \vec{x}(x,y,z) \in \Omega \quad (2-24)$$

where  $\Omega$  stands for the computational domain. The number of cell loops required for this calculation is proportional to the product of interface cell count multiplied by the domain cell count  $O(\text{interface cells} * \text{domain cells})$ ; the resulting number may grow enormously in 3-D simulations. Moreover, when this method is applied simultaneously with parallelization, the algorithm becomes inevitably time consuming. This is because there is no link between the geometrical locations of the parallel processor grid regions and the location of the liquid-gas interface, thus data exchange between all processors is executed so that the minimum distance to the interface can be computed in each processor. Therefore, a new method is developed in this work in order to resolve this issue.

### 2.4.1.2 Fast marching algorithm for the computation of iso-surfaces

In order to overcome these limitations, an algorithm similar to the work of Elias et al. [47] which was developed for finite elements is implemented in this work. The calculation of the distance function starts from the interface cell and then marches to neighboring cells following the direction of the interface normal unit vector  $\hat{n}$ . The advantage of this method is that only neighboring grid region processors have to exchange data, instead of data exchange between all processors, as required by the accurate distance algorithm.

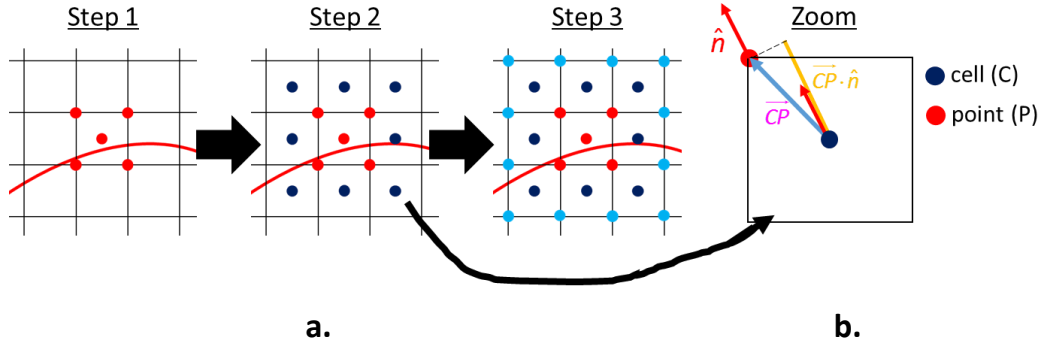


**Figure 2.5:** a) Schematic representation of the fast marching algorithm steps to calculate distance function starting from a single cell; step 1: red, step 2: blue and step 3: light blue. b) Calculation of the distance function at a random cell located far from the interface.

This fast-marching algorithm is presented schematically in Figure 2.5 and its basic three steps are summarized below:

- 1) A first cell loop is performed. The distance from the interface ( $df$ ) is calculated and stored at each node of the interface cells. Vector  $\hat{n}$  is copied from the cell centre to the nodes, while the cells used and all their points are flagged as visited.
- 2) A second cell loop is performed. The distance function is calculated in the cells where at least one node is flagged as visited, and equals the distance function stored at the node plus the distance of the node to the cell distance projected on the interface normal unit vector as (notation presented in Figure 2.5b):

$$df_c = \vec{CP} \cdot \hat{n} + df_n \quad (2-25)$$

If more than one nodes are flagged as visited inside a cell, the minimum distance function value from all node calculations is kept. Vector  $\hat{n}$  is copied from the nodes to the cell centre, while the cells used and all their points are flagged as visited.

- 3) A third cell loop is performed. If a cell is already visited, without having all of its nodes visited, the distance function is calculated in the remaining cell nodes using this time the distance function value at the cell centre as:

$$df_n = \vec{CP} \cdot \hat{n} + df_c \quad (2-26)$$

In this step, whenever a node is already visited, the minimum of the previously stored value and the newly calculated one is kept.

Steps 2 and 3 are repeated until all cells of the domain have been filled in with a distance function value. The three steps of the algorithm are shown in Figure 2.5a, while in Figure 2.5b the notation used in Eq. 2-25, 2-26 for the local calculation of the minimum distance from the interface is indicated.

The very simple idea of this algorithm is that the distance function is calculated on a local cell basis, using as a guide the interface unit vector which is copied from the interface cells to the nodes and then to the neighboring cells and nodes and so on. The accuracy of this algorithm, where the marching motion starts from the interface and moves in outwards direction, is definitely affected by cell alignment and marching direction.

However, the gain in computational time is massive, as the number of cell loops that are needed are proportional to the number of cells marched in the normal direction to the interface  $O(\text{interface cells} \times \text{marching cells along normal to interface})$ , which is significantly smaller than the previously reported accurate distance method, especially in large computational domains.

## 2.4.2 Refinement/Coarsening

After the calculation of the distance function in respect to the interface, the marking of the cells that should be refined/coarsened follows. This procedure is executed in Nlevels (number of refinement levels) number of stages, where the cells are refined progressively from the lowest to the highest level of refinement and coarsened towards the opposite direction. This procedure is incorporated in the Fluent software as a macro file, written in “scheme” language, and is presented in Table 2.4.

Stages	Refinement	Coarsening
1	0->1	Nlevels->Nlevels-1
2	1->2	Nlevels-1->Nlevels-2
3	2->3	Nlevels-2->Nlevels-3
...	...	...
Nlevels	Nlevels-1->Nlevels	1->0

**Table 2.4:** Refinement stages for refinement/coarsening procedure

Based on this grid adaption procedure, during each stage, refinement/coarsening for each cell is only executed one refinement level up/down. This procedure resolved an issue observed in Fluent versions prior to 16 and is very important to handle in CFD codes. Imagine two neighbouring cells that belong to different processors in a parallel run



(processor interface), and have the same level of refinement. If based on the local refinement algorithm described, the one cell needs to be refined while the other one needs to be coarsened, these two cells will end up having a difference of two levels of refinement. This could not happen based on the splitting algorithm of Fluent in which one face may split only in two faces and no more (hanging node adaption).

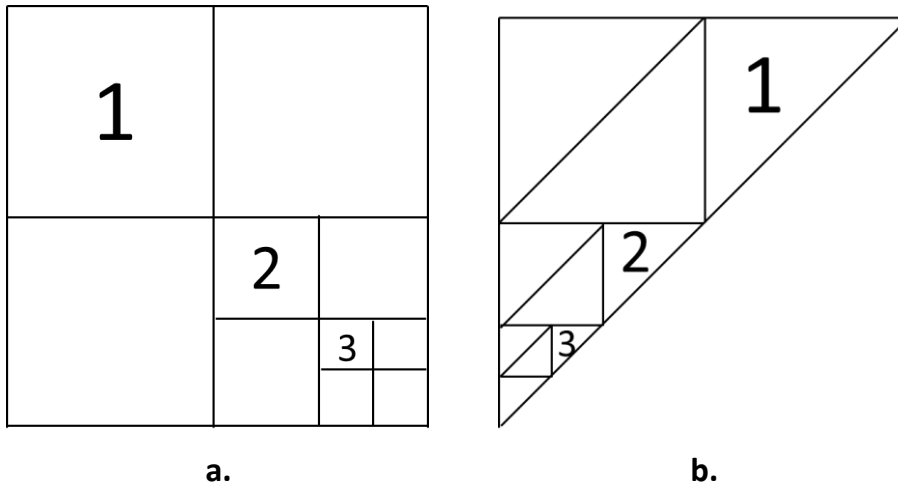


**Figure 2.6:** Splitting algorithm. Hanging node adaption

The local refinement algorithm not only saves computational time, but also is an easy way to tackle the advection problem (mentioned in Chapter 1), since the grid can be as “dense” as it “needs to be” (in order to keep high accuracy levels), but only at the region of interest.

The implementation of this technique is achieved through a User Defined Function (UDF), which is executed every N time steps so that the interface never exits the finest level of refinement cells. In this way, the gradients of volume fraction are computed in the region with the denser grid cells and it is guaranteed that the computed surface tension term that will be inserted in the momentum equation will always have the highest level of accuracy.

During every coarsening and refinement procedure, remapping/smoothing of all flow field variables at the newly created/erased cells is executed. Those cells exist at the limits of the refined region, thus far enough to retain accuracy levels high, thus achieving as well a significant decrease of the actual time of computations.

## 2.5 Wettability

Most dynamic contact angle models relate contact line velocity to the dynamic contact angle, which is inserted as a boundary condition. The dynamic contact angle models are briefly presented below. More info about the implementation of contact angle models is presented in Chapter 1.

### 2.5.1 Contact angle as Boundary Condition

When the contact angle is implemented as a boundary condition, the contact angle, either if it is a static or dynamic one, is implemented in the VOF model using a similar approach to the one presented in Brackbill et al. (Eq. 53 in their work) [98] and Ubbink (Eq. 2.22 in their work) [87].

Based on the contact angle value  $\theta$ , which should be prescribed, the normal to the interface unit vector at the wall boundary cells  $\hat{n}$  is calculated according to the following equation:

$$\hat{n} = \hat{n}_w \cos \theta + \hat{n}_t \sin \theta \quad (2-27)$$

so that the interface can form the prescribed angle  $\theta$ , when in contact with the wall. Figure 2.7 is presented for better understanding of Eq. 2-27 concept and notation.

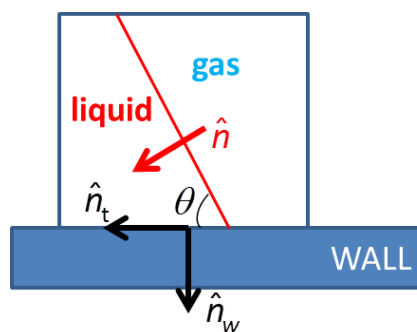


**Figure 2.7:** Unit vectors on the wall face, as well as unit free surface normal vector.

In particular, the calculation of this vector in the cells next to the wall boundary, influences the interface curvature calculation (Eq. 2-10) at the spreading droplet rim region, and in turn the surface tension force (Eq. 2-9) applied at the cells.

The procedure for prescribing the contact angle starts from locating the three-phase contact line, i.e. the droplet rim, or else the liquid-gas interface at the wall region. It was

found that when the contact angle is only prescribed at the cell which is cut by the  $\alpha=0.5$  iso-surface, i.e. where the contact line exists, this boundary condition was not enough to actually make the rim “form” the desired contact angle. A transition region, where the contact angle is applied as a BC is needed in order to reinforce the condition. This region is characterized by the non-zero volume fraction gradient condition, as in Roisman et al. [54] because in volume tracking algorithms the contact line is represented by a transition region, rather than the exact position of the contact line.

Afterwards, the contact line velocity is calculated for the implementation of any dynamic contact angle model. The contact line velocity is assumed to be the actual velocity calculated at each computational cell, in the triple-phase contact region as mentioned above, from which the velocity component parallel to the wall ( $\vec{u}_{cl}$ ) is derived, according to:

$$\vec{u}_{cl} = (\vec{u}_{cell} \cdot \hat{n}_t) \frac{\hat{n}_t}{|\hat{n}_t|} \quad (2-28)$$

Although more accurate methods for contact line velocity have been presented in the literature, based on the time derivative of the radius of the wetted area, as in Sikalo et al. [58] and Roisman et al. [54] ( $u_{cl}=dx_{cl}/dt$ ), the simple approximation used here can be easily extended to a three-dimensional case.

After the contact line velocity is found, the dot product of the velocity vector with the unit free surface normal provides the direction of contact line movement, i.e. if the rim is advancing or recoiling.

$$clDirection = \vec{u}_{cl} \cdot \hat{n}_t \quad (2-29)$$

If the resulting value is negative, this means that the rim is advancing ( $\hat{n}$  always points inside the liquid phase), while if it is positive, the rim is recoiling.

### 2.5.1.1 Quasi-dynamic contact angle mode

In the simplest possible advancing-receding contact angle model, a given fixed value for both the advancing and the receding contact angles is imposed as a boundary condition when the contact line spreads or recoils. This model has been used widely in literature, and can be found selectively in the works of Pasandideh et al. [152] and Berberovic et al. [90]. The basic approach is simply represented by the two equations:

$$\theta_{dyn} = \begin{cases} \theta_{adv} & \text{if } clDirection \geq 0 \\ \theta_{rec} & \text{if } clDirection < 0 \end{cases} \quad (2-30)$$

### 2.5.1.2 Kistler's law

In the work of Kistler [115], the dynamic contact angle is given as a function of the contact line velocity through the Capillary number and the inverse of Hoffman's function:

$$\theta_{dyn} = f_H \left[ Ca + f_H^{-1}(\theta_{eq}) \right] \quad (2-31)$$

$$f_H = \arccos \left\{ 1 - 2 \tanh \left[ 5.16 \left( \frac{x}{1 + 1.31x^{0.99}} \right) \right]^{0.706} \right\} \quad (2-32)$$

$$x = Ca + f_H^{-1}(\theta_{eq}) \quad (2-33)$$

$$Ca = \frac{\mu_l u_{cl}}{\sigma} \quad (2-34)$$

### 2.5.1.3 Shikhmurzaev's model

Shikhmurzaev [118] gave a relation for the dynamic contact angle, as a function of several parameters, i.e.:

$$\cos \theta_{dyn} = \cos \theta_{eq} - \frac{2u^* (a_1 + a_2 u_0^*)}{(1 - a_2) \left[ (a_1 + u^{*2})^{1/2} + u^* \right]} \quad (2-35)$$

$$u^* = a_3 \frac{\mu_l u_{cl}}{\sigma}, \quad u_0^* = \frac{\sin \theta_{dyn} - \theta_{dyn} \cos \theta_{dyn}}{\sin \theta_{dyn} \cos \theta_{dyn} - \theta_{dyn}} \quad (2-36)$$

where  $a_2=0.54$ ,  $a_3=12.5$ ,  $a_4=0.07$  are phenomenological constants (values taken from [119]).

Basically, the dynamic contact angle models of Kistler and Shikhmurzaev try to deal with the difference observed in experiments between the dynamic contact angle (at microscopic length scale) and the apparent contact angle (at macroscopic length scale) within the inner region near the triple line point. A wide range of empirical correlations can be found in literature (a comprehensive review is presented in the work of Saha and Mitra [119]), that relate the contact line velocity with the dynamic contact angle in order to account for this inner region. This is also addressed in the works of Sikalo et al. [170]

and Roisman et al. [54]. The differences in dimensionless spreading dynamics parameters (e.g. temporal evolution of spreading ratio, maximum spreading) which are observed between the simple quasi-dynamic model and these models may be related to that blurred distinction (Yokoi et al. [89]).

## 2.5.2 Wetting Force Model

The Wetting Force Model is a novel implementation for the contact angle boundary condition which is presented in this Thesis, in an effort to capture the complex physicochemical phenomena that appear at the contact line region and are manifested in the change in contact angle values throughout spreading and recoiling phases [114].

The basic concept relies on the work of Antonini et al. [171], where the authors derived a methodology for the prediction of the ‘adhesion’ force exerted on a droplet sliding down an inclined surface. The “adhesion force” acts at the contact line, and is responsible for drop capillary adhesion to the surface, which for a droplet of arbitrary shape is given by:

$$f_{adh} = -\sigma \int_0^L \cos \theta(l) \cos \psi(l) dl \quad (2-37)$$

where  $L$  is the total length of the contact line, and the angles  $\theta, \psi$  are shown in Figure 2.8 (from [171]). For the validation of their methodology, the magnitude of the “adhesion” force was explicitly calculated, from the component of gravitational force (Figure 2.8a) acting on the droplet parallel to the solid surface, at the exact moment when it starts moving and for this specific angle of inclination. The adhesion force is therefore related to the contact line shape and the contact angle values.

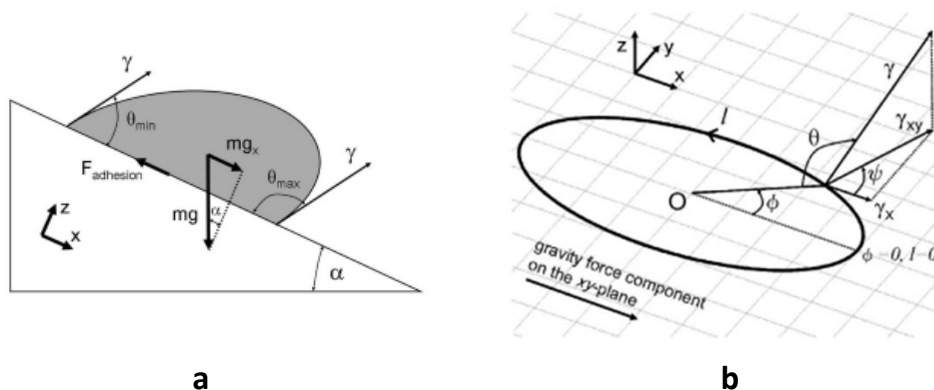


**Figure 2.8:** Adhesion force. a) Droplet sliding down an incline. At the moment it starts moving,  $f_{adh} = mg \sin \alpha$ . b) Projection of the contact area of the droplet on the incline. Reprinted with permission from [171] Copyright 2009 American Chemical Society.

When these values are not known, a simplified approach is typically used in many works, e.g. by Extrand and Kumagai [172], to estimate the capillary adhesion force. They refer to the adhesion force for solid/liquid/vapor systems, as being mathematically described by the following equation, for static conditions:

$$\frac{f_{adh}}{r} = K\sigma(\cos \theta_{rec} - \cos \theta_{adv}) \quad (2-38)$$

where K is a fitting factor, which changes by changing the liquid-solid system. In both previously mentioned cases, the adhesion force is related to the contact angle of the droplet and the contact line shape, but these equations refer to static or quasi-static conditions, i.e. when a droplet is at rest onto a solid surface and on the verge of starting to move. A more complete model that can be applied in dynamic contact lines should be derived, one that includes the idea of the ‘adhesion’ force.

In this Thesis, a new model is proposed that considers for the effect of an additional (except from the interfacial tension) contact line force on a moving contact line. This additional force term is assumed to be parallel to the wall and is expressed-in relation to eq. 2-37-as:

$$df_{WFM} = \sigma(\cos \theta_{eq} - \cos \theta_{dyn})dl = \sigma(\cos \theta_{eq} - \cos \theta_{dyn})rd\phi \quad (2-39)$$

Where the equivalence  $dl = rd\phi$  holds for a circular contact line, which is coherent with assumptions of axisymmetric flow for 2-D simulations. The direction of this stress term is presented in Figure 2.9 and is linked to the “adhesion” force reported before (eq. 2-38).

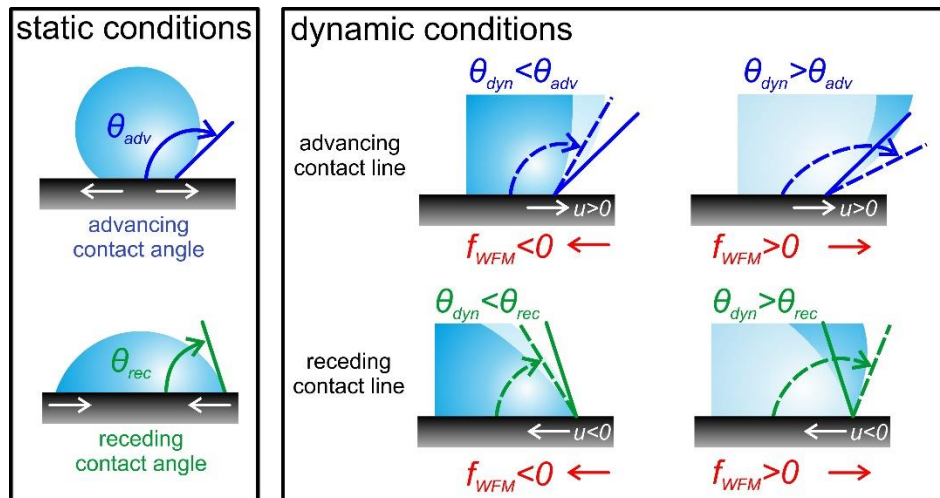


**Figure 2.9:** Direction of the proposed adhesion term at the contact line for dynamic conditions:  $f_{WFM}$  points to the left/right until  $\theta_{eq}$  is reached.

The driving force of this adhesion equation is the difference between the current apparent dynamic contact angle at the three phase contact line and the equilibrium angle. As this difference is increased, the magnitude of this force increases and thus its effect on droplet motion grows. As this model is preliminary tested only on axisymmetric cases, the force is proportional to the droplet radius.

In physical terms, the application of this extra “adhesion” force, only at the contact line, tends to restore the droplet shape to its static condition, i.e. to form an equilibrium angle, by either promoting or counterbalancing droplet further spreading/recoiling. For an advancing contact line, it is assumed that the equilibrium angle is the advancing contact angle, so the exerted adhesion force points in the right direction to restore the droplet static condition, i.e. to reach the advancing contact angle (Figure 2.9). For the receding phase, the concept is the same, as can be seen in Figure 2.9.

The new model proposed tries to deal with the dynamic contact angle problem from a different perspective. By incorporating a stress term into the Navier-Stokes momentum equation, this Wetting Force Model (WFM), as will be referred, avoids the typical imposition of a contact angle value as a boundary condition, but allows the flow field near the contact line to affect the adhesion term. In that way the microscopic change of the dynamic contact angle, as well as the macroscopic temporal evolution of the phenomenon, will change according to how this force aids or counteracts the droplet spreading onto the solid substrate. This stress term, therefore, would dynamically affect the formation of the dynamic contact angle in relation to its interaction with the standard surface tension force and viscous dissipation near the wall.

The magnitude of the stress term which is implemented in the momentum equation as a source term is given by the following expression:

$$\vec{f}_{WFM}^v = d\vec{f}_{WFM} / V_{cell} = \sigma (\cos \theta_{eq} - \cos \theta_{dyn}) r / V_{cell} \quad (2-40)$$

where:

$$\theta_{eq} = \begin{cases} \theta_{adv} & \text{if contLineDirection} \geq 0 \\ \theta_{rec} & \text{if contLineDirection} < 0 \end{cases} \quad (2-41)$$

Eq. 2-40 is consistent with the momentum equation (eq. 2-6) units and is applied at the cells lying in the vicinity of the contact line region, i.e. cells with volume fraction values between 0.05 and 0.95. The reasoning behind this choice of threshold values is presented in Appendix A.

The numerical procedure followed for the implementation of the wetting force is similar to the contact angle boundary condition as described in previous section. Contact line velocity and contact line direction (Eqs. 2-28, 2-29) are calculated for all cells in contact with the wall, where the volume fraction lies between the aforementioned threshold values. The contact line direction determines the choice of equilibrium angle (Eq. 2.40). The current dynamic contact angle value at each cell is calculated from the slope of the free surface normal in relation to the wall surface. For the cases examined in this Thesis, this additional stress term is inserted only in the radial velocity equation, since an axisymmetric approach is followed.

The significant advantage of the proposed approach, when compared to the standard boundary condition (BC) one, based on the work of Brackbill [98], is that by this methodology, one can really measure the temporal evolution of the dynamic angle the droplet forms, and compare this with available experimental data. This is shedding light on the complicated, not yet fully understood, underlying physical mechanisms controlling droplet impingement on any type of either flat or non-flat solid surfaces.

## 2.6 Sharpening Equation

When the sharpening of the liquid-gas interface is desired, the solution of an additional, sharpening equation, which was first proposed by Olsson et al. [90], adopted by Sato and Niceno [92] and Shukla et al. [93] and mostly used in Level-Set simulations is used. The applied pseudo-equation is:

$$\frac{\partial \phi}{\partial \tau_{pseudo}} + \beta \nabla \cdot [\phi(1-\phi)\hat{n}] = \beta \nabla \cdot (\epsilon \nabla \phi) \quad (2-42)$$

, where  $\phi$  is the volume fraction field taken right after the solution of Eq. 1-1,  $\epsilon$  is a sharpening constant which controls the thickness of the interface,  $\tau$  is pseudo-time and  $\beta$  is a constant proposed by Sato and Niceno [92] in order to avoid interface shape deformation. In their work, this constant is reported to take values in the range from 0.01 to 1. In this thesis,  $\beta$  is set constant and equal to 1, which by a number of numerical tests undertaken, under the specific setup, is proven to aid both in preserving a sharp interface, as well as a mass conservative volume fraction field. This equation is solved in pseudo-time (First-Order Implicit discretization in time), while the time-step is selected to be equal to the flow solution time-step.



This equation has three terms, namely the pseudo temporal term, the flux ('compression') term and the diffusion ('artificial diffusion') term. However, it is neither written in conservative form nor has any physical meaning. It is used as a 'correction' of the volume fraction field. As Shukla et al. [93] state, this equation "restores, or regularizes, the missing immiscibility condition of the two fluids". The flux and diffusion terms change sign across the interface and have opposite behaviour. The flux term 'compresses' the interface (values below 0.5 will get smaller, while values above 0.5 will tend to get higher), while the diffusion term 'diffuses' it. The thickness of the interface is therefore controlled by the strength of the diffusion term, i.e. by variable  $\epsilon$ , which takes the value of  $\Delta x/2$  [92], and  $\Delta x/3$  to achieve moderate or high sharpening (SHARP and HSHARP respectively). Variable  $\Delta x$  is the grid cell edge.

The flux term is discretized using QUICK scheme, while the rest term  $(1-\alpha)\cdot\hat{n}$  is approximated using central differences as proposed by Olsson et al. [91]. This choice is proven to be beneficial for the mass conservation of the method. At boundary faces, the flux term of this equation is set to zero, in order to "avoid any flow through the boundaries" as Olsson and Kreiss state [91].

In the case of liquid spreading on a solid surface, the wettability of the surface needs to be accounted for. The sharpening procedure, therefore, should be executed along the direction of the prescribed contact angle, while the sharpening procedure should not affect the solution near the wall boundary. Zahedi et al. [173] have dealt with this issue with introducing a regularized normal vector, that is derived from the solution of an equation containing the actual free surface normal, with a Dirichlet boundary condition that accounts for the contact angle. In a recent work, Sato and Niceno [174] set the normal to the wall component of free surface normal vector equal to zero in "wall layer cells", so that the sharpening procedure will act only towards the tangential to the wall direction. Moreover, they enforce the second and third terms in eq. 2-42 to be zero for the faces that are parallel to the wall boundary on "wall layer cells", minding a Cartesian grid. A major drawback of this method is that it is not easily and straightforward applicable in an unstructured grid, especially in the case of triangular elements.

On the other hand, in this Thesis a simpler approximation is employed which is easily applicable on unstructured grids, while the conservation of the volume fraction field is preserved based on numerous simple test cases performed. More specifically, the free surface normal vector in eq. 2-42 is calculated at the wall boundary cells from eq. 2-27, while  $\beta$  takes the value of 0.25 throughout the domain in order to enforce the contact

angle boundary condition, and the droplet rim is enforced to adjust to the prescribed contact angle value. This was not possible for  $\beta > 0.25$ . A local value of 0.25 can be applied near the three-phase contact line, while  $\beta=1$  throughout the remaining domain in future works.

The sharpening equation can be solved after volume fraction advection, and right before the solution of the momentum and pressure correction equations, as stated in previous works [90-93]. In this way, the momentum equation solved, contains the ‘corrected’ values of the volume fraction field. In this Thesis, however, in order to be more efficient, and since the volume fraction field is updated at the beginning of the time-step (explicit calculation), the sharpening equation is solved coupled with the momentum equation and the resulting ‘corrected’ volume fraction values are patched to the volume fraction field at the end of the time-step. By that means, the advection in the next time-step will commence on a diffusion-free basis. Such an algorithmic route decreases the required actual computational time, as this equation is neither solved before the momentum solution as in previous works [90-93], nor at the end of each time-step.

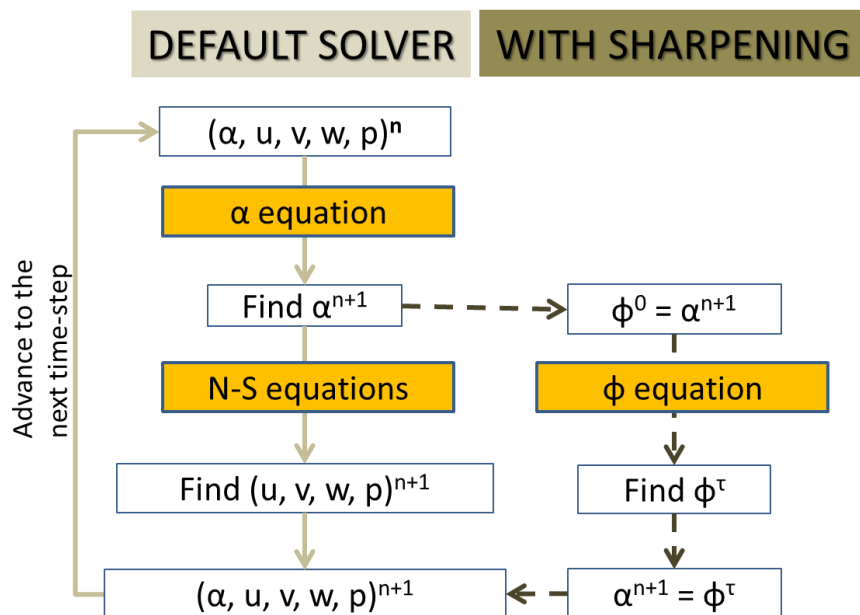


Figure 2.10: Outline of the Sharpening scheme used.

## 2.7 Mass Conservation Algorithm

For the case of the High Sharpening (HSHARP) scheme, the total mass of volume fraction is not conserved, and for that reason a simple mass conservation algorithm is used at the end of time-step in order to keep the total liquid mass constant.

According to this algorithm, firstly, all cells are divided in three categories, interior, interface and exterior cells, based on the cells own value and all direct neighbor values, if they lie between specific thresholds value that define the interface, the upper limit and lower limit (after numerical tests, the values of 0.1 and 0.9 are used respectively):

$$cell = \begin{cases} \text{exterior cell} & \left( \alpha_{cell} < \alpha_{low} \right) \\ \text{interface cell} & \text{if } \left( \alpha_{low} < \alpha_{cell} < \alpha_{up} \right) \\ \text{interior cell} & \left( \alpha_{up} < \alpha_{cell} \right) \end{cases} \quad (2-43)$$

for cell and direct neighbours

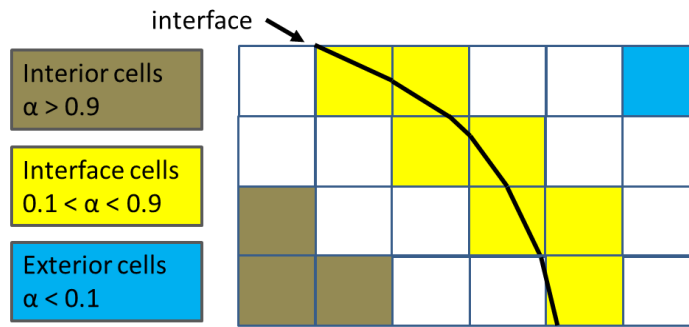


**Figure 2.11:** Cell categories used in the mass conservation algorithm.

Then, the total mass of the liquid phase is calculated and compared if found to be lower than the initial liquid phase mass (neglecting at this point cases with mass source/sink), the following procedure is followed:

- i) liquid mass is added to interior cells
- ii) the rest of the mass (if any) is added to the interface cells

In both steps, the total amount of mass which is missing (current mass - initial mass) is calculated as:

$$dm = m_{cur} - m_0 = \sum_{cells} \alpha_{cell} \rho_l V_{cell} - m_0 \quad (2-44)$$

While the maximum allowable liquid mass which can be added in all cells is:

$$dm_{add} = \sum_{cells} (1 - \alpha_{cell}) \rho_l V_{cell} \quad (2-45)$$

The change in volume fraction in each cell is given by:

$$\alpha_{cell,NEW} = \alpha_{cell} + (1 - \alpha_{cell}) \frac{dm}{dm_{add}} \quad (2-46)$$

Based on this equation, the integrated total mass which is added in all cells is equal to the missing mass (dm). In the case where the total mass is higher than the initial one, then:

- i) liquid mass is removed from exterior cells
- ii) the rest of the mass (if any) is removed from the interface cells

## 2.8 Droplet Initialization

For the initialization of the volume fraction values in the domain, and in order to have a smooth interface in the first time steps of the simulation, not only the zero and unity values of the liquid phase (spherical droplet) are initialized, but the interface values as well.

The identification of the interface cells is fairly easy. If all of the nodes of a random cell comply with the geometric restriction of the liquid phase shape, for example if all of the nodes of a cell are inside the droplet radius or not, then the value of one or zero is initialized for the volume fraction variable respectively. For the cells where not all of their nodes comply with the geometric restriction, an interface exists.

In Figure 2.12, the basic logic of the initialization procedure for a random interface cell is presented. Firstly, its dimension limits are found (min and max of x,y,z) and afterwards marker points along these limits are selected. The ratio between the points that are found inside the cell as well as inside the drop radius to the ones found inside the cell gives a good estimation of the cell volume fraction.

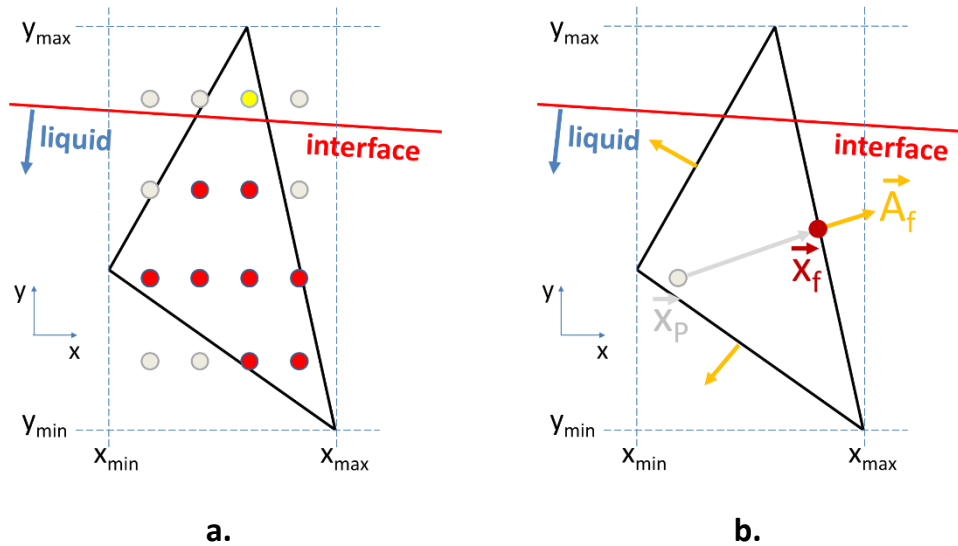


**Figure 2.12:** Volume fraction initialization at the interface cells, a) points to approximate volume fraction value b) point is inside the cell

In this way, the droplet mass at initialization is calculated more accurately, while interface is smoother than a 0-1 step function approach, which may affect the initial pressure distribution inside the droplet.

## 2.9 Model development using UDFs

The numerical model presented in this Chapter is based on ANSYS Fluent basic solver and capabilities. The addition of User Defined Functions (UDFs) to incorporate the models presented in previous sections is summarized in Table 2.5, where the UDF 'DEFINE\_' functions that were employed are given.

Fluent offers the possibility of handling refinement and coarsening of unstructured grids, parallel processing and a robust solver validated for many different applications. The customization of the software that is offered by the easy and efficient development of UDFs covers a large part of the solver, but not the whole.

Fluent DEFINE_ functions	Application
DEFINE_INIT	Droplet initialization Vapour Field initialization
DEFINE_ZONE_MOTION	Grid motion with droplet mean velocity
DEFINE_PROPERTY	Surface tension coefficient (varying with Temperature)
DEFINE_PROFILE	Dynamic contact angle
DEFINE_ADJUST	Calculations executed every iteration (ex. volume fraction gradient)
DEFINE_EXECUTE_AT_END	Calculations executed at the end of the time-step (local refinement distance function and mark cells to refine/coarsen, mass correction, writing intermediate result files)
DEFINE_SOURCE	WFM source terms for momentum equations
DEFINE_LINEARIZED_MASS_TRANSFER	Calculations for the mass transfer rate
DEFINE_SR_RATE	Surface reaction rate
DEFINE_UDS_UNSTEADY, DEFINE_UDS_FLUX, DEFINE_DIFFUSIVITY	Calculations for the terms (temporal, advection, diffusion) of the sharpening equation

**Table 2.5:** Fluent UDFs developed in this Thesis and their application



## Chapter 3

# Model Validation under realistic droplet flow conditions

In this Chapter the numerical methodology is validated against benchmark and realistic cases relating to droplet phenomena, so that the robustness of the numerical code is assessed. The new models are validated against available experimental data and new findings on the physical mechanisms that govern these phenomena are presented. Droplet-particle collisions in FCC reactors include, as mentioned in Chapter 1, evaporative reacting flows where droplets come in contact with solid particles. Breakdown of the physical processes include droplet motion in a gas medium, droplet impact onto flat and spherical surfaces. Moreover, the performance of the numerical models such as the sharpening equation, the Wetting Force Model and the local refinement algorithm are assessed.

### 3.1 Benchmark cases

#### 3.1.1 Introduction

In this section, two-phase flow advection tests are presented. The accuracy of interface advection in the numerical domain, as well as volume fraction smearing/diffusion levels are evaluated.

Comparison between the application of two different discretization schemes is presented. CICSAM [87] and the Modified-HRIC [88] discretization schemes are high resolution schemes [175] that combine nonlinear blending of upwind and downwind differencing schemes and ensure the boundedness of volume fraction values. From preliminary runs of a droplet accelerating inside a gas medium, as presented in Figure 3.1,



it was found that CICSAM is non-diffusive; however, it predicts unrealistic velocity values at the interface (Figure 3.1: a-red spots on the interface), which in turn may give rise to non-physical pressure predictions inside the liquid phase. On the other hand, the Modified-HRIC discretization scheme, produces more smooth velocity field; however, highly diffuses the interface (Figure 3.1: b). A comparison of the behavior between these two discretization schemes in a number of benchmark cases is also presented by Waclawczyk and Koronowicz [176], who reached to similar conclusions.

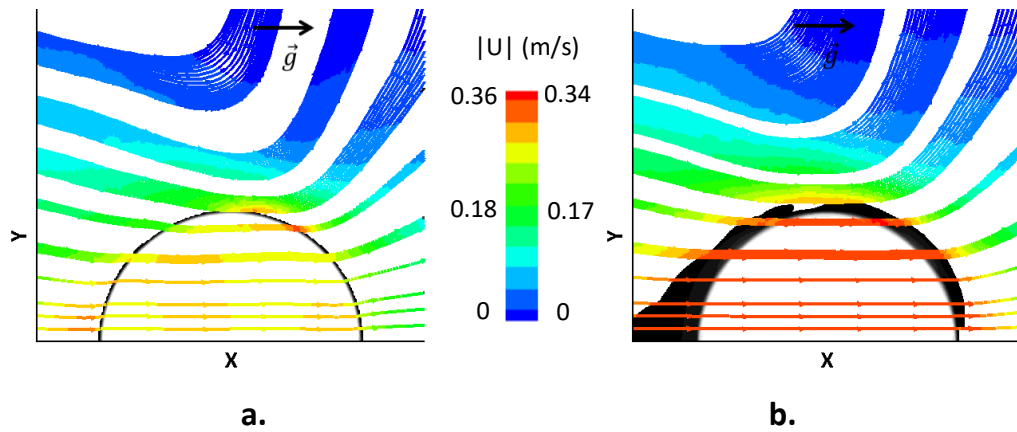


**Figure 3.1:** Comparison between a) CICSAM and b) Modified-HRIC discretization schemes for predicting the absolute velocity of a free-falling droplet after 30ms of simulation time (initial zero velocity). The volume fraction field is also plotted (gray-scale), values between 0.001 and 0.999.

In an effort to effectively compare these two schemes at realistic cases, the methods presented in the following Table are used. The sharpening algorithm is paired with the Modified-HRIC scheme so as to retain the smooth velocity field and achieve sharp interface.

Advection algorithms	Interface Thickness
CICSAM	Sharp
Modified-HRIC	Diffused
Modified-HRIC + SHARP	Moderate sharp
Modified-HRIC + HSHARP	Sharp

**Table 3.1:** Algorithms tested for volume fraction advection and interface thickness achieved

Moreover, comparison between the results obtained using a uniform grid against a dynamic one using local refinement algorithm is conducted.

### 3.1.2 Zalesak's disk

In Zalesak's disk [177] case, a slotted disk with dimensions and initial position as presented in Figure 3.2, is put in a unit square domain and is subjected to rotation under the influence of a stationary vortex field with velocity components:

$$u(y) = -\Omega \cdot (y - 0.5) \quad (3-1)$$

$$v(x) = \Omega \cdot (x - 0.5) \quad (3-2)$$

In these equations,  $\Omega$  is the rotation velocity, taken equal to  $\pi/3.14$ , so that one full rotation of the disk is completed within a timeframe of  $t=6.28s$ .

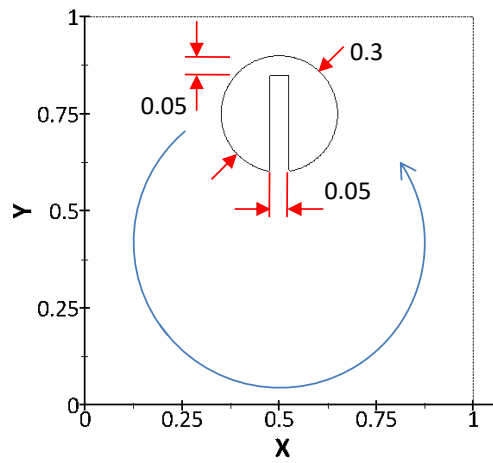


**Figure 3.2:** Initial domain and dimensions for Zalesak's disk benchmark case.

The numerical settings for all runs are given in Table 3.2. A fixed time-step is used, such that the Courant number can be kept at around 0.05. Two different uniform grid sizes are used, one coarse (64x64cells) and one fine (128x128). In the cases where dynamic local grid refinement is used, the base coarse grid is chosen to be 32x32cells, which when refined twice (at the interface) fits the accuracy of the fine grid. The distance from the interface, where the grid is locally refined, is chosen as  $D_0/6$ .

Parameter	Value
Courant	0.05 (fixed dt)
Grid size (cells)	64x64, 128x128, 32x32+locRef2
Locref distance	$D_0/6$
$t_{end}$ (s)	6.28 (1 revolution)

**Table 3.2:** Numerical settings for the Zalesak's disk benchmark case

The goal of this benchmark case is to successfully rotate the disk without any deformation. Results of the iso-line of  $\alpha=0.5$  after one revolution of the disk are presented in Figure 3.3. In the first row, the numerical results for the default discretization schemes of CICSAM and M-HRIC are presented. It is clear that the advection is not perfect for both schemes, even for the fine grid, while the use of dynamic local refinement has a slight effect on the disk shape in the form of small visible wrinkles inside the slot.

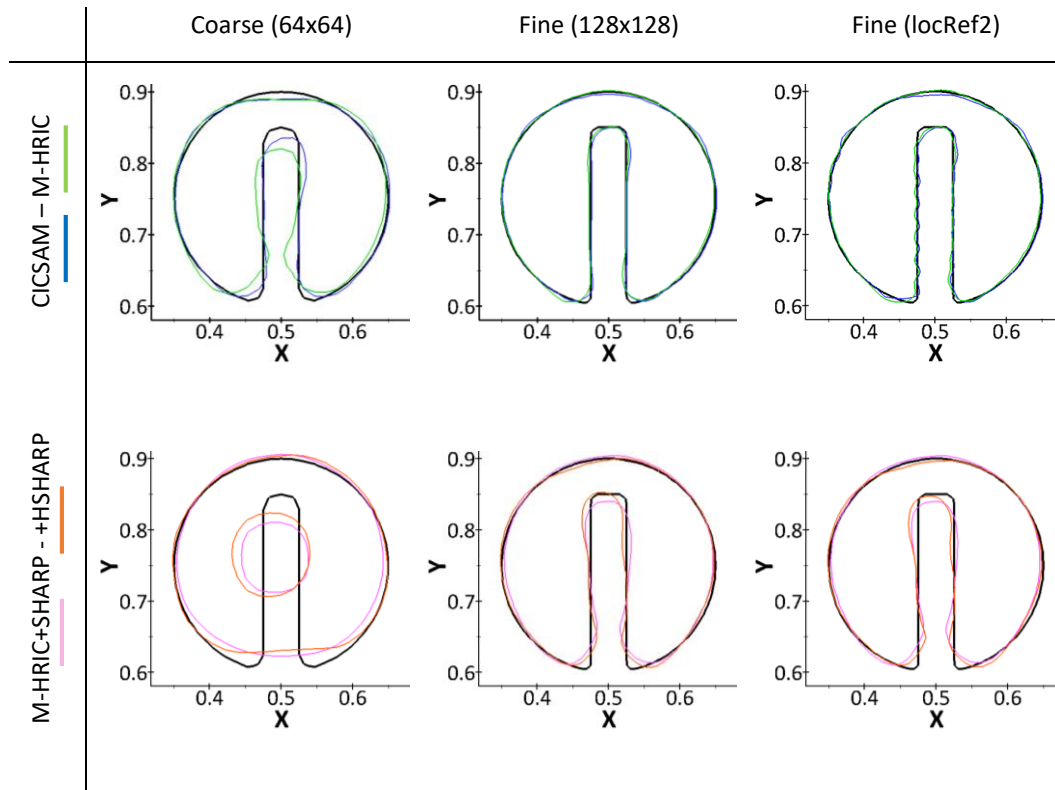


**Figure 3.3:** Zalesak's disk after one revolution. Iso-line of  $\alpha=0.5$  is plotted, together with the reference shape.

In the second row of Figure 3.3, the effect of the sharpening scheme is presented. For the coarse grid, the disk after one revolution has changed into a 'donut' shape. This is attributed to the way the sharpening equation works. More specifically, the  $\epsilon$  parameter which controls the interface thickness, will 'preserve' a constant thickness of approximately 2-4 cells unconditionally, i.e. unaffected by grid size. For that case, owed to the fact that the grid is coarse, when the sharpening equation is applied, the interface becomes slightly wider, and as a result the two parts of the slotted disk coalesce at the bottom into one and finally form a 'donut'. On the other hand, for the fine grid case, the effect of the sharpening scheme to the disk shape is minimal, especially for the case of M-HRIC+SHARP.

### 3.1.3 Single Vortex in a deformation field

In this benchmark case, which was first presented in [178], an initially static circular fluid body is placed in a rectangular domain and is subjected to the effect of a single vortex, described by the following stream function:

$$\Psi = \frac{1}{\pi} \sin^2(\pi x) \sin^2(\pi y) \quad (3-3)$$

The derived velocity components are found as:

$$u = -\frac{\partial \Psi}{\partial y}, \quad v = \frac{\partial \Psi}{\partial x} \quad (3-4)$$

As a result, the circular fluid body stretches to form a ‘fluid spiral’. The interface thicknesses of the deforming shape, as well as the numerical diffusion of values located at the tail of the fluid body during its ‘spiral motion’ are of importance.

The initial dimensions of the case are presented in Figure 3.4a, while in Figure 3.4b the exact solution at a time instant of  $t=2.5s$  is shown as calculated by the tracking of  $10^4$  massless particles placed at the interface of the circular fluid body following a Lagrangian approach.

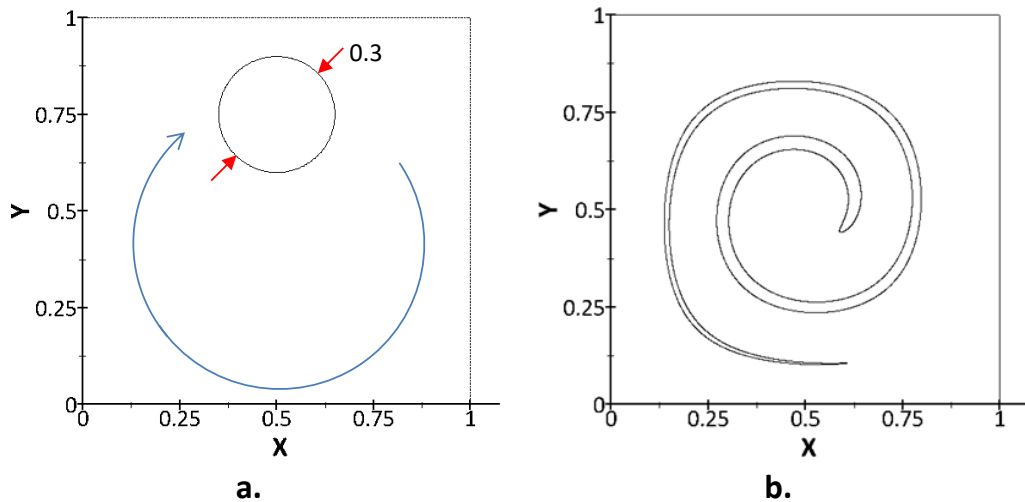


**Figure 3.4:** Initial domain and dimensions for Single Vortex benchmark case and exact solution at  $t=2.5$ .

Same settings with Table 3.2 are used, while in this case a fixed time-step corresponding to a Courant number of 0.2 is applied, while all runs are performed until an absolute time of 6 sec.

Figure 3.5 presents the numerical results of all runs at the reference time of  $t=2.5s$ , for a direct comparison of the different methods used. The iso-lines of  $\alpha=0.1,0.5,0.9$  are plotted to evaluate the smearing of volume fraction.

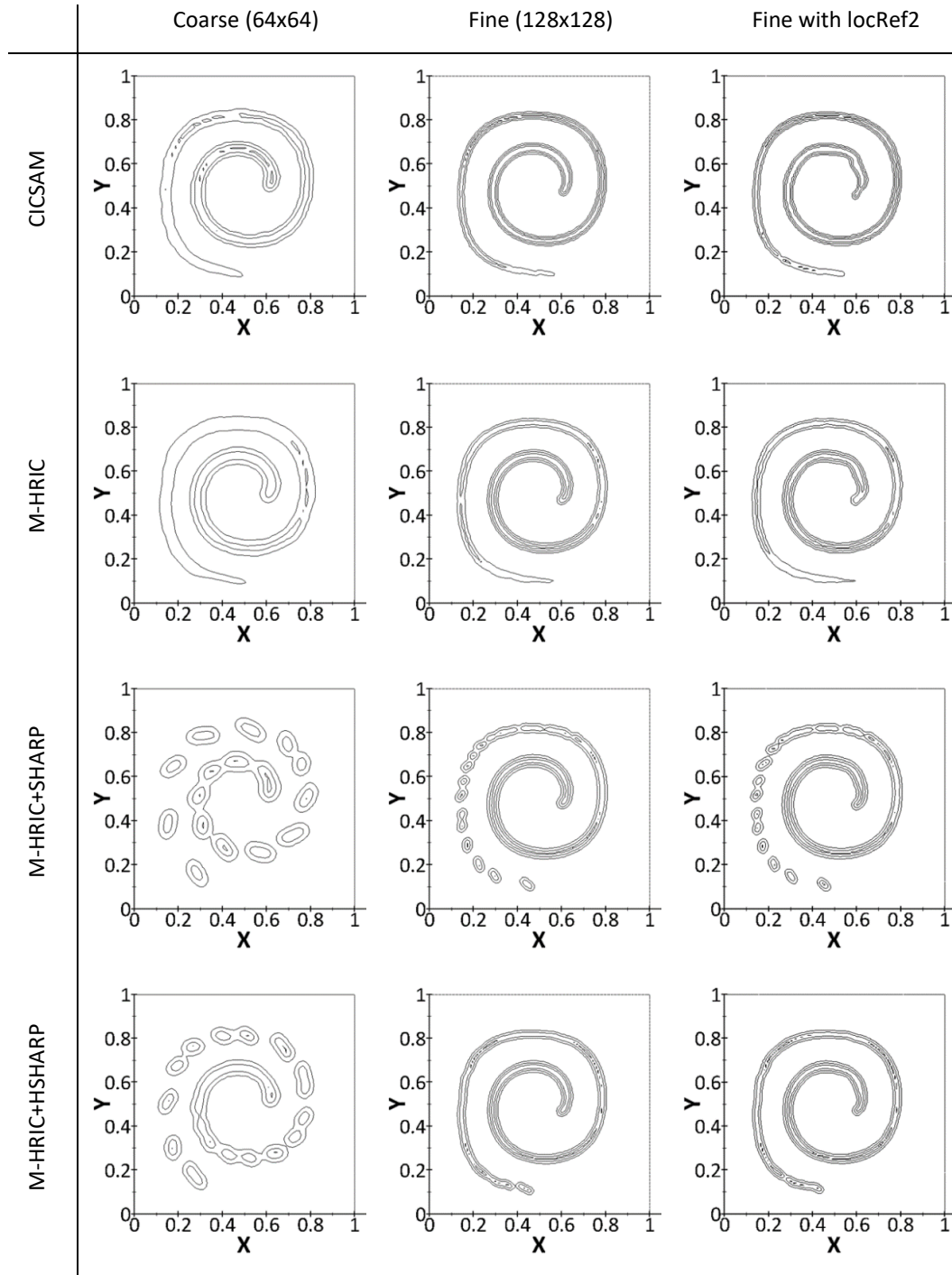


**Figure 3.5:** Single Vortex case at  $t=2.5$ . Isolines of  $\alpha=0.1, 0.5, 0.9$  are plotted.

For the coarse grid, it is obvious that in terms of diffusion CICSAM behaves in the best when compared to all other schemes. M-HRIC is the more diffusive, as expected, while

enhancing M-HRIC with the sharpening algorithm results in liquid mass fragmentation. While this is not the favorable result, it seems inevitable to avoid such a fragmentation for any applied sharpening algorithm (also observed in Sato and Niceno [92]), especially at regions where the liquid body becomes very thin. When this thin liquid form is represented by one or two cells, sharpening is executed along the direction of the free surface normal unit vector  $\hat{n}$ , i.e. from both sides of this thin liquid mass and thus it finally breaks.

In the fine grid case, the coupling of M-HRIC with sharpening results in a slight deformation of the liquid body. The application of default sharpening scheme (M-HRIC+SHARP) does not seem to improve the numerical results compared to the default M-HRIC. On the other hand, high sharpening improves significantly the derived results compared to M-HRIC in terms of diffusion (the isolines are closer together), whilst compared to CICSAM the tail of the fluid body is not diffused. It is very important to point out that constant interface thickness along the full length of the liquid mass is achieved when the sharpening algorithm is applied.

Finally, for all cases examined, the application of the dynamic local refinement technique does not affect the solution considerably, except for the cases of CICSAM and M-HRIC, where severe liquid body deformation is observed on its front face.

### 3.1.4 Conclusions

Based on the results of the aforementioned benchmark cases, it can be concluded that the numerical model gives satisfying results for the advection tests. CICSAM preserves a sharp interface; the same applies for the coupling of M-HRIC with the sharpening equation, while local refinement does not affect the solution considerably. The sharpening methodology does not affect the solution of the default M-HRIC, while it improves significantly the exhibited diffusion.

These benchmark cases are performed in much coarser grids than the ones usually employed for real conditions runs. In the following section, the flow field equations are solved as well.

## 3.2 Gravitational acceleration of a free-falling droplet

### 3.2.1 Introduction

Two-phase flow algorithms rely on the accurate representation of the surface tension force. Typically, many authors [95, 179, 180] use the case of a bubble rise in a quiescent liquid to validate their numerical models. However, few works exist in literature that simulate the opposite phenomenon, i.e. a liquid droplet accelerating inside a gas medium, a phenomenon that concerns this Thesis. In the works of [181, 182] the authors used a body-fitted grid to represent the liquid-gas interface, and applied the appropriate boundary conditions, while they calculated the drag coefficient. However, their model is limited to quasi-spherical droplets and is difficult to expand to deformable droplets.

In this Section, the case of a liquid droplet making a free-fall will be investigated. The fluids chosen are water and air, which exhibit large density and viscosity ratios, in order to magnify the arithmetic difficulties imposed by these discontinuities at the interface. Moreover, the size of the droplet is chosen to be very small ( $D_0 = 0.5\text{mm}$ ), thus implying quite high induced surface tension forces. In the book of Clift [183], the predicted shape of such a small droplet on freefall appears to be almost spherical (for Eotvos number =  $3.35\text{E-}02$ ,  $\log(\text{Morton}) = -11.76$  on Figure 2.5 on Clift book [183], Table 3.3).

The dimensionless numbers that govern the phenomenon are the Eotvos, Morton and the Reynolds numbers:

$$Eo = \frac{g\Delta\rho D_l^2}{\sigma} \quad (3-5)$$

$$Mo = \frac{g\mu_g^4\Delta\rho}{\rho_g\sigma^3} \quad (3-6)$$

$$Re = \frac{\rho u D}{\mu} \quad (3-7)$$

### 3.2.2 Analytical solution

In order to validate the CFD model, a simple 1-D model is developed, where the velocity of the droplet is calculated by a simple 1-D balance of forces acting on it, i.e. droplet weight, drag force induced by air surrounding the droplet and the buoyancy of displaced air:

$$m\vec{a} = \Sigma F_{body} = F_g - F_b - F_D \Rightarrow \rho_l V_l \frac{\partial u}{\partial t} = \rho_l V_l g - \rho_g V_l g - c_d \frac{1}{2} \rho_g u^2 A_l \Rightarrow$$

$$\frac{\partial u}{\partial t} = \left(1 - \frac{\rho_g}{\rho_l}\right) g - c_d \frac{1}{2} \frac{\rho_g}{\rho_l} \frac{A_l}{V_l} u^2 \quad (3-8)$$

Virtual mass and Basset forces are negligible for large density ratios. The ratio of  $A_{liq}/V_{liq}$  is equal to  $3/2D_o$  for a spherical droplet. Drag coefficient is calculated from the correlations given in Table 5.2 of [183]. Eq. 3-8 is solved implicitly using as stopping criterion the time when the droplet reaches its terminal velocity, i.e. when  $u_{new} - u_{old} < \epsilon$  (small number).

In Table 3.3 the initial conditions used for the solution of Eq. 3-8 are presented, as well as the results for terminal velocity and total distance covered by the droplet. The terminal velocity which is calculated, agrees quite well with Fig. 5.14 of [183] that concerns terminal velocities of viscous spheres. The results of this simple 1-D model are presented in Figure 3.6 and can be used for the validation of the CFD model.

Initial Conditions				Results	
$D_o$	0.5mm	$\mu_g$	1E-05 kg/ms	$u_{terminal}$	2.006 m/s
$U_o$	0m/s	$Mo$	1.7894E-12	$t$	703.8 ms
$\rho_l$	1000 kg/m <sup>3</sup>	$Eo$	3.35E-02	$X/D_o$	2187.7
$\rho_g$	1.225 kg/m <sup>3</sup>	$\Delta t$	1E-05	$Re_g$	68
$\mu_l$	0.001003 kg/ms	$\epsilon$	1E-05	$We$	26.97

**Table 3.3:** Initial Conditions and Results of the 1-D analytical solution of a water droplet on freefall.

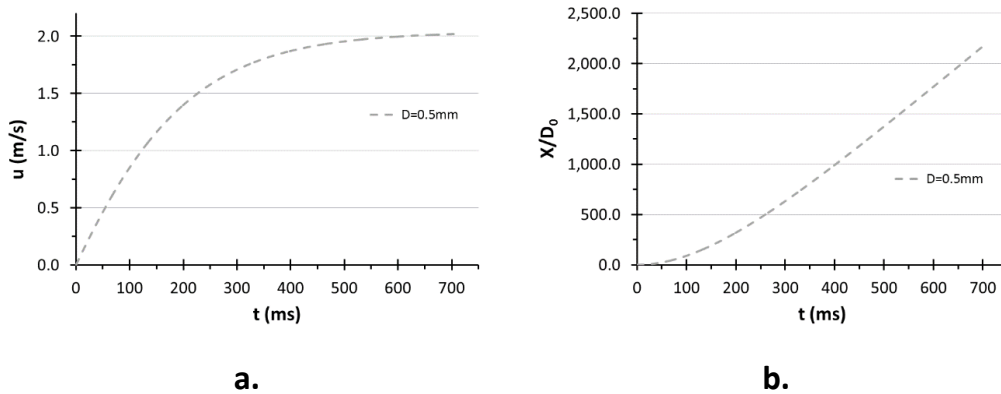


**Figure 3.6:** Temporal evolution of a) velocity and b) displacement of a single droplet accelerated by gravity. Results of the 1-D analytical solution.



### 3.2.3 Numerical domain

The distance covered by the droplet until it reaches the terminal velocity is almost 2,200 times its diameter. For this reason, a moving numerical grid is applied, in order to preserve its small size and high levels of accuracy. The velocity of the grid is updated in the beginning of every time-step and equals the mass averaged velocity of the droplet:

$$u_{grid} = u_{dr,mean} = \frac{\sum_{cell} u_{cell} m_{cell}}{\sum_{cell} m_{cell}} = \frac{\sum_{cell} u_{cell} \alpha_{cell} \rho_l V_{cell}}{\sum_{cell} \alpha_{cell} \rho_l V_{cell}} \quad (3-9)$$

In Figure 3.7, the axisymmetric numerical domain, along with the boundary conditions imposed, are presented. The droplet is initially placed in the center of the axis on a 100x50 cell grid with dimensions  $20D_o \times 10D_o$ . In the same figure, the local refinement region at the first time instant is depicted as well. The densest region extends to a distance of  $D_o/6$  from the interface.

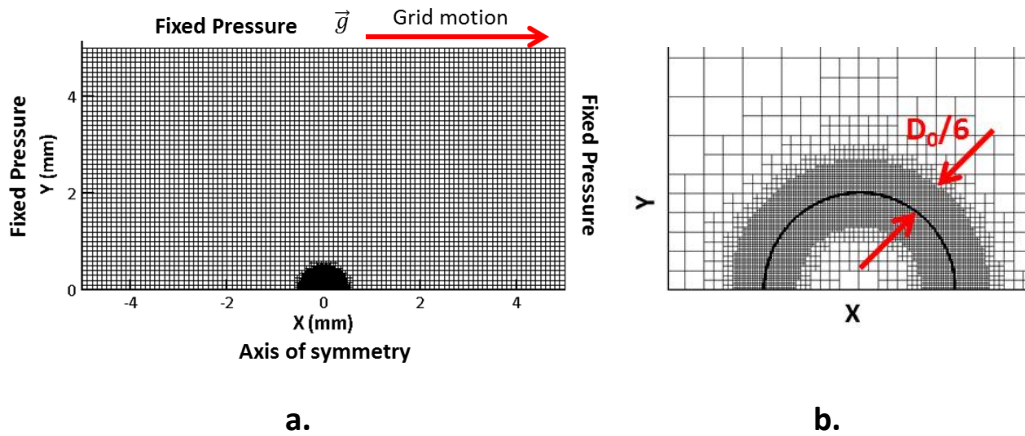


**Figure 3.7:** a) Initial Domain + Boundary conditions for the free-falling droplet case. b) grid locally refined around interface.

### 3.2.4 Cases studied

The properties for all cases investigated are presented in Table 3.4. The same methods for volume fraction advection are used (CICSAM, M-HRIC, M-HRIC+SHARP, M-HRIC+HSHARP). In the first 4 cases, the droplet starts from zero initial velocity and accelerates. The first 200ms are simulated owed to the large computational time required for the full description of the phenomenon, i.e. 700ms. Fixed time-step is used, achieving a maximum Courant number of 0.48. In the following 2 cases (5,6) the whole phenomenon, i.e. up to the time the droplet reaches its terminal velocity, is simulated.

The time-step used is variable always keeping a Courant number approximately equal to 0.25. The properties of water and air are presented in Appendix B.

Case No.	$U_0$ (m/s)	locRef lev.	cpR	$t_{end}$ (s) - Courant (max) - dt (s)	Method
1a,b,c					CICSAM
2a,b,c	0	4,5,6	40,80,160	0.2 - 0.48 - 2e-06, 1e-06, 5e-07	M-HRIC
3a,b,c					M-HRIC+SHARP
4a,b,c					M-HRIC+HSHARP
5	0	4	40	0.7 - 0.25 - Var.	M-HRIC+SHARP
6					M-HRIC+HSHARP
7	1.5	6	252	0.005 - 0.25 - Var.	M-HRIC+HSHARP

**Table 3.4:** Test cases Investigated for a 0.5mm droplet on freefall.

The last case examined (Case7) concerns the acceleration of a water droplet, starting from an initial velocity of 1.5m/s ( $\approx 0.75 \cdot u_{terminal}$ ), at a smaller domain ( $10D_o \times 5D_o$ ), using a thinner refinement region ( $D_o/30$ ), in order to save computational time. This case is run only for 5ms of simulation time, using a very dense grid, in order to investigate how the internal recirculation in the liquid phase develops.

Table 3.5 presents the number of cells required either using the proposed local grid refinement technique or an equivalent uniform grid, to achieve the same droplet discretization.

Ref. levels	#cells with locRef	#cells with uniform grid
1	5,180	20,000
2	5,888	80,000
3	6,998	320,000
4	9,086	1,280,000
5	13,238	5,120,000
6	21,728	20,480,000

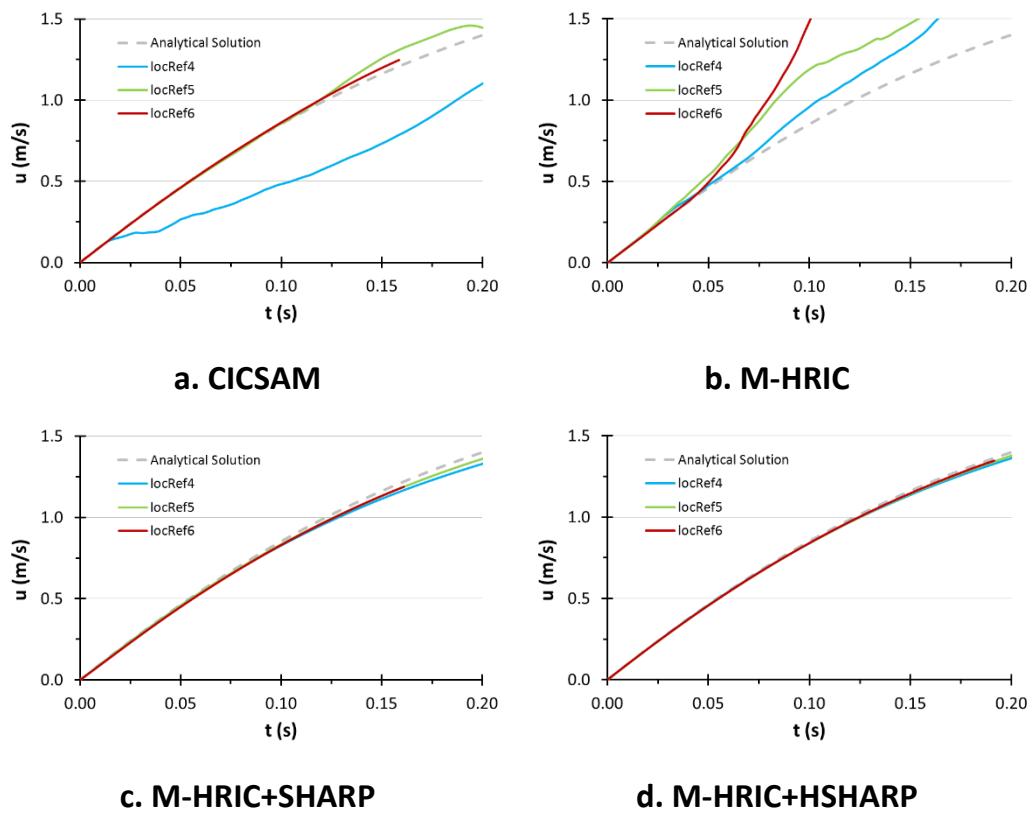
**Table 3.5:** Grid size for local refinement vs uniform refinement (same resolution at interface).

It is obvious that the use of local refinement decreases significantly the number of computational cells, while preserving the same grid resolution at the liquid-gas interface. Therefore, there is no point in using a uniform grid. For reasons of completeness however, a comparison between these two methods (local refinement and uniform refinement)

was conducted for the current case and it was found that the numerical accuracy is almost the same when using the local grid refinement technique, while the associated computational resources decrease by around 400%.

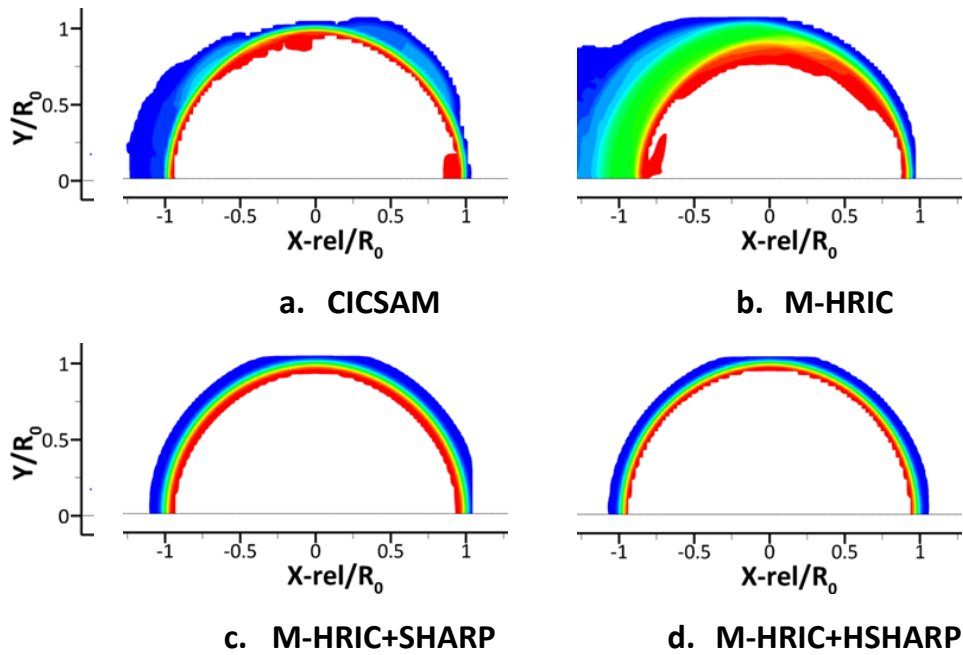
### 3.2.5 CFD results

Figure 3.8 presents the numerical results for the temporal evolution of mass averaged droplet velocity for Cases1-4 against the 1-D analytical solution for the first 200ms of the phenomenon. Additionally, the effect of grid density on the numerical results is presented.



**Figure 3.8:** Temporal evolution of droplet velocity as calculated from CFD compared with the 1-D analytical solution. Cases1-4.

For CICSAM and M-HRIC schemes, the deviation that is observed in the prediction of droplet velocity, particularly in the coarse and moderate meshes, is attributed to the diffusion of volume fraction. In Figure 3.9, volume fraction values between 0.001 and 0.999 are depicted in order to exhibit the aforementioned smearing.



**Figure 3.9:** Comparison between different methods (Cases1a-4a) with locRef4 for predicting the volume fraction field at  $t=200\text{ms}$ . Volume fraction values between 0.001 and 0.999 are shown.

It is evident that when using CICSAM and M-HRIC schemes and 40 cpR grid, the smearing of volume fraction values in the computational domain cannot be avoided. This points out that for such a coarse mesh, a sharpening scheme is required for the Eulerian interface tracking algorithms. Additionally, the use of High Sharpening (HSHARP) results in a constant interface of smaller thickness than what the SHARP predicts. In the case of fine mesh, the results are similar between all methods, except the M-HRIC, which exhibits diffusion in very small volume fraction values downwind the droplet, and this affects the droplet velocity prediction.

The effect of the sharpening algorithm is not limited in the suppression of volume fraction diffusion. The smooth transition of volume fraction values at the liquid-gas interface resulted by the application of the sharpening equation, allows for the calculation of smoother VOF gradients, which in turn are reflected to a smoother curvature profile and hence surface tension force. In Figure 3.10, the corresponding image of Figure 3.1: is shown for the prediction of the relative velocity streamlines, along with vectors and numerical diffusion using CICSAM and M-HRIC+SHARP at 200ms.

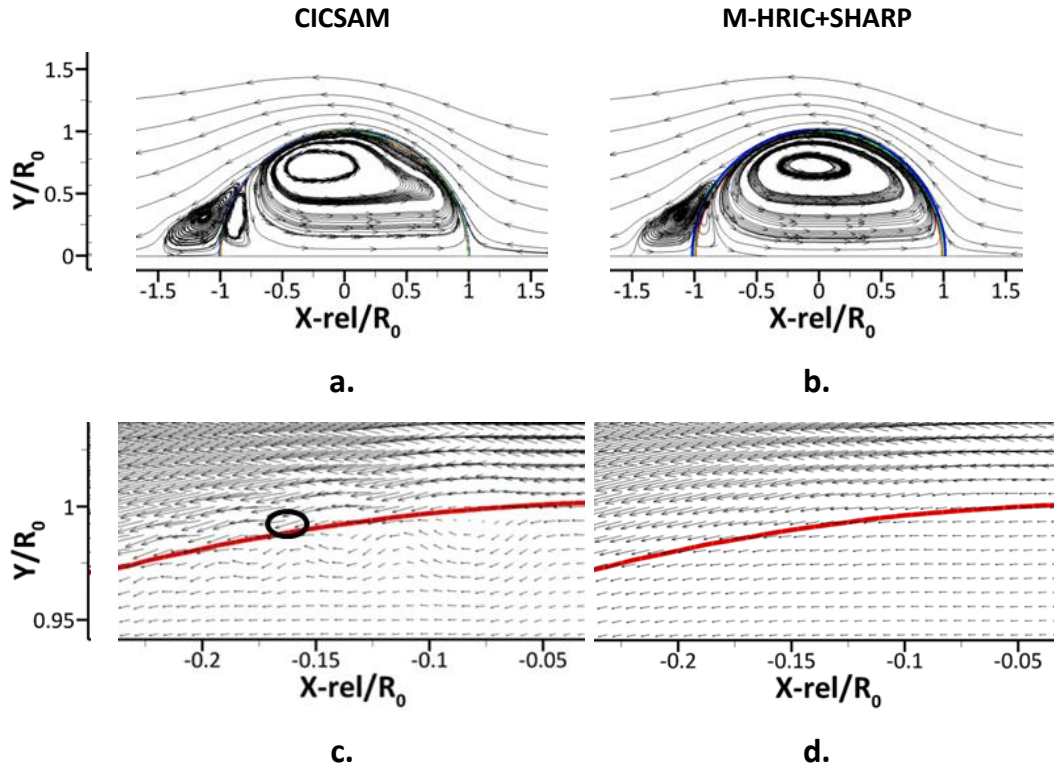


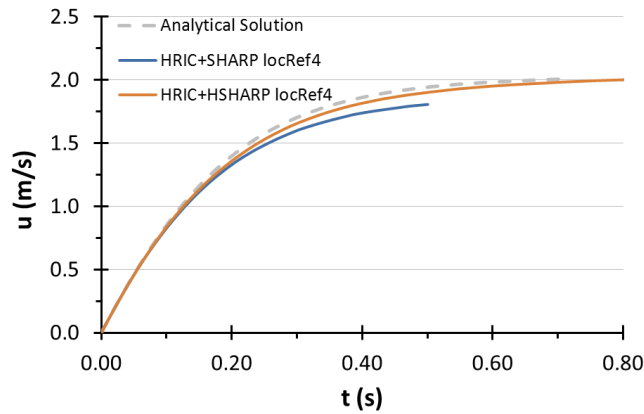
**Figure 3.10:** Comparison between Cases 1c and 3c, for the prediction of a-b) relative velocity field, as well as the volume fraction field values between 0.001 and 0.999 and c-d) velocity vectors at a zoomed region (reference vector inside black circle has magnitude 1.394m/s).

On one hand, the use of CICSAM discretization scheme results in an unphysical velocity field close to the interface, which originates in the false distribution of the volume fraction values at the interface as mentioned before. On the other hand, in the case of M-HRIC+SHARP the velocity field is smoother and it seems to be more reasonable than the previous one, as it corresponds to more accurate representation of the relative velocity streamlines, which are presented in Figure 3.10b. However, this slight difference in fine grids, does not seem to affect the solution significantly (Figure 3.8 – droplet velocity prediction). Moreover, the mean pressure value inside the liquid phase seems reasonable for all cases studied, except those with extensive volume fraction diffusion levels, as shown in Table 3.6.

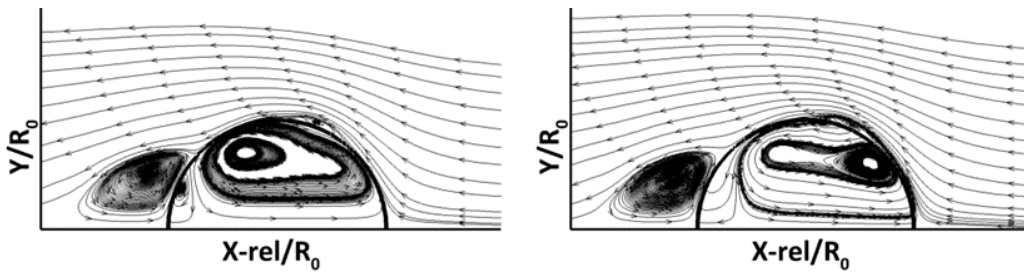
Case No	$(p-p_{\sigma\kappa})/p_{\sigma\kappa}\%$
1a,b,c	-1.29, -0.92, -0.34
2a,b,c	-3.69, -1.12, 0.02
3a,b,c	-1.98, -1.01, -0.54
4a,b,c	-1.36, -0.69, -0.4

**Table 3.6:** Mean pressure predicted inside the liquid phase. Reference pressure is  $p_{\sigma\kappa}=\sigma\kappa=2\sigma/R$ .

In order to shed light to the whole evolution of the phenomenon ( $t=700\text{ms}$ ), Cases 5 and 6 have been examined as well, for which a variable Courant is used. Figure 3.11 presents the corresponding numerical results against the analytical solution of the 1-D model, while locRef4 is selected for these runs so that the actual computational time can be kept as minimum as possible.



a.



b. M-HRIC+SHARP

c. M-HRIC+HSHARP

**Figure 3.11:** a) Temporal evolution of droplet velocity as calculated from CFD compared to the 1-D analytical solution. Relative velocity streamlines are depicted for b) Case 5 c) Case 6 at  $t=500\text{ms}$ .

The numerical results for the droplet acceleration temporal evolution seem very promising, as they are very close to the 1-D analytical solution. In the same Figure, the relative velocity streamlines are depicted. The recirculation at the droplet wake is well predicted, given that its dimension ( $L_w/D=0.51$ ) matches the data of [184] (Table 4.1 in reference). Overall M-HRIC+HSHARP delivers the best results, with a total of 1.36% relative error in terminal velocity prediction (at 700ms), which for the grid density applied ( $cpR=40$ ) is considered to be a satisfactory result.

For both of the aforementioned cases the internal liquid recirculation streamlines seem to be distorted, as the recirculation center fluctuates between droplet upwind and downwind locations (Figure 3.11). The reason for this fluctuating behavior is the

appearance of a small unphysical recirculation zone on the top of the droplet. A separation point seems to form, as the grid is not sufficiently dense to capture the boundary layer formed at the droplet surface. The flow detaches and further down the droplet surface reattaches again. Figure 3.12 presents a zoomed image at the location of this recirculation zone, as derived by the application of Cases4a,b,c, achieving a cpR of 40, 80 and 160 respectively.

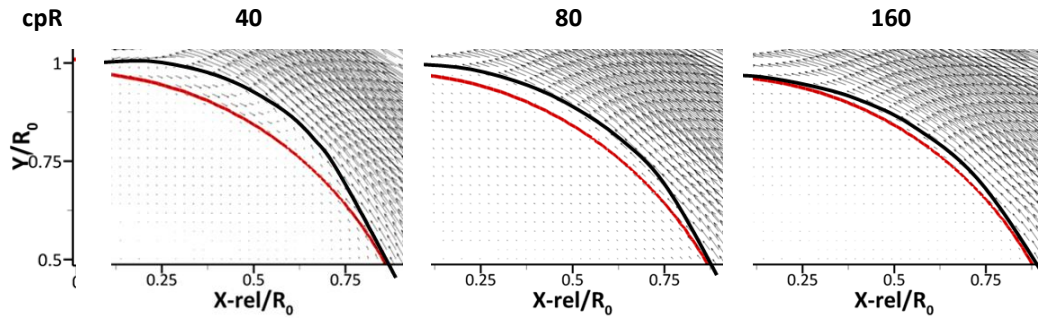


**Figure 3.12:** Boundary layer in droplet interface. Cases4a,b,c at  $t=200\text{ms}$ . Velocity vectors have the same units.

This figure clearly shows that the appearance of this zone is a numerical artefact, as it is grid dependent. As the cell size is decreased, the area of this recirculation zone decreases, however none of the grids employed are sufficient enough to capture in an efficient way the boundary layer formed at the top of the droplet. In [182], the authors mention that a grid density of 500 cpR is required to resolve this boundary layer.

In this light and in order to capture the correct internal recirculation shape, the grid density was decided to be further increased reaching a value of 252 cpR, in Case7. In this case, in order to save computational time, the initial droplet velocity is assumed to be equal to 1.5 m/s (approxim. 75% of terminal velocity). Figure 3.13 presents the numerical results taken after 5ms of actual droplet acceleration against corresponding numerical data from [182]. In the image taken, streamlines and vorticity iso-lines for a Re equal to 100, but for smaller density ratio ( $\rho_l/\rho_g=7$ ) are presented. These conditions are very close to the ones used in this study.

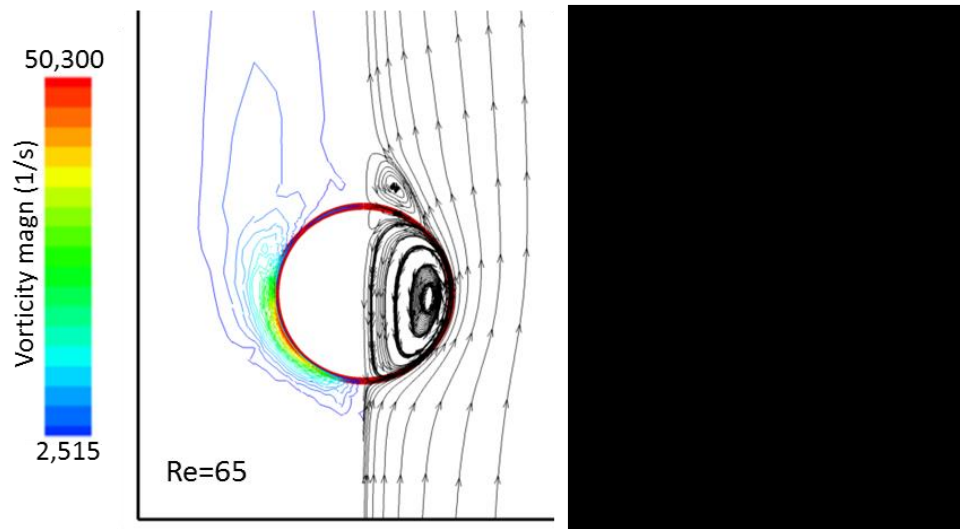


**Figure 3.13:** Comparison of internal (liquid) and external (gas) recirculation. Simulation results for Case7 obtained after 5ms of run. Image on the right taken from [182] Courtesy of ASME (Figure2b,  $Re=100$ ,  $\rho_l/\rho_g=7$ ).

Under such a high grid density, the induced liquid streamlines are not fluctuating, giving rise to the claim that the under-resolution of the boundary layer is responsible for the non-physical behavior discussed in Figure 3.11. The recirculation center is nicely located towards the upwind end of the droplet, while the vorticity magnitude iso-line predictions are similar to the data from [182], but not as smooth. This discrepancy can be attributed to two reasons: first that the two cases do not have the same exact terminal velocity and secondly the grid density in the gas phase is probably much lower than the required one.

### 3.2.6 Conclusions

In this Section, different methods for handling the volume fraction advection were evaluated in the case of a water droplet accelerating under the influence of gravity. The performance of the sharpening algorithm was also assessed in this realistic case.

The coupling of the sharpening equation with the M-HRIC discretization scheme is beneficial not only for the velocity, pressure fields which are now more uniform across the interface, but also the volume fraction field can be suppressed to a specific constant thickness imposed by the selected value of  $\epsilon$ . This numerical algorithm cannot be claimed to provide a more accurate solution in terms of liquid phase advection than the default M-HRIC and/or CICSAM, or alternatively, that it provides a higher accuracy advection algorithm. However, the smooth distribution of volume fraction values at the liquid-gas interface results in smooth gradient and curvature calculation, thus surface tension force.



Overall, for high grid densities ( $cpR \geq 80$ ), the numerical algorithms are expected to exhibit similar behavior in macroscopic flow field behavior (droplet average velocity, displacement etc).

## 3.3 Isothermal droplet impingement onto a flat surface

### 3.3.1 Introduction

In this section, the numerical model is employed to examine the dynamics of a droplet impinging on a solid flat surface. The performance of the dynamic contact angle models, namely Adv-Rec, Kistler's and Shikhmurzaev's models as well as the new WFM will be discussed. A comprehensive review on previous studies and available models concerning droplet impingement on a flat surface is given in Chapter 1. Based on this review, it was concluded that there is a gap in numerical literature concerning droplet impact at low and moderate  $We$  numbers. This will also be discussed in this section.

Simulation results for the droplet maximum spreading are compared against the following equation [32]:

$$\frac{D_{\max}}{D_0} = \sqrt{\frac{We + 12}{3(1 - \cos\theta) + 4(We / \sqrt{Re})}} \quad (3-10)$$

which takes into account the Reynolds, Weber numbers, and the contact angle formed at the end of the advancing phase. This correlation is based on an energy conservation, in terms of kinetic, surface energies and viscous dissipation for two time instants, before impact and at maximum spreading, as mentioned in Chapter 1. In this section, it will be referred to as Pasandideh's correlation [32].

### 3.3.2 Cases studied

The operating conditions for the nine cases studied are summarized in Table 3.7 and concern the impingement of a water droplet onto both hydrophilic and hydrophobic surfaces. A wide range of  $We$  numbers ranging from as low as 0.2 up to 120 are examined. Cases1-4 refer to the impingement on hydrophobic surfaces, while Cases5-9 concern hydrophilic surfaces. Particularly, Cases5,6 refer to very low Weber numbers (0.2-2), for which, as it is known, peculiar post-impingement liquid shapes are forming, further presented in the following sections.

Case No.	$u_o$ (m/s)	$D_o$ (mm)	$\theta_{adv}$ (°)	$\theta_{rec}$ (°)	We	Re	Ref
1.LW-HCA-HH	0.48	2.50	120	65	8	1200	[54]
2.MW-HCA-HH	1	2.28	107 (*90)	77	32	2280	[89]
3.MW-HCA-LH	1.18	2.75	105	95	53	3245	[43]
4.HW-HCA-LH	1.64	2.45	105	95	91	4018	[58]
5.VLW-MCA-LH	0.22	2.40	70*	70	2	527	[113]
6.VLW-LCA-LH	0.08	2.30	31*	31	0.2	184	[45]
7. LW-MCA-LH	0.76	2.40	70*	70	19	1821	[113]
8. MW-LCA-LH	1.18	3.04	10	6	59	3587	[43]
9. HW-MCA-HH	1.50	3.76	60 (*34)	22	117	5640	[55]

**Table 3.7:** Initial conditions for the droplet impingement on a flat wall. The following abbreviations are used: Weber number (W), advancing contact angle (CA) and contact angle hysteresis (H). Symbols VL, L, M, H represent the words very low, low, moderate and high. (\* equilibrium angles, when only the equilibrium angle is given, the advancing/receding angles take this value, as in Cases5-7.)

### 3.3.3 Numerical domain

In Figure 3.14a, the 2-D axisymmetric domain, comprising of 60x60 identical quadrilateral cells is shown, where local grid refinement has been applied at the liquid-gas interface. The droplet is initially placed at a distance of one diameter ( $D_o$ ) away from the flat surface, as shown in Figure 3.14b, in order to allow the gas fluid flow around the droplet develop in a physical way. Gravitational acceleration is directed towards the positive values of x axis. The initial domain is the same for all cases examined. Its total length is presented in Figure 3.14, which corresponds to dimensions ranging between 4 to 6.6  $D_o$ , based on the droplet diameters given in Table 3.7.

In Figure 3.14b, a zoomed area of the applied numerical grid around the moving droplet, along with the high resolution of the grid are shown. The distance of the highest refinement level from the interface is set at  $D_o/5$ , a safe choice to ensure that the interface always lies in the densest region of the computational domain.

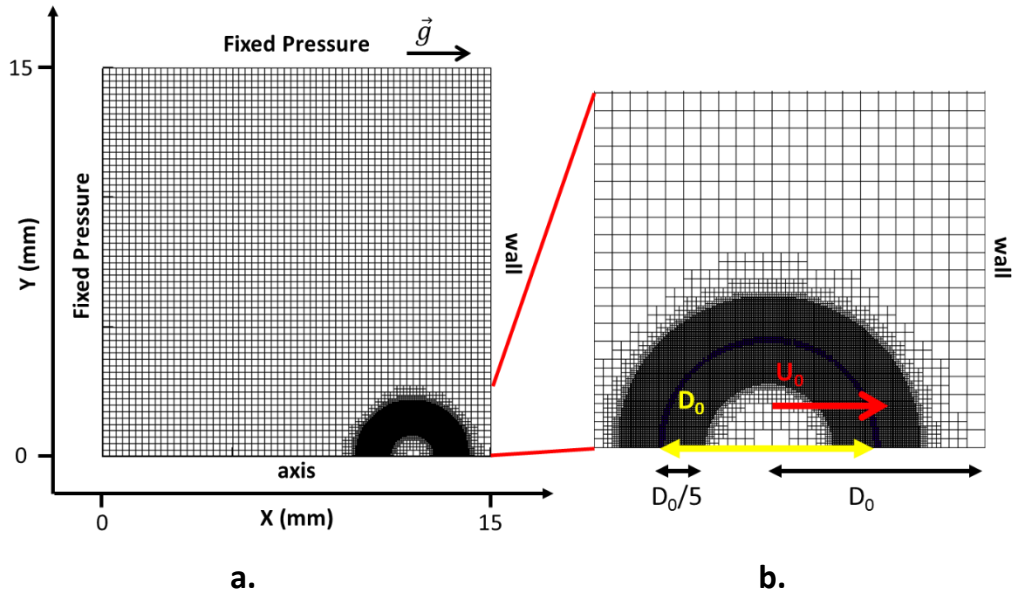


**Figure 3.14:** a) Initial Domain + Boundary conditions for all cases, b) Depiction of the local refinement technique.

Four levels of local refinement are used, achieving a minimum cell size of around  $\Delta x_{\text{initial}}/2^4 = 15.6\mu\text{m}$ . This translates to approximately 72-120 cpR for all the cases examined. A summary of the numerical settings applied for the current simulations is presented in the following Table.

Parameter	Value
Courant	0.25
Grid size (cells)	~15,000-30,000
Locref distance	$D_0/5$
cpR	72-120 (locRef4)

**Table 3.8:** Numerical settings for the droplet flat impingement case

In order to achieve the same accuracy at the interface, in the case of a uniform grid, a computational domain of around 1,000,000 cells would be required.

### 3.3.4 CFD results

#### 3.3.4.1 Grid size verification

The Wetting Force Model, as presented in Chapter 2, predicts the evolution of the dynamic contact angle and does not prescribe it. Therefore, it is important to examine the effect of grid size on the performance of this contact angle model, i.e. to prove whether

the magnitude of the force implemented numerically, as well as its interaction with the surface tension force, is not mesh-dependent. In Figure 3.15, the contact angle prediction for cases 1 (LW-HCA-HH) and 7 (LW-MCA-LH) that represent the impingement onto a hydrophobic and a hydrophilic surface respectively, are presented for locRef4 (default) and locRef6, where a cell size of around  $\Delta x/2^6 = 3.9\mu\text{m}$  is achieved at the droplet interface.

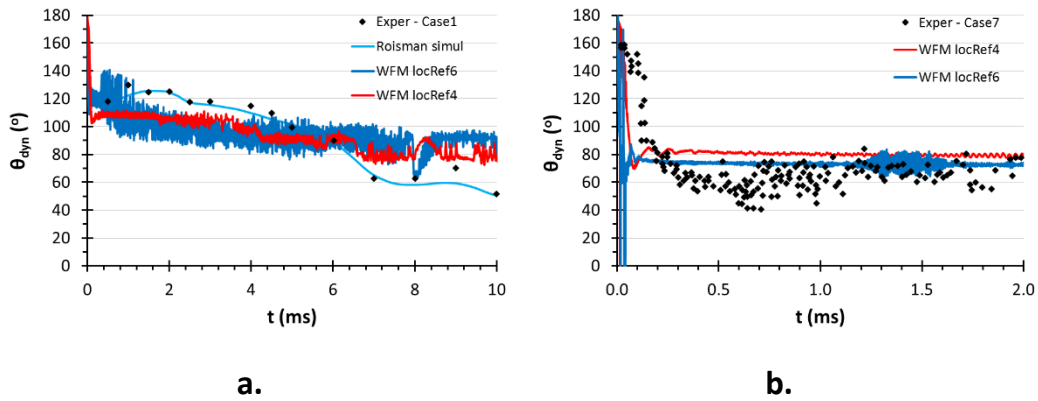


**Figure 3.15:** Effect of grid size for Cases a) 1. LW-HCA-HH and b) 7. LW-MCA-LH of Table 3.7. Comparison against a) experimental/numerical data from [54], b) experimental data [113].

In the same figure, the corresponding experimental/numerical data of previous works are shown. For Case1 (LW-HCA-HH) the experimental data of [54] are well fitted. In WFM, the dynamic contact angle is measured using the slope of the volume fraction gradient at the wall cells (as discussed in Chapter 2).

It is clear that the effect of grid size is minimal for both cases, while in Case7, the dynamic contact angle prediction slightly improves by the application of a fine grid. The “noise” observed in this figure can be attributed to the fluctuating sign change of the applied wetting force. More specifically, as the cell size at the droplet rim gets smaller, velocity field fluctuations affect the dynamic contact angle formed and numerically measured there, which in turn results in continuous direction changes of the exerted wetting stress. This oscillating behavior, may as well resemble the pinning of droplet during its spreading, where the contact angle is observed to fluctuate between two values as stated in [185], but this is a matter of future works. The same oscillating behavior is observed for Case7 (LW-MCA-LH), at the time when the dynamic contact angle reaches the set equilibrium value ( $\theta=70^\circ$ , Table 3.7). Overall, the numerical results are not considered to be highly dependent on the grid size.

### 3.3.4.2 Global performance of WFM

Figure 3.16 presents a comparison between the WFM simulation results and the experimentally measured data for maximum droplet spreading, as well as the estimates of Pasandideh’s correlation. Results for all cases (Table 3.7) are shown. On the left side of the figure, it is evident that the new model behaves satisfactorily for all cases, with the exception of Case5 (VLW-MCA-LH). On the right hand of the figure, the results are plotted against the Weber number, while a distinction between hydrophobic and hydrophilic surfaces is depicted.

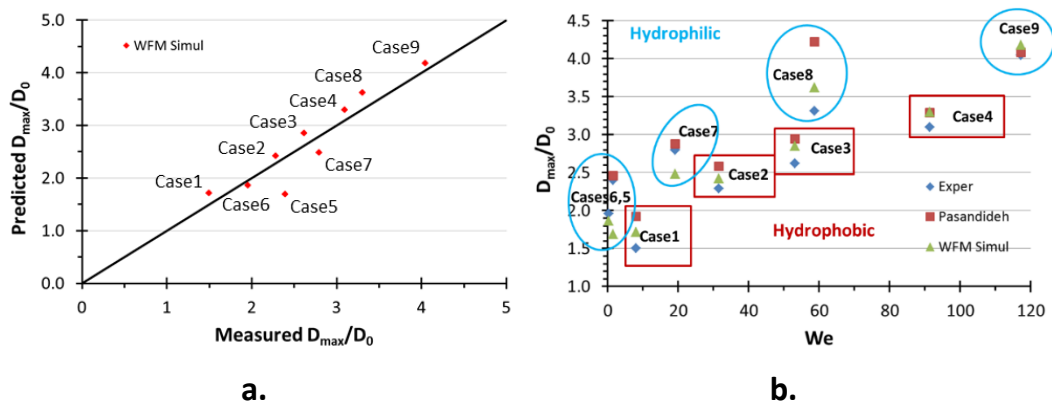


**Figure 3.16:** Summary of simulation results with the use of WFM model. a) Droplet maximum spreading plotted against the experimental values, b) Maximum spreading plotted against experimental values and results of Eq 3-10.

The WFM model predicts accurately the impingement onto dry hydrophobic surfaces, with a slight over-prediction (approx. 10%), while it is less accurate for the hydrophilic ones, particularly for moderate Weber numbers. For the latter cases, not a monotonic overestimation or underestimation of the model predictions against experimental data is tracked.

The results obtained by application of Pasandideh’s correlation overestimate in most cases the experimental droplet maximum spreading. Results for Case6 (VLW-LCA-LH) are not included in the figure, as the assumption of a viscous boundary layer influencing significantly energy dissipation is not valid for very low Reynolds numbers [31].

The droplet maximum spreading results after the application of the WFM are summarized in Table 3.9. Additionally, the respective relative errors between experimental measurements, current simulations and the Pasandideh’s correlation are given. Being able to predict the droplet maximum spreading for a variety of contact angles and Weber numbers, it can be claimed that the WFM can be trusted; moreover, a simple

grid dependency study showed that the results are not mesh affected. After that, a more detailed comparison of the model predictions will follow in the forthcoming sections.

Case No.	Dmax/Do			relError (%)		Ref
	Exper	WFM	Pasand	WFM-Exper	Pasand-Exper	
1.LW-HCA-HH	1.50	1.71	1.92	14.2	28.0	[54]
2.MW-HCA-HH	2.29	2.42	2.59	5.7	12.9	[89]
3.MW-HCA-LH	2.62	2.85	2.95	8.8	12.4	[43]
4.HW-HCA-LH	3.1	3.30	3.29	6.5	6.2	[58]
5.VLW-MCA-LH	2.4	1.69	2.46	-29.6	2.4	[113]
6.VLW-LCA-LH	1.96	1.86	5.00	-5.1	155.0	[45]
7. LW-MCA-LH	2.8	2.48	2.88	-11.4	2.7	[113]
8. MW-LCA-LH	3.31	3.62	4.22	9.4	27.6	[43]
9. HW-MCA-HH	4.05	4.18	4.09	3.2	0.9	[55]

**Table 3.9:** Summary of maximum droplet spreading WFM results, experimental data (refs in Table) and estimations from Pasandideh correlation (Eq. 3-10).

### 3.3.4.3 Dynamic contact angle evolution

The dynamic contact angle predictions for both hydrophobic and hydrophilic surfaces, as presented in Figure 3.15, serve as a sign of validity for the new WFM model, which can shed light in the temporal evolution of the phenomenon by not prescribing a contact angle value, but predicting it. In Case1 (LW-HCA-HH), the contact angle predicted by the WFM during the advancing phase is lower than the one measured during the experiments, which is a reason for the over-prediction of maximum spreading, as pointed out in the previous Section. The numerical results from [54], who used the Kistler’s dynamic contact angle model, almost perfectly approach the experimental data.

During the initial stage of impingement, as soon as the liquid droplet comes in contact with the surface,  $\theta_{dyn}$  is approximately  $180^\circ$ . Subsequently, the contact angle reduces rapidly to approximately  $110^\circ$ , which is lower than the advancing one ( $120^\circ$ ); therefore the stress term introduced points in the direction to accelerate the rim. The dynamic contact angle slowly reduces during the rest of the advancing phase, and drops suddenly to  $80^\circ$  at approximately 6.5ms, which can be set as the initiation of the receding phase; this value is higher than the receding contact angle value of  $65^\circ$ , thus the stress term decelerates the recoiling phase.

Contact line velocity exhibits similar behavior, as shown in Figure 3.17. The contact line velocity is the simple average velocity of all cells at the droplet rim region that are cut

by the liquid-gas interface, i.e. the isoline of  $\alpha=0.5$ . At first, a spike is observed when the droplet hits the surface, followed by significant reduction of its magnitude with time. The time interval between 5 and 6.5ms is considered to be the “hysteresis” time, i.e. the time needed for the contact angle to shift from  $\sim\theta_{adv}$  to  $\sim\theta_{rec}$ . During this stage, the contact line velocity fluctuates around zero. At later stages,  $t > 6.5$ ms, contact line velocity exhibits negative values, i.e. the droplet is recoiling, with substantially smaller magnitude than during the advancing phase.

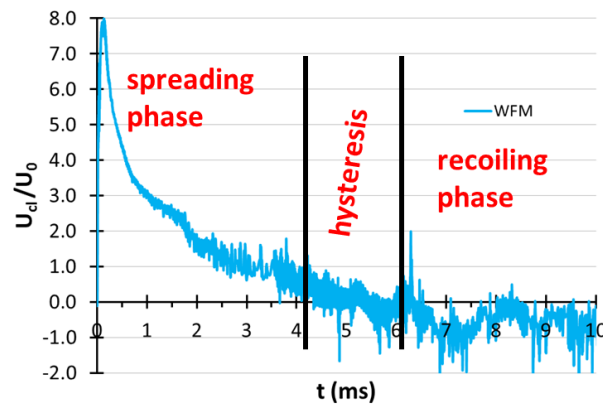


**Figure 3.17:** Contact line velocity temporal evolution for Case1. LW-HCA-HH.

For the impingement onto a hydrophilic surface, the dynamic contact angle prediction of Case7 (LW-MCA-LH) is presented in Figure 3.15 against the experimental data of [113]. During the initial stage of impingement, the contact angle again starts with a value of  $180^\circ$  and drops quite fast down to  $80^\circ$ . This trend is also observed in the experimental data; however, the duration of this period is underestimated by the simulation. Afterwards, a constant angle of around  $80^\circ$  is predicted by the model, while the experimental values lie between  $50^\circ$  and  $80^\circ$ .

#### 3.3.4.4 Wetting force magnitude vs surface tension

The following Figure 3.18 and Figure 3.19 show the surface tension force vectors as predicted by the numerical model for Case2 (MW-HCA-HH) and Case9 (HW-MCA-HH), when using the WFM and the Adv-Rec model. The wetting force vectors are also presented for the cases with WFM.

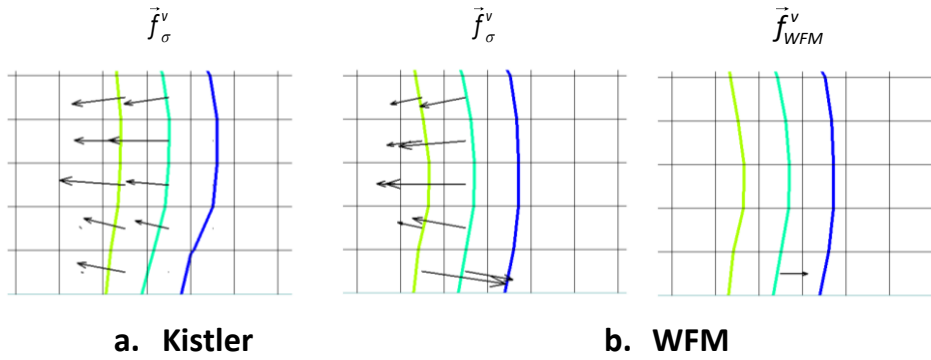


**Figure 3.18:** Surface tension and wetting force vectors predicted by a) Kistler’s model and b) WFM for Case2 (MW-HCA-HH) at  $t=2.7\text{ms}$ . Ref. vector  $\rightarrow (1.6e+07\text{N/m}^3)$ . Yellow, pink and blue lines represent 0.1, 0.5, 0.9  $\alpha$  isolines respectively.

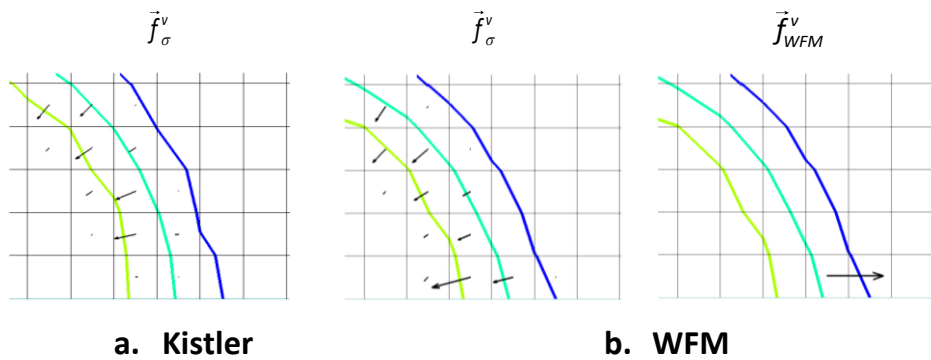


**Figure 3.19:** Surface tension and wetting force vectors predicted by a) Kistler’s model and b) WFM for Case9 (HW-MCA-HH) at  $t=3.1\text{ms}$ . Ref. vector  $\rightarrow (3e+07\text{N/m}^3)$ . Yellow, pink and blue lines represent 0.1, 0.5, 0.9  $\alpha$  isolines respectively.

The wetting force which is applied is of the same order of magnitude with the surface tension force, demonstrating that it can affect in a reasonable manner the contact angle formed at the droplet rim. The main difference between this model and default one, where the contact angle is implemented as a boundary condition (Kistler’s law here as an example), is that the induced surface tension force in the wall boundary cells is much more intense, which however does not exhibit any significant changes in the macroscopic evolution of the phenomenon.

### 3.3.4.5 Spreading on hydrophobic surfaces

The temporal evolution of the spreading diameter of a water droplet impinging onto solid hydrophobic surfaces is depicted in Figure 3.20 for cases 1-4 of Table 3.7. Simulation results using the WFM model and the dynamic contact angle models of Adv-Rec, Kistler and Shikhmurzaev are compared against the corresponding experimental/numerical data (when available).



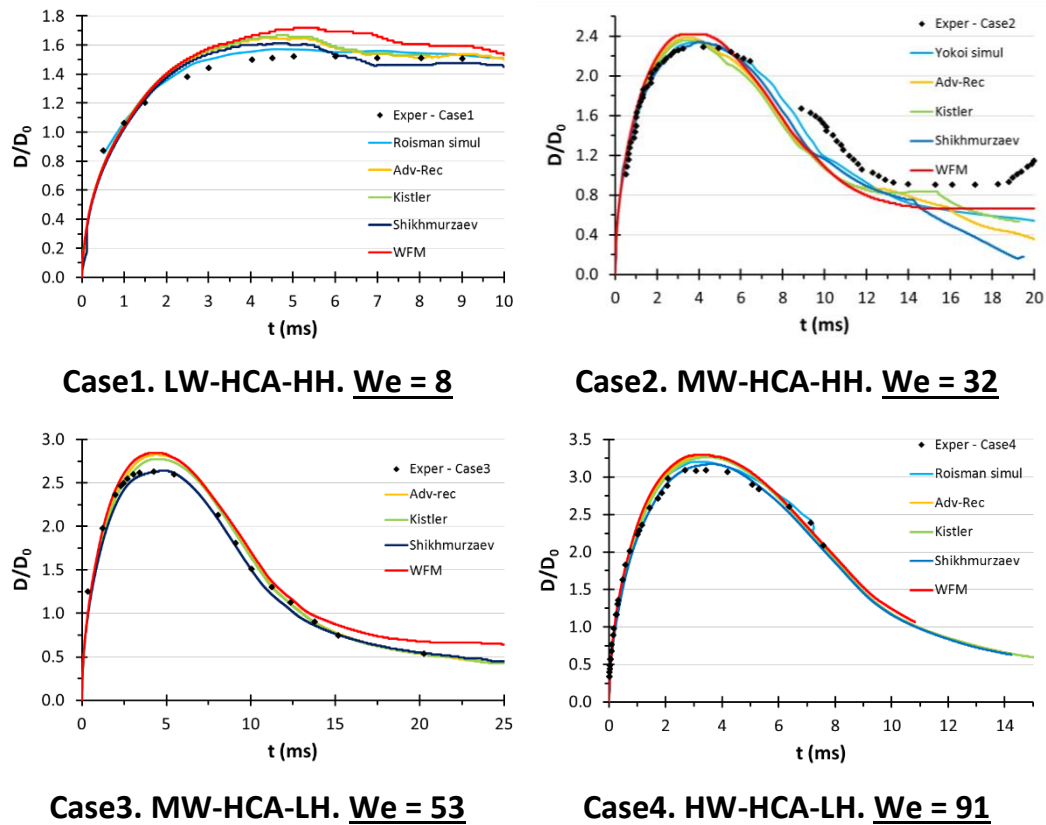


**Figure 3.20:** Comparison of WFM results and predictions from dynamic contact angle models against experimental/simulation data for the hydrophobic surfaces of Cases1-4 listed in Table 3.7 (where references can be found).

In general, the WFM overestimates slightly the maximum droplet spreading. Given that the proposed model calculates the contact angle rather than using it as a boundary condition, a good agreement between the results derived from the WFM and the experiments can be claimed.

Results from the application of the dynamic contact angle models are in good agreement with experimental data as well, while Shikhmurzaev's model seems to behave slightly better. This is attributed to the significant differences that arise in the contact angle prediction when using the dynamic contact angle models. As an example, assuming an arbitrary  $\theta_{eq} = 90^\circ$ , can give up to 20% difference in contact angle prediction as function of contact line velocity, when using Shikhmurzaev's instead of Kistler's model. This suggests that significant differences are expected when using different models.

In Figure 3.21 the WFM results of the droplet shape at characteristic times during the impingement process is presented and compared against photographs taken from experimental data for the conditions of Case3 (MW-HCA-LH). Simulation axisymmetric results are revolved around the axis of symmetry to produce the pseudo 3D images.

Droplet interface is represented by the  $\alpha=0.5$  iso-surface, while the droplet interior is cut in order to present both the dynamic grid refinement technique and velocity vectors. The pressure of the liquid phase is depicted at the wall surface, non-dimensionalised by the initial kinetic energy of the droplet, thus defining the pressure coefficient as:

$$C_p = \frac{p}{\frac{1}{2}\rho_0 u_0^2} \quad (3-11)$$

Simulation results are in good agreement with the experimental data. At the later stages of the recoiling phase (final 3 images), the same qualitative behavior is observed, the shapes are not exactly the same. In the final image, simulation suggests that the break-up of the satellite droplet has occurred, while in the experiment this phenomenon occurs later. Similar results are presented by Caviezel et al. [123], indicating a very good agreement between the results of the two codes.

Further information related to the phenomenon can be extracted by the simulation. At the initial stage of impingement,  $t=0-1.31\text{ms}$ ,  $C_p$  can reach up to 9.7, explained by pressure rise due to formation of a dimple upon drop impact [186]. During the rest of the spreading phase and the start of recoiling ( $t=3.14-6.02\text{ms}$ ),  $C_p$  is much lower, while the maximum value is observed at the droplet rim. As the retraction of liquid mass continues, pressure is building up on droplet center and the liquid follows an upward rebound motion. The induced flow field is typical for impingement cases. During the initial stage of the process, velocity magnitude can reach up to 6 times the initial impact velocity, while during the rest of the advancing and receding phases it is only 1.5 times the impact velocity. Moreover, the vortex located at the top of droplet rim clearly changes direction between time instances of 3.14ms and 6.02ms marking the spreading and receding phases respectively.

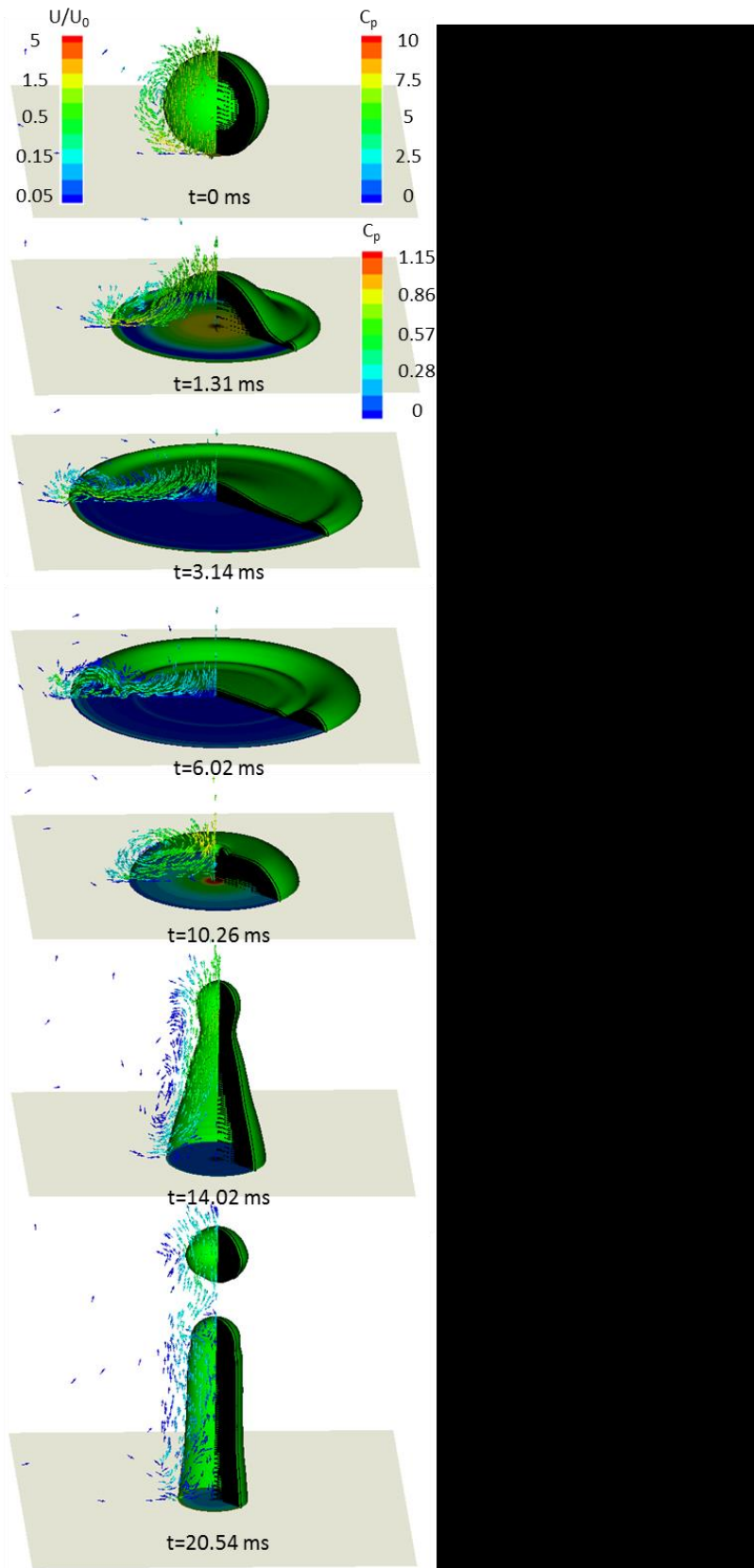


**Figure 3.21:** Comparison of WFM results against experimental data for Case3.MW-HCA-LH. Experimental images taken from [43], Courtesy of Springer.  $C_p$  contour and velocity vectors colored by velocity magnitude are plotted.  $C_p$  values below 0.01 are cutoff. The first  $C_p$  contour legend applies to the first two images, while the second one applies to all the following.

In Figure 3.22, experimental images taken from [58] are compared against the results of the WFM simulation for Case4 (HW-HCA-LH). Pressure contours, as well as the induced flow field during the process are presented.

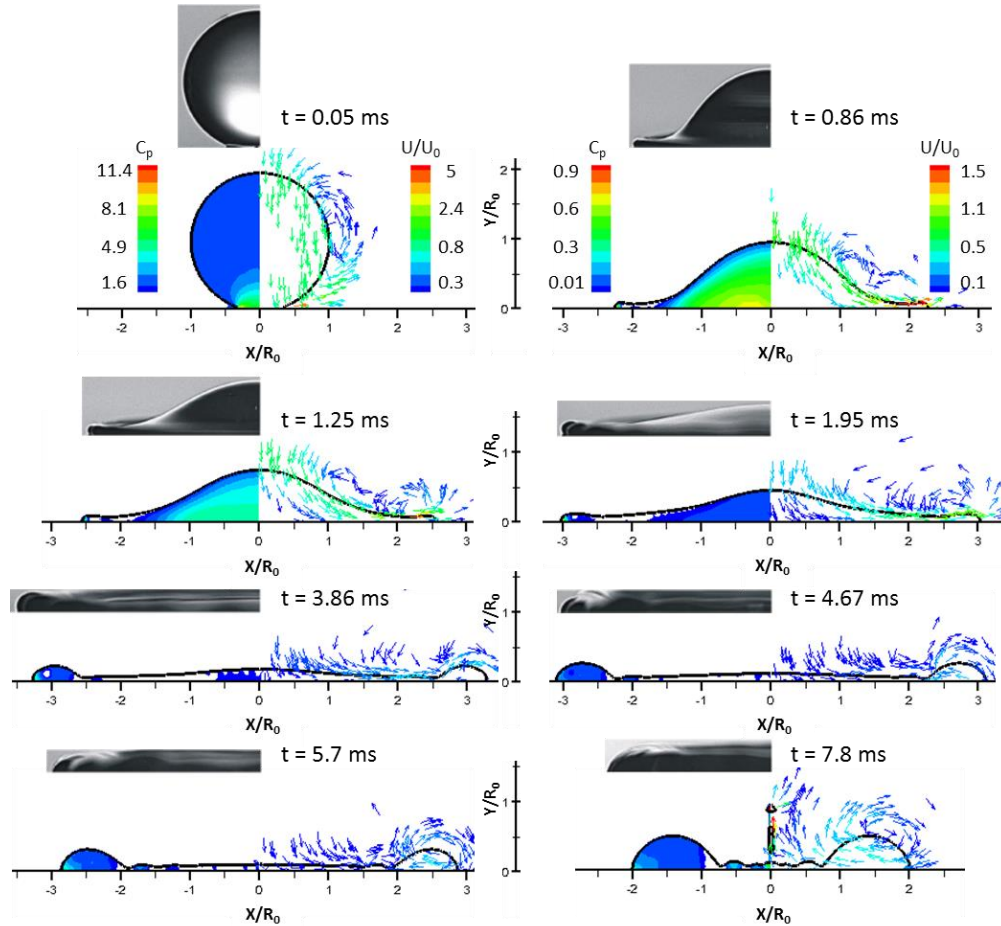


**Figure 3.22:** Comparison of WFM results against experimental data for Case4. HW-HCA-LH. Experimental images reproduced from [58] with permission from AIP Publishing LLC.  $C_p$  contour and velocity vectors colored by velocity magnitude are plotted.  $C_p$  values below 0.01 are cutoff. The first contour legends apply to the first image, while the second one applies to all the other.

Again, very good qualitative agreement is claimed between simulation and experiment. Similar impingement related info are observed, related to pressure, and velocity field. At  $t=7.8\text{ms}$  (final instance), the ejection of a small droplet on the symmetry axis is predicted, which originates from the coalescing liquid mass at the symmetry axis, as the droplet retracts.

In Figure 3.23, the spreading diameter is plotted against non-dimensional time, for all 4 cases concerning the impingement of a droplet onto hydrophobic surfaces. At the first stage of impingement ( $\tau < 0.1$ ), the kinematic phase [43], all four lines coincide in one,

depicting the uniform character of the impingement process, while afterwards, in the spreading phase, inertia dominates and the lines separate.

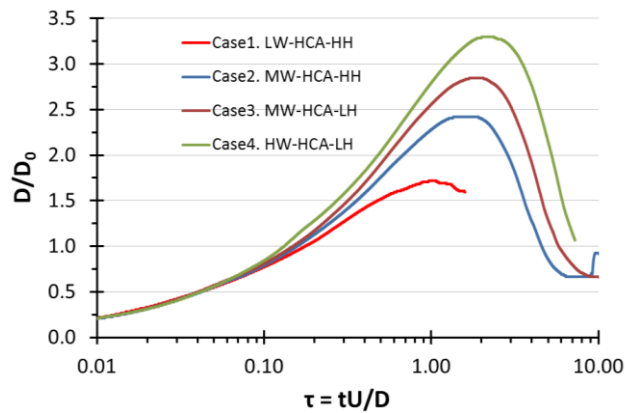


**Figure 3.23:** Non-dimensional spreading diameter from WFM simulation plotted against non-dimensional time for hydrophobic surfaces.  $\theta_{adv} = 105^\circ-120^\circ$ .  $We = 8-91$ , x-axis, logarithmic scale.

### 3.3.4.6 Spreading on hydrophilic surfaces

In Figure 3.24, the temporal evolution of the spreading diameter for a droplet impinging onto solid hydrophilic surfaces is depicted for cases 5,7- 9. The results presented in this section and the following one, especially those concerning low and moderate  $We$  numbers, present novel character. As stated in Chapter 1, there is a lack of numerical investigations in literature for water droplet impingement onto hydrophilic surfaces. Numerical results of [55] are presented for Case4.

For cases 5,7 experimental data are taken from [113], where the authors present measurements for the time evolution of the contact diameter only for the first 4ms of the process, while they only present the maximum diameter in another figure relating it to the Reynolds number. The comparison is therefore limited to this time interval (initial 4ms), while the respective comparison with the maximum spreading value is presented in Table 3.9 and Figure 3.16.

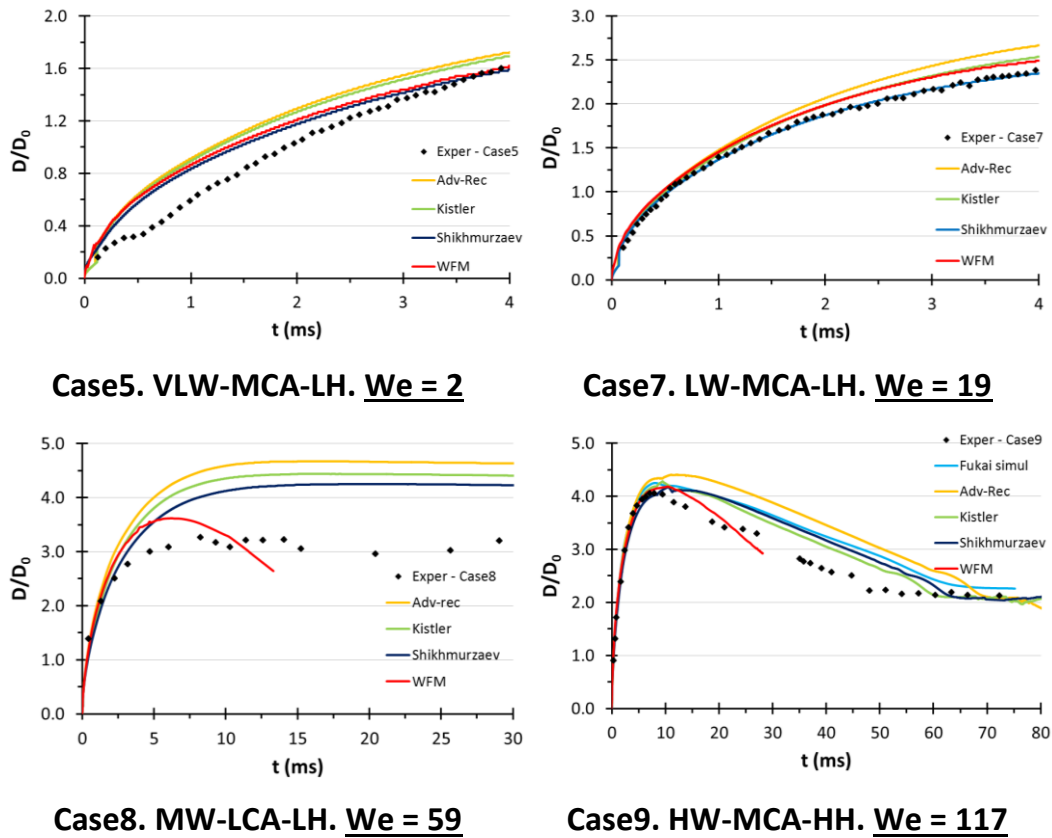


**Figure 3.24:** Comparison of WFM results and predictions from dynamic contact angle models against experimental/simulation data for the hydrophilic surfaces of cases 5,7-9 listed in Table 3.7 (where references can be found).

In Case5 (VLW-MCA-LH) all models overestimate droplet spreading for the initial 4ms. WFM seems to be closer to the experimental values, in comparison to the Adv-Rec and Kistler’s model, in contrast to what was seen in hydrophobic surfaces. Results between Shikhmurzaev’s and WFM are similar. Moreover, the slope of all model lines at 4ms is steeper than the corresponding experimental markers, which results in an underestimation of maximum spreading, as shown in Table 3.7. For higher Weber number (Case7. LW-MCA-LH), Shikhmurzaev’s model gives the best results, perfectly capturing the trend of the experimental values, while all other models, as well as the WFM are quite close as well.

In Case8 (MW-LCA-LH), a significant over-prediction of droplet spreading is predicted by the simulation, as it is shown in Figure 3.24. Using the very low contact angle value of  $10^\circ$  [43], none of the dynamic contact angle models was able to reach a non-dimensional maximum non-dimensional diameter of 3.31 as reported in the experiments. WFM predicts a maximum spreading substantially lower than the other models and significantly closer to the experiments. Moreover, the recoiling of the drop is predicted, unlike to what

the experiment suggests. Finally, for the high We Case9 (MW-LCA-LH), all models seem to behave better; the maximum spread is well captured. Once more, the WFM seems to behave slightly better during the advancing phase, but predicts a quicker recoiling phase.

The quicker recoiling phase predicted by the WFM is highlighted in Figure 3.25; the droplet shape and velocity vectors are shown for time instants close to the “hysteresis” time for the Case 9.

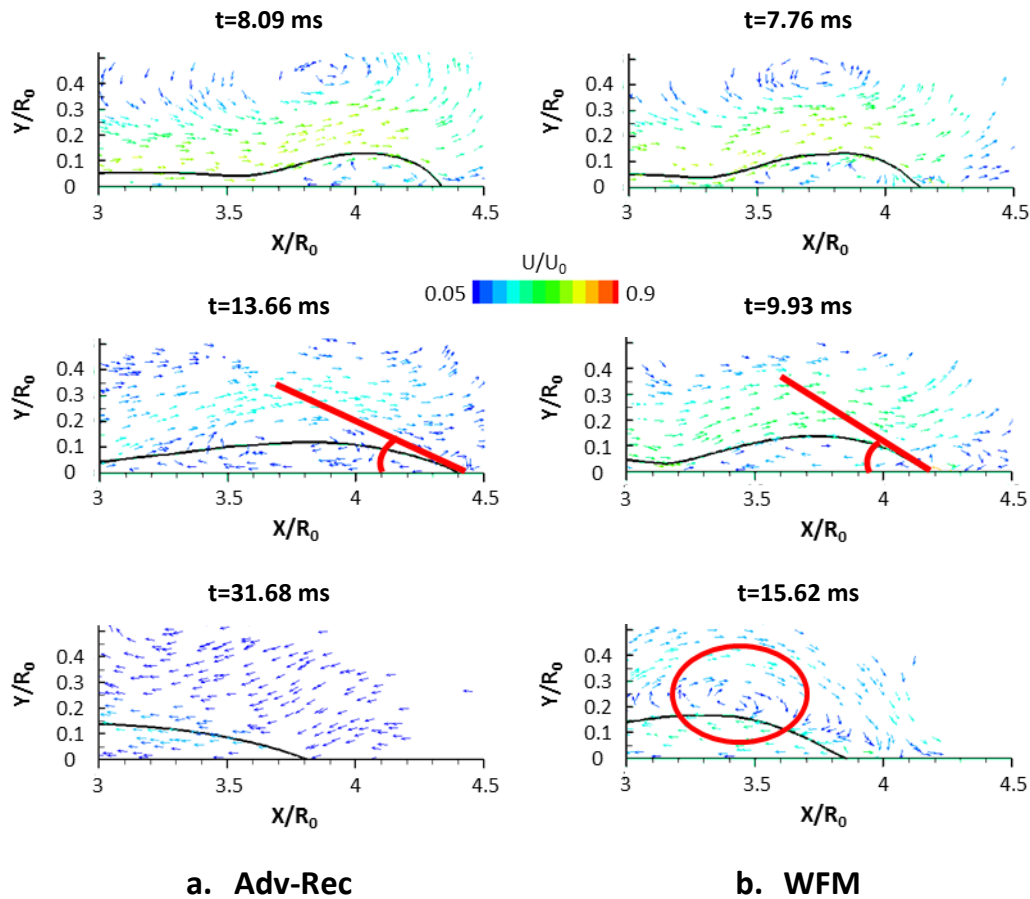
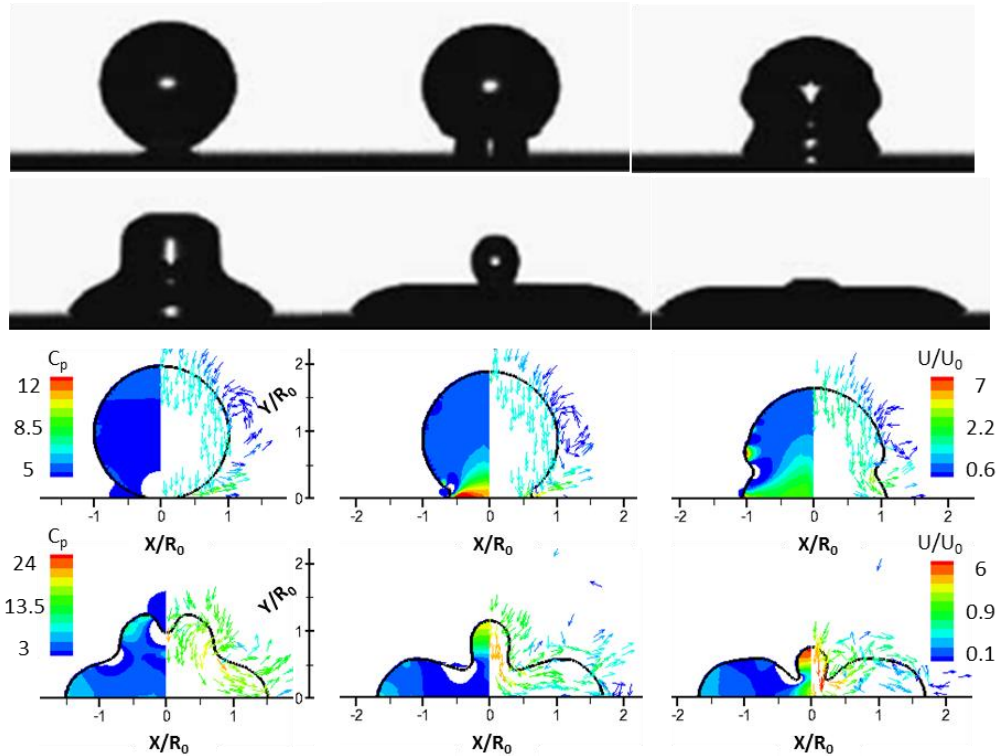


**Figure 3.25:** Prediction of “hysteresis” time for WFM in comparison to Adv-Rec model. Velocity vectors colored by velocity magnitude are plotted. Quicker recoiling phase is predicted by the WFM.

The hysteresis time lasts much longer for the Adv-Rec model; the rim “turns” to the recoiling angle at time instant  $t=13.66\text{ms}$  for this model, in conjunction with  $t=9.93\text{ms}$  for the WFM. The receding contact angle predicted by the WFM is clearly higher, which results in the quicker recoiling phase, as can be seen by the higher velocity values exhibited at the droplet rim at  $t=15.62\text{ms}$  for WFM. The simulation stopped at 30ms because droplet break-up in the symmetry axis was observed, and the present axisymmetric application of the WFM cannot be considered as valid afterwards.

In Figure 3.26, the shape of the drop at characteristic times for Case5 (VLW-MCA-LH) is presented against corresponding experimental data, showing good qualitative agreement.



$t_{\text{exp}} = 0.089, 1.157, 3.314, 4.272, 8.455, 10.146 \text{ ms}$

$t_{\text{sim}} = 0.089, 0.53, 1.5, 3.4, 5.49, 6.21 \text{ ms}$

**Figure 3.26:** Comparison of WFM results against experimental data for Case5. VLW-MCA-LH. Experimental images reprinted from [113] with permission from Elsevier.  $C_p$  contour and velocity vectors colored by velocity magnitude are plotted.  $C_p$  values below 0.01 are cutoff.

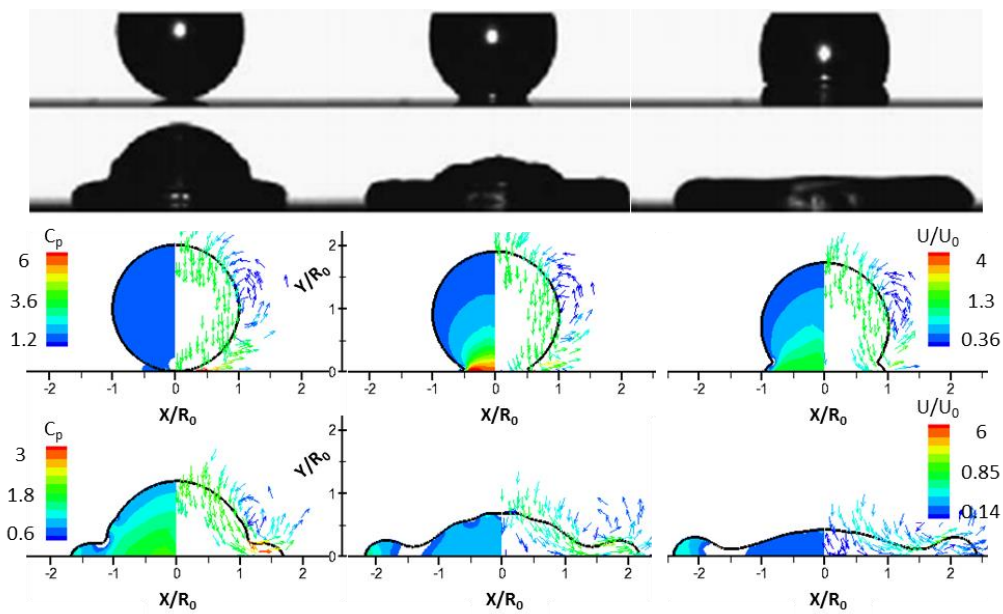
Simulation time is much smaller than the real time, as the droplet initial spreading is overestimated (Figure 3.24). For the first 4 images, the simulated droplet shapes are similar to the experimental ones, showing that the model can capture the odd shapes formed by the droplet at very low Weber numbers (2<sup>nd</sup> and 3<sup>rd</sup> image). For the following 2 images, a larger thickness of the liquid film is predicted, which deviates from the experiment; this is the main reason for the underestimation of maximum spreading. However, as the dynamic contact angle of  $70^\circ$  is used [113], whereas the authors observe a contact angle value of approximately  $15^\circ$  at the end of the relaxation phase. The high change in contact angle values is very difficult to be captured in a simulation.

The pressure contours for this case are rather peculiar. More specifically,  $C_p$  inside the droplet is higher than expected, exhibiting a minimum value of 3. This may be attributed



to the low impact velocity, or possibly to the spurious velocities that appear at the interface region and might induce an unrealistic pressure field. For higher Weber number, the effect of these velocities on the evolution of the impingement is minimal.

In Figure 3.27, the temporal evolution of impingement for Case7 (LW-MCA-LH) is compared against experimental photographs from the work of Roux et al. [113]. For this case there is both qualitative and quantitative agreement between simulation and experiment.



$t_{exp/sim} = 0, 0.132, 0.484, 1.452, 2.508, 3.608$  ms

**Figure 3.27:** Comparison of WFM results against experimental data for Case7. LW-MCA-LH. Experimental images reprinted from [113] with permission from Elsevier.  $C_p$  contour and velocity vectors colored by velocity magnitude are plotted.  $C_p$  values below 0.01 are cutoff.

The non-dimensional droplet diameter for all hydrophilic cases is presented in Figure 3.28. Time is non-dimensionalised by  $U_0^{-1/2}$ , as in [51]. Again, all lines coincide in one for the initial kinematic phase, while afterwards, in the spreading phase, the effect of inertia plays significant role. The values of x-axis do not correspond to a physical quantity.

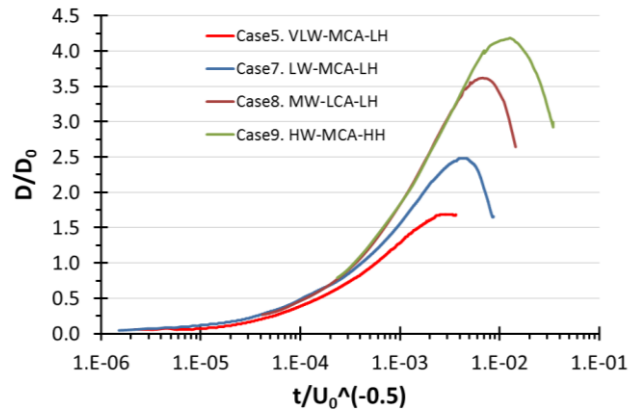
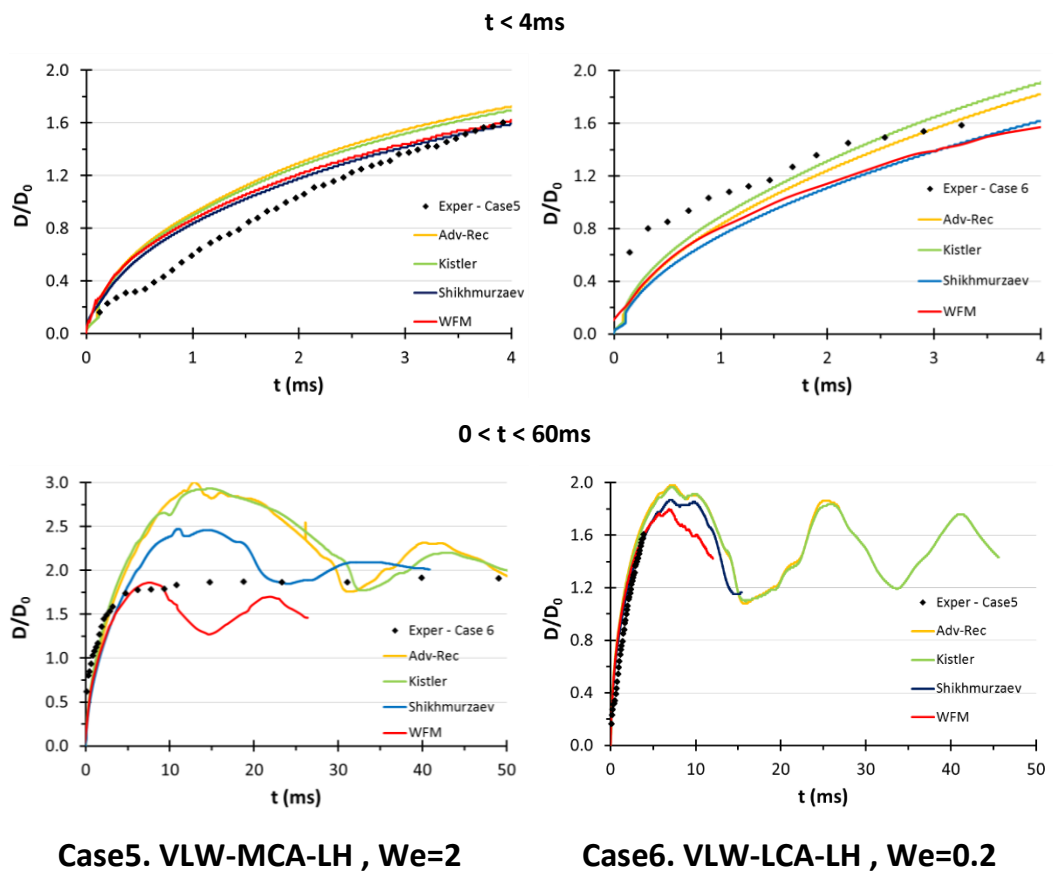


**Figure 3.28:** Non-dimensional spread factor from WFM simulation plotted against non-dimensional time for hydrophilic surfaces.  $\theta_{adv}=10^{\circ}-70^{\circ}$ .  $We=0.2-117$ , x-axis, logarithmic scale.

### 3.3.4.7 Impact at very low Weber numbers

An additional case (Case6 VLW-LCA-LH) for an extremely low Weber number ( $We=0.2$ ) is simulated, in order to investigate the significant under-prediction on maximum spreading exhibited in Case5 (VLW-MCA-LH) for  $We=2$ . Experimental data are taken from [45], where the authors only present a graph for the time evolution of droplet radius and do not present photographs.



**Case5. VLW-MCA-LH , We=2**

**Case6. VLW-LCA-LH , We=0.2**

**Figure 3.29:** Comparison of simulated results for very low Weber numbers.

The temporal evolution of contact diameter for both Case5 and Case6 is presented in Figure 3.29. For the initial 4 ms of the phenomenon, droplet spreading is overestimated in Case5 and underestimated in Case6. Concerning the whole phenomenon evolution ( $0 < t < 60\text{ms}$ ), the model cannot predict a slow deposition as seen during the experiments for Case6; after the droplet reaches its maximum radius, it oscillates until it comes to rest.

This behavior is also evident in Case5, showing that the dissipation of initial kinetic energy is not well predicted by the model. Based on the differences observed, it is concluded that the numerical simulation of droplet impingement at very low Weber numbers is difficult from a numerical point of view.

### 3.3.5 Conclusions

A general observation is that WFM, in contrast to hydrophobic surfaces, exhibits results which are closer to the experimental data compared against the Adv-Rec or Kistler's model, while a quicker recoiling phase is predicted for cases 8 (MW-LCA-LH) – 9 (HW-MCA-HH). Shikhmurzaev's model for dynamic contact angle behaves better in all cases presented, while Kistler's model for hydrophilic surfaces exhibits significant improvement in comparison to the Adv-Rec model. In hydrophobic surfaces the results for these models were similar.

## 3.4 Isothermal droplet impingement onto a spherical surface

### 3.4.1 Introduction

In Chapter 1, a comprehensive review was presented concerning the droplet impact on a spherical particle. It was concluded that there are limited studies, both numerical as well as experimental, that examine this phenomenon.

A crucial parameter that affects droplet-particle collision outcomes is the droplet-to-particle size ratio (DTP), defined as the ratio of the droplet diameter pre-impact to the particle diameter. The main aim of this section is to assess the performance of the numerical model to simulate droplet-particle collision phenomena, and then use this model to study the effect of DTP and We number, on the collision outcome. In this way, collision maps may be drawn and impact outcomes can be distinguished for a wide range of the parameters of interest, which has not been presented before.

The investigation of collisions between droplets and particles of similar size contributes to the physical understanding of similar processes happening in technological applications, as for example in FCC reactors.

### 3.4.2 Cases studied

The operating conditions of cases examined are summarized in Table 3.10. Cases 1 and 1a serve as a validation of the numerical model in non-flat surfaces; the effect of grid size on the results is assessed, while the experimental data of [21] are used for validating the model. In this work, the authors present experimental/numerical data for water droplet impacting onto a larger spherical solid cup at room temperature, under the effect of gravity. The remaining 8 cases refer to the parametric study, where the effect of DTP and We on the collision outcome is discussed.

Case No.	$u_0$ (m/s)	$D_p$ (mm)	DTP	We	Re	locRef	cpR
1	0.434	10	0.31	8	1336	4	52-82
1a	0.434	10	0.31	8	1336	5	104-164
2	0.97	10	0.31	40	2987	4	52-82
3	1.372	10	0.31	80	4224	4	52-82
4	0.434	5	0.62	8	1336	3	52-82
5	0.97	5	0.62	40	2987	3	52-82
6	1.372	5	0.62	80	4224	3	52-82
7	0.434	2.5	1.24	8	1336	2	52-82
8	0.97	2.5	1.24	40	2987	2	52-82
9	1.372	2.5	1.24	80	4224	2	52-82

**Table 3.10:** Simulated cases for droplet-particle collisions.  $D_0=3.1\text{mm}$ ,  $\theta=90^\circ$ .

Droplet size remains unchanged. The effect of DTP is investigated by varying the particle diameter, while the We number changes by varying the impact velocity. Gravitational acceleration is accounted for. The gravity force is of significance for the induced collision dynamics; Bond number which expresses the relation of gravity to surface tension forces is 1.3 for all cases, while Froude number which quantifies the relation of inertial to gravity forces ranges in between 2.5-7.9.

The fluids chosen are water and air at room temperature (properties in Appendix B). A static contact angle of  $90^\circ$  is applied at the wall surface in order to exclude the effect of this parameter on the collision dynamics. Moreover, this value is used in [21].

### 3.4.3 Numerical domain

The numerical three-dimensional domain employed for all cases, along with the applied boundary conditions are presented in Figure 3.30. The solid particle is represented by a fixed spherical wall surface, while a symmetry plane cuts the droplet in half to reduce the computational cost. The droplet is initially placed at a distance of one droplet diameter away from the spherical particle, to allow the development of the induced flow field prior to droplet impact.

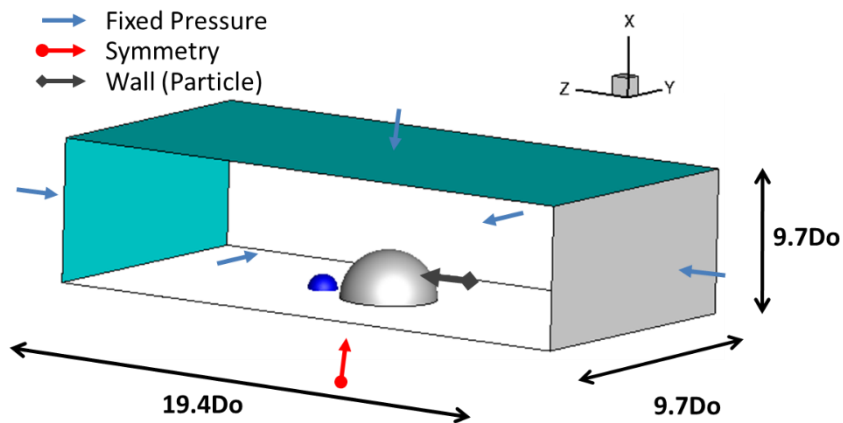


**Figure 3.30:** Computational domain along with the applied boundary conditions.

The size of the grids employed is presented in Table 3.11. Different grids are used for each set of particle diameters. The coarse, initial (after the application of locRef) and maximum grid size is given in the Table, as well as information relevant to the computational resources required for the runs to be performed.

Case No.	Coarse grid (mill cells)	Initial grid (mill cells)	Maximum grid (mill cells)	Processors	Time elapsed (days)	Uniform equiv. grid (mill cells)
1-3	0.051	0.183	1.55-2.45	12	15	208
4-6	0.19	0.257	0.9-1.55	12	10	97
7-9	0.363	0.469	1.04-1.1	12	5	23

**Table 3.11:** Number of cells and simulation times for all runs performed.

The computational grids contain hexahedron cells, while the grid lines are designed to start from the spherical particle and expand spherically in the flow domain, as shown in Figure 3.31.

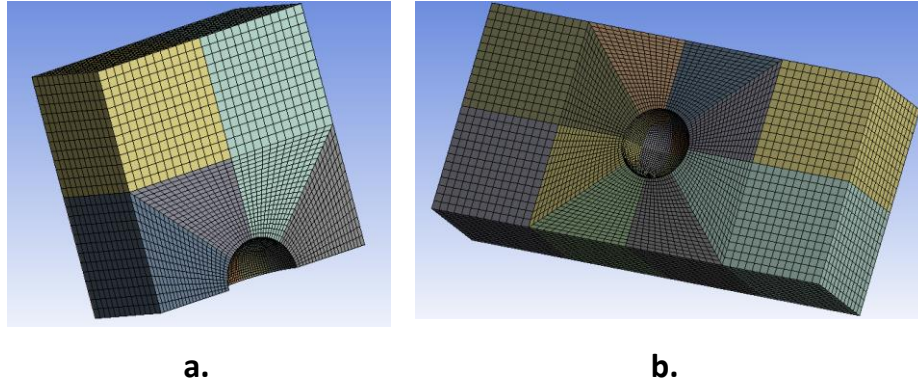


**Figure 3.31:** Computational grid used for a) the validation cases 1,1a and b) cases 2-9.

This choice results in varying cell size, and therefore varying cpR as observed in Table 3.10. For Case1a, the most computational expensive one, the particle wake side is not simulated, as it is known a priori [21] from the experimental observation that the droplet rebounds after impinging on the solid surface (Figure 3.31a).

The particle circumference is discretized by 104 cells, which is considered accurate enough to resolve the spherical particle shape. When changing the particle diameter, the same accuracy is achieved at the spherical particle surface, by using the appropriate locRef levels, as shown in Figure 3.32, except for Case1a, which acts as the validation of the applied numerical algorithm.

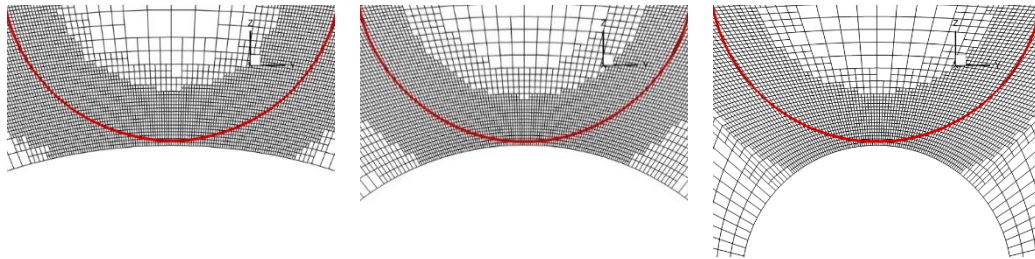


**Figure 3.32:** Same cell width achieved by using the appropriate locRef levels. a) cases 1-3, locRef4, b) cases 4-6, locRef3, c) cases 7-9, locRef2.  $\tau=0$ .

The numerical settings for the aforementioned cases are presented in Table 3.12.

Parameter	Value
Courant	0.25
Locref distance	14 cells
cpR	52-82

**Table 3.12:** Numerical settings for the droplet spherical impingement case

### 3.4.4 CFD results

#### 3.4.4.1 Reference case-droplet rebound

Figure 3.33 presents the numerical results of cases 1,1a, i.e. for locRef4 and 5 respectively. On the left side of the figure, the definition of the spreading diameter for the spherical particle case is shown, while on the right side, the derived numerical results for the spreading diameter are compared against the corresponding experimental/numerical data of [21].

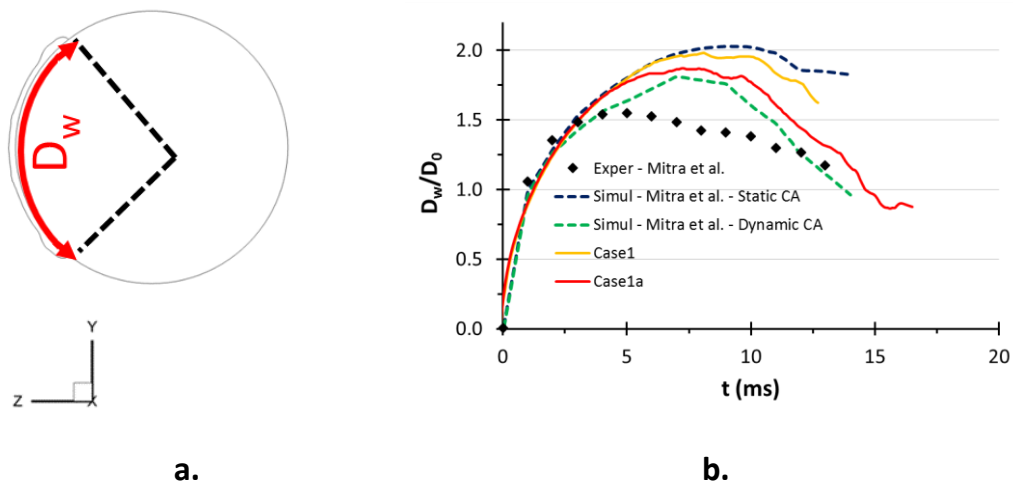


**Figure 3.33:** a) Spreading diameter  $D_w$  definition for spherical particle impacts; b) Temporal evolution of dimensionless droplet spreading diameter compared to experimental data and simulation results taken from Mitra et al. [21].

As the grid cell size decreases, the results can be regarded as more accurate. Moreover, the current results approach better the experimental data in conjunction with the corresponding simulations [21] for a static contact angle. In the dynamic contact angle case, the authors used the dynamic variation of the contact angle with time, as obtained from the experimental data, which allowed the numerical model to predict in a better way the temporal evolution of the phenomenon.

A direct comparison between experimental images and simulation results from [21] along with the results of the current model are presented in Figure 3.34. Overall, a good agreement is claimed for the current simulation results, especially during the recoiling phase.

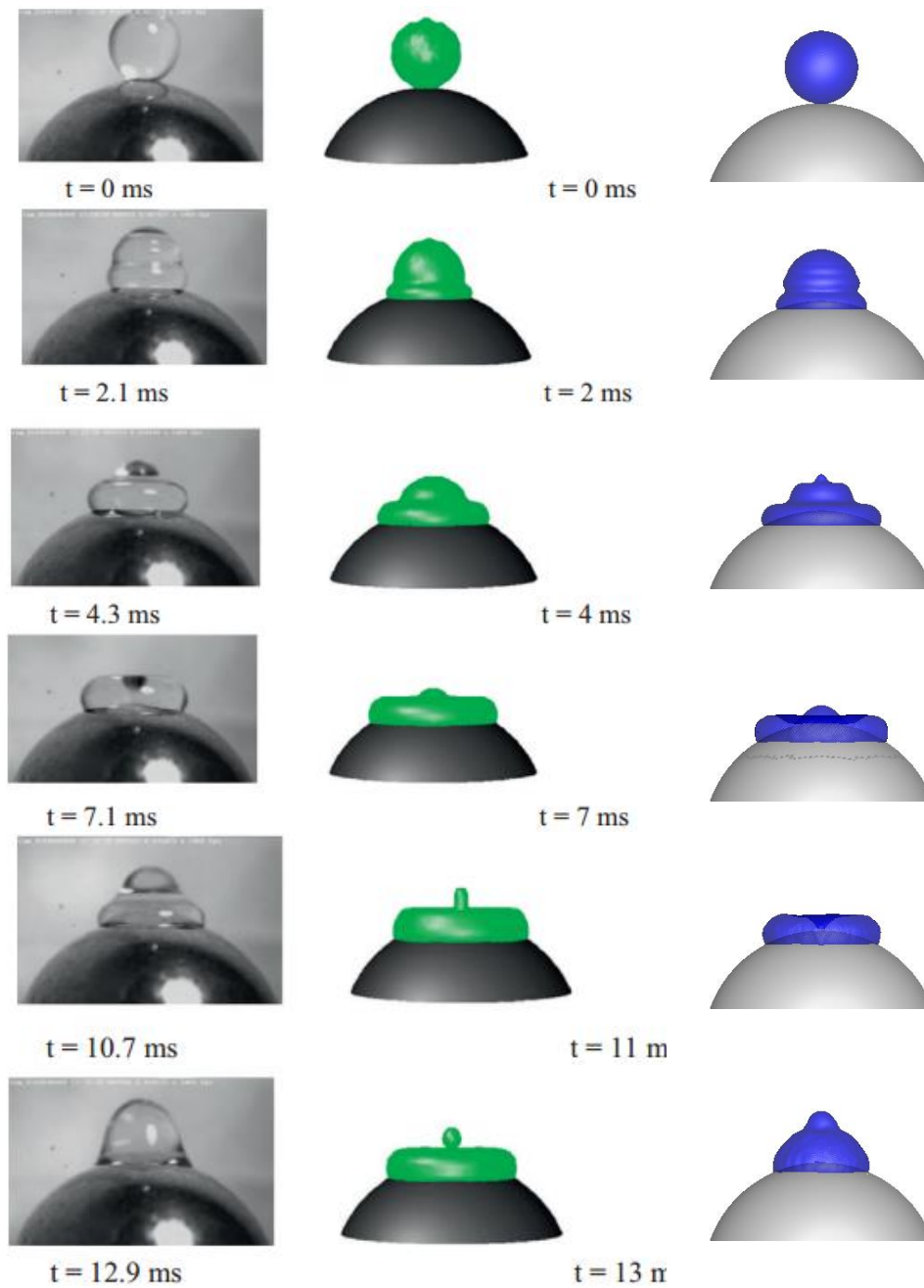


**Figure 3.34:** Comparison between experimental photos (left) and simulation results (center) as reprinted from [21] with permission from Elsevier against the present simulation results (right).

Small differences in the droplet shape between current simulation and experimental images are reflected to the over-estimation of droplet maximum spreading, as highlighted in Figure 3.33, and which can be attributed to the use of a static contact angle instead of the real values. Overall, the numerical model gives results within an acceptable level of agreement against the relevant experimental/numerical data.



### 3.4.4.2 Droplet-particle collisions for varying DTP and We

After the validation of the numerical model for the case of droplet impingement onto a spherical particle, a parametric study is performed in order to investigate the dynamics of the droplet-particle collisions under different impact conditions. The predicted collision outcomes are grouped and depicted in Figure 3.35a utilizing representative images for all cases examined. In Figure 9b the two distinctive outcome regimes, namely rebound and coating are separated by a curve. This critical curve results from the observation that coating will take place when the droplet initial kinetic energy is equal or higher than the surface energy needed to spread the film past the particle equator, i.e. when the following ratio equals to unity:

$$\frac{E_{kin}}{E_{0.5surf}} = \frac{m_o u_o^2 / 2}{\sigma A_{psurf} / 2} = \frac{\rho_o u_o^2 \pi D_o^3 / 12}{\sigma \pi D_p^2 / 2} = \left( \frac{\rho_o u_o^2 D_o}{\sigma} \right) \cdot \left( \frac{D_o}{D_p} \right)^2 \cdot \frac{1}{6} = We \cdot DTP^2 \cdot \frac{1}{6} \quad (3-12)$$

Simulation results for the collision outcome are spread nicely on the two sides of this limiting curve. It can be noticed that in Case3 (DTP=0.31, We=80), where the droplet breaks up after its collision with the solid particle, part of the liquid mass starts sliding downwards, thus marking the threshold from rebound to coating regime.

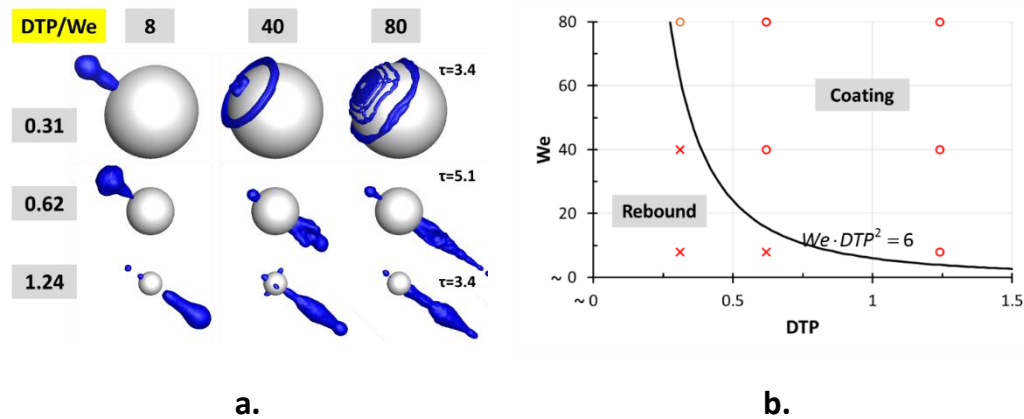


**Figure 3.35:** a) Droplet-particle collision outcomes for cases 1-9. b) We-DTP collision outcome map. Circle, 'x' markers denote coating/rebound regime respectively.

Based on the numerical results and the range of parameters studied, the transition from droplet rebound regime to full coating one is reinforced by both the increase of DTP as well as that of impact velocity. The inclusion of wettability effect is expected to shift the border line shown in Figure 3.35b. For example, in the case of droplet-particle collisions, where the particle material exhibits hydrophobic behavior, this line is expected

to be shifted towards higher We numbers for the same DTP, since hydrophobicity promotes rebound over coating.

For droplets of significantly smaller size than the solid particle, as in cases 1-3, the droplet rebounds after impact. For these cases, which are characterized by small DTP values, droplet-solid interaction resembles the behavior observed in flat surfaces, namely droplet rebound. During the initial stages of impingement, the droplet spreads onto the spherical surface until the surface tension force overweighs the initial drop kinetic energy and gravitational forces that promote spreading. Viscous dissipation prohibits the liquid free motion in both spreading/recoiling phases.

In Figure 3.36 the effect of impact velocity on maximum drop spreading on the solid particle is presented for cases 1-3.

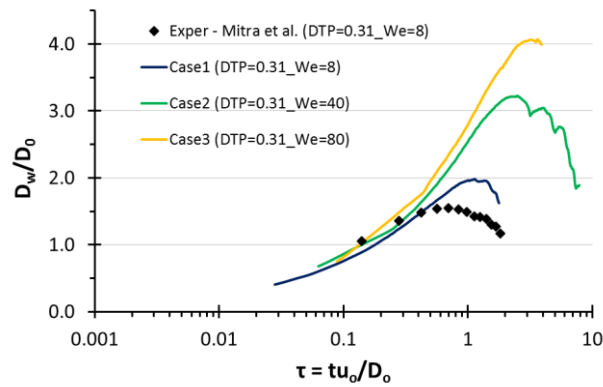


**Figure 3.36:** Effect of We number on the dimensionless wetting diameter for cases 1-3.

As the impact velocity increases, the droplet spreads further onto the solid particle. For the early stages of the phenomenon, in the kinematic phase, all lines coincide, as observed for the impingement on a flat surface in the previous section. At this initial stage wettability and We are not influential. For the case of moderate Weber number impacts (cases 2, 3), fragmentation of the liquid film that spreads/retracts on the solid particle is observed. For Case3, a significant part of the liquid mass starts sliding down towards the downstream side of impact.

In order to get an insight to the dynamics of spreading, the temporal evolution of the average liquid velocity along the axis of impact for cases 1-3 is presented in Figure 3.37. The mean velocity is calculated using:

$$w_{mean} = \frac{\sum_{c, \alpha > 0.5} \alpha \cdot V_{cell} \cdot w_{cell}}{\sum_{c, \alpha > 0.5} \alpha \cdot V_{cell}} \quad (3-13)$$

The collision outcome observed in Figure 3.35 complies with the mean velocity prediction.

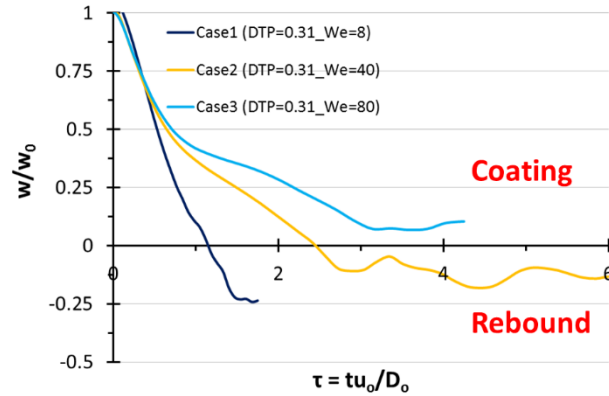


**Figure 3.37:** Effect of We number on the liquid phase mean velocity along the drop-particle axis (z direction) for cases 1-3.

As the impact velocity increases, the average liquid velocity decreases at a slower rate, implying that it takes longer for the viscous dissipation and surface tension forces to outweigh gravity and initial kinetic energy. For the high Weber number case, the volume weighted velocity is positive throughout the phenomenon, thus showing that a significant part of drop mass continues the sliding motion along the particle surface.

As the DTP increases, for cases 4-6, the transition to coating regime is enhanced, while the Weber number seems to be the decisive parameter. For very low Weber number, the droplet still rebounds from the solid surface, while for higher Weber numbers the droplet coats the particle (Figure 3.35).

A typical image of the coating regime is presented in Figure 3.38; the drop surface and symmetry plane are coloured by the velocity magnitude.

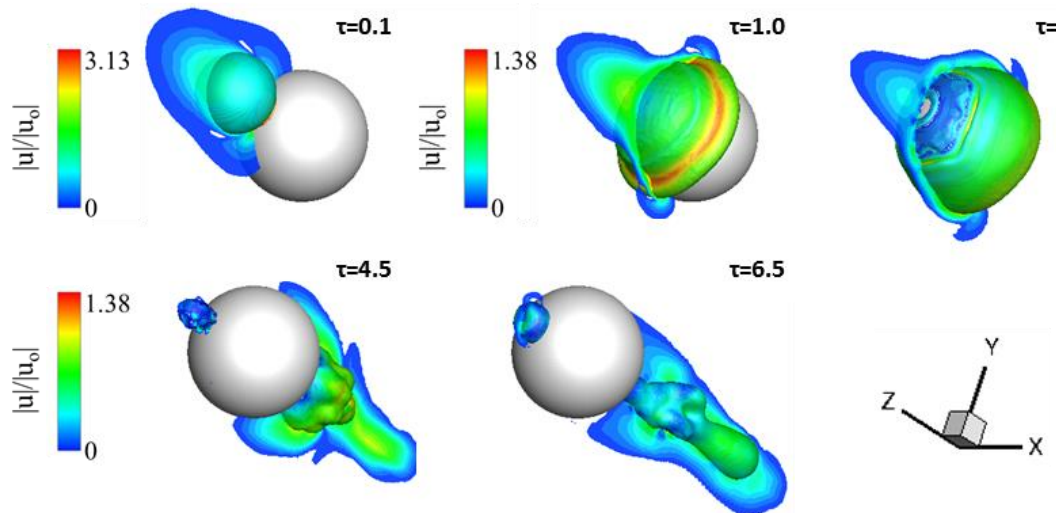


**Figure 3.38:** Temporal evolution of drop-particle collision for Case5 (DTP=0.62\_We=40). Drop iso-surface ( $\alpha=0.5$ ) and symmetry plane  $y=0$  coloured by the dimensionless velocity magnitude. Values below 0.15 are cut-off.

The droplet after hitting the solid particle spreads across its surface, up to the point where the liquid film thickness on the particle surface becomes so thin that inevitably breaks ( $\tau=2.1$ ). After this point, the liquid mass is separated in two distinct parts. The first one retracts on the solid particle surface, while the second one which contains most of the initial droplet mass, continues spreading until it accumulates behind the particle and forms an elongated ligament that leaves the particle surface. This ligament that is moving in the particle wake region may result to a small number of satellite droplets ( $\leq 3$ ). As the Weber number increases, the instabilities induced at the liquid flowing away from the particle get more intense and the ligament becomes thinner, as presented in Figure 3.35.

The coating outcome is summarized in Figure 3.39, where the following phenomena are observed: (a) particle coating ( $\tau=2$ ), (b) liquid mass accumulation in the particle wake region ( $\tau=6.8$ ) and (c) satellite drop injection ( $\tau=9.3$ ).

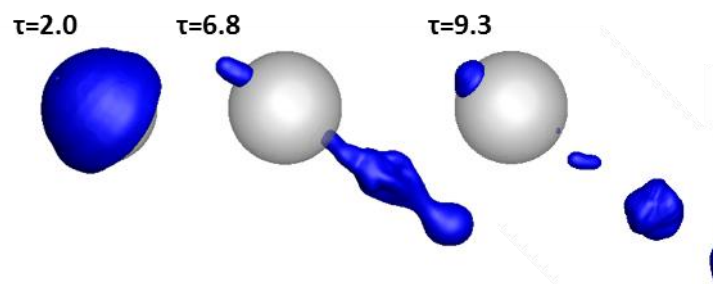


**Figure 3.39:** Droplet-particle collision mechanism (coating, mass accumulation and satellite drop formation) shown for Case5 (DTP=0.62\_We=40).

The aforementioned breakup mechanism is depicted in more detail in Figure 3.40. The liquid film becomes so thin that breaks up at some point and then under the influence of surface tension force tends to retract. During this deformation, an internal liquid recirculation zone is induced within the retracting rim, shown in Figure 3.40c. This recirculation marks the initiation of the retracting motion of the liquid mass.

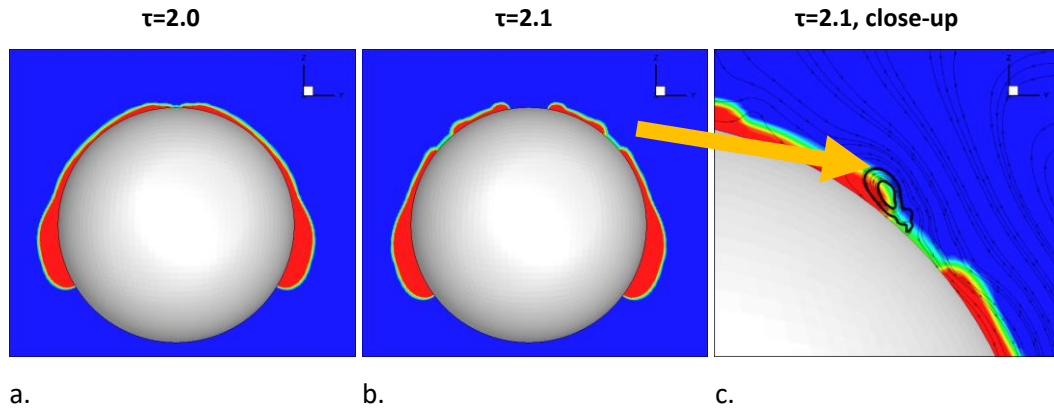


**Figure 3.40:** a, b) Evolution of thin film break-up and c) close up view of the break-up region.

Break-up occurs when under the simultaneous effect of the inertial, gravitational, viscous and surface tension forces, neck areas which are characterized by very small thickness, are developing on the spreading lamella. This physical mechanism is referred as end-pinching mechanism in the literature and the exact area of neck formation is highly dependent on the induced flow field characteristics, which stretch the liquid phase (lamella) making it very thin at the point of break-up. The exact position of the neck break-up is affected by the applied cell size. Based on previous studies [149, 161, 162], where a  $cpR$  in the range 72-120 is used, and this phenomenon is resolved, it is assumed that the applied cell size is able to reproduce the exact dynamics of the break-up mechanism.

The pressure field is similar to that observed when a drop impacts on a flat surface. Figure 3.41 presents the pressure coefficient for Case5 at the same time instants as in Figure 3.38. When the droplet impinges onto the solid particle,  $C_p$  rises up to almost 5 times the impact kinetic energy. At later stages corresponding to time instances of coating and formation of liquid ligaments, the liquid maximum pressure decreases.

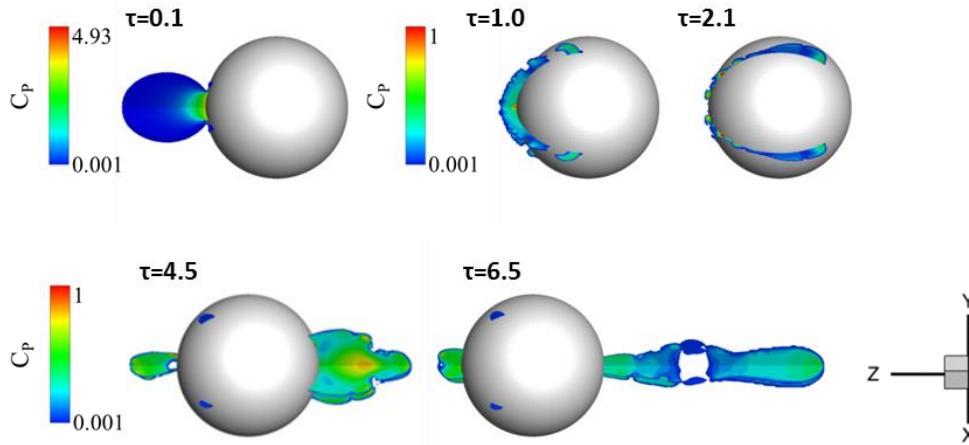


**Figure 3.41:** Temporal evolution of  $C_p$  for Case5 (DTP=0.62\_We=40) at slices  $x=0$  and symmetry plane  $y=0$ .

The liquid volume weighted velocity for the moderated and high DTP value cases 4-9 is presented in Figure 3.42. In Case4 the droplet rebounds from the solid particle, as it can be observed by the negative recoiling velocity, while in all other cases the droplet coats the solid particle. In cases 5,6 and cases 8,9, as We number increases, the average non-dimensional liquid velocity value follows a very similar trend, and towards the later stages of the phenomenon stabilizes at values around 0.5-0.8 of the impact velocity.

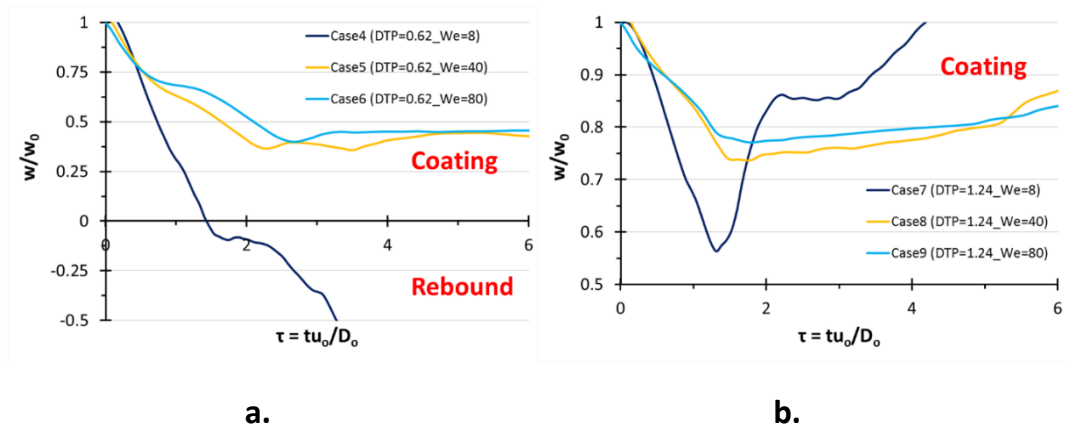


**Figure 3.42:** Effect of We number on the liquid phase mean velocity along the drop-particle axis ( $z$  direction) for a) cases 4-6 and b) cases 7-9.

### 3.4.4.3 Liquid film thickness

The liquid film thickness is another aspect of interest concerning the droplet-particle collision dynamics. In Figure 3.43a, the definition of the film thickness at the impact axis is presented, while Figure 3.43b-d shows the predictions for all cases examined. In the same Figure, phases 1 and 2 of the impact phenomenon are classified, based on [65]; the authors separate the temporal evolution of film thickness when a drop impacts a solid particle, in 3 phases, namely (a) the initial drop deformation phase, (b) the inertia dominated phase and (c) the viscosity dominated one.

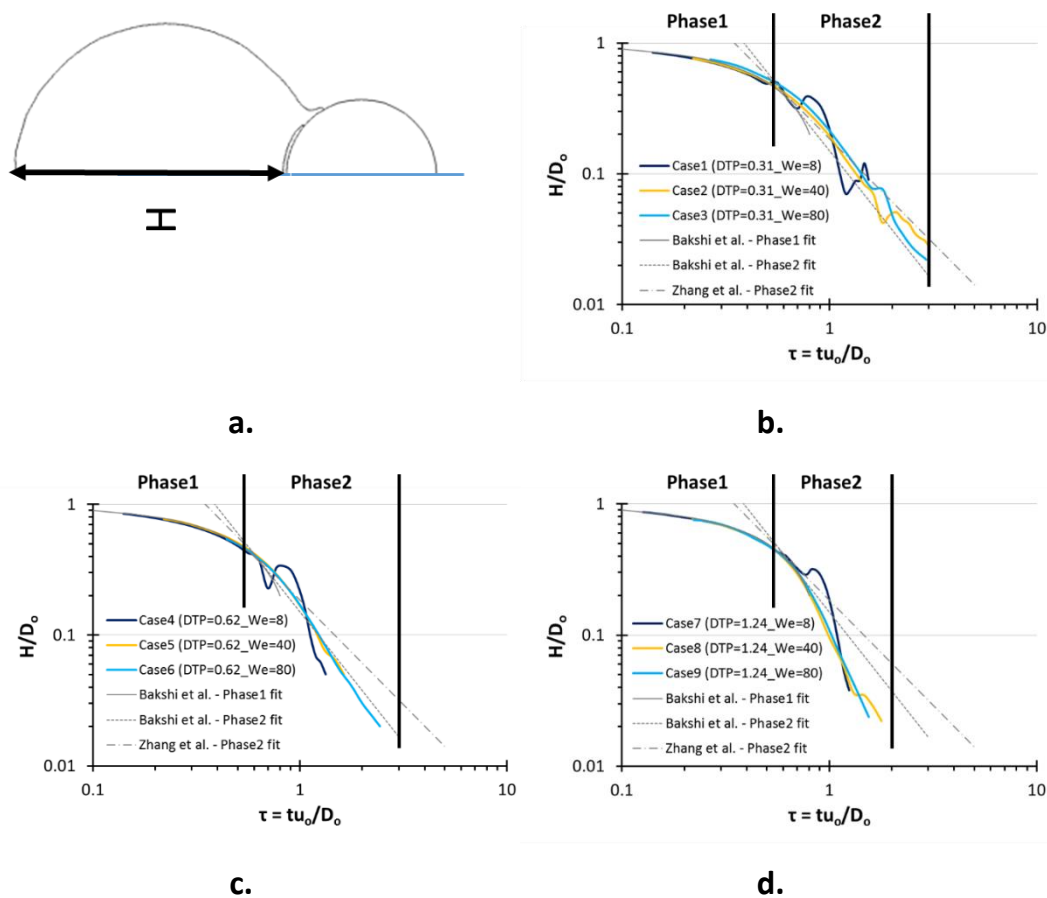


**Figure 3.43:** a) Definition of film thickness calculation at impact point, b, c, d) predicted non-dimensional film-thickness for cases 1-3, 4-6 and 7-9, respectively.

For phase 1, the fit proposed by [65, 187] given by the simple equation  $H/D_0 = 1 - \tau$  is shown. The current simulation results fit well with this correlation. For phase 2, the inertia dominated period, the correlation proposed by the experimental work [65] is  $H/D_0 = 1.5/\tau^2$ , while on the contrary, the LBM simulations of [187] indicated the relation  $H/D_0 = 1.85/\tau^{1.6}$ . In this work, it is shown that all film thickness curves follow a similar trend for

phase 2; however the slope of these curves varies with respect to the examined DTP value. For the lowest DTP value (0.31) examined in cases 1-3, the correlation given by Zhang et al. [187] gives the best fit. Increasing the DTP value to 0.62 in cases 4-6, a more steep decrease for liquid thickness is observed, which is closer to Bakshi et al. [65] fit. For the highest value of the DTP (1.24) in cases 6-9, phase2 is shorter, as it lasts for 2 units of non-dimensional time, while the slope is steeper than the one predicted by the aforementioned correlations. This is also shown in [65] (Figure 15 in their work), where the authors proposed different film thickness decrease slopes for different values of DTP using an analytical model for the prediction of the film flow. Their observations is thus justified in this work by using CFD analysis.

#### 3.4.4.4 Particle wetted area

Apart from the identification of the different collision outcomes, especially in the cases where coating is observed, the percentage of particle covered by liquid might be of interest. This investigation may aid engineering areas where maximization/minimization of contact between liquid droplets and solid particles is needed. In Figure 3.44, the effect of the We, DTP on the drop-particle wetting area is presented. Wetting area, is defined as the percentage of total particle area covered by liquid. This is calculated by:

$$wetted\ area = \frac{liquid\ area}{total\ area} = \frac{\sum_{wallf, \alpha > 0.5} \alpha \cdot A_{face}}{\sum_{wallf} A_{face}} \quad (3-14)$$

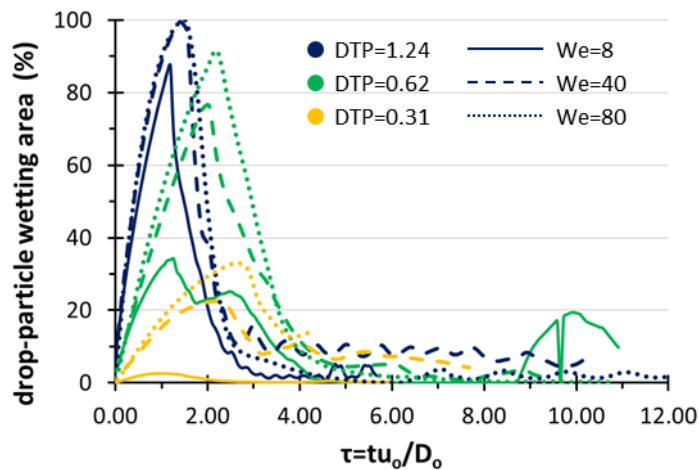


**Figure 3.44:** Temporal evolution of drop-particle wetted area coverage for cases 1-9 (We=8-80 and DTP=0.31-1.24).



As the particle gets smaller, i.e. DTP gets higher, particle coating gets more intense. For the smallest particle (DTP=1.24), the percentage of particle area, which is covered by liquid mass is above 80%, not only for very low, but also for moderate Weber number impacts. Therefore, high DTP values promote solid-liquid contact. Moreover, for these impacts (DTP>0.6, cases 4-9), it is observed that the total contact time is almost the same, regardless of the collision outcome. For lower DTP values, liquid-solid contact area is less. As it is shown in Figure 3.35, when colliding with large particles, the droplet rebounds just as it would do on a flat surface.

### 3.4.5 Conclusions

Based on the three-dimensional simulations, it is found that partial or full droplet rebound is promoted with very low We number and DTP values. As these values are increased, coating of the particle is favoured. Moreover, it is shown that for high Weber number values (>40) and low DTP values (<0.62) the mean velocity of the liquid mass that leaves the particle after its coating is between 0.5-0.8 times the droplet initial impact velocity.

## Chapter 4

# Single droplet-particle collisions in FCC injection zone

### 4.1 Introduction

In this Chapter, the developed and validated CFD model is employed to investigate different collision scenarios of a single droplet impinging onto a catalytic particle at conditions relevant to the injection zone of a typical FCC reactor. The operating conditions, as well as the physical properties of the fluids involved are chosen in such a way to resemble the realistic FCC conditions. Moreover, the inclusion of “cracking” reactions at the particle surface allows the examination of both the hydrodynamics as well as the chemical yield of collisions, and how these interact.

#### 4.1.1 Cracking Reactions

The basic principles of how catalytic cracking reactions are accommodated at the pores of the solid catalysts are presented in the textbook of Froment and Bischoff [67] and shown schematically in Figure 4.1. Initially, the reactants (heavy molecular weight gaseous species) are transported from the main stream to the catalyst surface, and then those that are small enough to fit, get inside the pores up to a catalytic site. There, the chemical reaction of cracking takes place, and afterwards the lighter weight products follow the same route in the opposite direction towards the particle surface and the gas stream. Catalysts act in a way like “molecular sieves”, blocking outside the large molecules and selectively picking to crack below a certain molecular size, as it is shown by a recent patent assigned to Exxonmobil Research And Engineering Company (with number US8513150 [1]) that concerns solid zeolite catalyst mesoporosity.

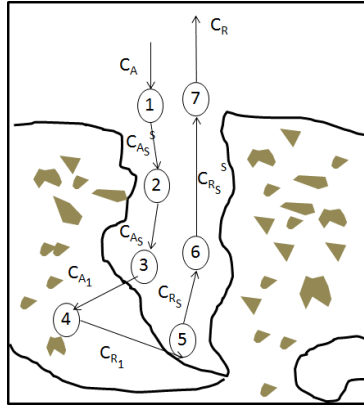


**Figure 4.1:** Steps of catalytic cracking reaction.

In the scope of the present study, however, the catalytic reactions can only be regarded from a wider perspective, meaning that the particle surface is represented by a spherical homogenous surface discretized by a finite number of faces, i.e. without discretizing the exact porous geometry. This is incorporated implicitly via the variable “SSA”, which stands for catalyst “Specific Surface Area”, given in  $\text{m}^2$  per catalyst weight, a typical value that characterizes porous solids. Reaction rate and kinetic constant  $k$  are given by the following expressions [188]:

$$RR' = \frac{RR}{SSA} \quad (4-1)$$

$$RR = k[X]^2 \quad (4-2)$$

$$k = Ae^{(-E_a/R_gT)} \quad (4-3)$$

, where the  $X$  in brackets is the molar concentration of the reactant. Following the SSA assumption, the wall area at each boundary particle cell represents the real pore area available for catalytic cracking reactions.

A simple 2-lump scheme is used to represent the cracking reactions that take place in the domain of interest, i.e. the single reaction of gasoil gas cracking at the surface of the catalyst to produce gasoline gas, is accounted for. The general overview of the path that the liquid gasoil follows throughout its collision with a catalyst is presented in Figure 4.2. Reaction rate kinetics are taken from [188], and are presented in Table 4.1.

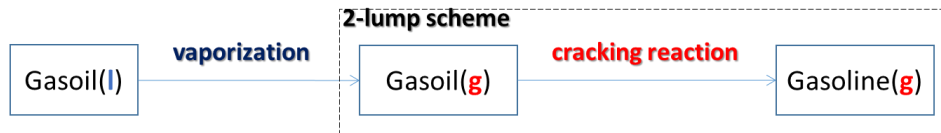


**Figure 4.2:** Cracking path used in this work. From gasoil liquid to gasoline gas.

Variable	Value
A	$0.4272e+13 \text{ m}^6 / (\text{kmol} \cdot \text{kg}_{cat} \cdot \text{s})$
$E_a$	21009.9 cal/mol
SSA	269 $\text{m}^2/\text{g}$

**Table 4.1:** Cracking reaction kinetics (pre-exponential factor, activation energy and SSA) taken from [188] for gasoil to gasoline reaction.

This 2-lump scheme acts as a first step towards the identification of how much may the micro-scale hydrodynamics affect the catalytic cracking yields, as well as the pore blocking mechanism. This coupling of single droplet-particle collision dynamics with the cracking surface reactions is realized for the first time in this study. The use of more elaborate lump schemes (4-12 lumps) as presented in Chapter 1, where more gas species are used in the mixture (LPG, light gases, coke) is not needed at this point, as it would rise the complexity of the problem without any significant conclusion that can be drawn. Moreover, minding the scales for droplet-particle collision dynamics (ms), coke formation is a reaction of higher time scales (s) and depends on residence time [4, 5, 10], thus the coke lump does not apply for the purposes of this PhD.

In numerical terms, in order to include this reaction mechanism, the additional transport of gasoline lump specie equation is solved (similar to Eq. 2-13), with the surface reaction boundary condition (Eq. 2-23).

#### 4.1.2 Liquid/Gas Properties

For the gasoil and gasoline lumps, the physical properties varying with temperature of n-pentacosane ( $\text{C}_{25}\text{H}_{52}$ ) and n-heptane ( $\text{C}_7\text{H}_{16}$ ) chemical species are used as representative of the fluids that appear in FCC (properties taken from [168, 189-191]). For petroleum fractions, the properties are typically calculated based on empirical correlations [192], and the uncertainty that arises from the use of these functions, as well as the range where these are valid, in contrast to single component hydrocarbons [189] where the properties values are given in a more straightforward fashion, is the key reason for this choice. The criteria for the choice of n-pentacosane and n-heptane are the

molecular weight and liquid density, based on values gathered from relevant works [4, 5, 7-11, 13, 14], for gasoil,  $MW_{lit}=226-450$ ,  $MW_{C_{25}H_{52}}=352.691$ ,  $\rho_{lit}=610-924.8$ ,  $\rho_{C_{25}H_{52}}=801.16$ , while for gasoline,  $MW_{lit}=100-117.8$ ,  $MW_{C_{7}H_{16}}=100.205$ .

The use of single component species to represent petroleum fractions has been also presented in another work [193], where a thermodynamic evaluation of the FCC reactor is performed. The fluidizing medium is considered to be water-vapor ( $H_2O$ ), commonly used in the FCC industry.

The physical properties used [168, 189, 190] refer to conditions of 101,325 Pa pressure, while the diffusivity concerns hydrocarbon-air mixtures. It is assumed that these properties do not change significantly for the operating conditions of the cases simulated in this study, referring to a 202,650 Pa operating pressure, where water vapour is the surrounding gas, as can be seen from the empirical work of [194] or similar ones.

## 4.2 Cases studied

The validation of the phase change CFD model for its use in this Chapter is presented in Appendix C. In this section, a parametric investigation on droplet-particle collision scenarios is presented. Table 4.2 presents the default operating conditions of the FCC injection zone used in all runs, while in Table 4.3, the simulation cases are presented, along with the main parameters studied, namely impact Weber number and particle temperature. All values are based on the literature review presented in Section 1.3.1

$p_{op}$ (Pa)	$T_0$ (K)	$T_g$ (K)	$D_p$ ( $\mu m$ )	$\theta$ ( $^\circ$ )
202,650	550	800	75	100

**Table 4.2:** Default operating conditions for all cases.

Case No.	DTP	$U_0$	$T_p$	We	Re	locRef
1	1	15	800	4266	2272	3
2	1	15	1000	4266	2272	3
3	1	30	800	17,062	4544	3
4	1	30	1000	17,062	4544	3
5	2	15	800	8531	4544	2
6	2	15	1000	8531	4544	2
7	2	30	800	34,124	9088	2
8	2	30	1000	34,124	9088	2

**Table 4.3:** Cases investigated for single droplet-particle collisions in FCC reactor injection zone.

Droplet impact velocity represents the relative velocity between liquid droplets-catalytic particles near the injection area. The impact velocity, takes two different values, i.e. 15 and 30 m/s, which represent low and moderate impact energy collisions. The particle temperature ranges between 800K and 1000K, which covers the entire spectra of catalyst temperatures inside the bed, from their inlet till steady-state condition has been established. The droplet to particle size ratio (DTP) is set equal to either 1 or 2, thus representing two typical injected droplet sizes selected from the range calculated from Chapter 1 (DTP= 0.67 – 6.67). Investigation of DTP values higher than two is out of the scope of the present work, as all collisions of this type are expected to lead to coating, and thus simpler models compared to the current CFD one may be used for the quantification of solid-liquid contact time, droplet deformation and gasoline yields.

The Weber number in all cases is extremely high, as the surface tension coefficient in such conditions (high temperature) is very low. Contact angle is assumed to take a value of 100° degrees. To the best of author’s knowledge no experimental values regarding the contact angles of heavy hydrocarbons on catalytic particles were tracked in the open literature. Nevertheless, its effect on the numerical results, for the range of conditions examined (drop levitation) is regarded to be small. It becomes significant only for the cases where direct liquid-solid contact is predicted.

### 4.3 Numerical domain

The 2D axisymmetric computational domain which is employed for the cases presented above, along with the applied boundary conditions, is presented in Figure 4.3.

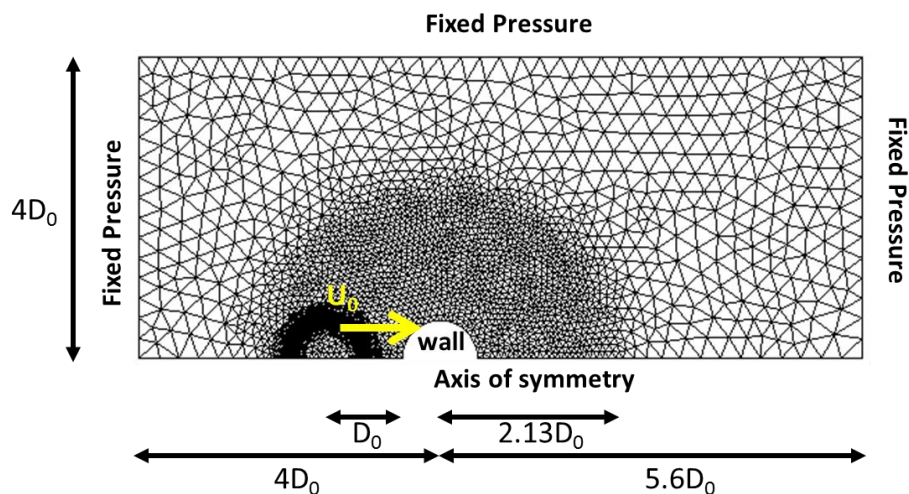


Figure 4.3: Computational domain used for the simulated cases.

Apart from the symmetry axis, in all other boundaries a fixed pressure ( $p_{op}$ ) is applied, while the particle is assumed to be stationary and is represented by wall boundary condition. In reality, when the droplet impinges onto the moving particle, momentum is transferred. This momentum exchange is neglected in this Thesis, as this would require not only the use of more complex models to capture the simultaneous motion of the solid particle (such as rigid solid body motion with mesh deformation, the Immersed Boundary Method or other) but also would add the direction of impact as an additional variable.

Concerning the mesh, triangular cells are used so as to retain the same cell size in the region where the droplet moves. The semi-circular circumference of the particle is split into 40 divisions in order to capture the circular geometry, which results in a cell width of  $5.89\mu\text{m}$  in the initial coarse grid. The same size is used in all cells inside the circular zone with dimensions shown in Figure 4.3, while in the rest of the domain the cell width is approximately  $20\mu\text{m}$ . The numerical settings for the single droplet-particle collision cases are given in Table 3.8.

Parameter	Value
Courant	0.25
Coarse wall discretization	40 divisions
Grid size (cells)	$\sim 14,000$ (DTP1) - $22,000$ (DTP2)
Locref distance	14 cells
cpR	51 (locRef3 for DTP1, locRef2 for DTP2)

**Table 4.4:** Numerical settings for the single droplet-particle collisions in FCC case.

A relatively low cpR value of 51 is chosen so that apart from 2D simulations, 3D simulations may be as well feasible, as is shown in Chapter 5. This value is enough to capture the levitation of the droplet on the hot-reacting particle surface, where the gas layer is resolved by 1-2 cells. This is shown in more detail in the next section (CFD Results).

The gasoil gas mass fraction is initialized following a simple function:

$$Y(\tilde{r}) = 1 - (1 - Y_{sat}(T_0)) \left( \frac{1}{1 - Y_{sat}(T_0)} \right)^{1-1/\tilde{r}}, \quad \tilde{r} = \text{MAX}(r/R_0, 1) \quad (4-4)$$

, where  $\tilde{r}$  is the normalized distance of each cell from droplet center. The interface is saturated ( $Y_{sat}$ ) based on the initial droplet temperature, while at infinity, the mass fraction reaches zero. A contour of the initial gasoil gas mass fraction is presented in Figure 4.4.

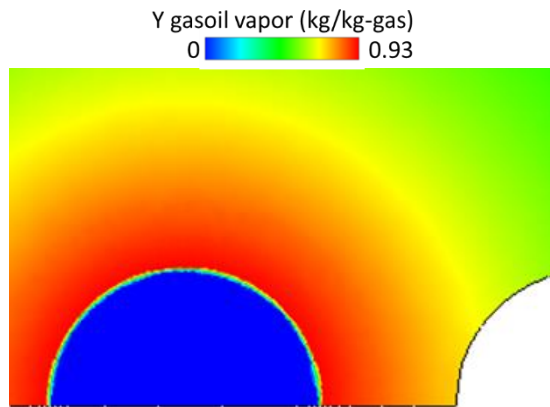


**Figure 4.4:** Gasoil gas mass fraction initialization.

This initialization function is employed in order to diminish numerical instabilities which were observed at the initial time steps of the simulation. For the initial conditions of these cases (high  $\Delta T = T_g - T_0 = 250\text{K}$ ,  $T_0 = 550\text{K}$  close to  $T_b = 629\text{K}$ ), intensive evaporation rate is calculated based on the local evaporation model until the interface reaches saturation. This initial intensive evaporation was seen to affect the local velocity field at the interface which finally diverges. The initial gasoil gas distribution is therefore required. Based on numerical tests performed, the initial function or constant value prescribed in the gasoil gas field does not affect the total gasoline yield which is formed at the end of the simulations.

## 4.4 CFD results

All results are presented in non-dimensional form, so that the comparison among all cases is direct and general conclusions can be drawn. Non-dimensional time  $\tau (=tu_0D_0)$  is set to zero at the time instant of impact.

### 4.4.1 Equally sized droplet-particle collisions, $DTP=1$

#### 4.4.1.1 Droplet deformation

In Figure 4.5, the evolution of droplet shape during the impingement process is depicted for cases 1 (top) and 3 (bottom), while in Figure 4.6 the same results are presented for cases 2 and 4. In these Figures low velocity impact cases (top) are separated



from high impact velocity ones (bottom) by the symmetry axis. The corresponding contour of the produced gasoline lump mass fraction is also shown.

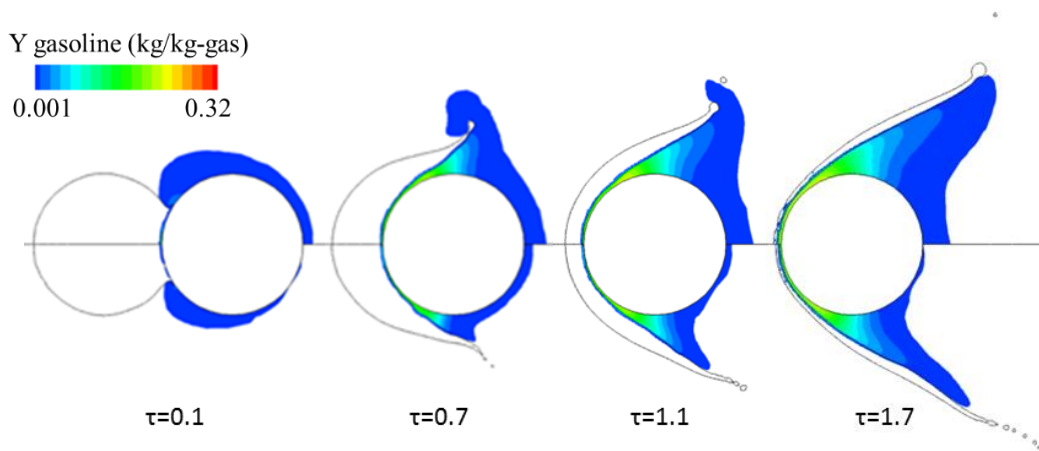


**Figure 4.5:** Effect of impact velocity on collision outcome for wall temperature 800K, Case1 (top), Case3 (bottom). Contour of the produced gasoline mass fraction (kg-gasoline/kg-gas).

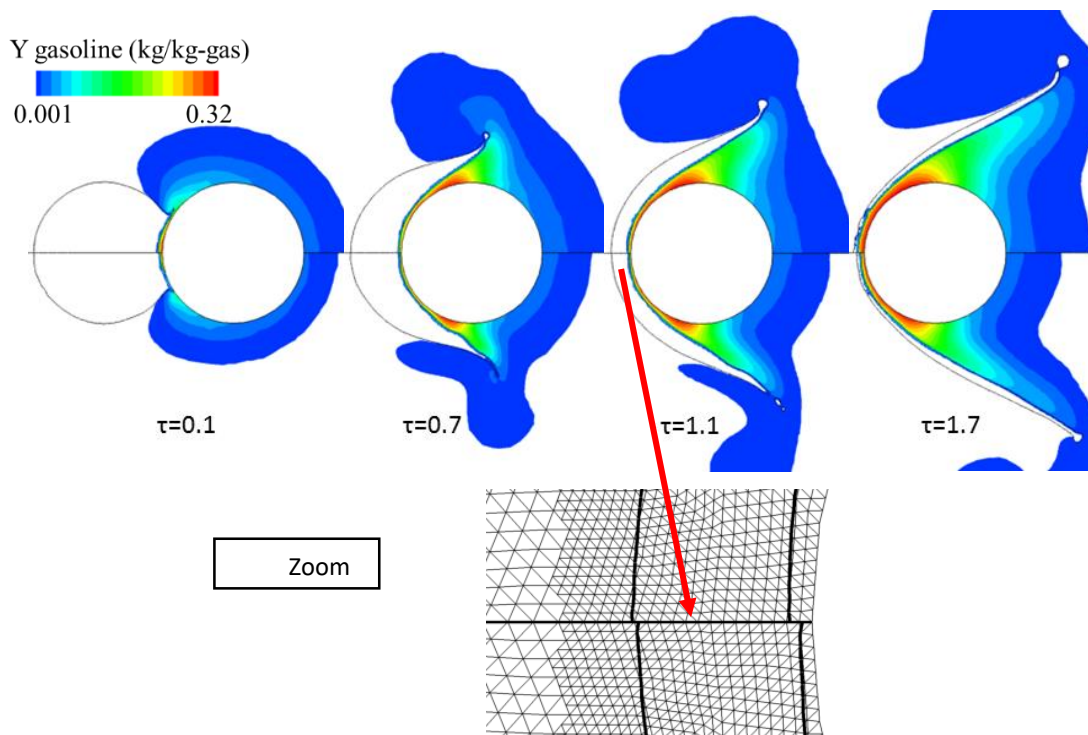


**Figure 4.6:** Effect of impact velocity on collision outcome for wall temperature 1000K, Case2 (top), Case4 (bottom). Contour of the produced gasoline mass fraction (kg-gasoline/kg-gas). Close up to the resolved gas layer cell thickness.

By firstly comparing Figure 4.5 and Figure 4.6, it is observed that the effect of temperature on the final hydrodynamic outcome of the whole phenomenon is minor, meaning that in all Cases 1-4, the droplet impacts the solid particle ( $\tau=0.1$ ), then deforms

as it moves along the particle periphery ( $\tau=0.7$ ), and forms a liquid sheet that moves away from the particle surface ( $\tau=1.1$ ). In other words, the macroscopic result of collision under different impact velocities in the range of 15-30 m/sec remains almost the same, irrespective of the catalytic particle temperature.

This liquid sheet becomes very thin ( $\tau=1.7$ ) and finally ( $\tau>2$ ) breaks up into numerous satellite droplets (torous shapes for 2D simulations), as shown in Figure 4.7 for Cases1-4. The main results are presented for dimensionless time below  $\tau=2$ , because the 2D axisymmetric simulations cannot predict break-up phenomena such as the ones presented in Figure 4.7, therefore this Figure serves only for revealing that after  $\tau=2$ , the deformed liquid sheet is expected to break-up into numerous satellite droplets. In Chapter 5, results for 3D simulations are compared against the ones shown at this point, revealing the break up mechanisms.

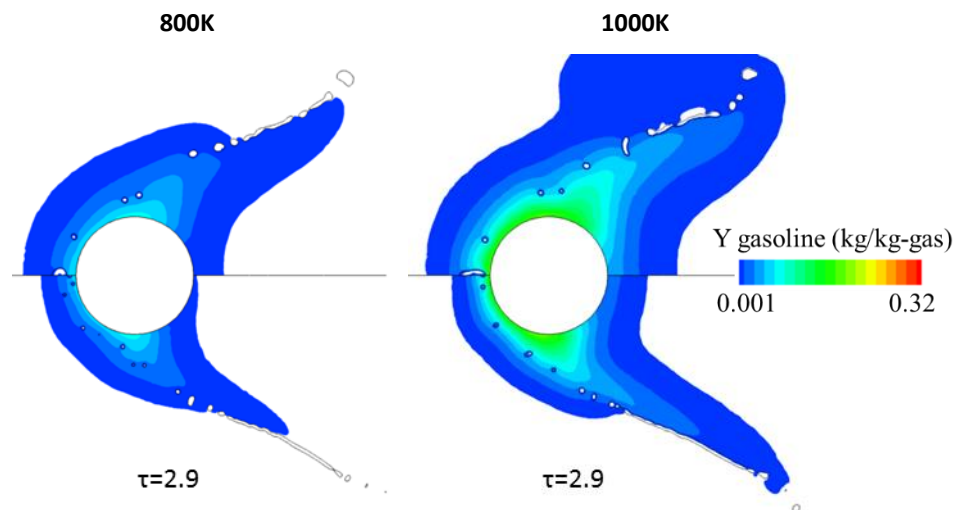


**Figure 4.7:** Breakup of the liquid sheet for cases 1-4. Case1 (up-left) - Case2 (up-right) – Case3 (bottom-left) – Case4(bottom-right). Contour of the produced gasoline mass fraction (kg-gasoline/kg-gas).

#### 4.4.1.2 Effect of impact velocity and temperature on gas layer thickness

Focusing now on the effect of impact velocity on the collision outcome, apart from small changes observed in the liquid sheet thickness and shape, significant differences are observed in the formed gas layer thickness that levitates the droplet in all cases 1-4. This gas layer is formed due to high evaporation rates and is reinforced by an upward gas motion induced by temperature gradient (hot catalyst) and density gradient (light gasoline production) resulting in pushing the droplet away. In Figure 4.8b, the non-

dimensional gas layer thickness is plotted against the non-dimensional time of the impingement phenomenon for cases 1-4.

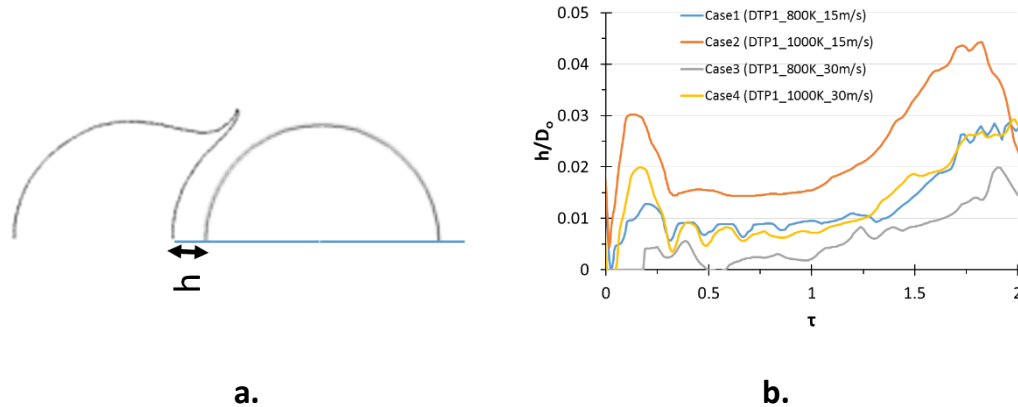


**Figure 4.8:** a) Definition of the vapour layer thickness at the impact point, b) Temporal evolution of the vapour layer thickness at the impact point for cases 1-4.

For the same catalyst temperature, as the kinetic energy of impact gets higher, the gas layer is more difficult to form since the drop momentum is higher (see Figure 4.6 zoom view), thus the smaller values observed in Figure 4.8. Additionally, as the catalyst temperature increases, for the same impact velocity, the cracking reaction is promoted through Arrhenius kinetics (Eq. 4-3), thus more gasoline is produced which poses a greater burden to the droplet coming in contact with the catalyst, justifying the thicker gas layer presented in Figure 4.8. The significant parameters that affect the thickness of the gas layer and thus the space provided for the catalyst to be active in cracking terms are the initial drop kinetic energy, viscous dissipation and the catalyst temperature. Moreover, from the CFD results it is observed that after the droplet impacts the catalytic particle, for a significant period of time ( $\tau < 0.5$ ), the drop initial kinetic energy pushes the droplet forward, while the evaporation of gasoil vapor and the formation of gasoline try to push it away. This back and forth motion is clearly seen in Figure 4.8 in the initial ( $\tau < 0.5$ ) perturbations of the gas layer thickness, while also in Figure 4.5 and Figure 4.6, at  $\tau = 0.7$ , it is observed that for the high impact velocity cases, the formation of (wavy like) perturbations, located at the inner surface of the liquid sheet, are clearly seen. These perturbations, as will be shown in Chapter 5, are numerical artefacts that are eliminated when the same case is solved in 3D domain.

Overall, in all cases (1-4), the gas layer thickness stabilizes for  $\tau > 0.5$  at a value of approximately 0.8-1.5% of the initial droplet diameter, i.e. in absolute values 0.6-1.125 $\mu\text{m}$  (resolved by 1-2 numerical cells, as shown in Figure 4.6). In Case3, the droplet initially touches the catalyst. The initial perturbation of the liquid phase imposed by this contact,

is expected to cause the earlier breakup of the formed lamella; this is evident by comparing Figure 4.5 (bottom) to Figure 4.6 (bottom), corresponding to Case4. The only difference between these cases is the particle initial temperature (800 vs 1000K) which does not influence the droplet mean temperature (maximum temperature difference of 1K between cases 3,4 depicted in Figure 4.15); therefore the droplet properties (surface tension, viscosity etc) do not change significantly and subsequently the initial droplet-catalyst contact can be held responsible for the earlier breakup. The gas layer formed justifies the comments of [10, 20] that film boiling regime is the principal regime of FCC operation.

#### 4.4.1.3 Induced Vortex rings

Another interesting aspect that is observed and is shown schematically in Figure 4.9 are the vortex rings induced at the vicinity of the expanding lamella rim, one on the top of the liquid sheet (outer ring) and a second one on the bottom (inner ring), expanding up to the particle wake region, during the impact. In this Figure, the gasoil vapour mass fraction is also presented. For higher initial drop kinetic energy (Figure 4.9b), the inner vortex ring bends slightly the deforming liquid sheet towards the catalytic particle. In general, as the axial momentum of the droplet overweighs the upward motion, the liquid sheet stays closer to the particle (Figure 4.5 for dimensionless times of 0.7 and 1.1).

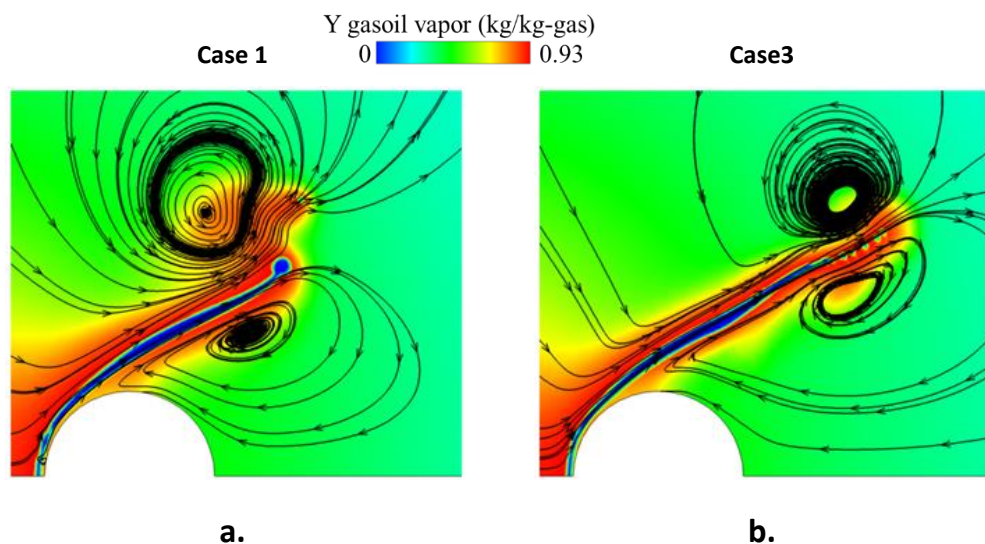


**Figure 4.9:** Vortex rings formed during impingement for a) Case1 (low impact velocity) and b) Case3 (high impact velocity) for wall temperature 800K at  $\tau=1.7$ . Figures coloured with gasoil vapour mass fraction (kg-gasoil vapour/kg-gas, blue colour denotes zero gasoil vapor, i.e. pure liquid phase).

#### 4.4.1.4 Cracking Yields

In Figure 4.10 the percentage of gasoil converted to gasoline, as well as the total reaction rate, i.e. the total number of moles of gasoline generated per second throughout the process are presented.

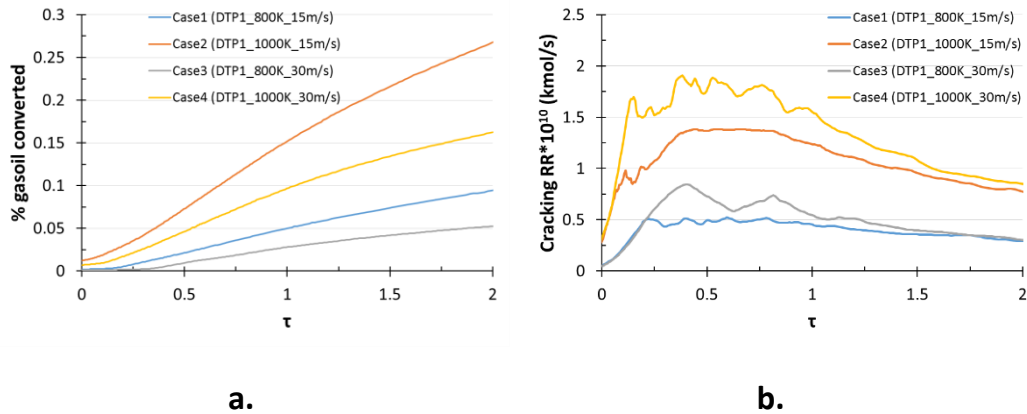


**Figure 4.10:** a) Percentage of gasoil converted to gasoline yield (kg-gasoline/kg-liq %) and b) cracking reaction rate, both plotted against non-dimensional time for cases 1-4.

It is clear that the high catalyst temperature impacts outweigh the low catalyst temperature ones in both diagrams as was clearly observed in Figure 4.5 and Figure 4.6. This is due to the thicker gas layer, which results from higher reaction kinetics. The resulting higher gas layer thickness offers more space for reactions to occur and promotes the production of higher gasoline yields. It is important to notice the total gasoline yields are 2.5-3 times higher for high catalyst temperature catalysts (Figure 4.10a).

Focusing now on the effect that the impact velocity has over the total yield of gasoline lump specie, a very interesting phenomenon is observed. Given the same catalyst temperature, although the cracking reaction rate is higher for the high impact velocity cases, the total gasoline yield is lower, which is again explained by the gas layer thickness differences between these cases (lower impact kinetic energy results in thicker layer). Moreover, the real contact time for the low impact velocity cases is much higher, thus higher gasoline yields are expected. As a matter of fact, low impact velocity promotes yield by 1.5-2 times, in comparison to high impact velocity ones.

## 4.4.2 Double sized droplet-particle collisions, DTP=2

### 4.4.2.1 Droplet deformation and gas layer thickness

The results for the double sized droplets are presented in Figure 4.11 and Figure 4.12 for cases 5,7 and cases 6,8 respectively. Overall, similar trends to the DTP=1 cases 1-4 are observed, meaning the droplet deforms into a liquid sheet that tends to move away from the particle surface. In high impact velocity cases 7 and 8 the liquid mass is entrained by the inner vortex ring, resulting in its sucking inside the wake region of the catalytic particle (downstream the catalyst), towards the symmetry axis.

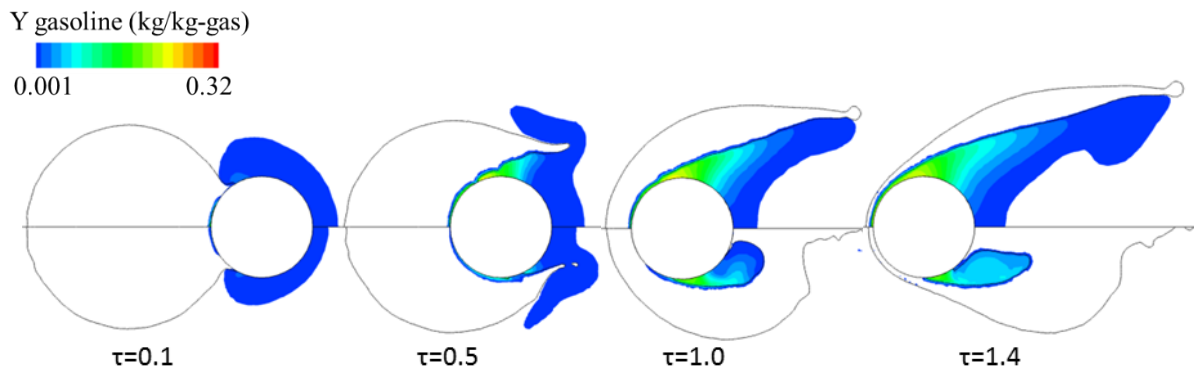


**Figure 4.11:** Effect of impact velocity on collision outcome for wall temperature 800K, Case5 (top), Case7 (bottom). Contour of the produced gasoline mass fraction (kg-gasoline/kg-gas).

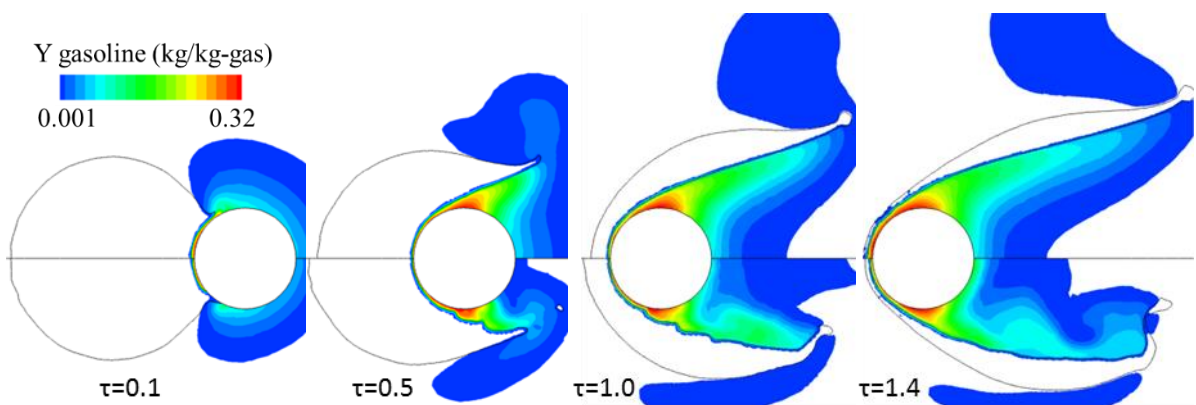


**Figure 4.12:** Effect of impact velocity on collision outcome for wall temperature 1000K, Case6 (top), Case8 (bottom). Contour of the produced gasoline mass fraction (kg-gasoline /kg-gas).

More specifically in Case7, where liquid accumulates at the symmetry axis, it can be doubted if the form liquid shape is representative of real conditions, since three dimensional effects occur. This is investigated in Chapter 5. The perturbations on the inner

side of the liquid sheet are visible both for low impact velocity Case5 ( $\tau=0.5$ ), as well as for high impact velocity Case8 ( $\tau=0.5$ ).

When the droplet is bigger, its initial kinetic energy is higher than the smaller one, which limits the formed gas layer thickness. This is observed in Figure 4.13, where the temporal evolution of the vapour layer thickness size is presented for cases 5-8.

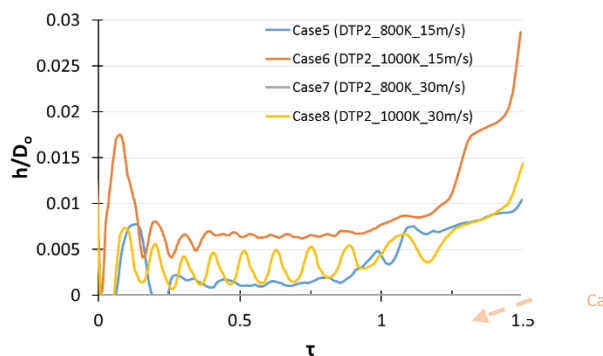


**Figure 4.13:** Temporal evolution of vapour layer thickness at impact point for cases 5-8.

It is evident that now the non-dimensional vapour layer thickness stabilizes at a smaller value than in cases 1-4, i.e. around 0.2-0.6% of the initial droplet diameter, a value of approximately 0.3-0.9 $\mu\text{m}$  (resolved by almost 1 cell). In Case7, which is the worst case scenario in terms of yield efficiency (low catalyst temperature and high drop kinetic energy), the droplet is in direct contact with the particle throughout the whole collision phenomenon. Such conditions occur within the injection zone of industrial FCC reactors, owed to the fact that liquid droplets are mostly characterized by high DTP values [10, 13, 16] and high velocities, resulting in long contact times with the catalytic particles, and subsequent higher probability of liquid-pore blocking and catalyst deactivation, which is a phenomenon experienced in industrial scales [3].

#### 4.4.2.2 Cracking Yields

Finally, the results for the gasoil conversion, as well as total reaction rate of cracking for cases 5-8 are presented in Figure 4.14. Similar trends are observed for all four (4) examined cases. The reaction rate values for cases 5-8 are higher than the corresponding of cases 1-4, while in contrast the percentage of gasoil converted is much lower. The higher reaction rates are attributed to the higher coverage of particle area in the case of double sized droplet, while the lower conversion is owed to higher liquid mass which is used to non-dimensionalize the gasoil conversion yield.

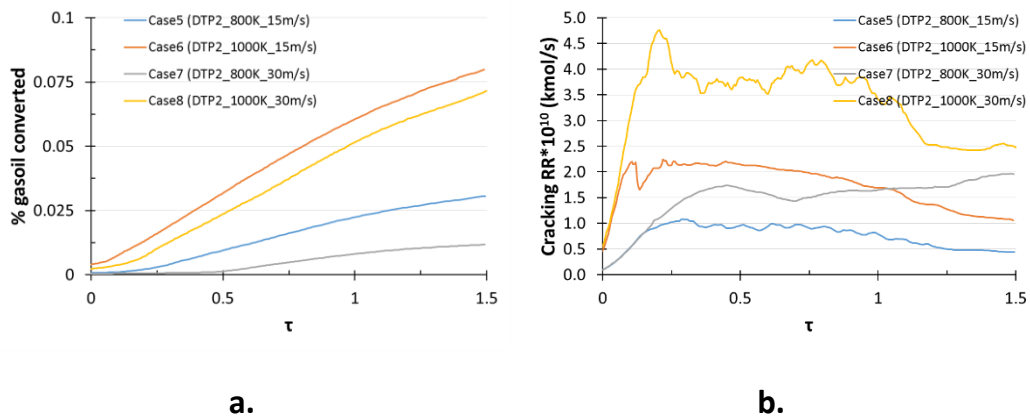


**Figure 4.14:** a) Percentage of gasoil converted to gasoline yield (kg-gasoline/kg-liq %) and b) cracking reaction rate, both plotted against non-dimensional time for cases 5-8.

#### 4.4.3 Global Performance of the model

What matters in most large scale models, concerning the outcome of droplet-particle collisions, is the state the droplet will be after it hits a particle. In Figure 4.15, the droplet mass, as well as the average droplet temperature are plotted against time. In an FCC reactor, a droplet after its collision with an equally sized particle loses up to 5% of its initial mass, while for double sized droplets the decrease is in the range of 2%. After the breakup of the liquid sheet into secondary droplets, for a non-dimensional time higher than 2, the liquid mass decrease is expected to be higher. It should be pointed out that the droplet mass loss in the cases with DTP=2, when expressed in (kg), is much larger when compared to cases with DTP=1, since in the former cases the droplet volume is 8 times higher than the latter ones. The temperature of the liquid that is travelling downstream the catalytic particle, is almost constant (decrease less than 2.5K) during the whole evolution, owed to high evaporation rates, which tend to keep the droplet temperature at a constant temperature state. In Case7 particularly, due to the direct contact between drop-particle the mean droplet temperature is expected to rise, as shown in Figure 4.15b.



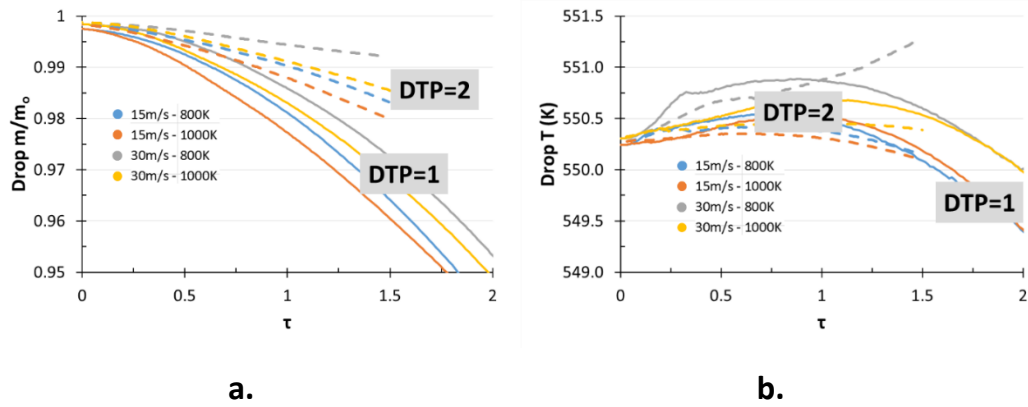


**Figure 4.15:** Droplet a) mass and b) temperature evolution for all cases, (solid lines-DTP1, dashed lines-DTP2).

The direction that the liquid mass will follow after its collision can be found by the drop maximum radial deformation, which is presented in Figure 4.16 for all cases examined (DTP=1, 2). It is evident that for high velocity and double sized droplet impacts, the remaining liquid mass will in fact stay closer to the drop-particle axis. As for Case7 in particular, the droplet will perform a “copy” impingent, meaning it will impact the following catalytic particle downstream with almost a spherical shape, as depicted in Figure 4.11,  $\tau=1.4$ . A  $D_y/D_0$  limiting value equal to around 1.25, differentiates “copy-impingement” from skirt-sheet formation, as it was named in the work of Gac and Gradon [19].

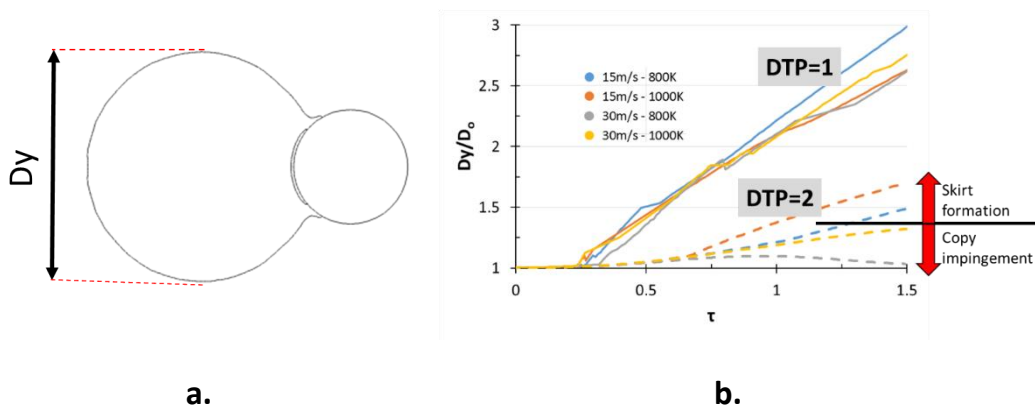


**Figure 4.16:** a) Definition of drop maximum radial deformation, b) Temporal evolution of the maximum radial deformation for all cases 1-8 (solid lines-DTP1, dashed lines-DTP2).

The mass weighted mean drop velocity is also very important. In Figure 4.17 it is shown that for DTP=1, the post impact secondary droplets will have approximately 75% of their parent droplet impact velocity, while for DTP=2, either the secondary droplets or the “copy” one will move at 90-95% of their parent droplet impact velocity.

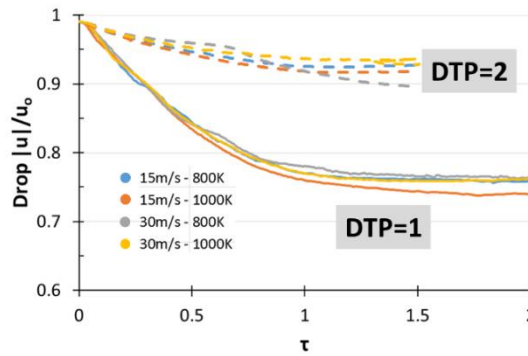


**Figure 4.17:** Droplet mass weighted velocity non-dimensionalized with impact velocity for all cases 1-8, (solid lines-DTP1, dashed lines-DTP2).

In Figure 4.18, the liquid film height for all cases simulated (cases 1-8) at the impact point on the symmetry axis is presented. The similarity in the trend of all lines reveals the dimensionless character this quantity follows during such type of impingements, as is also stated in isothermal works presented in Chapter 3 and in [65, 187].

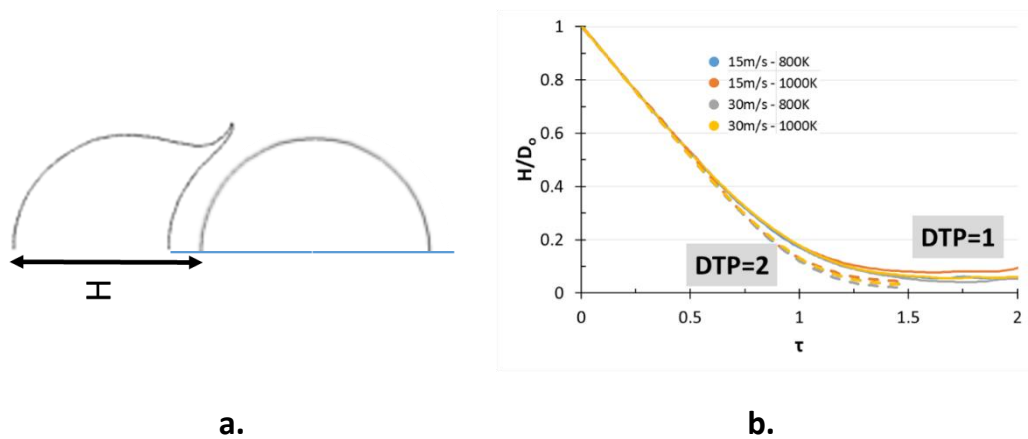


**Figure 4.18:** a) Definition of liquid film thickness, b) Temporal evolution of the non-dimensional liquid film thickness for all cases 1-8 (solid lines-DTP1, dashed lines-DTP2).

## 4.5 Conclusions

Based on all cases simulated, where the interest is turned towards limiting the possibility of liquid pore blocking and improving gasoline yields, Case7 was found to represent the worst case scenario. The operating conditions of this case are actually the most commonly found in current FCC operating units. On the other hand, Case2 acts as the best case scenario. Additionally, a further finding of this study is that gasoil conversion can be well linked with the direct solid-liquid contact which in our case is estimated by the predicted gas layer thickness formed in between the impacting droplet and the

catalyst. It was observed that as the temperature of the catalyst increases or the initial drop kinetic energy decreases, the gas layer is formed more easily, and therefore the possibility of liquid pore blockage decreases. Another way to estimate solid-liquid contact would be to measure the percentage of wall area which is actually covered in liquid as in Section 3.4.4.4. Finally, the best/worst case scenarios refer only to the operating conditions investigated.

The present model can be further applied for simulating additional range of values for the parameter of DTP (higher values actually appear in industry), which is an important controlling physics variable in terms of catalyst pore blockage mechanism and catalyst deactivation. Further numerical developments that can be made include the inclusion of momentum exchange between droplet/catalyst during collision and the investigation of the exact porous geometry.

## Chapter 5

# 3D droplet-particle cluster collisions in FCC injection zone

### 5.1 Introduction

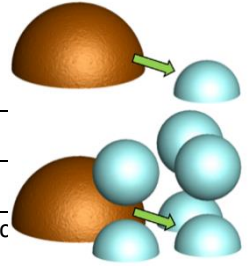
The context of this Chapter follows up the work presented in the previous one. Droplet-particle collisions simulated using 2D axisymmetric domains are extended to three-dimensions. Comparison between 2D/3D predictions is performed, while break-up mechanisms are investigated as well. Then, droplet impact onto a catalyst particle cluster is simulated, in an effort to examine real FCC collision dynamics and compare the hydrodynamic outcome, gas layer formed and cracking yields against the single droplet-particle collisions.

### 5.2 Cases studied

The simulations conducted in this Chapter are presented in Table 5.1. Firstly, three cases for single droplet-particle collisions are presented, exhibiting the same operating conditions as the corresponding 2D ones, in order to evaluate the efficiency/robustness of the 3D model, as there are no similar works to compare in literature, and additionally investigate the 3D flow details. The cases selected to serve for this verification represent two cases of  $DTP=1$ , where the effect of impact velocity is examined (Case2\* to Case4\*, 15m/s to 30m/s) and one of  $DTP=2$  (Case7\*) for the evaluation of  $DTP$  effect on the phenomenon evolution. Cases 2\* and 7\* additionally represent the best/worst case scenario in terms of gasoline yield production, based on the results presented in the previous Chapter. The enumeration of the cases is in correspondence to the 2D ones, using the multiplication symbol (example, Case2 in 2D becomes Case2\*).

Case No.	DTP	$U_0$ (m/s)	$T_p$ (K)	We	Re	locRef
3D Single droplet-particle collision						
2*	1	15	1000	4266	2272	3
4*	1	30	1000	17,062	4544	3
7*	2	30	800	34,124	9088	2
3-D Single droplet-particle cluster collision						
9	2	30	1000	34124	9088	2

**Table 5.1:** Cases investigated for droplet-particle/particle cluster collision in injection zone.



The final case presented in Table 5.1 represents the impact of a single droplet onto a particle cluster. As catalyst to oil ratio is high (Chapter 1), a droplet is expected to collide with many particles along its motion. Only one cluster formation scenario is simulated; the operating conditions of this scenario correspond to a realistic/representative collision situation which can be found in FCC reactors.

### 5.3 Numerical domain

The computational domain used for the case of single droplet-particle collision cases is depicted in Figure 5.1. For cases 2\* and 4\*, the total dimensions of the domain are similar to the 2D axisymmetric domain, which is actually shown as a slice in Figure 5.1.

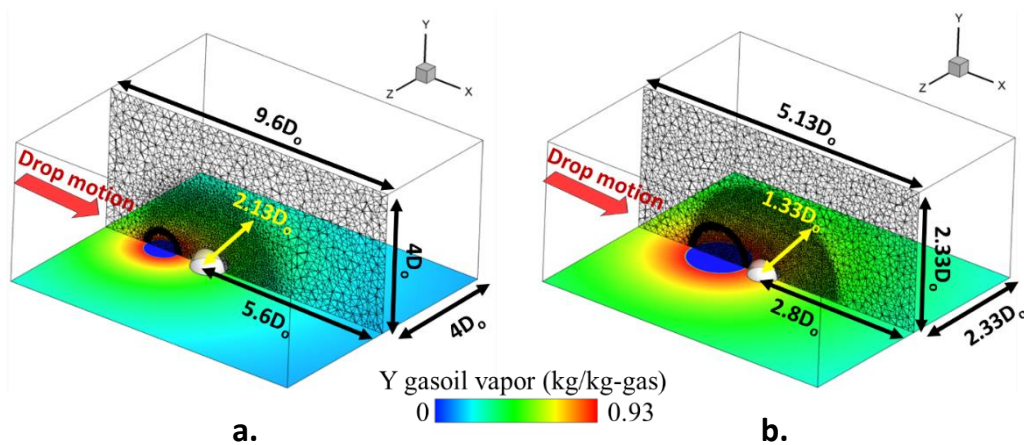


**Figure 5.1:** Computational domain used for cases a) 2\* and b) 4\*. Bottom plane coloured by gasoil vapour initial mass fraction.

For Case7\*, the total dimensions of the domain were much smaller than in the corresponding 2D case, in order to save computational time. Gasoil vapour mass fraction is initialized as in the 2D simulation, shown in Figure 5.1 as well.

In Figure 5.2, the numerical domain applied for Case9 is presented, using two different views. The domain dimensions are smaller compared to the domains presented in Figure 5.1, in order to limit the computational cost.

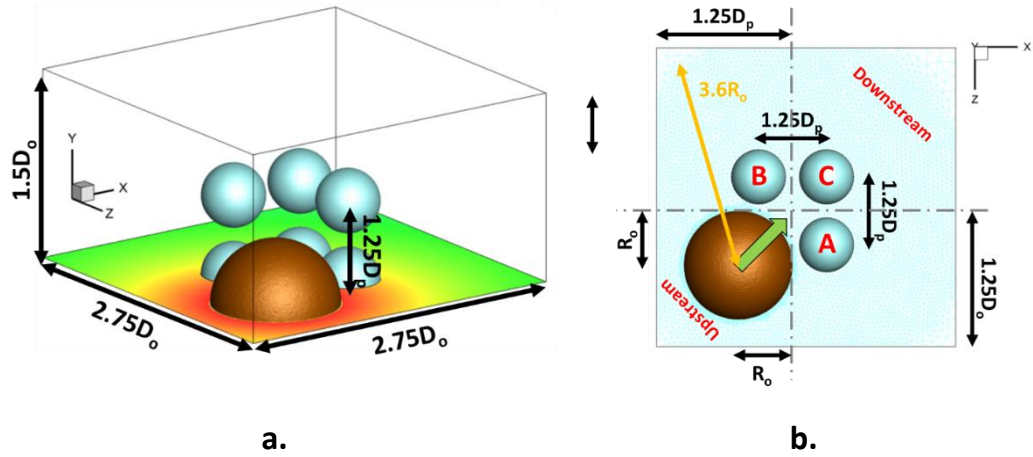


**Figure 5.2:** a) Computational domain used for the simulation of Case9. b) Particle cluster arrangement and notation used.

The arrangement of the particles in the cluster is as follows: three particles are in the same plane with the droplet half-symmetry plane, while the remaining 3 particles are located with an offset in the Y-axis direction. For easier readability of graphs that follow, the lower level particles, placed in the same plane as the droplet, will be named as  $A_l$ ,  $B_l$  and  $C_l$ , while the higher level ones will be referred to as  $A_h$ ,  $B_h$  and  $C_h$  (Figure 5.2b).

Numerical settings and boundary conditions are similar to the 2D axisymmetric case (Fixed Pressure in all open boundaries and wall to represent the particles). Additionally, a symmetry boundary condition cutting the droplet in half is applied in order to keep the computational effort at acceptable levels. Droplet is initially placed at a one droplet diameter distance away from the particle impact point for cases 2\*, 4\* and at a distance of  $D_o/5$  for Case7\*. Regarding Case9, the initial droplet distance is shown in Figure 5.2b.

The applied numerical grids for all cases comprise of tetrahedron cells. Cell sizes both at the refined spherical zone, as well as further away from it, match the ones used in the corresponding 2D cases. In Table 5.2, the size of the grids employed, as well as information relevant to the computational resources required for the runs to be performed are shown.

Case No.	Coarse grid (mill cells)	Initial grid (mill cells)	Max grid (mill cells)	Cores	Real time to run $\tau=1.5$ (days)	Uniform equival grid (mill cells)
2*	0.51	1.84	7.92	36	18	32.1
4*	0.51	1.84	7.94	36	54	32.1
7*	0.93	2.29	4.05	36	19	14.9
9	1.15	2.2	4.85	36	89	73.6

**Table 5.2:** Number of cells and simulation time for runs performed

## 5.4 CFD results

### 5.4.1 Equally sized droplet-particle collisions, DTP=1

#### 5.4.1.1 Droplet deformation and gas layer thickness (2D vs 3D)

In Figure 5.3, the temporal evolution of drop deformation throughout the process of its collision with the catalytic particle is presented both for cases 2\* (3D) and 2 (the corresponding 2D one). In this figure, the contours of gasoline mass fraction in gas phase are presented, while in the three-dimensional results, the iso-surface of  $\alpha=0.5$  is also shown in the background.

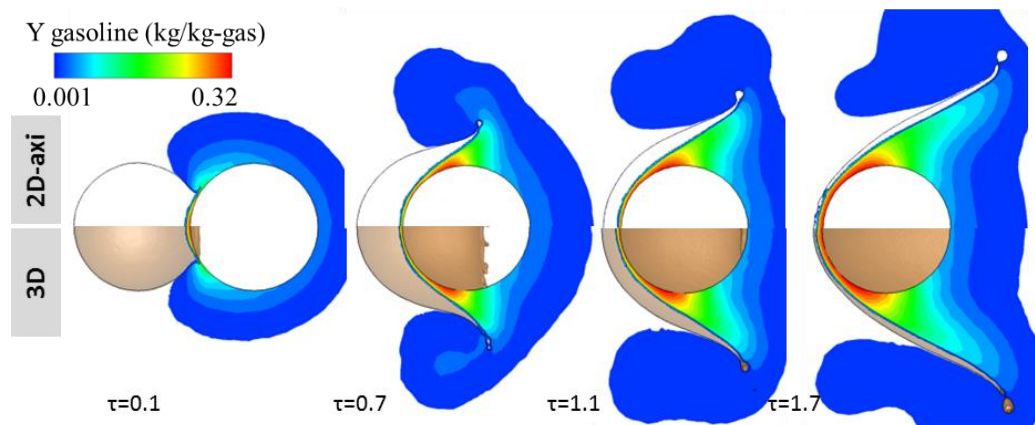


**Figure 5.3:** Effect of CFD simulation dimensions on collision outcome for a DTP=1,  $U_0=15\text{m/s}$ ,  $T_p=1,000\text{K}$  impact, Case2 (top), Case2\* (bottom). Contour of the produced gasoline mass fraction (kg-gasoline/kg-gas). The iso-surface of  $\alpha=0.5$  is depicted for the 3D case (bottom).

Results indicate that the droplet shape, as well as gasoline mass fraction distribution throughout the phenomenon are similar in both the 2D and the 3D cases. The droplet deforms into a thin liquid sheet that, moves away from the catalyst surface, as spreading along it. At  $\tau=0.7$ , the formation of fingers is observed in the three-dimensional case which

cannot be captured by the 2D simulation. These finger structures, as well as subsequent liquid sheet break-up are shown in 3D view in Figure 5.4, during the final stages of the phenomenon.

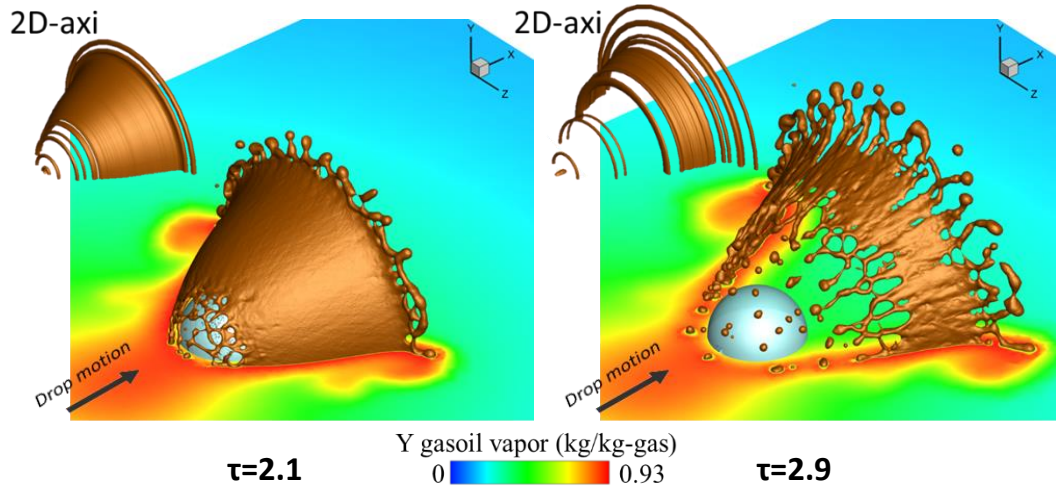


**Figure 5.4:** Formation of finger structures ( $\tau=2.1$ ) and sudden break-up ( $\tau=2.9$ ) are predicted in Case2\* (3D). Gasoil vapour mass fraction (kg-gasoil/kg-gas) is depicted on the symmetry boundary. Corresponding images from the revolution of 2D-axi results for 3D representation are added on top of the figure.

The expanding liquid sheet reaches its maximum deformation at approximately  $\tau=2.1$ , when it starts breaking-up on the impact side, probably due to high catalyst temperature that promotes higher evaporation rate. The break-up mechanism travels along the whole liquid expanding structure (lamella) up to time  $\tau=2.9$ , and the liquid form disintegrates violently in a large number of secondary droplets. The liquid form taken in this Figure resembles the “splash with ligaments” regime presented in the work of [195] for droplet impingement on a heated flat surface. On top of Figure 5.4 results from the corresponding 2D-axisymmetric simulations presented in Chapter 4 are depicted after revolution to produce the 3D images. As it is obvious that 2D simulation cannot actually represent the evolution of ligament break-up into satellite droplets. such axisymmetric results cannot be trusted for non-dimensional time higher than  $\tau=2$ .

Overall, the 3D numerical model behaves robustly, compared to the 2D axisymmetric results. Finger structure formation and subsequent sheet break-up are three-dimensional phenomena that start at approximately  $\tau=2$  and cannot be captured by the 2D simulations.

The same conclusions can be drawn for cases 4 and 4\* presented in Figure 5.5, following the similar droplet shapes and gasoline production levels for the 2D and 3D



approaches. The perturbations observed on the inner (particle) side of the liquid sheet at  $\tau=0.1$  and  $\tau=1.1$  in the axisymmetric case are not observed in the three dimensional one, as the predicted drop shape seems to be smoother. The formation of thinner finger structures is also predicted, a phenomenon which cannot be captured by 2D simulations.

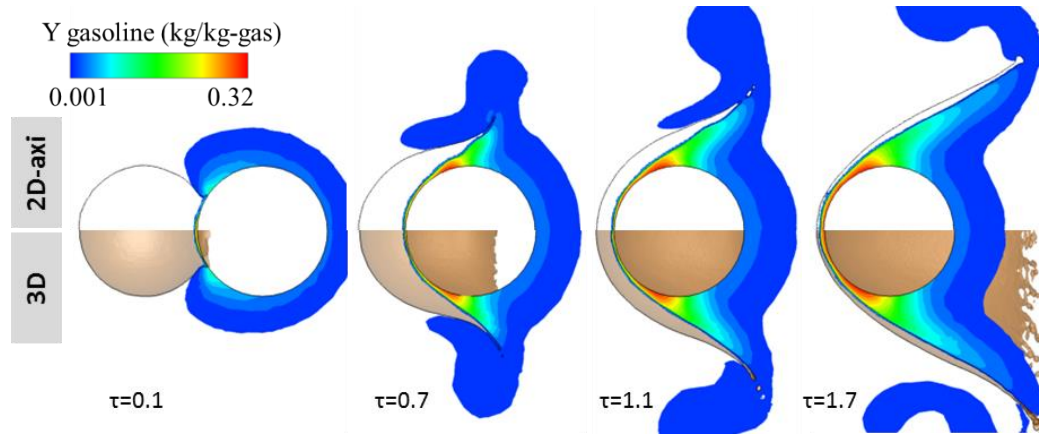


**Figure 5.5:** Effect of CFD simulation dimensions on collision outcome for a  $DTP=1$ ,  $U_0=30\text{m/s}$ ,  $T_p=1,000\text{K}$  impact, Case4 (top), Case4\* (bottom). Contour of the produced gasoline mass fraction (kg-gasoline/kg-gas). The iso-surface of  $\alpha=0.5$  is depicted for the 3D case (bottom).

The vapour layer thickness, formed in-between the droplet and the particle surface is presented in Figure 5.6 for 2D and 3D simulations.

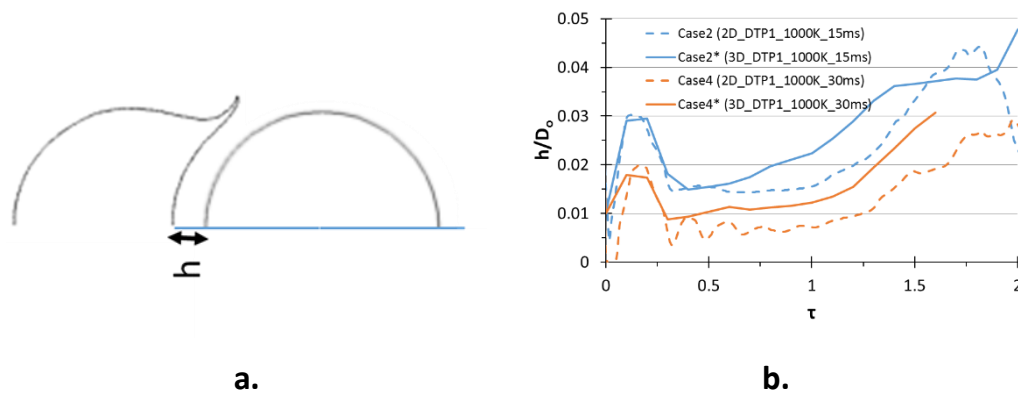


**Figure 5.6:** a) Definition of the vapour layer thickness at the impact point, b) Temporal evolution of the vapour layer thickness at the impact point for cases 2,2\*,4,4\*.

A slightly thicker vapour cushion is predicted in the three-dimensional domains for both the low/high impact velocity cases, especially for dimensionless times higher than  $\tau=0.5$ . For the latter case (Case4\*), a smoother transition in vapour thickness values for  $0.25 < \tau < 0.75$ . Overall, results indicate that there is both qualitative and quantitative agreement between 2D and 3D simulations.

### 5.4.1.2 Cracking Yields and global parameters (2D vs 3D)

Similar conclusions are drawn from observing gasoil conversion (gasoline production) levels, as well as surface cracking reaction rate throughout the phenomenon, as shown in Figure 5.7. The 2D cases seem to over predict slightly the reaction rate and products. Once again, the three-dimensional results are smoother for Case4\* compared to Case4.

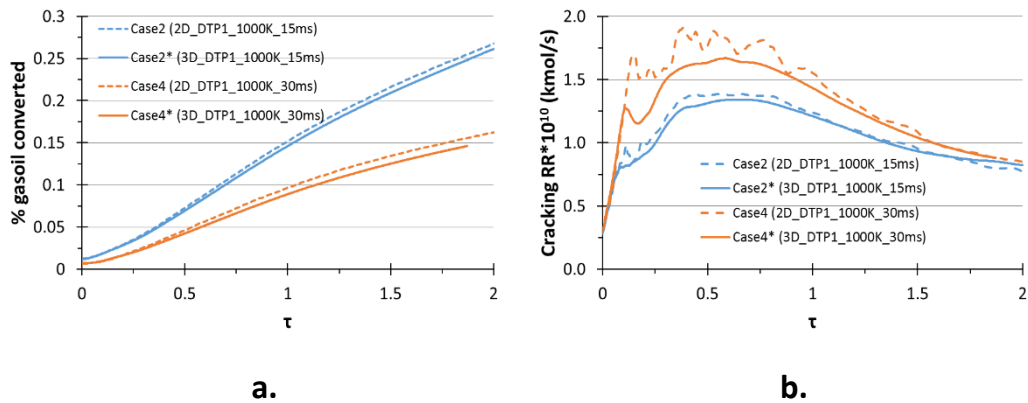


**Figure 5.7:** a) Percentage of gasoil converted to gasoline yield (kg-gasoline/kg-liq %) and b) cracking reaction rate, both plotted against non-dimensional time for cases 2,2\*,4,4\*.

Finally, similar results between 2D and 3D cases are also obtained for all important parameters such as droplet mean temperature, mean velocity and surface area. Therefore, it can be deduced that the 3D model is robust for DTP=1 cases, while certain three-dimensional phenomena such as finger structures and liquid sheet break-up can be captured. For  $\tau \leq 2$ , before the appearance of these phenomena, the axisymmetric simulations can be trusted.

## 5.4.2 Double sized droplet-particle collisions, DTP=2

### 5.4.2.1 Droplet deformation and gas layer thickness (2D vs 3D)

In Figure 5.8, the temporal evolution of droplet shapes is presented for cases 7\* (3D) and 7 (2D), along with the produced gasoline mass fraction. For this case, the results between 2D and 3D domains change significantly. In the 2D domain, it is observed that the droplet is sucked in ( $\tau=0.5$ ) by the wake vortex ring formed downstream the impacted solid particle. Subsequently, the expanding liquid sheet coalesce at the symmetry axis ( $\tau=1$ ) and progresses forward. On the contrary, in the 3D case, it is again observed that

the liquid sheet is sucked in by the wake vortex ring, however, much later during the collision process ( $\tau=1.4$ ). The liquid sheet forms a closed surface, which is hollow inside.

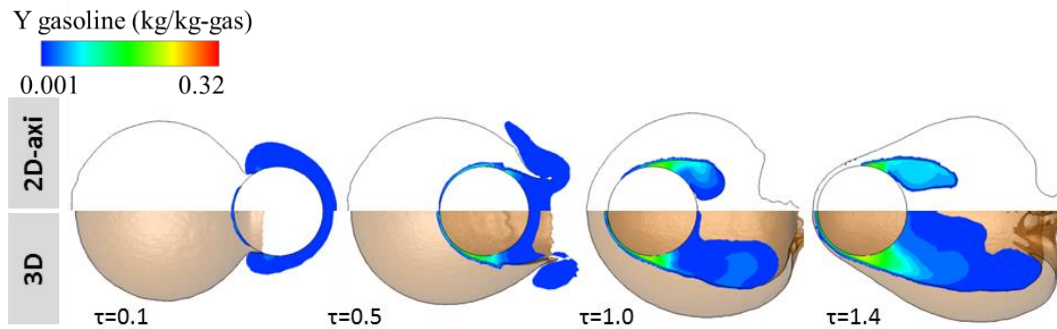


**Figure 5.8:** Effect of CFD simulation dimensions on collision outcome for a  $DTP=2$ ,  $U_0=30\text{m/s}$ ,  $T_p=800\text{K}$  impact, Case7 (top), Case7\* (bottom). Contour of the produced gasoline mass fraction (kg-gasoline/kg-gas). The iso-surface of  $\alpha=0.5$  is depicted for the 3D case (bottom).

For these specific conditions an “igloo” shaped form is presented in a close up view in Figure 5.9. At  $\tau=0.66$ , the “igloo” shape starts to form, which afterwards moves downstream from the impact side and accumulates to a liquid mass which resembles a shape similar to the initial one (“copy” droplet), but with its core to be empty of liquid (hollow).

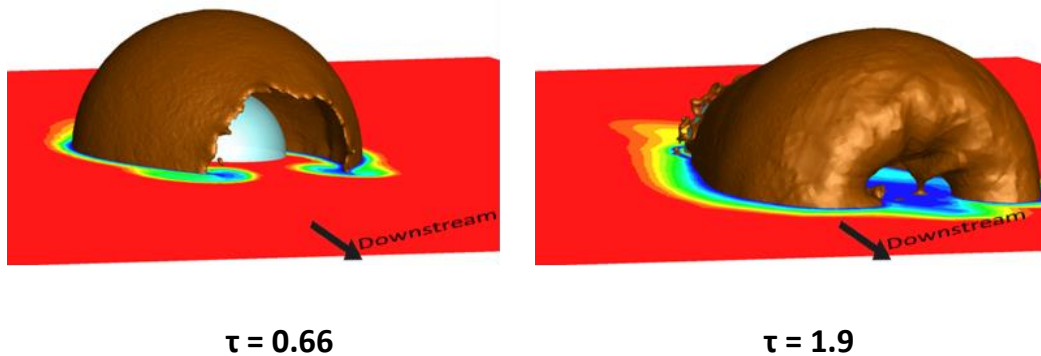


**Figure 5.9:** Igloo shaped form ( $\tau=0.66$ ) and “copy” droplet ( $\tau=1.9$ ) are predicted in the 3D Case7\*. Temperature contour (K) is depicted on the symmetry boundary.

This large difference between the 2D and 3D simulation on this case can be attributed to the different predicted liquid-solid contact, quantified in terms of vapour layer thickness, and presented in Figure 5.10. As the droplet moves along the particle surface, a very thin vapour layer is formed in the 3D domain, while for the 2D domain, the drop comes in direct contact with the solid surface throughout the whole phenomenon ( $h\sim 0$ ). This higher contact between solid-liquid does not allow the formed liquid sheet to move

away from the surface, and thus it is sucked in the wake region sooner than what is predicted in three dimensions.

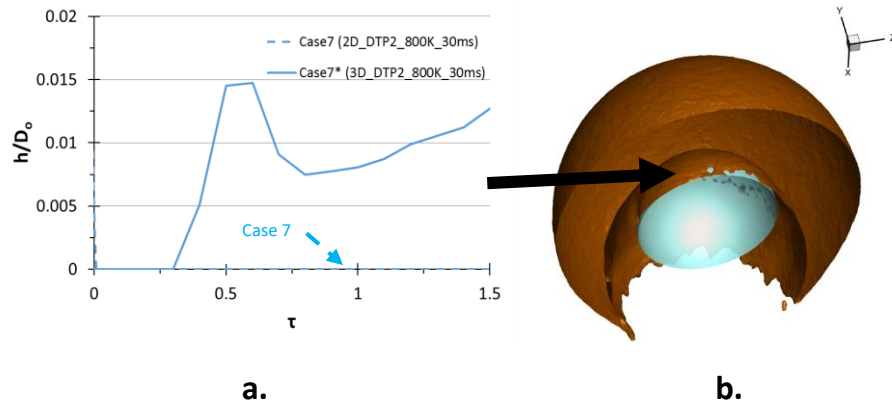


**Figure 5.10:** a) Vapour layer thickness temporal evolution for Cases 7,7\*, b) Solid particle partial wetting at  $\tau=0.66$  is predicted in the 3D case.

#### 5.4.2.2 Cracking Yields (2D vs 3D)

The significant difference observed in the gas layer thickness affects the conversion of gasoil, i.e. production of gasoline. As it seems from Figure 5.11, the formation of gasoline in the 3D case precedes the 2D one in time, as the vapour layer formed at approximately  $\tau=0.4$  (Figure 5.10) promotes cracking reactions and thus gasoline formation. On the other hand, the reaction rate in the 2D case is higher than in the 3D one, probably due to the fact that gasoline is also produced at the wake side of the droplet.

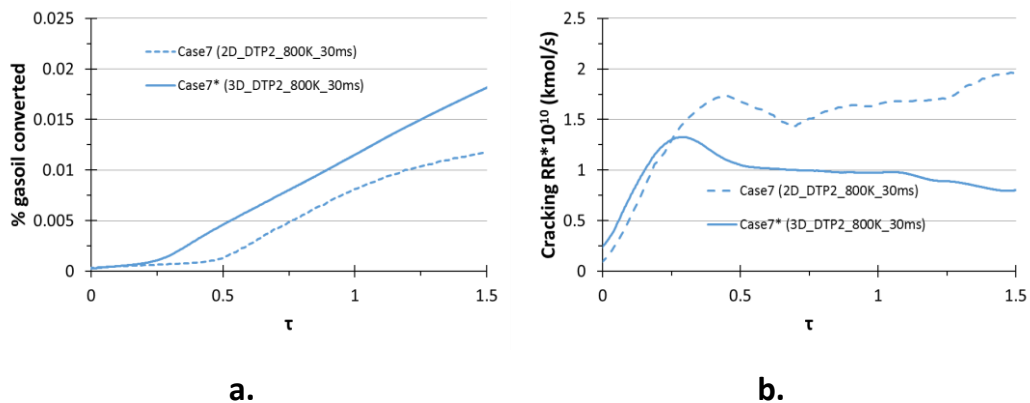


**Figure 5.11:** a) Percentage of gasoil converted to gasoline yield (kg-gasoline/kg-liq %) and b) cracking reaction rate, both plotted against non-dimensional time for cases 7,7\*.

Overall, in collisions where increased solid-liquid contact is expected, as in the case presented in this section, 2D axisymmetric simulations seem to fail in representing

correctly the physical phenomena predicted by the 3D model, especially the levitation of the droplet, followed by the subsequent production of gasoline. This is a very interesting observation, as the worst case scenario type cases will have to be simulated using 3D domains. In DTP=1 cases, where low solid-liquid contact is expected, results between 2D and 3D simulations are closer.

### 5.4.3 Droplet-particle cluster collisions

#### 5.4.3.1 Droplet deformation and gas layer thickness

In Figure 5.12, the temporal evolution of droplet shape after its impingement onto the particle cluster arrangement is presented, as viewed from a downstream position. On the top set of images, the drop-gas interface is presented, plotted with the use of the iso-surface of  $\alpha=0.5$ , while on the bottom set, a volume rendered representation of the produced gasoline lump specie is shown, coloured by gasoline mass fraction in the gas mixture.

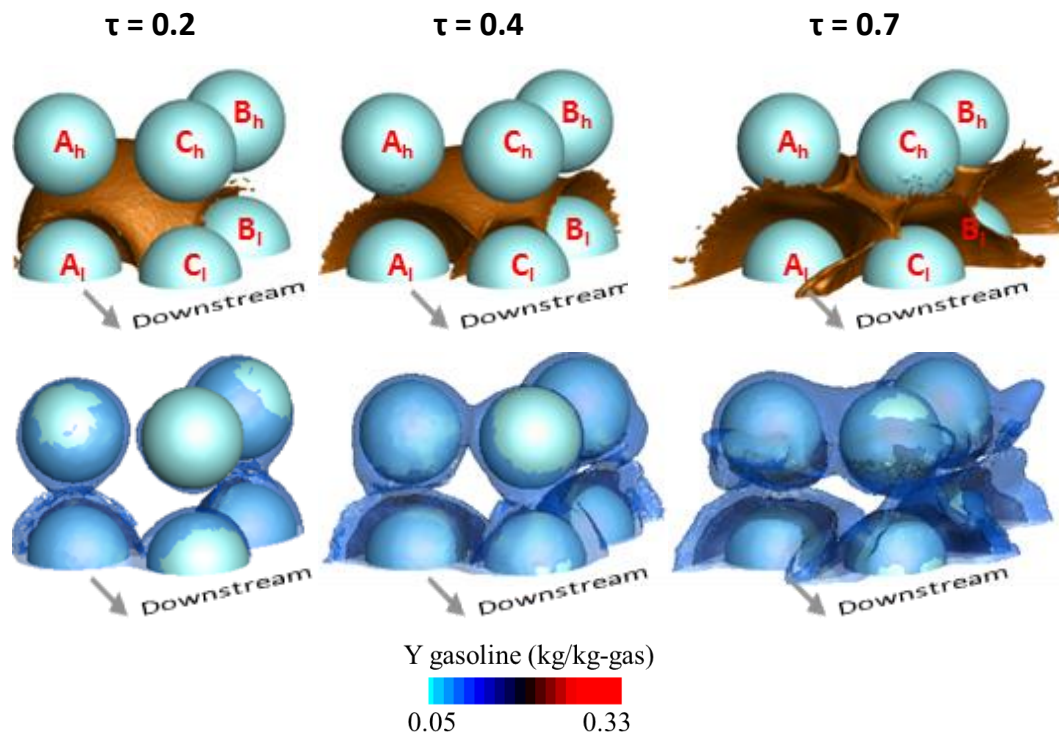


**Figure 5.12:** Drop impact onto a particle cluster. Top row shows iso-surface of  $\alpha=0.5$ , bottom row shows gasoline mass fraction volume rendering.

Time is non-dimensionalised, taking as impact reference point, i.e.  $t=0$ , the time instant when the droplet first touches one of the spherical catalyst particles. As the

droplet moves in between the space left from the presence of the solid particles, it starts to deform into a liquid sheet ( $\tau=0.2$ ) as observed in single droplet-particle collisions.

A vapour layer is again formed between the deforming liquid and the catalyst surface. Due to the presence of the high temperature catalysts, the approaching droplet evaporates at a high rate, producing gasoil vapour that subsequently reacts with the catalyst surface and cracks to gasoline. This formed vapour layer poses a barrier to droplet direct contact with the catalyst surface. The first stages of drop levitation on the surface of side particles  $A_i$  and  $B_i$  is presented in Figure 5.13 for  $\tau=0.05$ , where it is obvious that the drop only partially wets the solid surface.

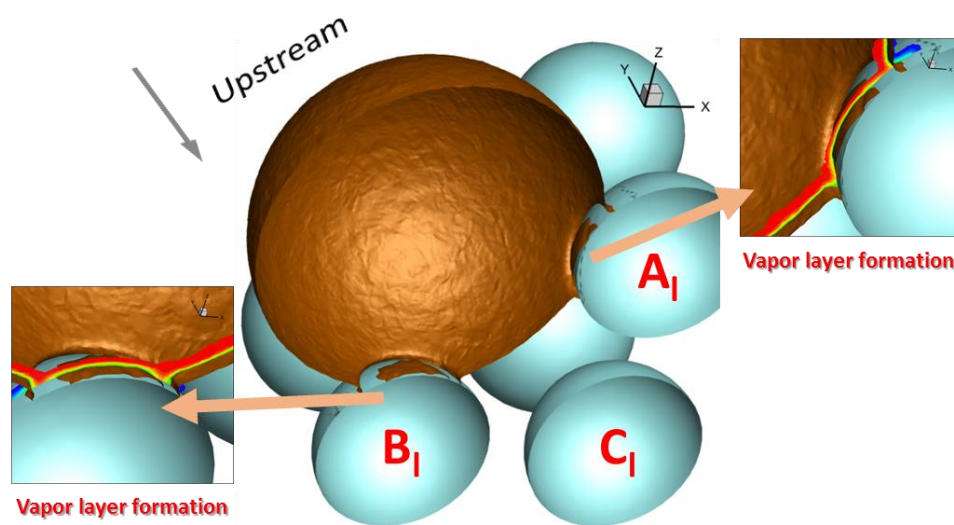


**Figure 5.13:** Vapour layer levitating droplet on top of particles ( $\tau=0.05$ ). Two slices of volume fraction field at the proximity of spherical particles are shown, where  $\alpha=0.001-0.999$ .

As the deformed liquid mass continues its motion across the gap among the particles, liquid sheets are formed close to each particle surface ( $\tau=0.4$ ), as they repel the liquid. This results in complex liquid forms presented in Figure 5.12,  $\tau=0.7$ . Afterwards, the expanding liquid sheet moves away from the side particles and approaches the central one ( $C_i$ ), it becomes clear that the flow induced by the presence of this centre particle dominates the evolution of the phenomenon. This is observed in Figure 5.12, at  $\tau=0.7$ , as the liquid sheet is repelled by the centre catalyst; thus leading the droplet to move towards the direction of the other two particles.

The gasoline lump formed follows the shape of the formed liquid sheet. At  $\tau=0.2$ , gasoline production is increased right after the particle impact, and is high at the point of impact. As the droplet moves inside the particle cluster, one by one the particles are

turned on (to produce gasoline). At  $\tau=0.4$ , the formed gasoline covers almost the whole particle surfaces, with the only exception the top level center particle. High levels of gasoline lump mass fraction are observed close to the impact point, and along the inner side of the formed liquid sheet.

For longer times of the process, the formed liquid sheet breaks-up into smaller satellite droplets as presented in Figure 5.14,  $\tau=1.05$ .

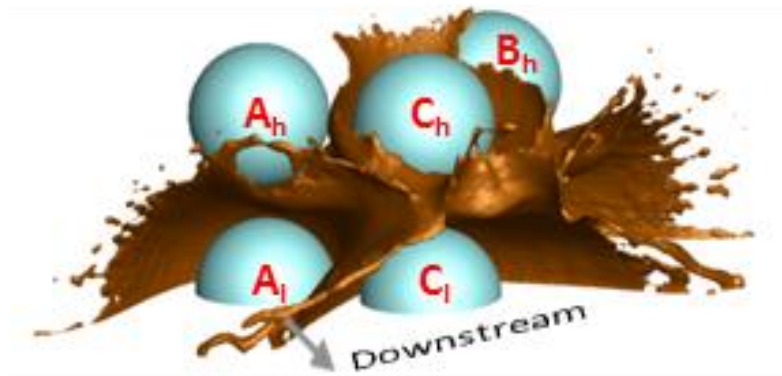


**Figure 5.14:** Drop break-up after impact on a particle cluster at  $\tau=1.05$ .

It appears that the most probable locations for liquid sheet breakup are the left and right bounds of the induced liquid shape. At these locations, the liquid sheet is thinner and easier to breakup, while the sheets surrounding the center particle are thicker. At  $\tau=1.05$  the central parts of the liquid sheet form a torus-like shape, which breaks up from the main liquid body. The break-up mechanism can be either driven by Rayleigh type instabilities, starting from either a torus-like or a finger shape, or due to the presence of surface tension, as also explained in [163]. From a numerical point of view, break-up is induced by surface tension or not adequate grid resolution. The prediction of sheet breakup exact time and place falls out of the scope of the current Thesis, where a qualitative prediction of drop breakup global locations can be claimed.

In Figure 5.15, close up views of the grid refinement are shown. On the left side, the symmetry plane and one ranging 2 degrees from the XZ diagonal are presented, while on the right side, a focus on the refined region is shown.

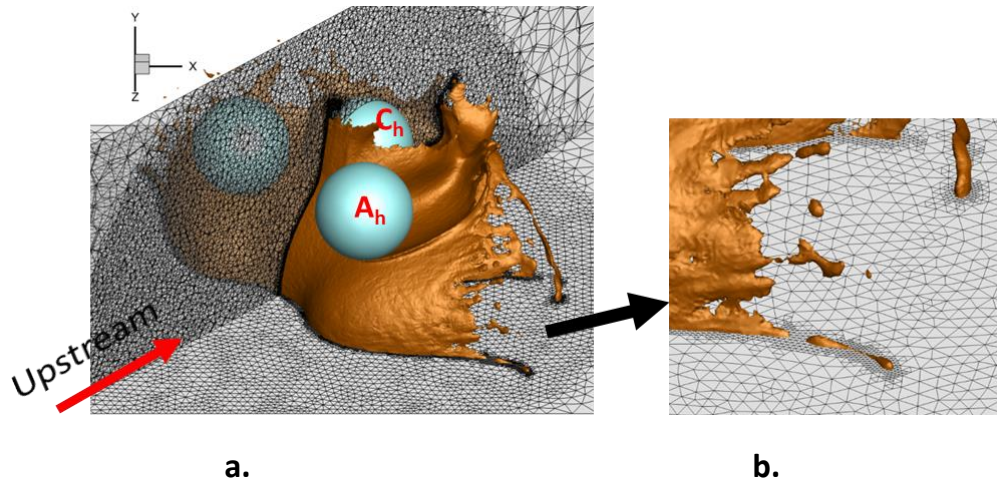


**Figure 5.15:** Local refinement algorithm application in the case of drop-particle cluster simulation case. a) Global view, b) Close-up view.

### 5.4.3.2 Velocity field and vortex rings

In Figure 5.16, the temporal evolution of the phenomenon is presented viewed from the upstream direction, where the droplet iso-surface ( $\alpha=0.5$ ) is coloured by the dimensionless velocity magnitude.

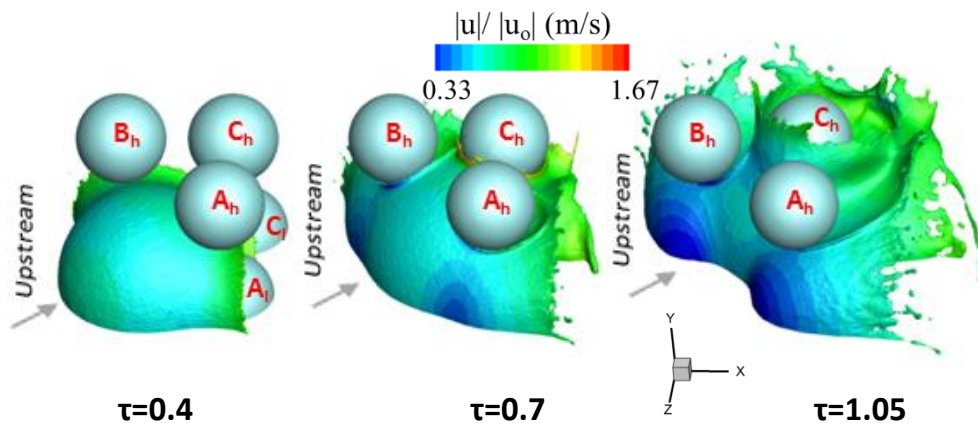


**Figure 5.16:** Temporal evolution of drop-particle cluster collision. Droplet is represented by the  $\alpha=0.5$  iso-surface coloured by velocity magnitude.

It is clear that at all time instances, the velocity magnitude is higher at the endpoint of the formed liquid mass. The liquid sheet is accelerated by the induced downstream the impact region fluid flow. Velocity values range in-between  $1/3$  and  $5/3$  of the impact velocity. These high velocity liquid jets break-up at some point, and then evaporate quicker as the interfacial area of liquid increases dramatically. In FCC reactors droplet break-up is desirable as it promotes quick evaporation and less solid-liquid contact which may result in catalyst pore blocking [3].



In Figure 5.17 the induced recirculation zones in the area of the impact wake region are shown for droplet impact on a single particle, as well as onto a particle cluster.

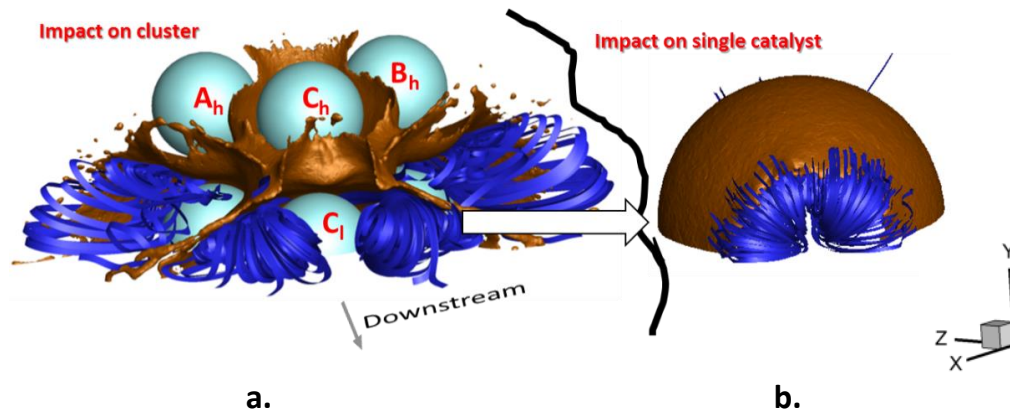


**Figure 5.17:** Recirculation zones induced by fluid flow at a)  $\tau=1.05$  for droplet impact onto a particle cluster, b)  $\tau=0.66$  for droplet impact onto a single particle.

It is obvious that the recirculation zones induced behind the center particle are similar to the single drop-particle ones, in the direction of impact. The side recirculation zones are rotated in a vertical direction. This is probably attributed to the center liquid sheet, which is pushed towards the sides and restricts the fluid flow in the wake region of the side particles to develop naturally.

#### 5.4.3.3 Cracking Yields and global parameters

In Figure 5.18 the gasoline production and total reaction rates for droplet impact onto a single particle (Case9), as well as onto a particle cluster are plotted against the non-dimensional time of the phenomenon. The values are non-dimensionalised by the number of particles that the droplet comes in contact with (1 and 9 respectively). It is predicted that the reaction rate as well as the gasoline production decreases when the droplet hits a particle cluster. The surface area that is in fact used for the production of gasoline in the present case is limited corresponding to nine single droplet-catalyst impacts.

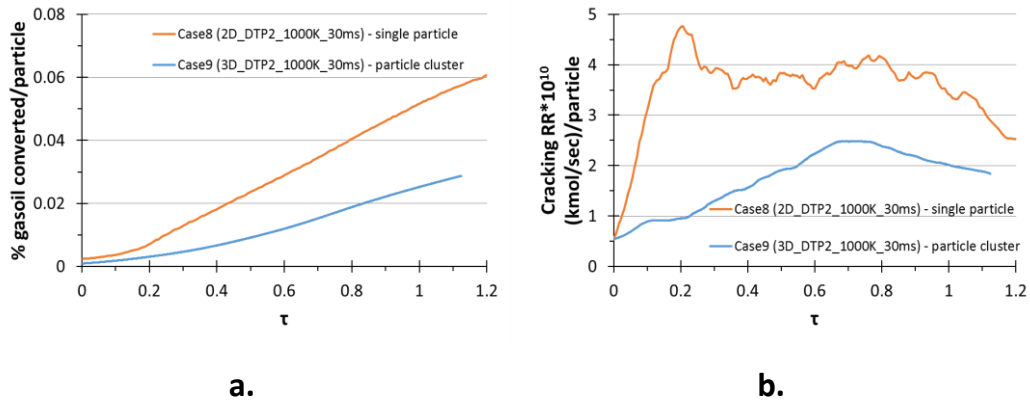


**Figure 5.18:** a) Percentage of gasoil converted to gasoline yield (kg-gasoline/kg-liq %) and b) cracking reaction rate, both plotted against non-dimensional time for cases 8 and 9.

In Figure 5.19, the droplet average temperature, as well as the non-dimensional drop mass are plotted against the non-dimensional time throughout the whole phenomenon for single droplet-catalyst collisions compared to droplet-cluster collisions.

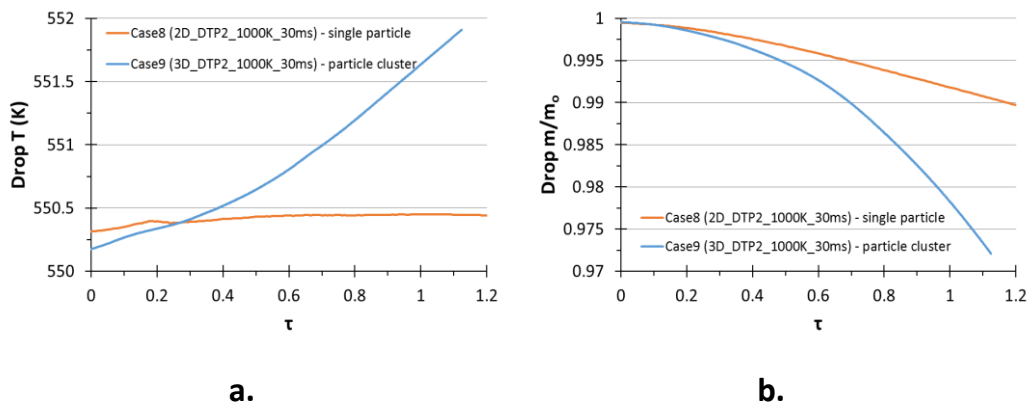


**Figure 5.19:** a) Droplet mean temperature and b) Non-dimensional mass, both plotted against non-dimensional time.

In the latter case, droplet temperature increases in time, in contrast to the general observations made for 2-D single droplet-particle collisions. The presence of nine particles in the cluster contribute to the local increase in gas temperature that results in the increase of heat convection towards the droplet mass. Droplet endures evaporation of its mass as it passes through the cluster of particles. However, when compared with the single drop case, the associated mass loss is increased only by 2% compared to the case of droplet impingement onto one catalyst particle for the same dimensionless period, which means that the particle cluster does not affect significantly the evaporation process and therefore the total mass loss of the droplet.

An interesting observation is made when investigating the particle surface coverage, which is presented in Figure 5.20. In this Figure, the percent of total particle area which is covered by liquid is plotted against the non-dimensional time for Case9. This is calculated as:

$$\frac{A_w}{A_p} = \frac{\sum_{wall-face} \alpha_{face} A_{face} \Big|_{\text{if } \alpha_{face} > 0.5}}{\sum_{wall-face} A_{face}} \quad (5-1)$$

From this figure, it is observed that the wetting of particles concerns only a very small percent of its area (up to 1.5%), where the liquid pore blocking mechanism is expected to happen. Moreover, as the droplet impacts all particles, one by one, a spike appears in this graph, where the droplet initially wets partially the particle surface up to the point that it is levitated by the formed vapor layer.

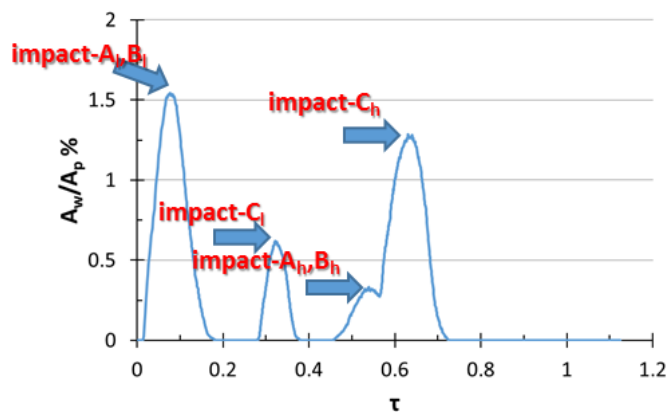


**Figure 5.20:** Temporal evolution of the percentage of particles' area which is wetted.

## 5.5 Conclusions

In this Chapter it was shown that the numerical model behaves robustly and gives similar results between 2D-axisymmetric and 3D domains, especially for the cases where decreased solid-liquid contact is expected (DTP=1, hot catalyst, low impact velocity). On the other hand, for the worst case scenario (DTP=2, cold catalyst, high impact velocity), which represents typical FCC droplet/particle sizes, was not reproduced exactly compared to the 2D results. More simulations are needed in order to further investigate this.

As concerns the droplet impact onto a particle cluster arrangement, results indicate that droplet lifetime does not change significantly in relation to the single drop-particle

collision case; however its breakup into more secondary droplets promotes a quicker evaporation time after the collision. It was found that the impingement of a gasoil droplet onto a particle cluster, instead on a single particle decreases catalytic cracking reaction yields as the corresponding contact area decreases.

Overall the numerical model behaves in a robust way. Further solid shaped geometrical configurations and their effect on the phenomenon evolution can be simulated with the proposed methodology, which considers as well the existence of complicated non-isothermal conditions.



# Chapter 6

## Conclusions and future work

### 6.1 Conclusions

In this work, a new methodology is developed to simulate drop-particle collisions under realistic FCC reactor conditions. The numerical model is capable of reproducing flow phenomena related to drop acceleration in free flow, drop impingement onto flat and spherical surfaces, drop heating and evaporation. Phase change, through a local evaporation model, and chemical reactions can be considered. Conclusions based on different drop flow scenarios are presented below.

The benchmark cases showed that using a local grid refinement technique does not affect considerably the solution of the drop deformation when compared against the results of a similar uniform grid and thus can be used to save computational time, while preserving high accuracy levels at the interface. Furthermore, it is shown that using CICSAM scheme in the volume fraction advection term discretization preserves a sharp interface. The coupling of M-HRIC scheme with a sharpening scheme behaves similarly. The sharpening methodology does not affect the solution of the default M-HRIC, while it improves significantly the exhibited diffusion.

In the case of drop acceleration under the effect of gravity, drop displacement and velocity predictions are well compared against the respective analytical solution of droplet motion. Drop acceleration from quiescence to terminal velocity is predicted accurately. Furthermore, it is shown that when using different advection discretization schemes, similar behavior is expected in macroscopic flow field development for high density grids ( $cpR \geq 80$ ). M-HRIC coupled with the sharpening algorithm achieves a sharp interface even in grids half this size. Moreover, this selection exhibits a smooth distribution of volume fraction values across the liquid-gas interface which in turn results in smooth gradient and curvature calculation, thus smooth surface tension force.

Numerical predictions of droplet impingement onto flat surfaces for a wide range of We numbers and surface wettability exhibit good comparison against a wide range of experimental data. Droplet maximum spreading agrees with the approximation given by the equation of Pasandideh, while the model gives insight into the pressure and velocity field distribution. As far as the dynamic contact angle models are concerned, results for the newly developed Wetting Force Model, Advancing-Receding, Shikhmurzaev's and Kistler's models are similar for hydrophobic surfaces. On the contrary, in hydrophilic surfaces, this work contributes to new insights, as a gap is reported for low and moderate Weber number impacts. As a general observation, WFM exhibits results which are closer to the experimental data compared against the other models, while a quicker recoiling phase is predicted. Overall, Shikhmurzaev's model behaves better in all cases presented, while Kistler's model for hydrophilic surfaces exhibits significant improvement in comparison to the Adv-Rec model. The new approach of implementing a stress term instead of a contact angle, as in WFM, exhibits promising results, however still needs further development to be applied in three dimensional runs.

In the case of droplet impingement onto a spherical surface, the dynamics are nicely captured by the numerical model, as the drop spreading coefficient and droplet shapes are compared against experimental data for a high DTP and low impact We number. Then, varying the We number and DTP, different collision outcomes are observed, namely rebound and coating, followed by secondary drop breakup in the latter case. Apart from pressure and velocity field predictions, which are similar to the flat surface impacts, new data are produced. The development of the liquid film height at the impact point is measured and compared against similar predictions or experimental data and is found to comply for the initial the initial drop deformation phase, while later in the inertia dominated phase changes in respect to the DTP. Furthermore, it is found that partial or full droplet rebound is promoted with very low We number and DTP values, while a critical curve separates the two collision outcomes. As these values are increased, coating of the particle is favoured. Finally, particle coverage, i.e. wetting surface area is calculated and it is shown that as the DTP increases, the wetted area increases until full coverage, when it becomes independent of the We number.

As concerns the droplet-particle collisions in FCC reactors, the major finding of the current work is that gasoil conversion is well linked with the direct solid-liquid contact. This is estimated by the predicted gas layer thickness formed in-between the impacting droplet and the catalyst. As the temperature of the catalyst increases or the initial drop

kinetic energy decreases, droplet is levitated more easily and a stable gas layer is formed. This favours gasoil conversion cracking reactions and limits the possibility of liquid pore blockage by non-evaporated liquid. However, typical droplet and particle diameters as well as impact velocities at current FCC reactors represent the worst case scenario in terms of the aforementioned criteria (conversion, liquid pore blocking). This shows that there is room for improvement in current FCC injection strategy, as hydrodynamic aspects are shown to affect the chemical output, which is not taken into account industrially.

The numerical model also gives new insights into the complex flow related to droplet-particle collisions under FCC reactor conditions, as it predicts the typical collision outcome. As soon as the droplet impacts the particle, it is levitated by the hot surface, while it spreads forming a thin liquid sheet that moves away from the particle surface. This sheet then shatters into a large number of satellite droplets.

Comparison between 2D-axisymmetric and 3D domains exhibits very good agreement, especially for the cases where decreased solid-liquid contact is expected (DTP=1, hot catalyst, low impact velocity). Droplet deformation, gas layer thickness and total gasoil conversion almost match between the different domains. For these conditions, two-dimensional runs can be used to get important insights, while computational time is saved. As the solid-liquid contact increases (DTP=2, cold catalyst, high impact velocity), which actually represents typical FCC droplet/particle sizes, 2D simulation cannot reproduce the 3D results.

Regarding the single droplet impact onto a particle cluster arrangement, results indicate that droplet lifetime does not change significantly in relation to the single drop-particle collision case; however its breakup into more secondary droplets promotes a quicker evaporation time after the collision. It is found that the impingement of a gasoil droplet onto a particle cluster, instead on a single particle decreases catalytic cracking reaction yields as the corresponding contact area decreases.

## 6.2 Future Work

In research, there is always room for improvement. In this section, my recommendations for future work are proposed, based on my experience, intuition and the results obtained.

First of all, the Wetting Force Model which is presented in the current Thesis, at its current state, is valid only for axisymmetric drops. The extension of this model to three



dimensions is proposed as a future task, although the reconstruction of the surface in all interface cells is needed, so that the contact line length can be approximated. Moreover, the extension of the WFM to study static or close-to-equilibrium conditions would also be a good idea in order to simulate the stick and slip behavior.

Regarding the drop-particle collisions, a significant development would be to treat the particle as a moving object, thus to include momentum exchange during the collision process. When the impact kinetic energies of the colliding parties become comparable, the outcome is expected to change. A good idea is to utilize the Immersed Boundary Method for the representation of the solid particle, as in [20], so that mesh deformation is avoided.

An important future task would be to look closely into the particle cooling process during the collision of the hot particle with the cold droplet. The energy equation inside the particle bulk will be solved, while the temperature at the particle surface will arise from the solution of the fluid and solid domains and not be constant. In Figure 6.1, preliminary runs performed with conjugate heat transfer are compared against the ones shown in this study, where the temperature of the surface is constant.

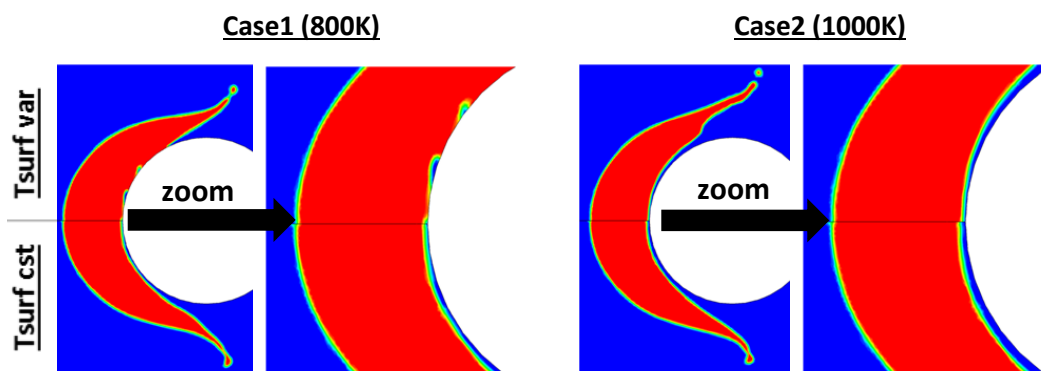


**Figure 6.1:** Effect of surface temperature boundary condition in vapour layer thickness prediction. Cases 1, 2 from Chapter 4,  $\tau=0.7$ .

A very interesting observation is revealed. The vapour layer thickness changes when the surface temperature is not constant. This suggests that as the particle cools down, solid-liquid contact will increase and therefore the collision outcome, in terms of hydrodynamics as well as chemical output, will change.

On a different perspective, the numerical investigation of the exact porous geometry of the catalytic particle, and how the liquid flows inside, as well as the exact simulation of the “cracking sites” seems an intriguing challenge.

In terms of model development, a main future task would be to broaden the spectrum where the current two-phase numerical model behaves robustly. Decreasing the parasitic currents will help in capturing flows with very low  $We$  numbers, such as micro-fluidic pipes and junctions for the production of droplets or emulsions, flow inside porous solids. Boiling or high-pressure evaporation (supercritical) model development will aid in the prediction of liquid droplet flows inside Internal Combustion Engines or Rockets. Finally, addressing the compressibility of the liquid or gas phases by implementing and solving for the compressible Navier-Stokes equations can help to reproduce phenomena like droplet deformation by the impact of a shock wave.



# Appendix A

## WFM implementation details

In Appendix A, a brief documentation of the implementation details and the rationale behind the incorporation of the WFM in the Navier-Stokes solver is presented.

A stress term is added in the momentum equation as mentioned in section 2.5.2. The “default” approach is to add this term at the boundary wall cells where interface can be found, i.e where volume fraction gradient value is non-zero, as referred in the wettability section 2.5. However, when this criterion was used for the application of the WFM, an unphysical velocity field was predicted at the contact line region, especially at the hysteresis time, that is at the end of the advancing phase and right before recoiling begins. This is presented schematically in Figure A.1.

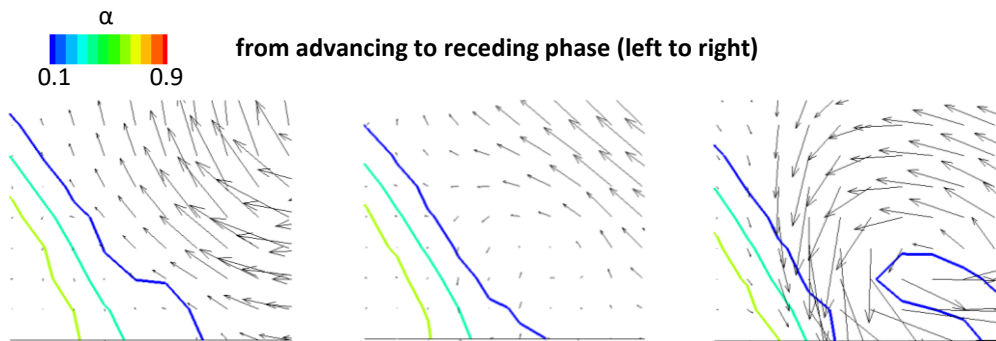


**Figure A.1:** Unphysical diffusion of volume fraction field, followed by the breakup of small secondary droplet observed when the WFM is applied in a wide region around the contact line. Velocity vectors are plotted in the same manner for all images.

The stress term applied at the contact line cells points outwards, in order to turn the rim to capture the lower receding contact angle. This affects the local flow field and culminates in the unphysical breakup of small secondary droplets, as observed in Figure A.1.

For surfaces that exhibit substantial contact angle hysteresis,  $\theta_{adv}-\theta_{rec}$ , this unphysical phenomenon becomes more intense. In order to avoid such unphysical behaviour, two alternative strategies can be implemented:

- Calculate the contact line velocity as the mass weighted average of all neighbouring cells related to the reference boundary cell, so that liquid velocity dominates
- Consider an additional criterion for the location of the interface cells with certain threshold volume fraction values

The first test proved to be unsuccessful, while the second appeared valid for all cases examined, using the threshold values of 0.05 and 0.95 as the most representative for interface tracking.

## Appendix B

### Properties of fluids used in the Thesis

In Appendix B, the physical properties of the fluids used in the simulations are presented, accompanied by the corresponding references. Constant properties were used in isothermal runs, while in cases with heat transfer, temperature dependent properties are incorporated. The fluid properties are summarized in Table B.1.

Fluid	properties library
water (l)	constant [175]
air (g)	constant [175], T-dependent [191]
n-heptane (l/g)	T-dependent [191]
n-decane (l/g)	T-dependent [191]
n-pentacosane (l/g)	T-dependent [168, 189, 190]

**Table B.1:** Fluids and property libraries used in the Thesis.



## Appendix C

# Validation of the evaporation model

In Appendix C, a brief description of the phase change model validation is presented. This is divided in two parts, firstly evaluate the behavior of the model in single drop evaporation and secondly test its performance in real cases similar to this study (hot wall impingement).

For the initial validation of the phase change model under operating conditions concerning the present study (evaporation of free flowing/suspended heavy hydrocarbons, with more than 20 carbon atoms, at high gas temperatures in the range of 800-1000K), scarce experimental material can be found in literature. In the work of Wong and Lin [196], concerning n-decane droplets, the ambient temperature reaches 1,000K, however the gas flowing towards the suspended droplet affects evaporation. For the correct simulation of this phenomenon, in terms of CFD, the coupled solution of the phase change model with flow equations (as in [154]) is needed, a task considered to be computationally expensive, since this phenomenon lasts many seconds. On the other hand in Nomura et al. [197], gas temperature varies between 400 and 1000K and gas pressure between 0.1-5MPa for the case of n-heptane droplet evaporation under microgravity conditions, while for these specific conditions gas velocity was considered to be of minor importance. Therefore, it was decided this work to be used for the validation of the phase change model as standalone, without its coupling with flow equations. It should be pointed out that in their work, Nomura et al. [197] mention that droplet diameter ranges between 600 and 800  $\mu\text{m}$ , initially set at room temperature. In this study a mean 700 $\mu\text{m}$  droplet is initialized at 293.15K in the domain presented in Figure C.1. The initial grid consists of 2,682 elements, while 4 levels of local refinement are additionally applied. The size of the domain is very large, so that the temperature of the gas phase is not affected, due to heat transfer of hot gas to the cold droplet.



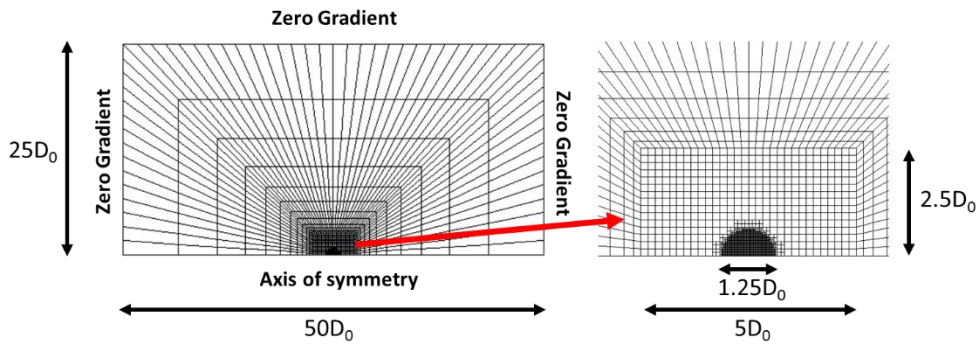


**Figure C.1:** Computational domain used for the validation of the CFD evaporation model in single droplet evaporation.

In Figure C.2 the results of the phase change model for the temporal evolution of the squared droplet diameter are compared against the experimental values of [197]. The evaporation model is deemed to be reliable and can be used for the investigation of heavy hydrocarbons, applicable in this study. Additionally, the average droplet temporal evolution is as well depicted, for which no experimental data were given.

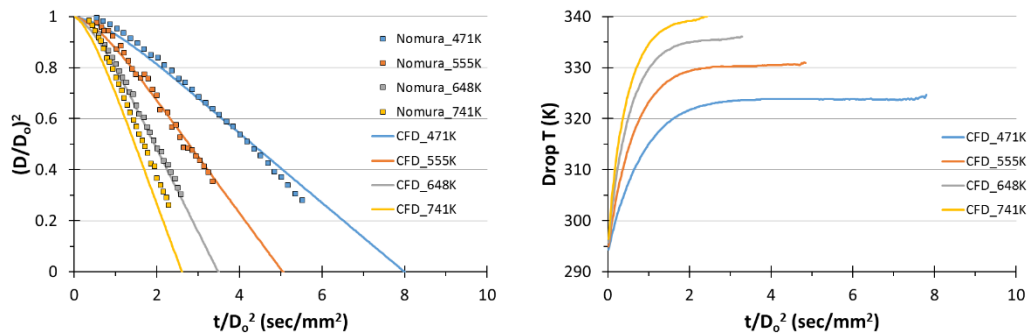


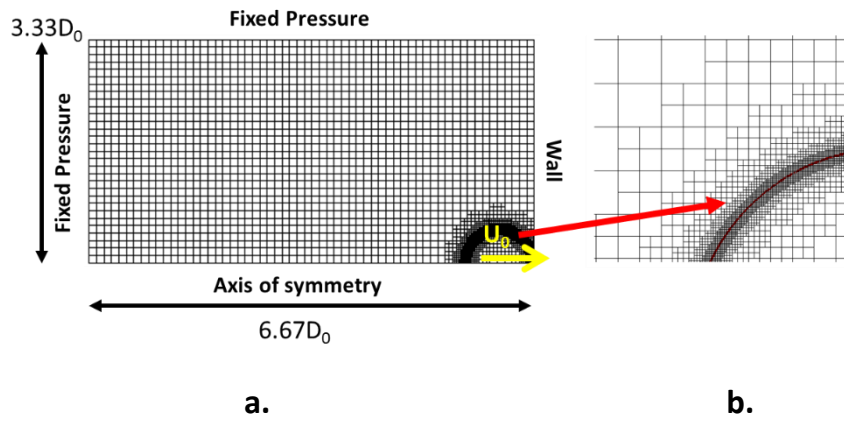
**Figure C.2:** Validation of the CFD phase change model against the experiments of [197] for n-heptane droplets evaporating at 101,325 Pa.

For the second validation, the phase change model needs to be tested in cases where the flow equations are solved. The behaviour of the numerical model in the case of droplet impingement onto a heated wall under droplet heating (direct solid-liquid contact) and film boiling conditions, both of which are of interest to this study, needs to be evaluated. The experimental observations of Qiao and Chandra [198] serve this goal; respective properties are presented in Table C.1. Although in [17, 21] the authors present experimental data for drop impact onto a heated particle, these data were not used for validation since they only refer to film boiling conditions (in [21], although cases for lower surface temperatures exist, data are not adequate for validation).

Case No.	$D_0$ (mm)	$u_0$ (m/s)	$T_{i,0}$ (K)	$T_g$ (K)	$u_g$ (m/s)	$T_w$ (K)	cpR
V1-V2-V3	1.5	0.8	298	298	0	451-463-483	144

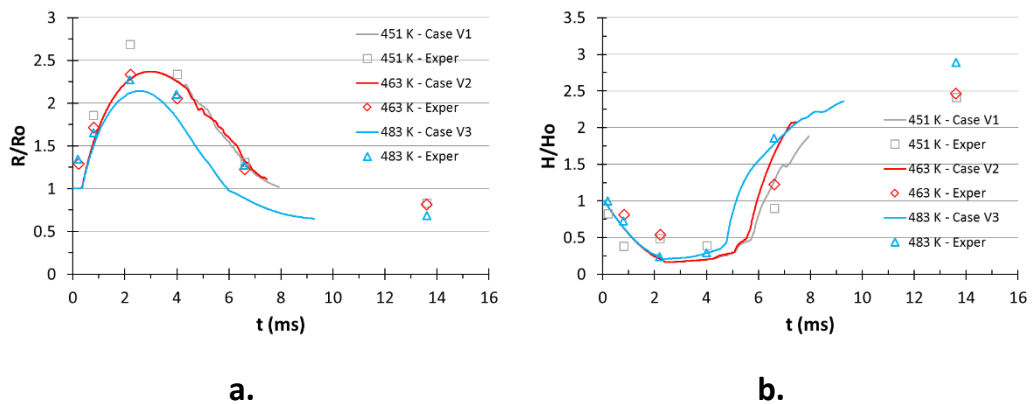
**Table C.1:** Test cases investigated for the validation of the CFD phase change model in drop impact on a heated wall, n-heptane, contact angle  $100^\circ$  [198].

Figure C.3 presents the applied CFD domain and boundary conditions, while the derived numerical results for both the non-dimensional droplet spreading and liquid height are shown in Figure C.4 and compared against the experimental values of [198].



**Figure C.3:** a) Computational domain (grid=30x60 cells) used for the validation of the CFD model in hot wall impingement cases, b) 5 levels of local refinement used in order to resolve the thin vapour layer.

The cpR number used in these cases is very high (144), so that the vapour layer thickness can be resolved explicitly and not through the coupled solution of an additional equation for the vapour layer thickness as in [20, 199]. CFD results seem to be in good agreement with the experimental values.



**Figure C.4:** Temporal evolution of a) maximum non-dimensional radius and b) maximum non-dimensional height of spreading droplet for the 3 cases examined against experimental data of [198].

In Figure C.5, contours of temperature and n-heptane vapour mass fraction are presented for selected time instants throughout the phenomenon. In the first two cases, a vapour bubble is formed in the centre of the spreading droplet.

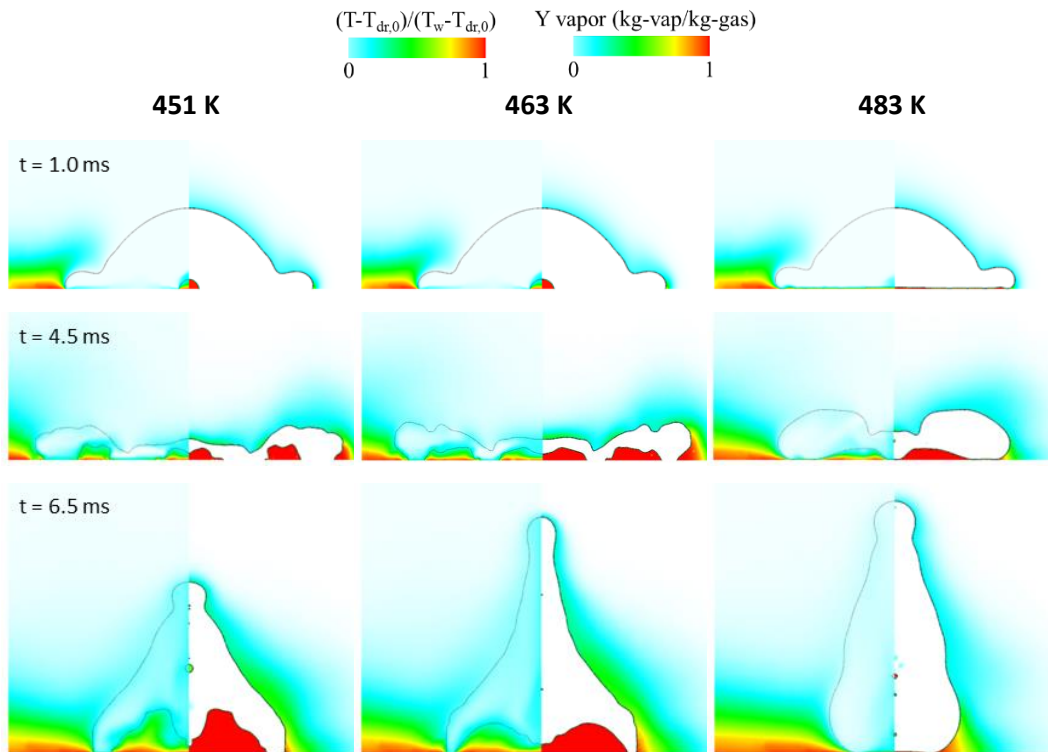


**Figure C.5:** Temporal evolution of drop deformation for validation cases of impingement on a heated wall. Images split in two sides, left side-non-dimensional temperature, right side-heptane vapour mass fraction (kg-vap/kg-gas).

This bubble grows widely and finally merges with the bubble formed under the retracting droplet rim. In the third case, the levitation of the droplet due to the appearance of a vapour layer is observed. The numerical model is able to resolve this vapour layer formed in-between the droplet and the solid surface.

# Contributions

During my 4-year research I had the opportunity to travel, participate and present my ongoing work in international conferences, while I was fortunate to publish my findings in well-respected international scientific journals. The list of my achievements is given below:

---

## Conferences (oldest first)

---

1. Malgarinos I., Marengo M., Antonini C., Nikolopoulos N., Strotos G., & Gavaises M., “A new model for droplet – solid surface interaction. Impingement onto hydrophilic and super-hydrophobic surfaces”, ILASS – Europe 2013, 25th European Conference on liquid Atomization & Spray Systems, Chania, Greece, 01-04 Sep. 2013.
  2. Malgarinos I., Nikolopoulos N., Marengo M., Antonini C., & Gavaises M., “Formulation and implementation of a new wetting model applicable in the case of droplet(s) spreading on solid substrates.”, 2nd International Conference on Numerical Methods in Multiphase Flows (ICNMMF-II), Darmstadt, Germany, 30 Jun – 2 Jul 2014.
  3. Malgarinos I., Nikolopoulos N., & Gavaises M. “Simulation of a freefalling single droplet using the VOF model coupled with an interface compression algorithm.”, ILASS – Europe 2014, 26th Annual Conference on Liquid Atomization and Spray Systems, Bremen, Germany, 8-10 Sep. 2014.
  4. Malgarinos I., Nikolopoulos N., & Gavaises M. “Droplet-spherical particle collision using the VOF methodology.”, FLOW 2014, 9th Greek National Conference on Fluid Flow Phenomena, Athens, Greece, 12-13 Dec. 2014. (Greek title: “Κρούση σταγονιδίου πάνω σε σφαιρικό σωματίδιο χρησιμοποιώντας τη μεθοδολογία VOF”)
  5. Malgarinos I., Nikolopoulos N., & Gavaises M. “Droplet-Particle Collisions Inside a Fluid Catalytic Cracking Reactor. A Numerical Study”, ILASS - Europe 2016, 27th Annual Conference on Liquid Atomization and Spray Systems, Brighton, UK, 4-7 Sep. 2016.
-

1. Malgarinos I., N. Nikolopoulos, M. Marengo, C. Antonini and M. Gavaises, VOF simulations of the contact angle dynamics during the drop spreading: Standard models and a new wetting force model. *Advances in Colloid and Interface Science*, 2014. 212(0): p. 1-20.
  2. Malgarinos I., N. Nikolopoulos, and M. Gavaises, Coupling a local adaptive grid refinement technique with an interface sharpening scheme for the simulation of two-phase flow and free-surface flows using VOF methodology. *Journal of Computational Physics*, 2015. 300: p. 732-753.
  3. Malgarinos I., N. Nikolopoulos, and M. Gavaises, A numerical study on droplet-particle collision dynamics. *International Journal of Heat and Fluid Flow*, 2016. 61, Part B: p. 499-509.
  4. Malgarinos I., N. Nikolopoulos, and M. Gavaises, Numerical investigation of heavy fuel droplet-particle collisions in the injection zone of a Fluid Catalytic Cracking reactor, Part I: Numerical model and 2D simulations. *Fuel Processing Technology*, 2017. 156: p. 317-330.
  5. Malgarinos I., N. Nikolopoulos, and M. Gavaises, Numerical investigation of heavy fuel droplet-particle collisions in the injection zone of a Fluid Catalytic Cracking reactor, part II: 3D simulations. *Fuel Processing Technology*, 2017. 156: p 43-53.
-

# Bibliography

1. Wu, J., *Extra mesoporous Y zeolite*, 2013, Google Patents.
2. Vogt, E.T.C. and B.M. Weckhuysen, *Fluid catalytic cracking: recent developments on the grand old lady of zeolite catalysis*. *Chemical Society Reviews*, 2015. **44**(20): p. 7342-7370.
3. Huang, Z. and T.C. Ho, *Effect of thermolysis on resid droplet vaporization in fluid catalytic cracking*. *Chemical Engineering Journal*, 2003. **91**(1): p. 45-58.
4. Chang, J., et al., *Computational investigation of hydrodynamics and cracking reaction in a heavy oil riser reactor*. *Particuology*, 2012. **10**(2): p. 184-195.
5. Lopes, G.C., et al., *Three-dimensional modeling of fluid catalytic cracking industrial riser flow and reactions*. *Computers & Chemical Engineering*, 2011. **35**(11): p. 2159-2168.
6. Li, T., et al., *Numerical investigation of FLUID COKING™ units, Part I: Hydrodynamics of a scaled cold flow model*. *The Canadian Journal of Chemical Engineering*, 2012. **90**(2): p. 442-456.
7. Ahsan, M., *Prediction of gasoline yield in a fluid catalytic cracking (FCC) riser using k-epsilon turbulence and 4-lump kinetic models: A computational fluid dynamics (CFD) approach*. *Journal of King Saud University - Engineering Sciences*, (0).
8. Chang, J., et al., *Computational investigation of the hydrodynamics, heat transfer and kinetic reaction in an FCC gasoline riser*. *Chemical Engineering Science*, 2014. **111**(0): p. 170-179.
9. Wu, C., et al., *CFD-DEM simulation of gas-solid reacting flows in fluid catalytic cracking (FCC) process*. *Chemical Engineering Science*, 2010. **65**(1): p. 542-549.
10. Nayak, S.V., S.L. Joshi, and V.V. Ranade, *Modeling of vaporization and cracking of liquid oil injected in a gas-solid riser*. *Chemical Engineering Science*, 2005. **60**(22): p. 6049-6066.
11. Theologos, K.N., A.I. Lygeros, and N.C. Markatos, *Feedstock atomization effects on FCC riser reactors selectivity*. *Chemical Engineering Science*, 1999. **54**(22): p. 5617-5625.
12. Ahmadi Motlagh, A.H., et al., *Experimental analysis of volatile liquid injection into a fluidized bed*. *Particuology*.
13. Gao, J., et al., *Simulations of gas-liquid-solid 3-phase flow and reaction in FCC riser reactors*. *AIChE Journal*, 2001. **47**(3): p. 677-692.
14. Chang, S.L. and C.Q. Zhou, *Simulation of FCC riser flow with multiphase heat transfer and cracking reactions*. *Computational Mechanics*, 2003. **31**(6): p. 519-532.
15. Behjat, Y., S. Shahhosseini, and M.A. Marvast, *Simulation study of droplet vaporization effects on gas-solid fluidized bed*. *Journal of the Taiwan Institute of Chemical Engineers*, 2011. **42**(3): p. 419-427.
16. Patel, R., et al., *Effect of injection zone cracking on fluid catalytic cracking*. *AIChE Journal*, 2013. **59**(4): p. 1226-1235.

17. Ge, Y., *3D numerical study on droplet-solid collisions in the Leidenfrost regime*, 2005, The Ohio State University: Ann Arbor. p. 246-246 p.
18. Sadeghbeigi, R., *Fluid Catalytic Cracking Handbook: An Expert Guide to the Practical Operation, Design, and Optimization of FCC Units* 2012: Butterworth-Heinemann.
19. Gac, J.M. and L. Gradoń, *Lattice-Boltzmann modeling of collisions between droplets and particles*. Colloids and Surfaces A: Physicochemical and Engineering Aspects, 2014. **441**(0): p. 831-836.
20. Ge, Y. and L.-S. Fan, *Droplet-particle collision mechanics with film-boiling evaporation*. Journal of Fluid Mechanics, 2007. **573**: p. 311-337.
21. Mitra, S., et al., *Droplet impact dynamics on a spherical particle*. Chemical Engineering Science, 2013. **100**(0): p. 105-119.
22. Young, T., *An Essay on the Cohesion of Fluids*. Philosophical Transactions of the Royal Society of London, 1805. **95**: p. 65-87.
23. Worthington, A.M., *On the Forms Assumed by Drops of Liquids Falling Vertically on a Horizontal Plate*. Proceedings of the Royal Society of London, 1876. **25**(171-178): p. 261-272.
24. Rein, M., *Phenomena of liquid drop impact on solid and liquid surfaces*. Fluid Dynamics Research, 1993. **12**(2): p. 61-93.
25. Yarin, A.L., *DROP IMPACT DYNAMICS: Splashing, Spreading, Receding, Bouncing*. Annual Review of Fluid Mechanics, 2006. **38**(1): p. 159-192.
26. Marengo, M., et al., *Drop collisions with simple and complex surfaces*. Current Opinion in Colloid & Interface Science, 2011. **16**(4): p. 292-302.
27. Rioboo, R., C. Tropea, and M. Marengo, *Outcomes from a drop impact on solid surfaces*. Atomization and Sprays, 2001. **11**(2): p. 12.
28. Dussan, E.B., *On the Spreading of Liquids on Solid Surfaces: Static and Dynamic Contact Lines*. Annual Review of Fluid Mechanics, 1979. **11**(1): p. 371-400.
29. Gennes, P.G.D., *Wetting: statics and dynamics*. Reviews of Modern Physics, 1985. **57**(3): p. 827-863.
30. Shikhmurzaev, Y.D., *Singularities at the moving contact line. Mathematical, physical and computational aspects*. Physica D: Nonlinear Phenomena, 2006. **217**(2): p. 121-133.
31. Chandra, S. and C.T. Avedisian, *On the Collision of a Droplet with a Solid Surface*. Proceedings of the Royal Society of London. Series A: Mathematical and Physical Sciences, 1991. **432**(1884): p. 13-41.
32. Pasandideh-Fard, M., et al., *Capillary effects during droplet impact on a solid surface*. Physics of Fluids, 1996. **8**(3): p. 650-659.
33. Mao, T., D.C.S. Kuhn, and H. Tran, *Spread and rebound of liquid droplets upon impact on flat surfaces*. AIChE Journal, 1997. **43**(9): p. 2169-2179.
34. Ukiwe, C. and D.Y. Kwok, *On the Maximum Spreading Diameter of Impacting Droplets on Well-Prepared Solid Surfaces*. Langmuir, 2004. **21**(2): p. 666-673.
35. Vadillo, D.C., et al., *Dynamic contact angle effects onto the maximum drop impact spreading on solid surfaces*. Physics of Fluids, 2009. **21**(12): p. 122002-8.
36. Kim, H.Y. and J.H. Chun, *The recoiling of liquid droplets upon collision with solid surfaces*. Physics of Fluids, 2001. **13**(3): p. 643-659.
37. An, S.M. and S.Y. Lee, *One-dimensional model for the prediction of impact dynamics of a shear-thinning liquid drop on dry solid surfaces*. Atomization and Sprays, 2012. **22**(5): p. 371-389.
38. Scheller, B.L. and D.W. Bousfield, *Newtonian drop impact with a solid surface*. AIChE Journal, 1995. **41**(6): p. 1357-1367.

39. Zhang, X. and O.A. Basaran, *Dynamic Surface Tension Effects in Impact of a Drop with a Solid Surface*. Journal of colloid and interface science, 1997. **187**(1): p. 166-178.
40. Range, K. and F. Feuillebois, *Influence of Surface Roughness on Liquid Drop Impact*. Journal of colloid and interface science, 1998. **203**(1): p. 16-30.
41. Crooks, R., J. Cooper-White, and D.V. Boger, *The role of dynamic surface tension and elasticity on the dynamics of drop impact*. Chemical Engineering Science, 2001. **56**(19): p. 5575-5592.
42. Richard, D., C. Clanet, and D. Quéré, *Surface phenomena: Contact time of a bouncing drop*. Nature, 2002. **417**(6891): p. 811-811.
43. Rioboo, R., M. Marengo, and C. Tropea, *Time evolution of liquid drop impact onto solid, dry surfaces*. Experiments in Fluids, 2002. **33**(1): p. 112-124.
44. Sikalo, S., et al., *Analysis of impact of droplets on horizontal surfaces*. Experimental Thermal and Fluid Science, 2002. **25**(7): p. 503-510.
45. Park, H., et al., *Single drop impaction on a solid surface*. AIChE Journal, 2003. **49**(10): p. 2461-2471.
46. Clanet, C., et al., *Maximal deformation of an impacting drop*. Journal of Fluid Mechanics, 2004. **517**: p. 199-208.
47. Elias, R.N., M.A. Martins, and A.L. Coutinho, *Simple finite element-based computation of distance functions in unstructured grids*. International journal for numerical methods in engineering, 2007. **72**(9): p. 1095-1110.
48. Bartolo, D., C. Josserand, and D. Bonn, *Retraction dynamics of aqueous drops upon impact on non-wetting surfaces*. Journal of Fluid Mechanics, 2005. **545**: p. 329-338.
49. Bayer, I.S. and C.M. Megaridis, *Contact angle dynamics in droplets impacting on flat surfaces with different wetting characteristics*. Journal of Fluid Mechanics, 2006. **558**: p. 415-449.
50. Hung, Y.-L., et al., *Initial wetting velocity of droplet impact and spreading: Water on glass and parafilm*. Colloids and Surfaces A: Physicochemical and Engineering Aspects, 2011. **384**(1-3): p. 172-179.
51. Antonini, C., A. Amirfazli, and M. Marengo, *Drop impact and wettability: From hydrophilic to superhydrophobic surfaces*. Physics of Fluids, 2012. **24**(10): p. 102104-13.
52. Antonini, C., et al., *Drop Rebound after Impact: The Role of the Receding Contact Angle*. Langmuir, 2013. **29**(52): p. 16045-50.
53. Jiang, T.-S., O.H. Soo-Gun, and J.C. Slattery, *Correlation for dynamic contact angle*. Journal of colloid and interface science, 1979. **69**(1): p. 74-77.
54. Roisman, I.V., et al., *Drop impact onto a dry surface: Role of the dynamic contact angle*. Colloids and Surfaces A: Physicochemical and Engineering Aspects, 2008. **322**(1-3): p. 183-191.
55. Fukai, J., et al., *Wetting effects on the spreading of a liquid droplet colliding with a flat surface: Experiment and modeling*. Physics of Fluids, 1995. **7**(2): p. 236-247.
56. Bussmann, M., S. Chandra, and J. Mostaghimi, *Modeling the splash of a droplet impacting a solid surface*. Physics of Fluids, 2000. **12**(12): p. 3121-3132.
57. Francois, M. and W. Shyy, *Computations of drop dynamics with the immersed boundary method, Part 2: Drop impact and heat transfer*. Numerical Heat Transfer, Part B: Fundamentals, 2003. **44**(2): p. 119-143.
58. Sikalo, S., et al., *Dynamic contact angle of spreading droplets: Experiments and simulations*. Physics of Fluids, 2005. **17**(6): p. 062103-13.



59. Ganesan, S., *On the dynamic contact angle in simulation of impinging droplets with sharp interface methods*. *Microfluidics and Nanofluidics*, 2013. **14**(3-4): p. 615-625.
60. Gunjal, P.R., V.V. Ranade, and R.V. Chaudhari, *Dynamics of drop impact on solid surface: Experiments and VOF simulations*. *AIChE Journal*, 2005. **51**(1): p. 59-78.
61. Levin, Z. and P.V. Hobbs, *Splashing of Water Drops on Solid and Wetted Surfaces: Hydrodynamics and Charge Separation*. *Philosophical Transactions of the Royal Society of London. Series A, Mathematical and Physical Sciences*, 1971. **269**(1200): p. 555-585.
62. Hardalupas, Y., A.M.K.P. Taylor, and J.H. Wilkins, *Experimental investigation of sub-millimetre droplet impingement on to spherical surfaces*. *International Journal of Heat and Fluid Flow*, 1999. **20**(5): p. 477-485.
63. Pasandideh-Fard, M., M. Bussmann, and S. Chandra, *SIMULATING DROPLET IMPACT ON A SUBSTRATE OF ARBITRARY SHAPE 2001*. **11**(4): p. 397-414.
64. Gunjal, P.R., V.V. Ranade, and R.V. Chaudhari, *Experimental and computational study of liquid drop over flat and spherical surfaces*. *Catalysis Today*, 2003. **79-80**(0): p. 267-273.
65. Bakshi, S., I.V. Roisman, and C. Tropea, *Investigations on the impact of a drop onto a small spherical target*. *Physics of Fluids (1994-present)*, 2007. **19**(3): p. -.
66. Bangonde, S., P. Nikure, and V.V. Buwa, *Numerical Simulations of Dynamics of Drop Impact and Spreading on Cylindrical and Spherical Surfaces*. Presented at GLS-9/8th World Congress of Chemical Engineering held at Montreal, Canada (August 23-27), 2009.
67. Froment, G.F. and K.B. Bischoff, *Chemical reactor analysis and design*1979: Wiley.
68. Sechenyh, V. and A. Amirfazli, *An experimental study for impact of a drop onto a particle in mid-air: The influence of particle wettability*. *Journal of Fluids and Structures*, 2016. **66**(Supplement C): p. 282-292.
69. Banitabaei, S.A. and A. Amirfazli, *Droplet impact onto a solid sphere: Effect of wettability and impact velocity*. *Physics of Fluids*, 2017. **29**(6): p. 062111.
70. Ancheyta, J., *Modeling and Simulation of Catalytic Reactors for Petroleum Refining*2011: Wiley.
71. Jakobsen, H.A., *Chemical Reactor Modeling: Multiphase Reactive Flows*2008: Springer.
72. Weekman, V.W. and D.M. Nace, *Kinetics of catalytic cracking selectivity in fixed, moving, and fluid bed reactors*. *AIChE Journal*, 1970. **16**(3): p. 397-404.
73. Yen, L.C., R.E. Wrench, and A.S. Ong, *Reaction kinetic correlation equation predicts fluid catalytic cracking coke yields*. *Journal Name: Oil Gas J.; (United States); Journal Volume: 86:2, 1988: p. Medium: X; Size: Pages: 67-69.*
74. Gupta, A. and D. Subba Rao, *Model for the performance of a fluid catalytic cracking (FCC) riser reactor: effect of feed atomization*. *Chemical Engineering Science*, 2001. **56**(15): p. 4489-4503.
75. Hirt, C.W. and B.D. Nichols, *Volume of fluid (VOF) method for the dynamics of free boundaries*. *Journal of Computational Physics*, 1981. **39**(1): p. 201-225.
76. Osher, S. and R. Fedkiw, *Level Set Methods and Dynamic Implicit Surfaces*. *Applied Mathematical Sciences*2003: Springer-Verlag New York.
77. Ryskin, G. and L. Leal, *Numerical solution of free-boundary problems in fluid mechanics. Part 1. The finite-difference technique*. *Journal of Fluid Mechanics*, 1984. **148**: p. 1-17.
78. Tryggvason, G., et al., *A front-tracking method for the computations of multiphase flow*. *Journal of Computational Physics*, 2001. **169**(2): p. 708-759.

79. Enright, D., et al., *A Hybrid Particle Level Set Method for Improved Interface Capturing*. Journal of Computational Physics, 2002. **183**(1): p. 83-116.
80. Singh, R., *Three-dimensional marker-based multiphase flow computation using adaptive Cartesian grid techniques*, 2006, University of Florida.
81. Youngs, D.L., *Time-dependent multi-material flow with large fluid distortion*. Numerical methods for fluid dynamics, 1982. **24**(2): p. 273-285.
82. Renardy, Y. and M. Renardy, *PROST: A Parabolic Reconstruction of Surface Tension for the Volume-of-Fluid Method*. Journal of Computational Physics, 2002. **183**(2): p. 400-421.
83. Scardovelli, R. and S. Zaleski, *Interface reconstruction with least-square fit and split Eulerian–Lagrangian advection*. International Journal for Numerical Methods in Fluids, 2003. **41**(3): p. 251-274.
84. Scardovelli, R. and S. Zaleski, *Analytical Relations Connecting Linear Interfaces and Volume Fractions in Rectangular Grids*. Journal of Computational Physics, 2000. **164**(1): p. 228-237.
85. Owkes, M. and O. Desjardins, *A computational framework for conservative, three-dimensional, unsplit, geometric transport with application to the volume-of-fluid (VOF) method*. Journal of Computational Physics, 2014. **270**: p. 587-612.
86. Roenby, J., H. Bredmose, and H. Jasak, *A computational method for sharp interface advection*. Royal Society Open Science, 2016. **3**(11).
87. Ubbink, O., *Numerical prediction of two fluid systems with sharp interfaces*, 1997, Imperial College.
88. Muzaferija, S., et al., *A Two-Fluid Navier-Stokes Solver to Simulate Water Entry*. 22nd Symposium on Naval Hydrodynamics, Washington, DC,, 1998: p. 638-651.
89. Yokoi, K., et al., *Numerical studies of the influence of the dynamic contact angle on a droplet impacting on a dry surface*. Physics of Fluids, 2009. **21**(7): p. 072102-12.
90. Olsson, E. and G. Kreiss, *A conservative level set method for two phase flow*. Journal of Computational Physics, 2005. **210**(1): p. 225-246.
91. Olsson, E., G. Kreiss, and S. Zahedi, *A conservative level set method for two phase flow II*. Journal of Computational Physics, 2007. **225**(1): p. 785-807.
92. Sato, Y. and B. Ničeno, *A conservative local interface sharpening scheme for the constrained interpolation profile method*. International Journal for Numerical Methods in Fluids, 2012. **70**(4): p. 441-467.
93. Shukla, R.K., C. Pantano, and J.B. Freund, *An interface capturing method for the simulation of multi-phase compressible flows*. Journal of Computational Physics, 2010. **229**(19): p. 7411-7439.
94. Weller, H.G., *A new approach to VOF-based interface capturing methods for incompressible and compressible flow*2008, Technical Report TR/HGW/04: Open CFD Ltd.
95. So, K.K., X.Y. Hu, and N.A. Adams, *Anti-diffusion method for interface steepening in two-phase incompressible flow*. Journal of Computational Physics, 2011. **230**(13): p. 5155-5177.
96. So, K.K., X.Y. Hu, and N.A. Adams, *Anti-diffusion interface sharpening technique for two-phase compressible flow simulations*. Journal of Computational Physics, 2012. **231**(11): p. 4304-4323.
97. Lentine, M., et al., *Simulating free surface flow with very large time steps*, in *Proceedings of the 11th ACM SIGGRAPH / Eurographics conference on Computer Animation*2012, Eurographics Association: Lausanne, Switzerland. p. 107-116.
98. Brackbill, J.U., D.B. Kothe, and C. Zemach, *A continuum method for modeling surface tension*. Journal of Computational Physics, 1992. **100**(2): p. 335-354.

99. Lafaurie, B., et al., *Modelling Merging and Fragmentation in Multiphase Flows with SURFER*. Journal of Computational Physics, 1994. **113**(1): p. 134-147.
100. Cummins, S.J., M.M. Francois, and D.B. Kothe, *Estimating curvature from volume fractions*. Computers & Structures, 2005. **83**(6–7): p. 425-434.
101. Yokoi, K., *A practical numerical framework for free surface flows based on CLSVOF method, multi-moment methods and density-scaled CSF model: Numerical simulations of droplet splashing*. Journal of Computational Physics, 2013. **232**(1): p. 252-271.
102. Sussman, M. and E.G. Puckett, *A Coupled Level Set and Volume-of-Fluid Method for Computing 3D and Axisymmetric Incompressible Two-Phase Flows*. Journal of Computational Physics, 2000. **162**(2): p. 301-337.
103. Ménard, T., S. Tanguy, and A. Berlemont, *Coupling level set/VOF/ghost fluid methods: Validation and application to 3D simulation of the primary break-up of a liquid jet*. International Journal of Multiphase Flow, 2007. **33**(5): p. 510-524.
104. Dianat, M., M. Skarysz, and A. Garmory, *A Coupled Level Set and Volume of Fluid method for automotive exterior water management applications*. International Journal of Multiphase Flow, 2017. **91**: p. 19-38.
105. Fedkiw, R., *The Ghost Fluid Method for Numerical Treatment of Discontinuities and Interfaces*, in *Godunov Methods*, E.F. Toro, Editor 2001, Springer US. p. 309-317.
106. Helmsen, J., P. Colella, and E.G. Puckett, *Non-convex profile evolution in two dimensions using volume of fluids*. LBNL Technical Report LBNL-40693, Lawrence Berkeley National Laboratory, 1997.
107. Sussman, M., *A second order coupled level set and volume-of-fluid method for computing growth and collapse of vapor bubbles*. Journal of Computational Physics, 2003. **187**(1): p. 110-136.
108. Popinet, S., *An accurate adaptive solver for surface-tension-driven interfacial flows*. Journal of Computational Physics, 2009. **228**(16): p. 5838-5866.
109. Ito, K., et al., *A high-precision calculation method for interface normal and curvature on an unstructured grid*. Journal of Computational Physics, 2014. **273**: p. 38-53.
110. Ivey, C.B. and P. Moin, *Accurate interface normal and curvature estimates on three-dimensional unstructured non-convex polyhedral meshes*. Journal of Computational Physics, 2015. **300**: p. 365-386.
111. Francois, M.M., et al., *A balanced-force algorithm for continuous and sharp interfacial surface tension models within a volume tracking framework*. Journal of Computational Physics, 2006. **213**(1): p. 141-173.
112. Denner, F. and B.G.M. van Wachem, *Fully-Coupled Balanced-Force VOF Framework for Arbitrary Meshes with Least-Squares Curvature Evaluation from Volume Fractions*. Numerical Heat Transfer, Part B: Fundamentals, 2014. **65**(3): p. 218-255.
113. Roux, D.C. and J.J. Cooper-White, *Dynamics of water spreading on a glass surface*. Journal of colloid and interface science, 2004. **277**(2): p. 424-436.
114. de Gennes, P.G., *Wetting: statics and dynamics*. Reviews of Modern Physics, 1985. **57**(3): p. 827-863.
115. Kistler, S.F., *Hydrodynamics of wetting*. Wettability, 1993. **311**.
116. Tanner, L.H., *The spreading of silicone oil drops on horizontal surfaces*. Journal of Physics D: Applied Physics, 1979. **12**(9): p. 1473.
117. Hoffman, R.L., *A study of the advancing interface. I. Interface shape in liquid—gas systems*. Journal of colloid and interface science, 1975. **50**(2): p. 228-241.
118. Shikhmurzaev, Y.D., *Capillary flows with forming interfaces* 2007: CRC Press.

119. Ashish Saha, A. and S.K. Mitra, *Effect of dynamic contact angle in a volume of fluid (VOF) model for a microfluidic capillary flow*. Journal of colloid and interface science, 2009. **339**(2): p. 461-480.
120. Sui, Y., H. Ding, and P.D.M. Spelt, *Numerical Simulations of Flows with Moving Contact Lines*. Annual Review of Fluid Mechanics, 2014. **46**(1): p. 97-119.
121. Shin, S. and D. Juric, *Simulation of droplet impact on a solid surface using the level contour reconstruction method*. Journal of Mechanical Science and Technology, 2009. **23**(9): p. 2434-2443.
122. Mukherjee, S. and J. Abraham, *Investigations of drop impact on dry walls with a lattice-Boltzmann model*. Journal of colloid and interface science, 2007. **312**(2): p. 341-354.
123. Caviezel, D., C. Narayanan, and D. Lakehal, *Adherence and bouncing of liquid droplets impacting on dry surfaces*. Microfluidics and Nanofluidics, 2008. **5**(4): p. 469-478.
124. Griebel, M. and M. Klitz, *Simulation of Droplet Impact with Dynamic Contact Angle Boundary Conditions*. INS Preprint No. 1302, 2013.
125. Spelt, P.D.M., *Shear flow past two-dimensional droplets pinned or moving on an adhering channel wall at moderate Reynolds numbers: a numerical study*. Journal of Fluid Mechanics, 2006. **561**: p. 439-463.
126. Liu, H., et al., *Sharp interface Cartesian grid method II: A technique for simulating droplet interactions with surfaces of arbitrary shape*. Journal of Computational Physics, 2005. **210**(1): p. 32-54.
127. Clift, R., J.R. Grace, and M.E. Weber, *Bubbles, drops and particles* 1978, New York: Academic Press.
128. Sirignano, W.A., *Fluid Dynamics and Transport of Droplets and Sprays* 1999: Cambridge University Press.
129. Bird, R.B., W.E. Stewart, and E.N. Lightfoot, *Transport Phenomena*. 2nd ed 2002, New York: Wiley.
130. Asano, K., *Mass Transfer – from Fundamentals to Modern Industrial Applications* 2006, Weinheim, Germany: Wiley VCH Verlag GmbH & Co. KGaA.
131. Erbil, H.Y., *Evaporation of pure liquid sessile and spherical suspended drops: A review*. Advances in Colloid and Interface Science, 2012. **170**(1–2): p. 67-86.
132. Hertz, H., *Ueber die Verdunstung der Flüssigkeiten, insbesondere des Quecksilbers, im luftleeren Raume*. Annalen der Physik, 1882. **253**(10): p. 177-193.
133. Knudsen, M., *Die maximale Verdampfungsgeschwindigkeit des Quecksilbers*. Annalen der Physik, 1915. **352**(13): p. 697-708.
134. Rensizbulut, M. and R.J. Haywood, *Transient droplet evaporation with variable properties and internal circulation at intermediate Reynolds numbers*. International Journal of Multiphase flow, 1988. **14**(2): p. 189-202.
135. Haywood, R.J., R. Nafziger, and M. Rensizbulut, *Detailed examination of gas and liquid phase transient processes in convective droplet evaporation*. Journal of Heat Transfer, 1989. **111**(2): p. 495-502.
136. Chiang, C.H., M.S. Raju, and W.A. Sirignano, *Numerical analysis of convecting, vaporizing fuel droplet with variable properties*. International Journal of Heat and Mass Transfer, 1992. **35**(5): p. 1307-1324.
137. Megaridis, C.M., *Comparison between experimental measurements and numerical predictions of internal temperature distributions of a droplet vaporizing under high-temperature convective conditions*. Combustion and Flame, 1993. **93**(3): p. 287-302.

138. Shih, A.T. and C.M. Megaridis, *Suspended droplet evaporation modeling in a laminar convective environment*. Combustion and Flame, 1995. **102**(3): p. 256-270.
139. Shih, A.T. and C.M. Megaridis, *Thermocapillary flow effects on convective droplet evaporation*. International Journal of Heat and Mass Transfer, 1996. **39**(2): p. 247-257.
140. Abou Al-Sood, M.M. and M. Birouk, *A numerical study of the effect of turbulence on mass transfer from a single fuel droplet evaporating in a hot convective flow*. International Journal of Thermal Sciences, 2007. **46**(8): p. 779-789.
141. Raghuram, S., et al., *Two-phase modeling of evaporation characteristics of blended methanol-ethanol droplets*. International Journal of Multiphase flow, 2013. **52**(0): p. 46-59.
142. Megaridis, C.M. and W.A. Sirignano, *Numerical modeling of a vaporizing multicomponent droplet*. Symposium (International) on Combustion, 1990. **23**(1): p. 1413-1421.
143. Megaridis, C.M. and W.A. Sirignano, *Multicomponent droplet vaporization in a laminar convective environment*. Combustion Science and Technology, 1992. **87**(1-6): p. 27-44.
144. Megaridis, C.M., *Liquid-Phase Variable Property Effects in Multicomponent Droplet Convective Evaporation*. Combustion Science and Technology, 1993. **92**(4): p. 291 - 311.
145. Renksizbulut, M. and M. Bussmann, *Multicomponent droplet evaporation at intermediate Reynolds numbers*. International Journal of Heat and Mass Transfer, 1993. **36**(11): p. 2827-2835.
146. Zhang, H., *Evaporation of a suspended droplet in forced convective high-pressure environments*. Combustion Science and Technology, 2003. **175**(12): p. 2237-2268.
147. Ytrehus, T. and S. Østmo, *Kinetic theory approach to interphase processes*. International Journal of Multiphase Flow, 1996. **22**(1): p. 133-155.
148. Sazhin, S.S., *Advanced models of fuel droplet heating and evaporation*. Progress in Energy and Combustion Science, 2006. **32**(2): p. 162-214.
149. Nikolopoulos, N., A. Theodorakakos, and G. Bergeles, *A numerical investigation of the evaporation process of a liquid droplet impinging onto a hot substrate*. International Journal of Heat and Mass Transfer, 2007. **50**(1-2): p. 303-319.
150. Strotos, G., et al., *Non-dimensionalisation parameters for predicting the cooling effectiveness of droplets impinging on moderate temperature solid surfaces*. International Journal of Thermal Sciences, 2011. **50**(5): p. 698-711.
151. Strotos, G., et al., *Numerical investigation on the evaporation of droplets depositing on heated surfaces at low Weber numbers*. International Journal of Heat and Mass Transfer, 2008. **51**(7-8): p. 1516-1529.
152. Pasandideh-Fard, M., et al., *Cooling effectiveness of a water drop impinging on a hot surface*. International Journal of Heat and Fluid Flow, 2001. **22**(2): p. 201-210.
153. Schlottke, J. and B. Weigand, *Direct numerical simulation of evaporating droplets*. Journal of Computational Physics, 2008. **227**(10): p. 5215-5237.
154. Strotos, G., et al., *Numerical investigation of the evaporation of two-component droplets*. Fuel, 2011. **90**(4): p. 1492-1507.
155. Banerjee, R., *Numerical investigation of evaporation of a single ethanol/isooctane droplet*. Fuel, 2013. **107**(0): p. 724-739.
156. Ghata, N. and B.D. Shaw, *Computational modeling of the effects of support fibers on evaporation of fiber-supported droplets in reduced gravity*. International Journal of Heat and Mass Transfer, 2014. **77**: p. 22-36.

157. Harvie, D.J.E. and D.F. Fletcher, *A hydrodynamic and thermodynamic simulation of droplet impacts on hot surfaces, Part I: theoretical model*. International Journal of Heat and Mass Transfer, 2001. **44**(14): p. 2633-2642.
158. Gumulya, M., et al., *Evaporation of a droplet on a heated spherical particle*. Chemical Engineering Journal, 2015. **278**: p. 309-319.
159. Hardt, S. and F. Wondra, *Evaporation model for interfacial flows based on a continuum-field representation of the source terms*. J. Comput. Phys., 2008. **227**(11): p. 5871-5895.
160. *FLUENT 14.5. Theory Guide*, 2011.
161. Nikolopoulos, N., K.S. Nikas, and G. Bergeles, *A numerical investigation of central binary collision of droplets*. Computers & Fluids, 2009. **38**(6): p. 1191-1202.
162. Nikolopoulos, N., A. Theodorakakos, and G. Bergeles, *Normal impingement of a droplet onto a wall film: a numerical investigation*. International Journal of Heat and Fluid Flow, 2005. **26**(1): p. 119-132.
163. Nikolopoulos, N., A. Theodorakakos, and G. Bergeles, *Three-dimensional numerical investigation of a droplet impinging normally onto a wall film*. Journal of Computational Physics, 2007. **225**(1): p. 322-341.
164. Strotos, G., et al., *Numerical investigation of the cooling effectiveness of a droplet impinging on a heated surface*. International Journal of Heat and Mass Transfer, 2008. **51**(19–20): p. 4728-4742.
165. Strotos, G., et al., *Cooling effectiveness of droplets at low Weber numbers: Effect of temperature*. International Journal of Thermal Sciences, 2013. **72**(0): p. 60-72.
166. *FLUENT 14.5, Theory Guide*. 2011.
167. Kryukov, A.P., V.Y. Levashov, and S.S. Sazhin, *Evaporation of diesel fuel droplets: kinetic versus hydrodynamic models*. International Journal of Heat and Mass Transfer, 2004. **47**(12–13): p. 2541-2549.
168. Yaws, C.L., P.K. Narasimhan, and C. Gabbula, *Yaws' Handbook of Antoine Coefficients for Vapor Pressure (2nd Electronic Edition)*, 2009, Knovel.
169. Theodorakakos, A. and G. Bergeles, *Simulation of sharp gas–liquid interface using VOF method and adaptive grid local refinement around the interface*. International Journal for Numerical Methods in Fluids, 2004. **45**(4): p. 421-439.
170. Šikalo, Š., C. Tropea, and E.N. Ganić, *Impact of droplets onto inclined surfaces*. Journal of colloid and interface science, 2005. **286**(2): p. 661-669.
171. Antonini, C., et al., *General Methodology for Evaluating the Adhesion Force of Drops and Bubbles on Solid Surfaces*. Langmuir, 2009. **25**(11): p. 6143-6154.
172. Extrand, C.W. and Y. Kumagai, *Liquid Drops on an Inclined Plane: The Relation between Contact Angles, Drop Shape, and Retentive Force*. Journal of colloid and interface science, 1995. **170**(2): p. 515-521.
173. Zahedi, S., K. Gustavsson, and G. Kreiss, *A conservative level set method for contact line dynamics*. Journal of Computational Physics, 2009. **228**(17): p. 6361-6375.
174. Sato, Y. and B. Ničeno, *A new contact line treatment for a conservative level set method*. Journal of Computational Physics, 2012. **231**(10): p. 3887-3895.
175. *FLUENT, User's Guide, version 14.5*. ANSYS Inc., 2011.
176. Waclawczyk, T. and T. Koronowicz, *Comparison of CICSAM and HRIC High-Resolution Schemes for interface capturing*. Journal of Theoretical and Applied Mechanics, 2008. **46**(2): p. 325-345.
177. Zalesak, S., *Fully multidimensional flux-corrected transport algorithms for fluids*. J. Comput. Phys., 1979. **31**: p. 335-362.
178. Rider, W.J. and D.B. Kothe, *Reconstructing Volume Tracking*. Journal of Computational Physics, 1998. **141**(2): p. 112-152.

179. Ankit, V., R. Babu, and M.K. Das, *Modelling of a Single Bubble Rising in a Liquid Column*, in *Fluid Mechanics and Fluid Power – Contemporary Research: Proceedings of the 5th International and 41st National Conference on FMFP 2014*, A.K. Saha, et al., Editors. 2017, Springer India: New Delhi. p. 1059-1068.
180. Cano-Lozano, J.C., et al., *The use of Volume of Fluid technique to analyze multiphase flows: Specific case of bubble rising in still liquids*. Applied Mathematical Modelling, 2015. **39**(12): p. 3290-3305.
181. Boháček, J., *Effect of flow parameters of water and air atomized sprays on cooling intensity of hot surfaces*, 2011, Brno University of Technology.
182. Feng, Z.-G. and E.E. Michaelides, *Drag Coefficients of Viscous Spheres at Intermediate and High Reynolds Numbers*. Journal of Fluids Engineering, 2001. **123**(4): p. 841-849.
183. Clift, R., J.R. Grace, and M.E. Weber, *Bubbles, drops, and particles*, ed. J.R. Grace and M.E. Weber 1978, New York: Academic Press.
184. Michaelides, E.E., *Particles, Bubbles & Drops: Their Motion, Heat And Mass Transfer* 2006: World Scientific Publ.
185. Killion, J.D. and S. Garimella, *Simulation of Pendant Droplets and Falling Films in Horizontal Tube Absorbers*. Journal of Heat Transfer, 2005. **126**(6): p. 1003-1013.
186. Maitra, T., et al., *On the Nanoengineering of Superhydrophobic and Impalement Resistant Surface Textures below the Freezing Temperature*. Nano Letters, 2013. **14**(1): p. 172-82.
187. Zhang, D., K. Papadakis, and S. Gu, *Application of a high density ratio lattice-Boltzmann model for the droplet impingement on flat and spherical surfaces*. International Journal of Thermal Sciences, 2014. **84**(0): p. 75-85.
188. Gianetto, A., et al., *Fluid Catalytic Cracking Catalyst for Reformulated Gasolines. Kinetic Modeling*. Industrial & Engineering Chemistry Research, 1994. **33**(12): p. 3053-3062.
189. Yaws, C.L., *Thermophysical Properties of Chemicals and Hydrocarbons* 2014: Elsevier Science.
190. Yaws, C.L., *Transport Properties of Chemicals and Hydrocarbons* 2014: Elsevier Science.
191. Green, D.W. and R.H. Perry, *Perry's Chemical Engineers' Handbook, Eighth Edition* 2007: McGraw-Hill Education.
192. Riazi, R., *Characterization and Properties of Petroleum Fractions* 2005: ASTM International.
193. Du, Y., et al., *An integrated methodology for the modeling of Fluid Catalytic Cracking (FCC) riser reactor*. Applied Petrochemical Research, 2014. **4**(4): p. 423-433.
194. Fuller, E.N., P.D. Schettler, and J.C. Giddings, *NEW METHOD FOR PREDICTION OF BINARY GAS-PHASE DIFFUSION COEFFICIENTS*. Industrial & Engineering Chemistry, 1966. **58**(5): p. 18-27.
195. Mahulkar, A.V., G.B. Marin, and G.J. Heynderickx, *Droplet-wall interaction upon impingement of heavy hydrocarbon droplets on a heated wall*. Chemical Engineering Science, 2015. **130**: p. 275-289.
196. Wong, S.C. and A.C. Lin, *Internal temperature distributions of droplets vaporizing in high-temperature convective flows*. Journal of Fluid Mechanics, 1992. **237**: p. 671-687.
197. Nomura, H., et al., *Experimental study on high-pressure droplet evaporation using microgravity conditions*. Symposium (International) on Combustion, 1996. **26**(1): p. 1267-1273.

198. Qiao, Y.M. and S. Chandra, *Boiling of droplets on a hot surface in low gravity*. International Journal of Heat and Mass Transfer, 1996. **39**(7): p. 1379-1393.
199. Harvie, D.J.E. and D.F. Fletcher, *A hydrodynamic and thermodynamic simulation of droplet impacts on hot surfaces, Part II: validation and applications*. International Journal of Heat and Mass Transfer, 2001. **44**(14): p. 2643-2659.